BREAKING NEW GROUND

AALBORG UNIVERSITY

REMOVAL OF **AUDIBLE RESONANCE** FROM TURF TANK LINE MARKING ROBOT & DESIGN OF **ALL-WHEEL DRIVE** ROBOTIC **LAWN MOWER**

Institute for Materials and Production
Electro-Mechanical System Design
Fibigerstræde 16
9220 Aalborg Øst

Title:

Removal of Audible Resonance from Turf Tank Line Marking Robot & Design of All-Wheel Drive Robotic Lawn Mower

Project:

Long Thesis

Project period:

September 2024 - June 2025

Project group:

EMSD3/4-8

Participants:

Daniel Sylvester Jeppesen
Mads Trygve Tygesen
Peter Morley

Supervisor:

Peter Omand Rasmussen

Report page count: 128

Appendix page count: 25

Total page count: 156

Concluded: 30th of May

Abstract

The project is written in collaboration with Turf Tank, which is a company specialising in line marking robots. They are looking to branch out into industrial-grade robotic lawn mowers. Turf tanks current in development mower is large and designed for cutting large open areas quickly. It is not designed for very rough terrain, such as sometimes found in the semi-rough or rough on a golf course, or for tighter areas in between trees and the like. Therefore, a smaller all-terrain mower is developed in this project, which aims to fulfil tasks which the large mower is not designed to handle. However, their line marking robot has certain issues, which sometimes cause significant audible noise or terrain damage. These problems are to be solved first, so the issues are not transferred over to Turf Tanks in development lawn mower or the prototype to be designed in this project. The audible noise problem is investigated and found to come from resonance in the chassis excited by the motor control. Due to costs, it is not desired to alter the mechanical system, so a software solution is wanted. Several things are implemented, the velocity estimate is improved, the control is tuned for a first-order response where possible, and filtering is applied to the velocity estimate to filter out the resonant frequencies. Removal of the audible noise is successful, and the controller bandwidth is increased in the process. The line marking robot's performance is marginally improved. The terrain damage is found to stem from wheel slip, and as such this is to be avoided in the design of the mower. The learnings from the line marking robot are carried over to Turf Tank's mower design and the prototype in this project, ensuring they will not have the same issues. The small mower focuses on off-road capabilities and maintaining good cutting quality. For this all wheel drive and suspension is added. An articulated steering configuration is chosen which enables zero turning and low mechanical complexity. To be able to control this, a model of the system is created, and non-linear state-dependent control is developed afterwards. Furthermore, a suspension model is created to determine the performance effects of adding suspension, and eventually for tuning the suspension for the mower. Ultimately, the mower is tested at Aalborg golf course. Here, satisfactory cutting quality is achieved. The mower fulfils the majority of the requirements set. Several things have been learned from the mower concept developed in this project, which can be utilised in further development as described in the future work chapter.

Preface

The following master's thesis is written by a group of Electro-Mechanical System Design students at Aalborg University between the 2nd of September 2024 and the 30th of May 2025.

The group would like to sincerely thank Turf Tank ApS for their engagement in the project collaboration, for providing a workplace for each group member, for financing the project, providing a robot for testing and letting the group eat at the canteen.

The group would like to extend special thanks to Søren Elton Mark, Lead System Engineer at Turf Tank ApS, for his time and effort dedicated to the project.

The group would like to thank Aalborg Golf Club for their engagement in the process of defining requirements for the mower, letting the group use their golf course for testing and lending the grass prism.

The group would like to thank Peter Omand Rasmussen for his guidance.

Reading Guide

Throughout the report, references will follow the Vancouver method. In the text, references to scientific articles, books, Technical documentation and web pages will be shown with the corresponding number that the given source is assigned in the bibliography.

Equation references are in parentheses. As such equation x.y will be replaced by Eqn. (x.y)

When bold letters are used, it indicates a vector, if the letter is lower case $\mathbf{x}$, and a matrix, if the letter is upper case $\mathbf{X}$.

Figures without listed sources are original creations by the authors of this report.

Summary

This project is in collaboration with Turf Tank. Turf Tank specialises in line marking robots, primarily for sports applications. They are currently also branching out into the industrial robotic lawn mower market. Currently, their Turf Tank Two and Lite line marking robots are facing problems with audible noise. During line marking, it sometimes abruptly starts vibrating. The robots also sometimes damage the fields they are painting, if they are composed of loose soil, which is also undesirable. This leads to the following initial problems:

- The Turf Tank Two robot is noisy while operating.
- Turf Tank robots sometimes damage field surfaces.

Turf Tank wants to find the root cause behind these issues and investigate whether a software solution exists which does not decrease trajectory tracking performance. This is due to the potentially large expense of mass-recalling all robots and making mechanical changes. They would also like to avoid transferring these issues to their robotic lawn mower in development.

Turf Tank's in development mower is made to cover large and smooth grass fields present at golf courses and sports fields, among others. In the future, Turf Tank may want to expand their operating area to cover more challenging terrain with slopes up to 80 %. This leads to an investigation of the following:

- How can a robotic mower be developed for operation on the terrain specified by Turf Tank?

The Turf Tank Two and Lite are differential drive robots with bent sheet aluminium frames. The control system is based around an model-predictive control (MPC) trajectory controller and 120° commutation motor velocity control. It is assumed that the problems stem from the motor control, and the trajectory controller is therefore left untouched. Before the problem analysis, a benchmark of the trajectory tracking performance using Turf Tank's validation trajectory is performed. This is used for comparison later. As part of fixing the issues, Turf Tank also wants to transition from 120° commutation to field-oriented control (FOC). Turf Tank has already implemented FOC, but it only made the problems worse. The starting point for the investigation is therefore this FOC implementation. The implementation is separated into its parts: the output transform, the modulation scheme, the velocity estimation and the controller. Each is individually analysed. No unexpected or problematic behaviour is found in any of the parts. Next, a frequency spectrum of the robot chassis is generated by striking the robot with a hammer and recording the audio. This showed spikes at frequencies low enough to be potentially problematic, which are hypothesised to be the cause of the audible noise issue. This is noted and will also be used for setting requirements for the mower.

The cause of the surface damage is analysed with visual material provided by Turf Tank. In a video, it is discovered that the robot's wheels slip when the surface is damaged. The points where slip occurs align with discontinuities in the trajectory when transitioning from a line to a circular arc and vice versa.

Based on the analyses, the problem is formulated:

How can a software solution be developed for the line marking robots, such that it can perform line marking without audible excitation of the robot's natural frequencies while obtaining equivalent or better trajectory tracking performance to the currently in use commutated control along with mitigating torque inputs causing the wheels to slip?

The problem statement only concerns the audible noise problems for the Turf Tank Two and Lite. The surface damage problem will instead be considered for the design of the mower.

Based on the problem statement and the performed benchmark, requirements and wishes are formulated. Four different solutions are proposed: detuning of FOC implementation, tuning the FOC implementation for a first-order response, revamping the velocity estimate and a combined solution utilising the previous two along with a feedback current gain, notch filter and bumpless transfer.

Detuning the FOC implementation by scaling the gains by a factor < 1 results in a solution that fulfils the requirements, but decreases performance regarding the wishes. Different solutions are therefore explored.

First-order linear velocity dynamics are achieved by first constructing a simplified and undamped dynamic model. A proportional-integral (PI) controller is applied and tuned using pole-zero cancellation to achieve approximate first-order dynamics. This solution performs worse than the benchmark and thereby does not fulfil the requirements.

Multiple methods for improving the velocity estimation are reviewed wrt. their hardware requirements and performance implications from hardware tolerances. Based on the review, the "combined" method is chosen for its low complexity and promising performance characteristics. The method combines time and positional information from the digital signals encoders generate during rotation. The method is implemented on the STM32F446ZE present on the Turf Tank Two and Lite using the microcontroller (μC)'s hardware peripherals due to the high rate of encoder edges. Due to hardware limitations, it is only possible to gather data on a quarter of the edges generated by the encoder. The method is also modified such that the estimated velocity decays toward zero if the data rate is decreasing. Implementing the method reduces the noise on the velocity estimate while maintaining the bandwidth. This allows the FOC controller gains to be increased, fulfilling the requirements and increasing performance concerning the wishes.

The last proposed solution builds on top of the new velocity estimate. A notch filter corresponding to the vibration frequency observed in the problem analysis is added to the feedback. An additional gain is also added to the current in the control structure. This moves the system poles further from each other. A bumpless transfer based on the velocity reference is also added to compensate for the lower bandwidth of the velocity estimate at lower speeds. All these additions allow increasing the closed-loop control bandwidth further. This solution fulfils the requirements and performs better concerning the wishes. First-order dynamics are achieved with zero angular velocity, but the trajectory tracking performance only improves marginally.

With the solution for the line marking robot completed, the project was ready to progress on to designing a new prototype robotic lawn mower while keeping in mind the knowledge gained from the work with the line marking robot. This begins with a formulation of requirements and wishes the prototype should fulfil. These are formulated in collaboration with Turf Tank as well as Aalborg Golf Club. The focus is put on terrain going capabilities and maintaining good cutting quality. Effort is also put into a clear definition of how cut grass is

to be measured, how to determine if specific areas should be cut per the requirements or if they lie outside the terrain the robot can be expected to perform well on.

After the definition of requirements, wishes and the clarification of how to measure grass and when requirements are to be met, the focus is put on a technical analysis. This has the goal of gathering the necessary theory allowing for making educated decisions and calculations when designing the prototype mower. The technical analysis starts with a dive into off road theory, gathered from several different books on the subject. This touches subjects such as terrain theory, the forces acting on a off-road vehicle, generation of thrust in off-road terrain and how different vehicle parameters affect this and lastly the theory of tyre lugs and how these can be used to improve the tractive effort of the vehicle.

From the technical analysis it is clear that maintaining contact with the terrain is important to be able to transfer power from wheels to terrain and generate thrust. Therefore suspension is examined next, this is done through a half-car suspension model. Here suspensions effects on contact time and cutting quality is examined through a series of simulations. To have proper terrain data for the model, a terrain measurement device is designed and produced. This is used at Aalborg Golf Club to gather terrain data at a site where the mower is expected to operate. Through this analysis suspension is found to have a significant positive effect on both contact time and cutting quality.

Based on the technical analysis several insights are gained which are used in the solution design of the prototype mower. The solution design starts with a concept generation where concepts are chosen for the steering mechanism, the suspension type and the drive unit. Here focus is put on off-road performance, mechanical simplicity and proper sensor feedback from the drive units. Four regular tyres with all wheel drive is selected, powered by an in wheel planetary gearbox and motor combination. For the suspension, double wishbones are chosen because of simplicity and the room they make for the outboard motor. The steering concept consists of a fixed front axle and a rotating rear axle. After designing the mechanical system, the electrical system for the robot is designed with a focus on functionality and safety. For safety, a dead man's switch is added, allowing for remote deactivation of the mower.

A control system is developed that takes a model-based approach. The mower dynamics are modelled with a Lagrangian approach. First, the constrained dynamics are obtained. The system is then transformed to an unconstrained form, from which a non-linear state-space model can be formulated. The system is over-actuated and therefore an input transformation is utilised to alleviate this problem. The model is then used to develop a non-linear state-dependent feedback controller. This is done to obtain linear and decoupled dynamics. This is implemented and validated through experiments.

Through testing it is found that the implemented control can result in excessive wheel slip, due to a lack of a true vehicle velocity. To combat this a model following approach is used to estimate what the individual wheel velocities should be. This data is then used to redistribute torque to reduce wheel slip and to utilise traction better on the wheels that are not slipping. Through testing, these implementations are found to reduce the severity of the observed problems.

Finally, the mower is tested at Aalborg Golf Club and at the field of Kristian Rytter ApS. Here it is found to fulfil the majority of requirements and wishes. However, some requirements were not possible to test due to various reasons, and therefore concluded upon. Lastly, proposals for future work are made.

Contents

*

Acronyms

Acronyms

μC	Microcontroller
ADC	Analog to digital converter
AWD	All wheel drive
CAD	Computer-aided design
CAN bus	Controller area network bus
CC1IF	Capture compare 1 interrupt flag
CCR	Capture compare register
CoM	Center of mass
CPR	Counts per revolution
CPU	Central processing unit
CTE	Cross-track error
DDMR	Differential-drive mobile robot
DMA	Direct memory access
DNL	Differential non-linearity
DoF	Degree of freedom
EoM	Equation of motion
FEA	Finite element analysis
FIFO	First-in first-out
FOC	Field-oriented control
GNSS	Global navigation satellite system
GUI	Graphical user interface
HPF	High-pass filter
ICR	Instantaneous centre of rotation
IMU	Inertial measurement unit
ISR	Interrupt service routine
LCM	Least common multiple
LiPo	Lithium-Ion Polymer
LPF	Low-pass filter
MACE	Mean absolute cut error

MACTE	Mean absolute cross-track error
MAPS	Magnetic angle position sensor
MoI	Moment of inertia
MOSFET	Metal-oxide-semiconductor field-effect transistor
MPC	Model-predictive control
NDTR	Number of data to be transferred
NVI	Newest value index
OPAMP	Operational amplifier
PD	Proportional-derivative
PI	Proportional-integral
PMSM	Permanent magnet synchronous motor
PPR	Pulses per revolution
PWM	Pulse-width modulation
RAM	Random-access memory
RC	Radio control
RMS	Root mean square
RMSCE	Root mean square cut error
RMSCTE	Root mean square cross-track error
RTK-GNSS	Real-time kinematic positioning - global navigation satellite system
RTOS	Real-time operating system
SPWM	Sine-triangle pulse width modulation
TPU	Thermoplastic polyurethane

1 | Introduction

This project is written in collaboration with Turf Tank. Turf Tank is a company that specialises in autonomous line marking of fields within various sports. These sports can be anything from football to lacrosse to athletics and many more. The line marking is carried out using line marking robots as seen in Figure 1.1.

Figure 1.1
Picture showing the Turf Tank Two robot [1].

The line marking robot presented in Figure 1.1 is named Turf Tank Two, which is their newest version of line marking robots. The robot follows a trajectory, such as the lines of a football field. Simultaneously, a sprayer, mounted below the white box in Figure 1.1, paints onto the field to draw the lines.

Turf Tank is also expanding their services into the industrial lawn mowing business. They are currently developing a robotic lawn mover focused on cutting grass at golf courses and sports fields. Their mower is designed to have a large cutting capacity by having a cutting width of 105 cm and an operating speed of 2 m/s. In terms of mobility, their robot is designed to operate on flat to moderately sloped terrain without too large curvature, obstacles or narrow passages. An example of this terrain is golf course fairways, semi rough in most areas and sports fields. If Turf Tank in the future wants to expand their mowing services to cover more challenging terrain that their current in-development mower cannot operate on, an additional mower is needed. As a result, Turf Tank has an interest in the development of a proof-of-principle prototype (hereafter referenced as prototype) mower that enables mowing on this more challenging terrain. This involves operating on slopes of up to 80 % with larger curvature and more uneven terrain surfaces with, for example, larger indents, holes and roots. These terrain conditions are, for example, present at golf courses on the semi-rough, rough and banks around sports fields. A mower prototype can enable Turf Tank to obtain knowledge on what is required to enable operation on

this more challenging terrain. Turf Tank can thereby have a more informed basis to make business decisions on whether or not they want to add this type of mower to their product line-up.

However, before developing a mower prototype, Turf Tank wants to solve two problems with the line marking robot. The robot sometimes makes unwanted audible noise and damages the terrain on specific surface types. By finding their root causes and solving these problems, Turf Tank wants to ensure that these problems are not carried over to their mower in development. In solving these problems, trajectory tracking performance cannot be worsened.

The quality of the line marking largely depends on the robot's ability to follow the trajectory with high accuracy. This is in part obtained by locating the robot with high accuracy. How this accuracy is obtained will be described in later chapters. The robot's location relative to the trajectory can then be used as input for the motor control that moves the robot.

Turf Tank evaluates the performance of their robot trajectory tracking systems on one parameter cross-track error (CTE). CTE is pictured in Figure 1.2. Here, it is seen that CTE is defined as the perpendicular distance the robot is from the desired trajectory.

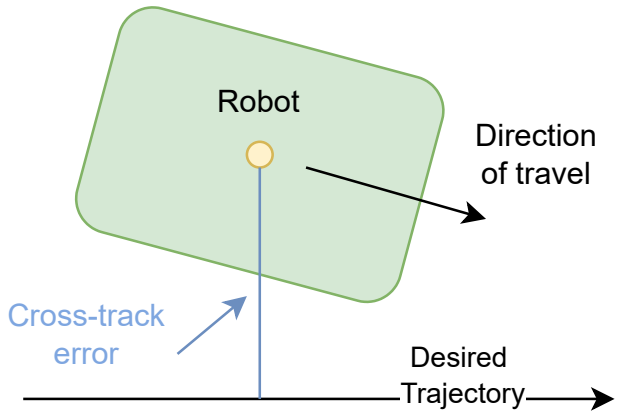

Figure 1.2
Illustration showing the physical understanding of CTE.

With the Turf Tank Two's current control scheme, the motors are controlled using 120° commutation, allowing the robot to stay within the tolerance of ±7,6 mm[1]. The robot is audibly noisy during operation, which is unpleasant. Therefore, Turf Tank wants to eliminate the audible noise while maintaining accuracy, and in conjunction with the attempted fix for the audible noise, they have also decided to move to FOC. Their implementation of FOC has, however, shown to be unacceptable as the audible noise levels have increased. From this comes a wish to fix their implementation of FOC such that the original audible noise problem is removed while retaining equivalent or better performance to the 120° commutation control.

The second problem Turf Tank is damage to some terrain surfaces the robot operates on. This causes unsightly markings and an uneven surface. An example of a damaged clay tennis court is seen in Figure 1.3. This is an unwanted behaviour as customers do not want their fields damaged. As a result, Turf Tank wants to solve this problem.

Figure 1.3
Example of tennis court damaged by Turf Tanks line marking robot [1].

Due to the large number of robots that Turf Tank already has in service around the world, recalling these to make physical changes as solutions to the above-discussed problems would be costly. Possible solutions are limited to software changes, with hardware changes reserved for future revisions of the robot. This limitation is an addition to Turf Tank's two problems, consisting of field surface damage and noisy operation.

A problem analysis is thus carried out to determine the underlying issues causing the following initial problems:

- The Turf Tank Two robot is audibly noisy while operating.
- Turf Tank robots sometimes damage field surfaces.

Following the analysis and improvements made for the line marking robots, development of a mower prototype will take place. This will be focused on obtaining the necessary performance of the vehicle, for it to be able to cut grass acceptably on the terrain, which will be specified later in the requirements.

For the mower development, a requirement definition followed by a technical analysis is carried out to investigate:

- How can a robotic mower be developed for operation on the terrain specified by Turf Tank?

2 | Problem Analysis

In this chapter, a problem analysis will be performed on the two initial problems with audible noise and terrain surface damage. This will start with a general overview of the Turf Tank Two's mechanical and control systems. This will involve getting a more detailed understanding of the system in control of positioning the Turf Tank Robot when following a trajectory. Following that, a baseline performance test of Turf Tanks 120° commutation control will be performed such that the trajectory tracking performance of Turf Tanks FOC implementation can be assessed. As Turf Tanks problem is audible noise, it is of interest to investigate two areas of the robot for the root causes of the issue. This consists of the control system, including the FOC implementation, the natural frequencies of the line marking robot and the motor mounting on the line marking robot.

Secondly, Turf Tank's problem of damaging terrain surfaces will be investigated. This will be done by first characterising unacceptable terrain surface damage. Here, photos and videos provided by Turf Tank will be used for the characterisation. This will be followed by an analysis of the causes of unacceptable terrain damage. Here, video material with corresponding data from the trajectory tracking control loop will be analysed.

2.1 Turf Tank Two General Overview

In the following section, a general overview of the Turf Tank Two robot will be given. This will first involve a short introduction to the mechanical system with a focus on the drivetrain, followed by an explanation of the control system of the line marking robot.

Mechanical System

As can be seen from Figure 2.1, the current iteration of Turf Tank's robots is a simple platform, from a mechanical drivetrain perspective.

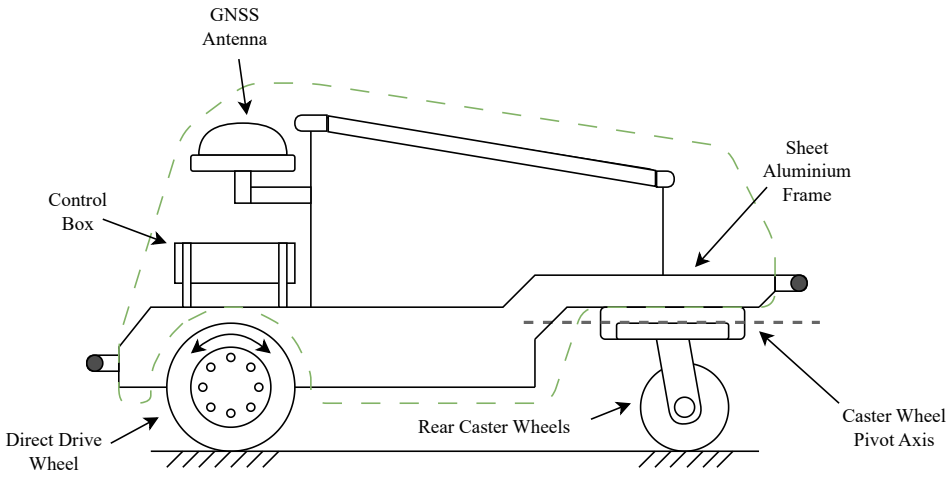

Figure 2.1

Sketch showing the primary components of the Turf Tank Two.

The robot consists of a frame made of bent aluminium sheets, and two 15-pole pair direct drive permanent magnet synchronous motors (PMSMs) mounted directly to the frame at the front of the robot. The line marking robot is therefore set up in a differential drive configuration. The PMSMs are out-runners, meaning the rotor is the outer shell of the motor. On this shell, a tyre is moulded to create a complete tyre/motor assembly, which is mounted to the frame by the stator shaft. Two caster wheels are mounted at the rear of the robot, on a pivoting bracket to allow for roll relative to the terrain. The pivot axis can be seen in Figure 2.1. This allows four-wheel contact on an arbitrary doubly curved surface. With the mechanical components of the line marking robot's drive train described, the control system of the Turf Tank Two robot will be described next.

Trajectory tracking Control System of the Turf Tank Two

The following section will explain the trajectory tracking control system further. This will be done with a block diagram that can be seen in Figure 2.2. The block diagram shows the trajectory tracking control loop.

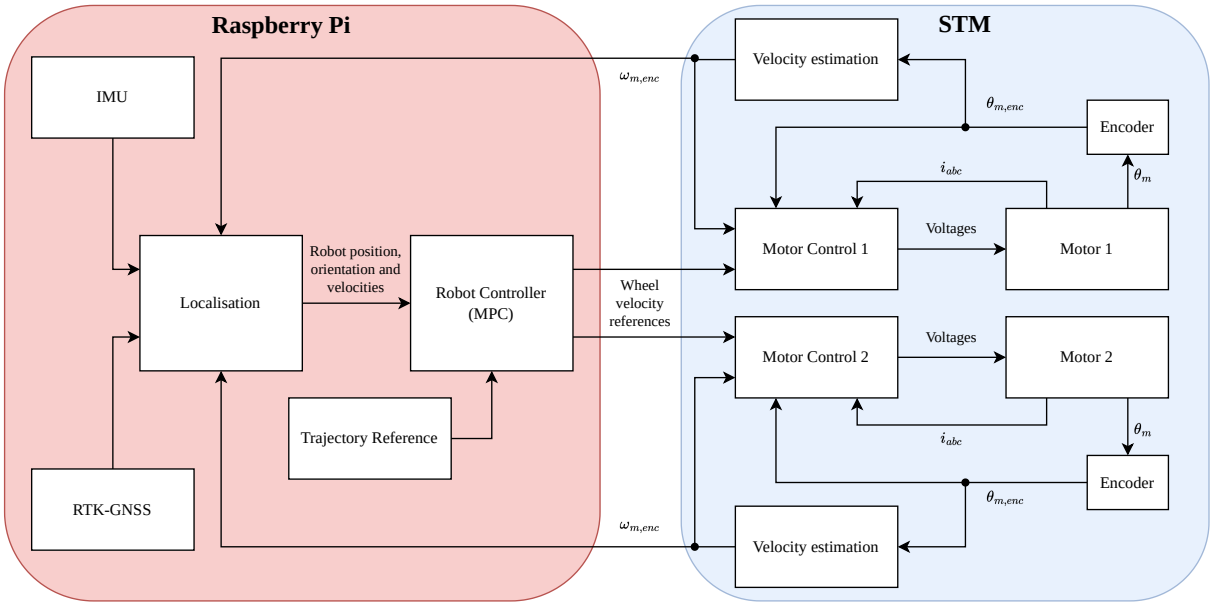

Figure 2.2

Figure showing the general control structure operating on the robot. The red box contains the responsibilities of the Raspberry Pi and the blue of the μC

The control loop starts on the Raspberry Pi with the localisation algorithm, which estimates the robot's position, orientation, and linear and angular velocities by fusing real-time kinematic positioning - global navigation satellite system (RTK-GNSS), inertial measurement unit (IMU) and motor velocity measurements. The RTK-GNSS measurements are obtained using a global navigation satellite system (GNSS) module on the robot, along with an external fixed reference station. The reference station transmits corrective data to the robot to enhance the accuracy of the GNSS measurements. The IMU measures linear acceleration, angular velocities and orientation and the motor velocity measurements are obtained from the μC. This estimate and the reference trajectory are fed to the MPC robot controller, which computes the wheel velocity references by optimisation of various weighted parameters over the prediction horizon. These parameters include but are not limited to CTE, linear velocity error, linear velocity reference derivative, and angular velocity reference derivative. The mechanical prediction model in the robot controller is based on two decoupled and linear first-order models from angular and linear velocity references to linear and angular velocity, each with their own fixed time constant. The linear and angular velocity references are then transformed into wheel velocity references and transmitted to the μC,

which controls the two motors. In each motor control loop, the phase currents i_{abc} and encoded position $\theta_{m,enc}$ are measured. The wheel velocity $\omega_{m,enc}$ is then estimated from encoder position measurements. The output is generated using a PI controller and 120° commutation control of a three-phase single-level voltage source pulse-width modulation (PWM) inverter.

With the trajectory tracking control system of the Turf Tank Two robot described, baseline performance of their 120° commutation control will be established in the next section.

Baseline Performance of 120° Commutation Control

As mentioned in Chapter 1, Turf Tank has a problem with removing audible noise from their implementation of FOC while maintaining equivalent or better performance to their commutated control. Turf tank evaluates their control performance on CTE, which is defined in Chapter 1. To ensure that accuracy is maintained, a baseline benchmark of the currently in use commutated control is performed. The trajectory used is a validation trajectory provided by Turf Tank and can be seen in Figure 2.3.

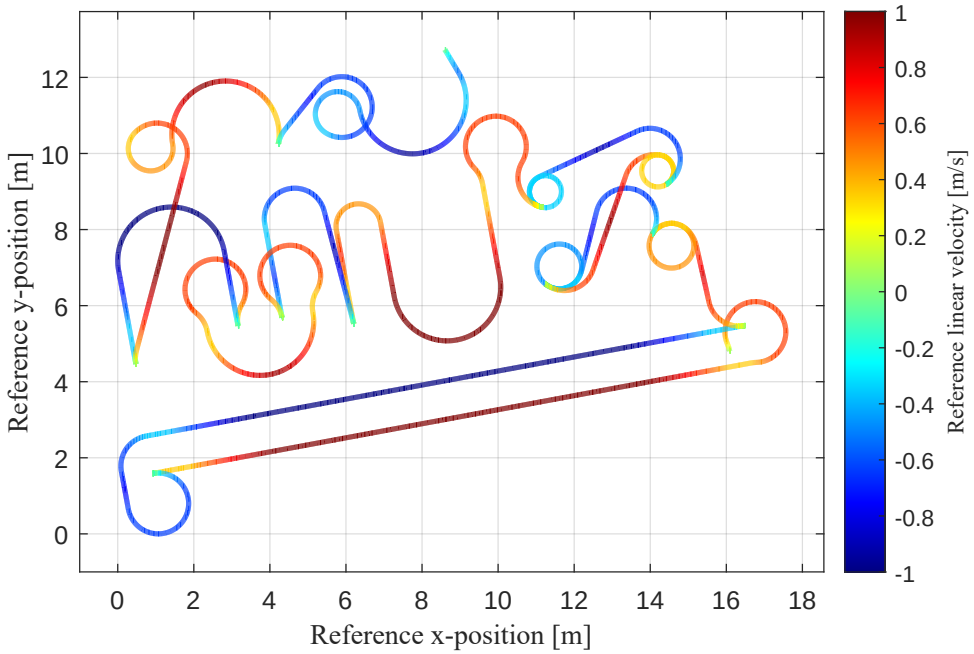

Figure 2.3

Turf Tank's validation trajectory used to establish the baseline performance of Turf Tank's 120° commutation control. The trajectory approximately starts in the coordinate (17,5). The colour bar on the right shows the colour corresponding to the linear velocity reference at each location.

The validation trajectory gives good insight into the trajectory tracking performance as the robot is put through many of the manoeuvres performed while line marking. The test is performed at Kristian Rytter ApS' field located next to Turf Tanks headquarters. The grass field is of low quality, meaning it is not smooth, slippery and with many bumps and holes. A higher quality grass field, similar to customers' fields, would have been preferable to minimise deviations between tests and to make comparisons between control structures more reliable. There were at the time of this project no other test facilities available. The baseline test and tests performed in later chapters will therefore all be performed at Kristian Rytter ApS' field.

The validation trajectory is run and a plot of the CTE is shown in Figure 2.4. This is the absolute value normalised

by the maximum absolute CTE from the test.

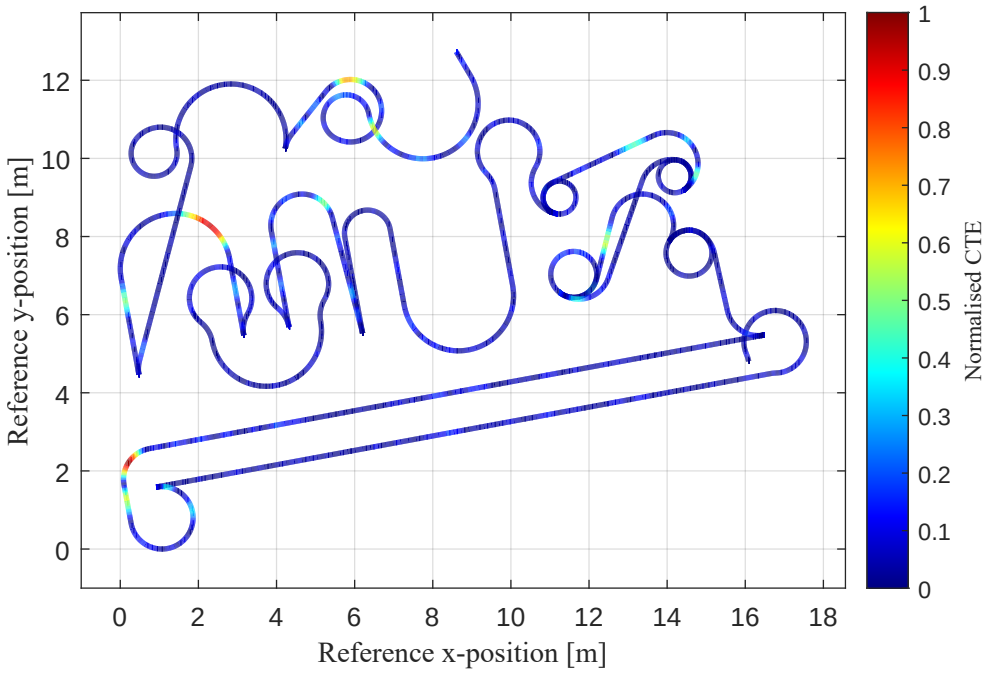

Figure 2.4

Normalised CTE from performing Turf Tanks validation trajectory at Kristian Rytter ApS' field. The CTE is from using Turf Tank's commutated control currently in use on their robots in service.

Inspecting Figure 2.4, the CTE is generally consistently low, except in specific manoeuvres. These manoeuvres are transitions from lines to arcs, with the highest values when driving backwards. This occurs at approximately (6 m,12 m) in Figure 2.4. To evaluate the trajectory tracking accuracy, the metrics in Eqn. (2.1) will be used.

$$\text{MACTE} = \frac{1}{L}\int |\text{CTE}| dS, \qquad \text{RMSCTE} = \sqrt{\frac{1}{L}\int \text{CTE}^2 \text{d}S} \tag{2.1}$$

mean absolute cross-track error (MACTE) is the mean absolute CTE, root mean square cross-track error (RMSCTE) is the root mean square CTE, L is the total trajectory length, and dS is the increment in the length travelled along the trajectory.

The reason for integrating along the trajectory instead of in time is that the error between the reference trajectory and the resulting painted trajectory is important. These metrics should not be influenced by the velocity of the robot, as this is not important for the end result.

The MACTE and RMSCTE performance metrics are chosen because they give a broad representation of the tracking performance. MACTE gives an insight into the mean error, and RMSCTE an insight into the error if outliers are penalised higher, similar to the mean and standard deviation of a normal distribution. The validation pattern is ≈150 m long, which is deemed enough for reliable comparisons. With the baseline performance established, the motor control system will be analysed, followed by an investigation of the robot's natural frequencies.

2.2 Analysis of Turf Tanks Control System

In the following section Turf Tank's implementation of FOC will be described. This is done to initially check if there are any indicators as to where the problem with audible noise can originate from, and to establish an understanding of their implementation. Turf Tanks FOC implementation will be described using the block diagram seen in Figure 2.5.

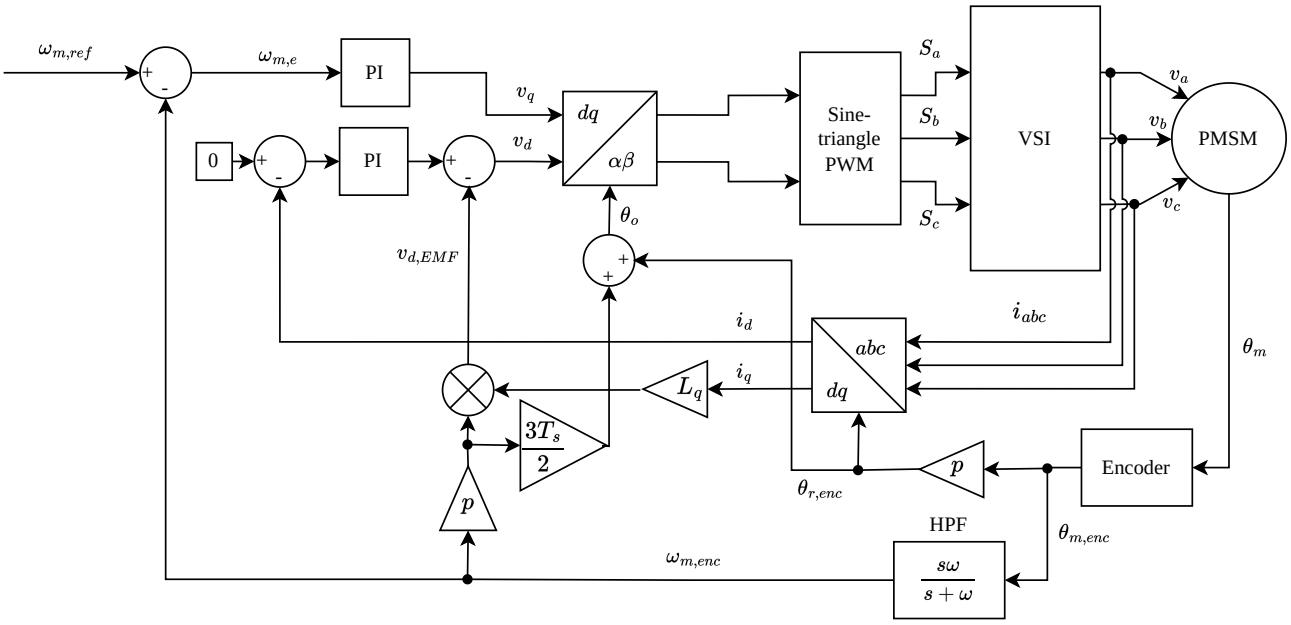

Figure 2.5

Turf Tanks current FOC implementation.

Firstly, the three-phase currents i_{abc} and the encoder position $\theta_{m,enc}$ are sampled. The phase currents are measured using low-side shunt resistors, operational amplifier (OPAMP) circuits and an analog to digital converter (ADC) in the μC, while all the low-side MOSFETs are ON. A counter in the μC increments or decrements following the rotation of the magnetic encoder. The currents are then transformed from abc to $dq0$ using the sampled encoder position, and the velocity $\omega_{m,enc}$ is estimated using a 45 Hz high-pass filter (HPF) applied to the position. The HPF is a differentiator and low-pass filter (LPF) in series with a resulting transfer function of $\frac{s\omega}{s+\omega}$, which can also be seen in the bottom right of Figure 2.5. The d-axis current error and velocity error are then calculated. The d-axis voltage output is then generated using a PI controller on the d-axis current error. The d-axis reference is always set to zero as the PMSM is non-salient and field-weakening is not used. The q-axis voltage is generated using a PI controller on the velocity error. This deviates slightly from the traditional q-axis structure of a velocity controller cascaded with a PI q-axis current controller. The d-axis back-EMF and cross-coupling disturbances are computed based on the motor parameters and the estimated velocity. They are then added to the d-axis output. The controller outputs are then transformed to $\alpha\beta$ coordinates. The output angle θ_o is computed from the sampled encoder position and the HPF velocity multiplied by the number of pole pairs p and $\frac{3}{2}$ sample times T_s, to compensate for the movement of the motor during the unit delay between calculation and output. This delay is inherent to the μC hardware implementation of motor control because the duty cycle for each switch is preloaded and applied at the next control loop interrupt. The extra $\frac{1}{2}$ on top of the unit delay, then comes from the desire to match the desired output angle on average during a sample period. The output is finally applied using a sine-triangle pulse width modulation (SPWM) approach.

When looking at Turf Tanks' implementation of FOC, there are no immediate indicators of where the problem

with the robot making audible noise could be. To narrow in on where the audible noise problem stems from, data will be analysed from Turf Tank's implementation of FOC when audible noise is present.

Performance Evaluation

In the following section Turf Tanks implementation of FOC and their tuned PI controllers to generate the d-axis and q-axis voltages will be tested. The control will be tested with the validation trajectory presented in Section 2.1. The test location on Kristian Rytter ApS' field is roughly the same within 5 m. The robot controller used for this test will be kept constant throughout all tests in later sections with FOC. The trajectory tracking performance will be evaluated, and data from the motor control loop will also be analysed.

The PI gains for the q-axis voltage controller are set by Turf Tank to be 1,5 for the P-gain and 18,75 for the I-gain, and the PI gains for the d-axis voltage controller have been tuned to be $50 \cdot 2\pi L_d$ for the P-gain and $50 \cdot 2\pi R_s$ for the I-gain, based on pole-zero cancellation. With these controller gains, the line marking robot made lots of audible noise while following the validation trajectory. The audible noise can be heard in the video named (Turf Tank Two Making Audible Noise.MOV) in Appendix A.12 and a frequency spectrum of the noise is plotted in Figure 2.6.

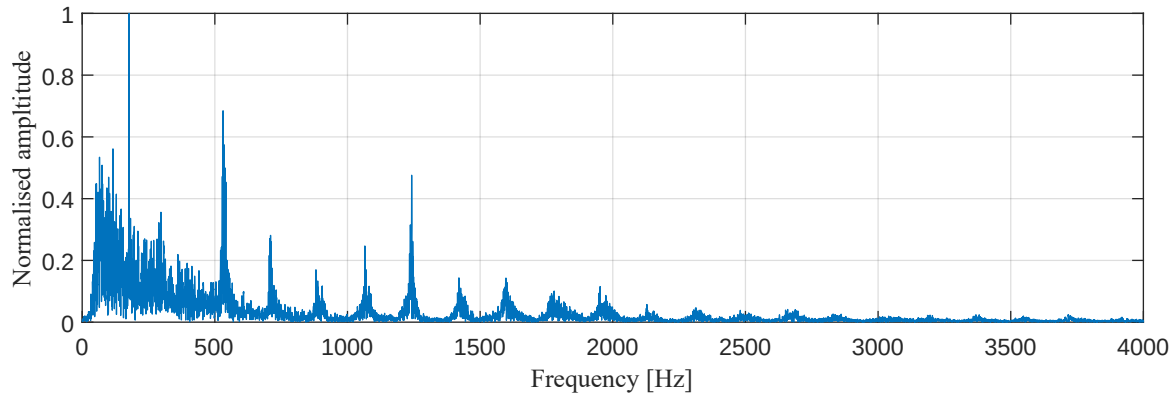

Figure 2.6

Frequency spectrum of the audible noise from the robot.

In the audible noise spectrum, there is an amplitude spike at approximately 180 Hz and following harmonics at integer multiples of this frequency. Motor data while performing the validation trajectory will also be analysed. The right wheel velocity, velocity reference, i_q, and v_q can be seen in Figure 2.7.

In Figure 2.7a, it can be seen that the estimated velocity oscillates along with the q-axis voltage and current in Figure 2.7b. It can also be seen that the q-axis voltage in Figure 2.7 does not reach saturation of $\frac{2V_{DC}}{3} = 16\,\text{V}$, meaning that the velocity control is not unstable. When analysing the frequency of the plotted variables' oscillations in Figure 2.7a, they are also approximately 180 Hz. The oscillations are also observed to be independent of velocity.

The trajectory tracking performance of Turf Tanks FOC implementation is also evaluated. The results are similar to those seen in Figure 2.4 regarding where the largest CTE errors occur. The main outliers again come from when the robot is driving backwards and transitioning between lines and arcs. The MACTE and RMSCTE are improved by 13 % and 21 % respectively. This means that the trajectory tracking performance of Turf Tanks FOC implementation and controller gains has better performance than the 120° commutated control. This must

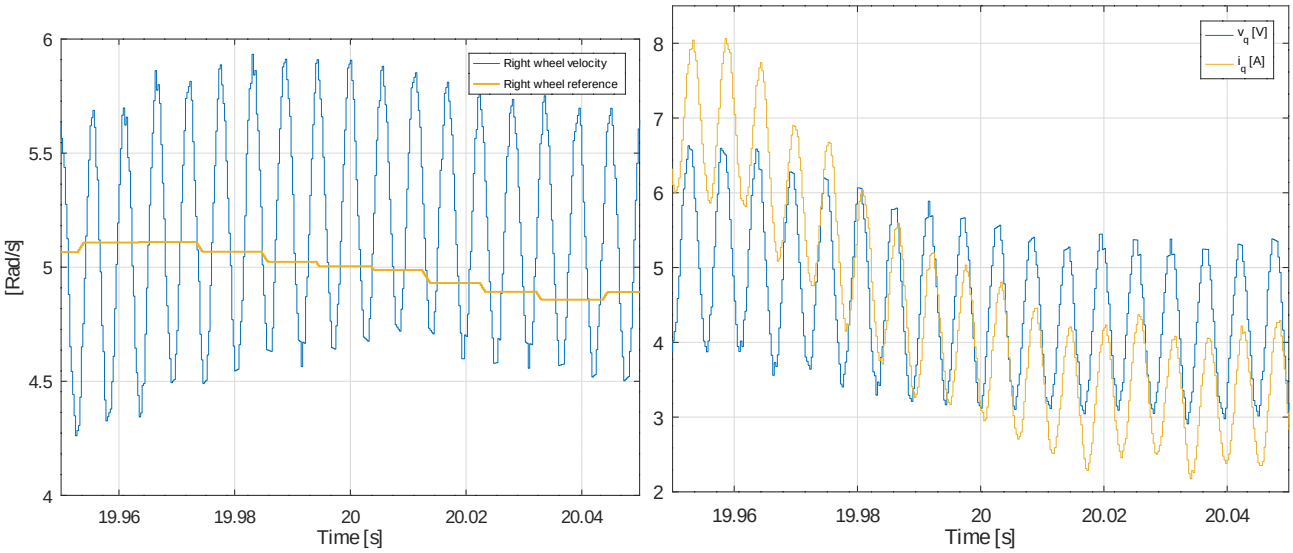

(a) *Right wheel velocity and reference during audible noise.*

(b) *Right wheel q voltage and current during audible noise.*

Figure 2.7

System state trajectories for the right wheel, while the robot is oscillating and noisy.

mean the robot can make loud, audible noise while maintaining adequate performance.

To begin the investigation into the source of the oscillations, each element of the FOC implementation will be tested in the next section.

Analysis of FOC Subcomponents

In the following section, the elements of Turf Tank's implemented FOC will be tested to check if they function correctly. This involves the modulation scheme, the output transform, PI controllers and velocity estimate. This will be done with a test where the PI velocity controller will be exchanged with open-loop $\frac{V}{f}$ control. The test is performed with a Turf Tank Two robot where the wheels are lifted from the ground. The implementation of $\frac{V}{f}$ control can be seen in Figure 2.8.

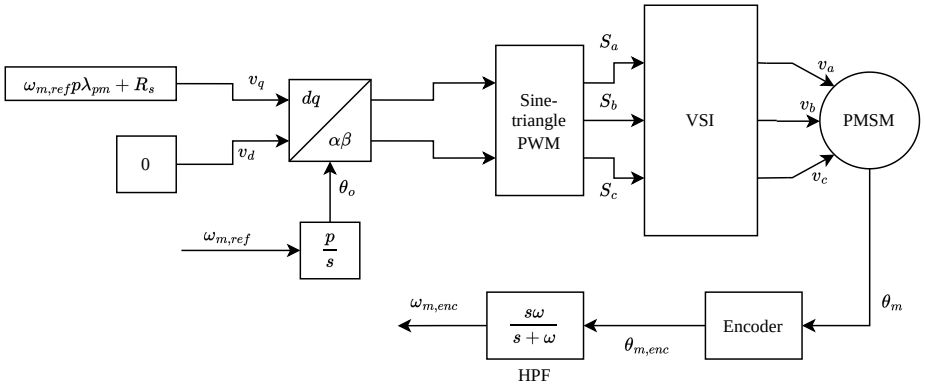

Figure 2.8

Block diagram of the $\frac{V}{f}$ control setup.

The modulation scheme is tested by defining a constant direction input vector in dq and varying the output angle corresponding to a desired velocity of 5 rad/s. This constant vector is then transformed to $\alpha\beta$-coordinates using the varying output angle and fed to the SPWM modulation scheme to calculate the inverter leg duty cycles.

These duty cycles are then used to calculate the resulting $\alpha\beta$ components and plotted in Figure 2.9 for a single motor.

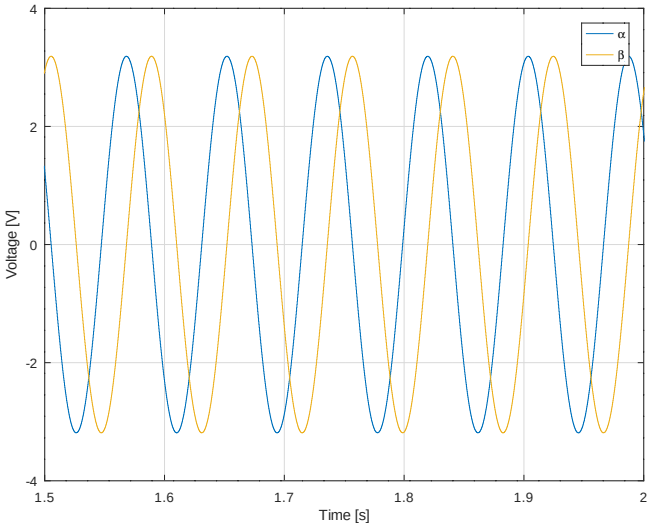

Figure 2.9

$\alpha\beta$ voltages calculated from the inverter leg duty cycles.

As expected, two sine waves of the same amplitude and frequency with a 90° phase difference are output. The frequency of 11,93 Hz also matches the desired velocity of 5 rad/s = 0,8 Hz $\left(\frac{5p}{2\pi} = 11{,}93\,\text{Hz}\right)$. This verifies the Park and Clarke transforms and SPWM scheme work.

Secondly, the functionality of the encoder reading and HPF velocity estimate is tested. The goal is to observe if the 180 Hz oscillations originate from the HPF estimation method or position feedback. A discrete simulation of the HPF with a perfect velocity of 5 rad/s = 0,8 Hz is first performed. The input to the HPF is generated by integrating the constant velocity and quantising it to the encoder resolution. This is done to replicate a perfect encoder and thereby isolate the HPF velocity estimation method. A sample rate of 4 kHz is used, and the generated output can be seen in Figure 2.10.

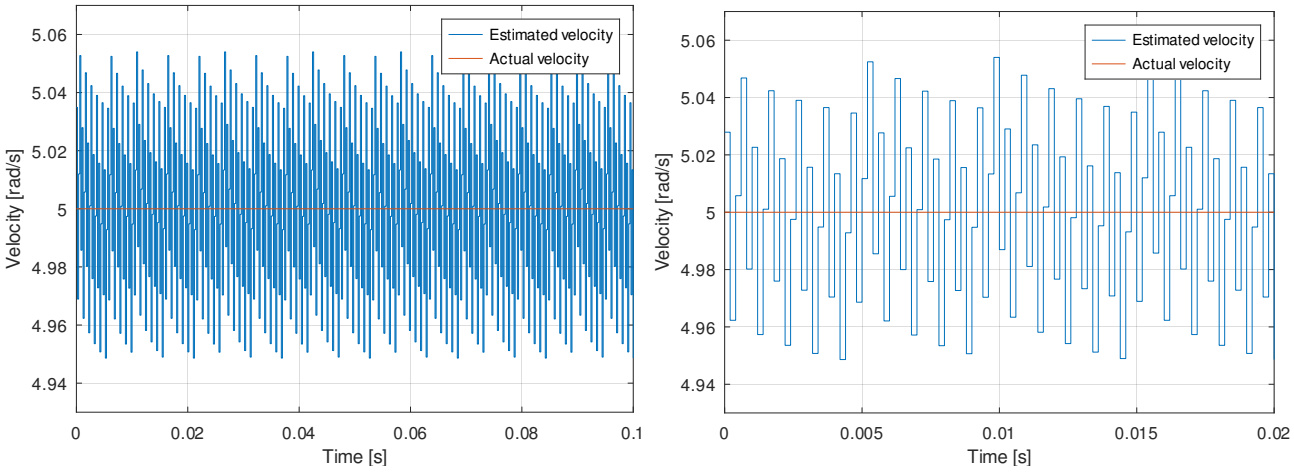

(a) 100 ms **(b)** 20 ms

Figure 2.10

HPF output over different timescales after the output has settled

As seen in Figure 2.10, the quantised nature of the position measurement introduces a noisy limit cycle around

the actual velocity, even when quantisation is perfectly even. This is inherent to quantised analogue signals. Quantisation in sampled systems manifests as additive white noise [2, p. 4], raising the overall noise floor. This is undesirable, as this increases the need for noise attenuation in the control loop. It does, however, not amplify specific frequencies and is thereby not expected to be the cause of the noise.

During the previous $\frac{V}{f}$ control test, the encoder reading and HPF velocity estimate were logged, but not used as feedback in the motor control. The HPF velocity estimate of the left and right motor can be seen in Figure 2.11.

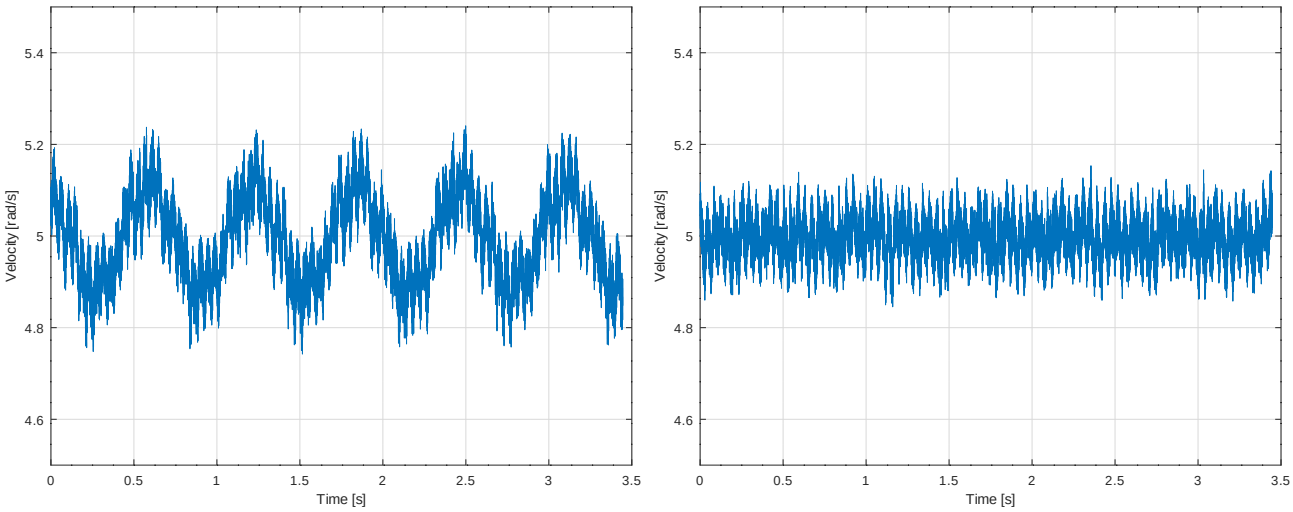

(a) *Left motor.* **(b)** *Right motor.*

Figure 2.11
HPF output for each robot motor with V/F control

During the tests, the robot never made audible noises comparable to when driving with Turf Tank's implementation of FOC. From the velocity estimate, high-frequency noise is present, along with two lower frequencies. A frequency of approximately 24 Hz is present in both signals, and a lower frequency of approximately 1,6 Hz is only present on the left motor. The frequency of approximately 24 Hz stems from the eccentricity of the rotor relative to the stator, which has two periods for each electrical revolution, leading to $2 \cdot 11{,}93\,\text{Hz} \approx 24\,\text{Hz}$. The frequency of 1,6 Hz comes from the integral non-linearity of the magnetic encoder, caused by off-axis misalignment of the rotor-mounted magnet and the sensor [3], which causes an error that has two periods per revolution. A frequency spectrum of each signal is generated to verify the above frequencies and can be seen in Figure 2.12. The amplitudes are plotted up to 500 Hz, as the amplitudes for frequencies above are practically zero, due to the 45 Hz HPF.

Here, the frequencies of 1,6 Hz and 24 Hz are present, along with some harmonics. However, an additional frequency at $\approx$ 215 Hz is present in both spectra. This frequency stems from cogging torque, which has LCM $(n_s, 2p)$ periods per revolution, where LCM is the least common multiple and n_s is the number of stator teeth and $2p$ is the number of poles. With 27 stator teeth and 30 poles, the LCM becomes 270, resulting in a frequency of ≈ 215 Hz at 5 rad/s. This frequency is in the problematic region around 180 Hz, but the amplitude is only $\approx 4 \cdot 10^{-3}$ rad/s, so it is thought to be insignificant and not the cause of the audible noise.

The 1,6 Hz and 24 Hz frequencies are linearly dependent on velocity, but the frequency of 180 Hz is present during operation regardless of velocity. Accounting for velocity dependence, the frequencies still do not enter the problematic region around 180 Hz, as the maximum wheel velocity during the trajectory is 11 rad/s.

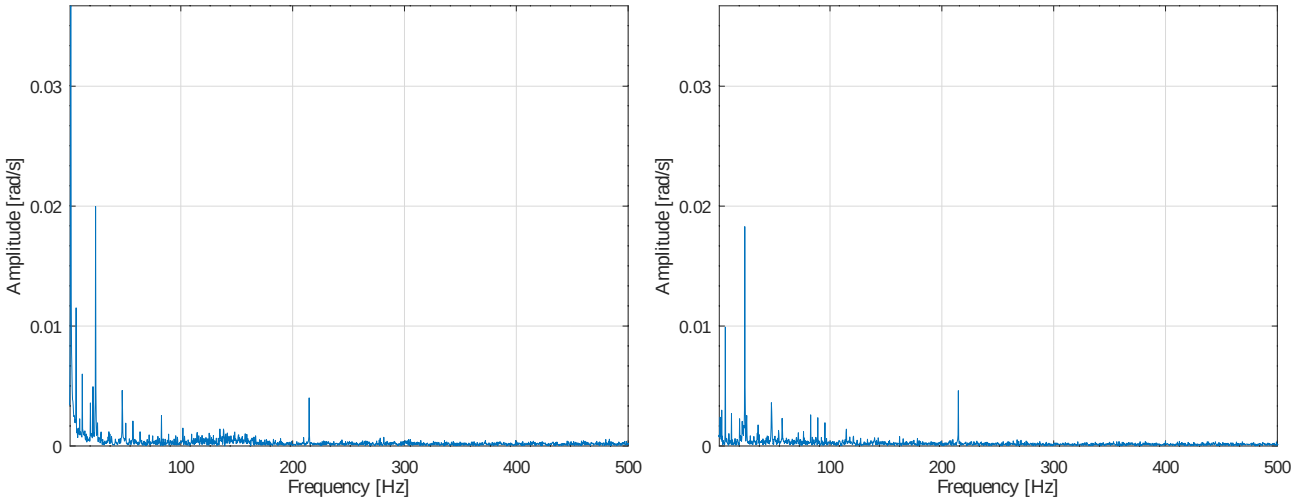

(a) *Left motor.*

(b) *Right motor.*

Figure 2.12

Frequency spectrum of the HPF output.

From the results of the $\frac{V}{f}$ control test, it can be concluded that the modulation scheme, encoder position and velocity estimate function correctly and are therefore not deemed to be the source of the 180 Hz frequency. As a result, Turf Tank's implementation of the velocity PI controller with anti-windup is inspected as this is one of the last components to be analysed from Turf Tank's implementation of FOC. A representation of their PI controller code implementation can be seen below, which is updated each motor control loop running at 4 kHz.

$$\omega_{err} = \omega_{ref} - \omega_m \tag{2.2}$$

$$\omega_{err,int} = \omega_{err,int} + v_{q,realised} \tag{2.3}$$

$$v_q = K_p \omega_{err} + \omega_{err,int} \tag{2.4}$$

$$\omega_{err,int} = \omega_{err,int} - v_q + K_i T_s \omega_{err} \tag{2.5}$$

In the first line, the velocity error ω_{err} is calculated from the difference between the velocity reference ω_{ref} and the estimated velocity ω_m. On the second line, the realised output voltage $v_{q,realised}$, accounting for saturation, is added to the integrator state $\omega_{err,int}$. This realised voltage is calculated from the inverter leg duty cycles. On the third line, the desired output v_q is computed by multiplying the proportional gain K_p and the error and adding the error integral $\omega_{err,int}$. On the last line, the error is integrated using a forward Euler scheme and the desired output is subtracted from the error integral state. Adding the realised output and subtracting the desired output from the error integral constitutes the anti-windup scheme. Turf Tank's implementation has no issues that should inject frequencies into the control loop. However, forward Euler integration is generally not good practice. This is because it can map stable poles in the continuous time domain to unstable poles in the discrete domain. This is currently not a problem, though, as the system is not unstable, but should be corrected to backward Euler or the trapezoidal method to avoid potential problems in the future.

From the performed test, it can be concluded that every individual component of Turf Tanks implemented FOC functions correctly. The mechanical system will then be analysed next.

2.3 Analysis of Mechanical System

The analysis of the mechanical system is done regarding the motor mounting and natural frequencies in the chassis. The motor mounting on the line marking robot is seen in Figure 2.13.

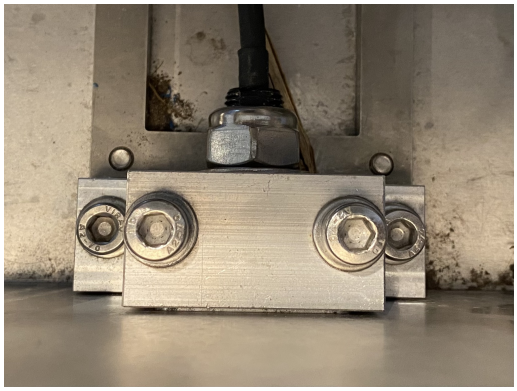

Figure 2.13
Motor mounting on Turf Tank Two robot.

Here, the motor is mounted directly to the chassis without any damping or decoupling, meaning that a vibrating chassis can affect the encoder reading. A test is conducted to figure out if the Turf Tank Two has any problematic natural frequencies. Natural frequencies can generally be stated to be problematic if the excitation frequency is within $\frac{1}{3}$ to three times the natural frequency [4]. The experiment is performed by striking the robot with a hammer and recording the audio with a mobile phone. The resulting amplitude spectrum varies slightly depending on where the robot is hit with the hammer. Because of that the plate where the motors are mounted on is chosen as the most relevant location to hit the robot. The resulting amplitude spectrum can be seen in Figure 2.14.

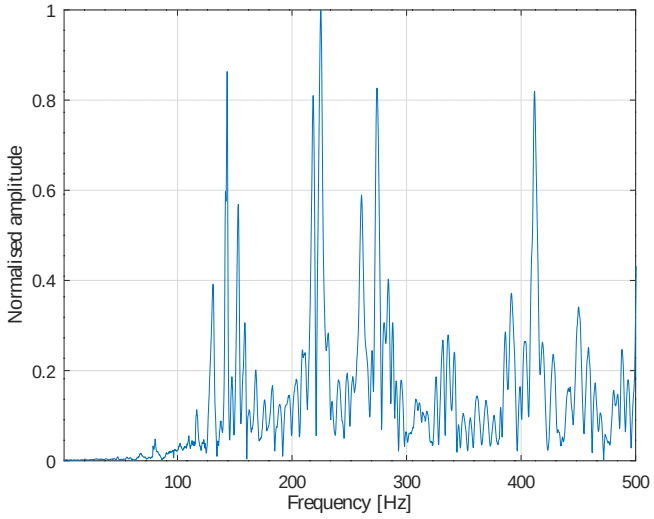

Figure 2.14
Frequency spectrum of the impulse response of the Turf Tank Two.

When looking at the amplitude spectrum in Figure 2.14 it is seen that there are significant peaks at approximately 150 Hz, 230 Hz, 280 Hz and 420 Hz. These peaks are natural frequencies of some of the Turf Tank Two components. The analysis in Section 2.2 showed the robot oscillating with a frequency of 180 Hz, which is within $\frac{1}{3}$ to three times the natural frequencies observed in Figure 2.14. The reason for the robot oscillating at 180 Hz and for example not the peak at 150 Hz could be because the FOC alters the system dynamics. Based on the analysis performed in this chapter, the root cause of the audible noise is the excitation of low natural frequencies in the robot chassis. The vibrations are not isolated from the position feedback due to the rigid motor mounting, allowing them to enter the control loop. Additionally, the HPF velocity estimate is also inherently noisy, due to the encoder quantisation, increasing the requirements for noise attenuation.

The audible noise has now been analysed, and the root cause has been presented. As mentioned earlier in

Chapter 1, the second problem to be analysed is that Turf Tanks line marking robots sometimes damage the terrain surfaces they operate upon. This will be done in the next section.

2.4 Damage of Terrain Surfaces

As mentioned in Chapter 1, Turf Tank faces a challenge in that they sometimes damage specific terrain surfaces when performing line marking. Damage to terrain surfaces is unwanted by Turf Tank's customers as they are primarily pro-sport for whom field quality is all-important. The occasional damage is limited to tennis courts, baseball fields and other fields composed of loose soil, and is not an issue on grass or turf. Turf tank knows loose soil surfaces are generally more vulnerable to damage and as such this section aims to investigate the root causes leading to damage to these surfaces. An introduction will first be given to what is characterised as terrain surface damage. Then, an analysis of the problem will be performed. This will be done using data delivered by Turf Tank. The data consists of video material and data from the line marking robot's trajectory tracking control loop.

Characterisation of Terrain Damage

For the characterisation of field surface damage, Communication with Turf Tanks customers will not be performed. Turf Tank is therefore chosen as the representative of their customers' viewpoints in characterising terrain surface damage. If the functionality of the field is affected, the surface is characterised as damaged. An example of surface damage can be seen in Figure 2.15.

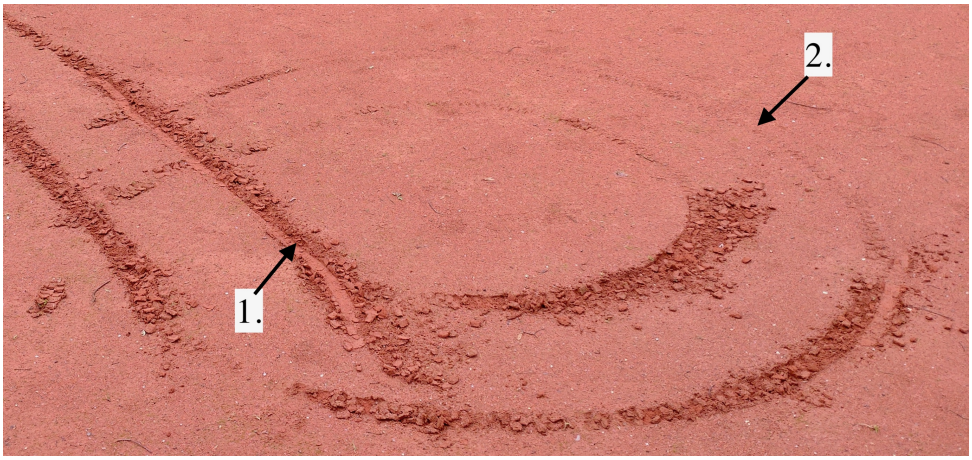

Figure 2.15

Marks on tennis court after line marking robot has driven around on it. Marked with 1. is surface damage. Marked with 2. are the track marks created by the robot [1].

The picture is taken on a tennis court. For a tennis court, the intended functionality of the tennis court is to be as smooth as possible, such that the tennis ball bounces predictably. Marked with an arrow and the number 1. is an example of field surface damage. This is because large indents have been made in the tennis court where a tennis ball's bounce will be affected. Also marked on Figure 2.15 with an arrow and the number 2 is wheel marks left by the robot. These marks are, however, negligible as they do not affect the functionality of the tennis court.

With field surface damage characterised, the root cause of field surface damage will be investigated next.

Analysis of Terrain Surface Damage

To investigate the causes of terrain surface damage, visual analysis coupled with data provided by Turf Tank is used. The images and data are from a baseball court, where the Turf Tank line marking robot has damaged the surface. In Figure 2.16, a series of frames is extracted from the moment the terrain surface of a baseball field is damaged.

(a) *Frame 1.* **(b)** *Frame 2.* **(c)** *Frame 3.*

Figure 2.16

Three frames from a video of the Turf Tank Two robot damaging the surface of a baseball field. The leftmost image is the first frame. The area of interest is marked with a circle behind the front tyre [1].

The area of interest is marked with a blue circle. The leftmost picture is the last frame from the video before the baseball surface is damaged. In the next two frames in figures 2.16b and 2.16c it is observed that the wheel slips momentarily and shoots some of the baseball soil up into the air behind the front tyre. In the analysis of the video, the wheel slips every time the baseball field is damaged.

When investigating the trajectory reference at the moments when the surface is damaged, a correlation is clear. In Figure 2.17, an illustration of the trajectory reference for the robot controller is shown. The red circle marks the point at which the wheel slips.

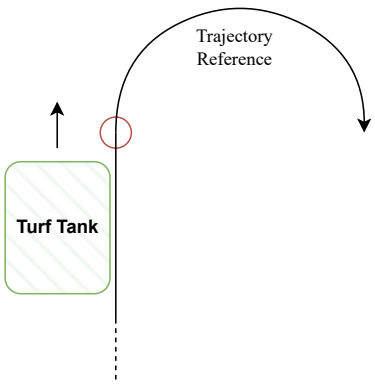

Figure 2.17

Visualisation of discontinuity in the trajectory reference when transitioning from a line to a curve.

The trajectory states that the line-marking robot should drive straight and then transition to a curve. This causes a discontinuity in the trajectory that corresponds to a demand for infinite acceleration. To counteract this, Turf Tank has implemented a rate limiter on the velocity reference of 40 rad/s^2 to the motors. The rate limiter intro-

duces a trajectory tracking error and is, as a result, wanted as high as possible. When inspecting motor control loop data from the line marking robot's left motor during the momentary slip in Figure 2.16 the issue is verified. This data is plotted in Figure 2.18.

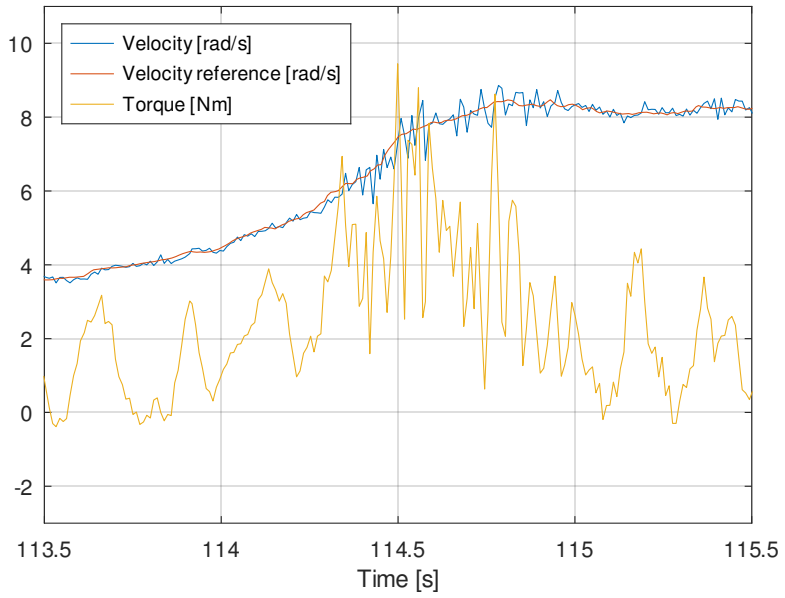

Figure 2.18

Velocity reference, motor velocity and motor torque from when the line marking robot's wheel slips.

The wheel slip occurs at approximately 114,35 s. The orange line, which is the wheel velocity reference, gets a higher slope, meaning an increase in demanded acceleration. This equates to a higher demanded torque to obtain the acceleration, which is visible as the yellow line in Figure 2.18. Shortly after, the motor velocity, which is the blue line, spikes above the velocity reference and starts over- and undershooting the velocity reference repeatedly. This is because the wheel loses traction with the baseball surface and starts slipping, which causes the inertia of the system to suddenly drop, causing the overshoot. It is therefore important that the wheels of the line marking robot do not slip to mitigate field surface damage. As a result, the demanded torque should not be higher than what the terrain can support.

With the initial problem analysed of Turf Tank sometimes damaging the field surfaces when performing line marking, a problem statement is formulated in the following section.

2.5 Problem Statement

As mentioned earlier in Chapter 1, Turf Tank is developing a mower and has an interest in a mower prototype that can operate on terrain where their mower cannot operate. Turf Tank, however, has problems with their line marking robots making audible noise and terrain surface damage that they do not want to carry over to their mower in development and the mower prototype for this project. Therefore, a problem analysis has first been performed on Turf Tank's initial problems as stated in Chapter 1:

- The Turf Tank Two robot is audibly noisy while operating.
- Turf Tank robots sometimes damage field surfaces.

Knowledge is obtained through the problem analysis of the root causes of Turf Tank's initial problems. The root cause of Turf Tank's problem with their line marking robots making audible noise is analysed to be due

to natural frequencies in the chassis being excited by the robot's motor control. This is in part a result of the motors being mounted directly to the robot chassis without any damping, and the output containing frequencies within the problematic region of $\frac{1}{3}$ to three times a natural frequency. Additionally, the HPF velocity estimate is inherently noisy due to the encoder quantisation, increasing the need for noise attenuation.

Turf Tank's problem with sometimes damaging field surfaces is analysed to be caused by the robot wheels slipping. Wheel slip is observed to mostly happen in trajectories when transitioning from a line to an arc and vice versa. This is because these changes in the trajectory lead to high torque demands that cannot be transferred to the field surface.

Solutions to the line marking robots will first be explored before starting the development of the mower prototype. This will be done based on the following problem statement:

How can a software solution utilising FOC be developed for the line marking robots, such that it can perform line marking without audible excitation of the robot's natural frequencies while obtaining equivalent or better trajectory tracking performance to the currently in use $120°$ ***commutation control along with mitigating torque inputs causing the wheels to slip?***

2.6 Scope

The scope of the line marking solution will be defined in the following section. A solution for Turf Tanks line marking robots that sometimes damaging field surfaces unacceptably will not be developed in this project. The mitigation of unacceptable field surface damage will, however, be considered during the development of a mower prototype for Turf Tank. A solution for Turf Tank's problem with their line marking robots making audible noise will be developed. With the scope defined, requirements and wishes are formulated for Turf Tank's problem with their line marking robots making audible noise.

2.7 Requirements and Wishes

To develop a solution to the problem statement in Section 2.5, requirements and wishes are formulated in the following section. Requirements must be fulfilled for the solution to be viable. Performance regarding the wishes is expected to improve the quality of the solution.

Requirements

- Robot natural frequencies must not be excited to cause audible noise.
- The velocity control must be stable with the wheels not in contact with a surface.
- MACTE must be equivalent or better than the 120° commutation control.
- RMSCTE must be equivalent or better than the 120° commutation control.

It is stated that the velocity control must be stable with the wheels not in contact with a surface. This requirement stems from the line marking robot being propped up while running setup. As such the wheels must be able to function properly while floating. They also need to be stable in this situation in case a wheel loses traction or in general contact with the ground while operating.

Wishes

In addition to the requirements, a few wishes for the resulting system dynamics are presented. The first is an increased velocity control bandwidth. This will allow the robot controller to be retuned and theoretically achieve a smaller MACTE and RMSCTE. A better-fitting model for the robot controller is also of interest. Therefore, Linear and decoupled linear and angular velocity dynamics. If the system dynamics match the model, the robot controller can make better predictions. Summarising, this leads to two wishes:

- Maximise velocity control bandwidth.
- Linear and decoupled linear and angular velocity dynamics.

3 | Solutions for Resonance Elimination and Performance Improvements for the Line Marking Robot

In this chapter, solutions will be investigated to solve the problem statement formulated in Section 2.5. This will be done with the goal of fulfilling the requirements and improve performance regarding the wishes as possible defined in Section 2.7. In the problem analysis, it is determined that natural frequencies in the robot chassis are the root cause of the problem. Additionally, the velocity estimation method is also noisy due to the encoder quantisation. As a result, software solutions will be investigated that can stop the natural frequencies and increase the velocity control bandwidth.

Four software solutions will be presented in this chapter:

- The first solution is a retune of Turf Tanks velocity controller.
- The second solution is tuning the velocity controller to have a linear first-order response at zero angular velocity.
- The third solution is a new velocity estimation method to mitigate the encoder quantisation noise, followed by retune of the velocity controller
- The fourth solution is a combination of the previous two solutions with additional notch filtering targeting the resonance frequency

3.1 First Solution: Tuning of FOC Velocity Controller

The first solution that is investigated to reduce the excitation of the natural frequencies of the robot chassis is to detune the velocity controller. If the PI controller gains are lowered, the noise attenuation should be improved and the natural frequencies excited less.

The process of detuning the PI velocity controller is done by scaling down the gains set by Turf Tank and then running the validation trajectory and lifting the robot to test if it is stable with the wheels not in contact with the surface. The gains are lowered if the robot makes audible noise during the trajectory or while lifted. The gains are initially set by Turf Tank at P = 1,5 and I = 18,75. Through an iterative process, the controller gains are reduced to a P-gain of 1 and an I-gain of 12,5, where the robot made no audible noise. This resulted in a MACTE improvement of 11 % and a RMSCTE improvement of 18 % relative to the 120° commutation control baseline. The detuned controller thereby fulfils the requirements defined in Section 2.7. When analysing the CTE data, the same behaviour is seen as in the baseline test of Turf Tanks 120° commutation control. The outliers in CTE again occur when transitioning from a line to an arc and vice versa. This is both when driving forward and backwards, but worst backwards. The bandwidth of the velocity controller is lowered as a result of the gains being lowered, but it does not negatively affect the trajectory tracking performance. This is expected to

be because the wheel velocity estimates fed back to the robot controller are less noisy, reducing the noise in the estimated robot position. And in turn making it easier for the robot controller to follow the wanted trajectory.

To check if the wish of linear and decoupled first-order linear and angular velocity dynamics is fulfilled, the step response for each of these will be tested. Based on Figure 2.3, the angular velocity steps will be at a linear velocity of ±0,5 m/s while in contact with asphalt and the linear velocity step is chosen to be from 0,5 m/s to 0,75 m/s, with an angular velocity of 0 rad/s. The chosen velocities are within the line marking operating velocity range. The results for each step can be seen in Figure 3.1.

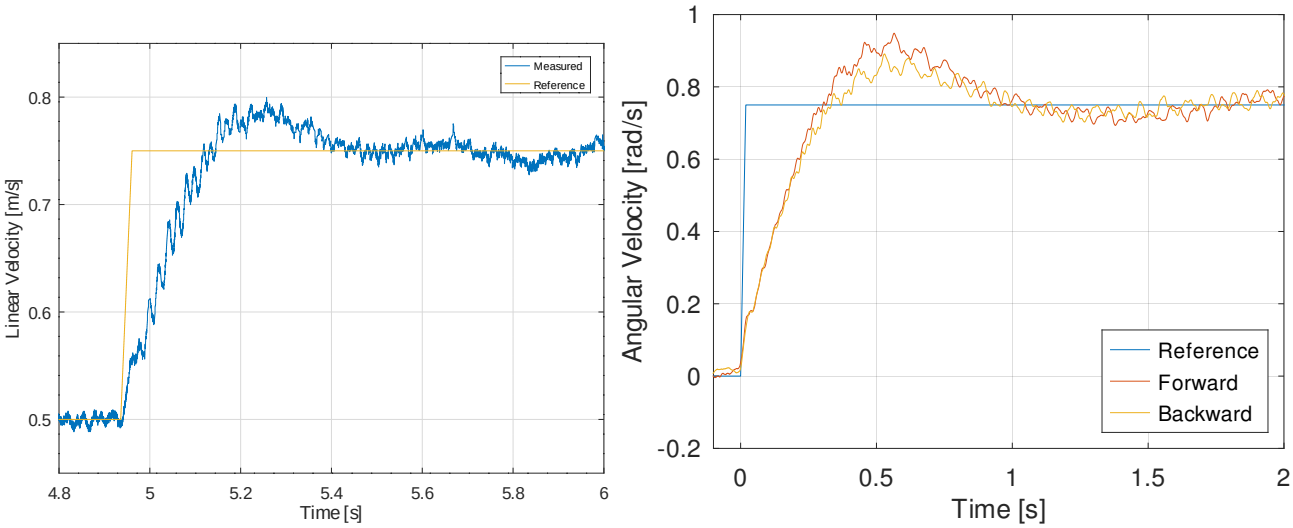

(a) *Linear velocity step response from* 0,5 m/s *to* 0,75 m/s.

(b) *Angular velocity step response from* 0 rad/s *to* 0,75 rad/s. *The data is filtered with a symmetric moving mean to make the differences easier to spot.*

Figure 3.1

Step response tests with PI velocity controller gains set to 1 P-gain and 12,5 I-gain. The angular step responses are performed with a linear velocity of 0,5 m/s *and then stepped in angular velocity from* 0 rad/s *to* 0,75 rad/s.

It can be seen in Figure 3.1a that the linear velocity of the robot does not have a first-order response characteristic. The same can be observed for the angular velocity step responses of the robot in Figure 3.1b. The periodic oscillations seen after the controller settling are caused by the previously explained encoder eccentricity as illustrated earlier in Figure 2.11a.

It can then be concluded that the solution does not fulfil the wish of linear and decoupled first-order linear and angular velocity dynamics defined in Section 2.7. The performance concerning the first wish, maximisation of the velocity control bandwidth, is also worsened. When the PI controller gains are lowered, the bandwidth of the velocity controller is decreased. As a result of the wishes not being fulfilled or worsened, it is of interest to investigate if other solutions can be implemented to improve the performance concerning the wishes. This will start with an investigation of whether linear and decoupled first-order linear and angular velocity dynamics can be obtained.

3.2 Second Solution: Tuning for First-Order Response

To achieve the desired first-order dynamics, the dynamics of the robot are first examined to understand what this requires from the control. A differential-drive mobile robot (DDMR) model is presented in [5] and will be used for the analysis. The model is presented on the standard state space $\dot{\mathbf{x}} = \mathbf{Ax} + \mathbf{Bu}$ form and can be seen in

Eqn. (3.1) accompanied by Figure 3.2. The derivation of the model can be seen in Appendix A.1.

$$\frac{d}{dt}\begin{bmatrix} v \\ \omega \end{bmatrix} = \begin{bmatrix} 0 & \frac{2dm_c r^2 \omega}{2I_w + mr^2} \\ -\frac{dm_c r^2 \omega}{Ir^2 + 2I_w L^2} & 0 \end{bmatrix} \begin{bmatrix} v \\ \omega \end{bmatrix} + \begin{bmatrix} \frac{r}{2I_w + mr^2} & \frac{r}{2I_w + mr^2} \\ -\frac{Lr}{Ir^2 + 2I_w L^2} & \frac{Lr}{Ir^2 + 2I_w L^2} \end{bmatrix} \begin{bmatrix} \mathcal{T}_L \\ \mathcal{T}_R \end{bmatrix} \tag{3.1}$$

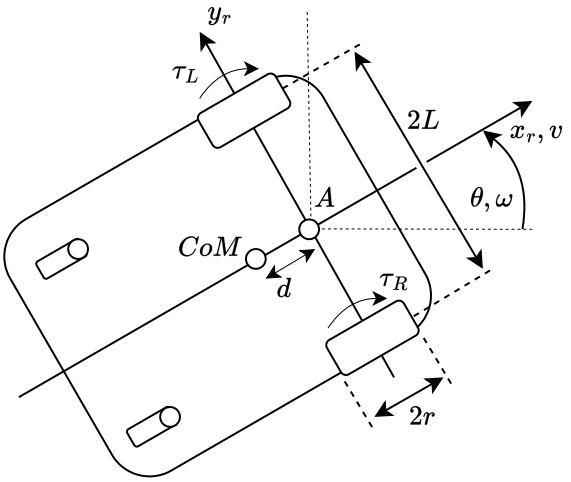

Figure 3.2
Illustration of Turf Tanks robot and the notation used for the DDMR model presented in Eqn. (3.1).

Where point A is the origin of the robot reference frame in which the states are defined, v is the linear robot velocity, ω is the angular robot velocity, τ_L is the left wheel torque, τ_R is right wheel torque, d is the center of mass (CoM) offset from the origin, r is the wheel radius and L is half the wheel axle length, m is the total mass of the robot $m = m_c + 2m_w$, where m_c is the robot mass without the wheels and m_w is the wheel mass. I is the total rotational moment of inertia about point A $I = I_c + m_c d^2 + 2m_w L^2 + 2I_m$, where I_c is the robot inertia about its' CoM and I_m is wheel rotational inertia about an axis parallel to x_r through the wheel's CoM.

The model has a non-linear coupling between the linear and angular velocity, as the magnitude of the off-diagonal entries is proportional to the angular velocity ω. This means that there is no coupling between the states at zero angular velocity. Each motor torque also affects both states. Achieving linear and decoupled linear and angular velocity dynamics is possible using a centralised control structure. However, implementing requires making architectural changes to the robot software, as each motor control loop currently cannot share any data. Making these changes is deemed outside the scope of the project, and as such, achieving a complete decoupling will not be investigated further. Though a linear first-order linear velocity response can be achieved in one situation, where the angular velocity is zero and both inputs are identical. In this case, the linear velocity dynamics reduce to an integrator:

$$\dot{v} = \frac{2r}{2I_w + mr^2}\mathcal{T}_{LR} \tag{3.2}$$

Where $\mathcal{T}_{LR}$ is the sum of both identical motor torques.

This situation is present in line marking trajectories. The robot is never planned to accelerate in its linear velocity when painting arcs. This means that linear acceleration only occurs when the robot is not rotating, where the coupling is not in effect. As a result, a model will be constructed that ignores the cross-coupling terms in the next section. This simplified mechanical model will be used to tune a new controller to obtain a linear first-order linear velocity step response.

System Modelling

An approximate single-wheel model of the Turf Tank Two will be created to design and evaluate control structures. This model will consist of a standard non-salient FOC PMAC motor and an undamped first-order mechanical model, based on the simplified model from above. The FOC model is explained in further detail in [6]

but will be summarised in Eqn. (3.3).

$$\frac{\mathrm{d}i_d}{\mathrm{d}t} = \frac{v_d - R_s i_d + \omega_m p L_q i_q}{L_d} \tag{3.3a}$$

$$\frac{\mathrm{d}i_q}{\mathrm{d}t} = \frac{v_q - R_s i_q - \omega_m p \left(\lambda_{pm} + L_d i_d\right)}{L_q} \tag{3.3b}$$

$$T_e = \frac{3}{2} p \lambda_{pm} i_q \tag{3.3c}$$

Where i_d and i_q are the dq-axes currents, R_s is the phase resistance, L_d and L_q are the dq-axes inductances, ω_m is the mechanical velocity, p is the number of pole pairs, λ_{pm} is the permanent magnet flux linkage amplitude and T_e is torque developed by the motor.

An undamped mechanical model is then appended in Eqn. (3.4).

$$\frac{\mathrm{d}\omega_m}{\mathrm{d}t} = \frac{T_e}{J} \tag{3.4}$$

Where J is the equivalent rotational moment of inertia (MoI), given by either $\frac{2I_w + mr^2}{2}$ or I_w, depending on whether the wheel contacts the ground or not. This parameter, therefore, changes drastically when the wheel slips or loses contact with the ground. Therefore, it will be used to evaluate system stability during slip or no ground contact, which is a requirement. Friction is omitted due to the large variation depending on the surface type, and due to its small influence on the $v_q \rightarrow \omega_m$ gain compared to the back-EMF. This is explained in Appendix A.2.

The FOC motor model is non-linear due to cross-coupling terms in Eqn. (3.3a) and Eqn. (3.3b), which complicates evaluating stability and performance. The motor is non-salient, meaning the dq-inductances are equal. This means the d-axis current will always be controlled to 0, due to it not contributing to the developed torque. Therefore, if the d-axis current controller performs as intended, the last term in Eqn. (3.3b) can be neglected. Turf Tanks implemented d-axis controller is tested by running the motors and giving some different q-axis voltage inputs. The results can be seen in Figure 3.3. The d-axis controller is deemed to perform satisfactorily as it keeps the d-axis current within ±0,3 A.

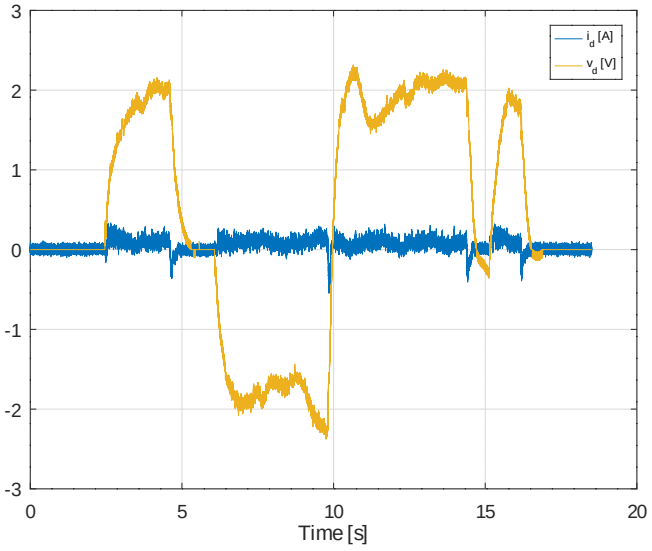

Figure 3.3

The d-axis current is effectively controlled to within ±0,3 A

From this, the model can now be reduced to a linear second-order model as seen in Eqn. (3.5).

$$\frac{\mathrm{d}i_q}{\mathrm{d}t} = \frac{v_q - R_s i_q - \omega_m p \lambda_{pm}}{L_q} \tag{3.5a}$$

$$\frac{\mathrm{d}\omega_m}{\mathrm{d}t} = \frac{3p\lambda_{pm} i_q}{2J} \tag{3.5b}$$

$$\frac{\Omega(s)}{V_q(s)} = \frac{3p\lambda_{pm}}{2JL_q s^2 + 2JRs + 3p^2\lambda_{pm}^2} \tag{3.5c}$$

With poles at:

$$s = -\frac{R}{2L_q} \pm \frac{\sqrt{J\left(JR^2 - 6\lambda_{pm}^2 p^2 L_q\right)}}{2JL_q} \tag{3.6}$$

The motor parameters and inertia are provided by Turf Tank. Their accuracy will be evaluated later. The full list of parameters can be seen in Table 3.1.

Parameter	R_s [Ω]	L_d/L_q [µH]	λ_{pm} [Wb]	p	J [kg m^2]
No slip	0,340	805	0,038	15	0,312
Slip/lifted	−||−	−||−	−||−	−||−	0,012

Table 3.1

System parameters with and without the robot wheels in contact with the ground. The inertia of the system is the only parameter that changes when contact is lost with the ground.

Evaluating the system poles with no slip and slip results in the following

$$\text{No slip: } s = -417{,}7 \;\&\; -4{,}650, \qquad \text{Slip: } s = -211{,}2 \pm 76{,}51\mathrm{i} \tag{3.7}$$

With no slip, the model simplifies to two first-order systems in series, but with slip, the poles become complex conjugates.

The PI controller will be tuned for a first-order response with no slip. This will be obtained by pole-zero cancellation. The PI controller zero is placed on top of the mechanical pole at −4,650. This means the ratio $\frac{K_i}{K_p} = 4{,}650$ must be maintained to achieve a first-order response. This tuning method is not very robust towards parameter changes, as they result in the pole moving and not being completely cancelled by the zero. The response first mimics first-order, but then slowly creeps towards the reference at the end. Keeping the same K_p of 1 from the original controller, K_i becomes 4,650. Closing the loop with the 45 Hz HPF in the feedback results in the transfer function in Eqn. (3.8).

$$\frac{(3K_p\lambda_{pm}p)s^2 + (3K_i\lambda_{pm}p + 3K_p\lambda_{pm}\omega_{HPF}p + 3K_i\lambda_{pm}\omega_{HPF}p)s + 3K_i\lambda_{pm}\omega_{HPF}p}{(2JL_q)s^4 + (2JL_q\omega_{HPF} + 2JR_s)s^3 + \left(2JR_s\omega_{HPF} + 3\lambda_{pm}^2p^2\right)s^2 + \left(K_p\lambda_{pm}\omega_{HPF}p + \lambda_{pm}^2\omega_{HPF}p^2\right)s + 3K_i\lambda_{pm}\omega_{HPF}p} \tag{3.8}$$

The rotational inertia is only present in the denominator of Eqn. (3.8), affecting the poles and stability of the system, meaning the zeros will stay the same no matter the inertia. The poles and zeroes of the transfer function with wheel slip and without wheel slip are shown in Table 3.2. The poles are shifted slightly due to the HPF in the feedback path, but the pole-zero cancellation is maintained, and the pole at 8,57 becomes the dominating pole. It is also interesting to see how much the poles change in the two situations. Two poles under slip conditions become complex conjugates with an angle of 71°, indicating loss of stability margin. The pole-zero cancellation

is also lost due to the pole in the last row moving from −4,660 to −3. The loss of the first-order response under slip conditions is, however, not important, due to stability being the only requirement in this scenario.

No slip poles	No slip zeros	Slip poles	Slip zeros
−432,6	−282,7	−523,1	−282,7
−259,3	−4,650	−89,48+257,2i	−4,650
−8,570		−89,48−257,2i	
−4,660		−3,000	

Table 3.2

Closed loop system poles with and without the wheel having contact with the surface.

The PI gains of 1 P-gain and 4,65 I-gain are set, and the same linear step as in Figure 3.1a is performed. The resulting step response is shown in Figure 3.4.

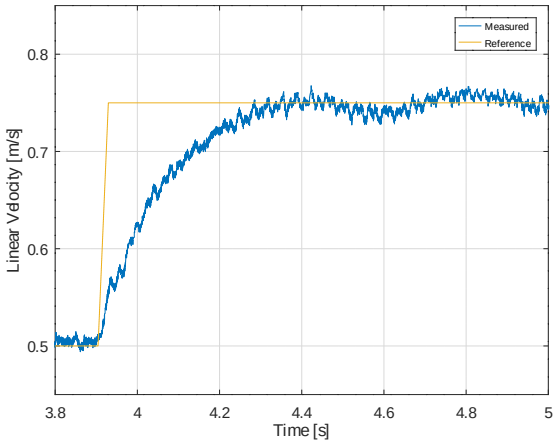

Figure 3.4

Linear velocity step with approximate first-order response.

The settling time of ≈0,45 s matches the models dominant pole at −8,570. The response is also practically first-order, which again verifies the model. Because of this, the model parameters are also assumed to be sufficiently accurate, and experiments to determine these will therefore not be performed.

The periodic oscillations after the reference velocity is reached are caused by the left wheel encoder's eccentricity, as seen multiple times earlier, for example, in Figure 2.11a. As seen in Figure 3.4, the linear velocity dynamics are now approximately first-order. With a time constant of approximately 0,1 s. An attempt is now made to raise the controller gains without the robot making audible noise. This was however not possible, resulting in a P-gain being maintained at 1 and an I-gain being lowered to 4,65. This means that the size of the P-gain is maintained and the I-gain is lowered compared to the viable controller tuned earlier in Section 3.1.

The control is again tested by performing Turf Tanks validation trajectory. From analysing the CTE data, the same behaviour regarding outliers in CTE is observed as in all the previous performed validation trajectory tests. The largest outliers in CTE occur when transitioning from a line to an arc and vice versa. This is both when driving forward and backwards, but worst backwards. The MACTE is increased by 8,7 % and the RMSCTE is increased by 12 %, which are both worse than the baseline performance of Turf Tank's 120° commutation control. The resulting controller gains fulfil the wish of a first-order linear velocity dynamics, but the bandwidth is lower than the viable controller tuned in Section 3.1. Obtaining linear first-order linear velocity dynamics at no angular velocity does not seem to improve the trajectory tracking performance. The reduction in bandwidth and thereby disturbance rejection is deemed to be the cause of the reduction in performance. With the wish of raising the bandwidth of the wheel velocity controllers other methods for velocity estimation will be investigated in the next section.

3.3 Third Solution: Improving Velocity Controller Performance

The next initiative that is taken to raise the bandwidth of the velocity controller is investigating new methods for estimating the motor velocity. This is based on the observation in Section 2.2 showing that the HPF velocity estimate is noisy due to the encoder position quantisation. The HPF described in Section 2.2 is based on a fixed time step method, where it is updated each motor control loop. There are several ways of implementing fix time methods where Turf Tank have done it with a HPF. Fix time methods are fundamentally based on derivative approximations based on fixed sample time position data. A simple example is a backward difference:

$$\omega_k \approx \frac{\theta_k - \theta_{k-1}}{T_s} \tag{3.9}$$

Here, T_s is fixed sample time, ω_k is the approximated velocity at the current sample k, θ_k is the position at the current sample and θ_{k-1} is the position at the previous sample.

Fixed time methods are a common way to utilise encoder data to generate velocity estimates, and at higher speeds they function well. However, when operating at lower speeds where there may no longer be a change in encoder position between samples, the performance of this method starts to degrade, due to time delta between edges on the encoder signal. Here the signal to quantisation noise ratio becomes higher the lower the speed is. This gives the incentive to investigate methods that are less sensitive to quantisation and has a better low speed estimation performance.

Strategies for Obtaining Velocity Estimates from an Incremental Encoder

The first step in trying to improve upon the current strategy of a fixed time based method used by Turf Tank, in the form of a HPF as described in Section 2.2 is done by gathering knowledge on what different strategies exist. In general, these velocity estimation strategies are grouped into three categories: fixed displacement, a combined method or model-based solutions such as estimates based on observers and the like. Each of these options has their set of strengths and weaknesses, and choosing the right one will generally always present some sort of compromise. The following is a look into the strengths and weaknesses of the three methods, to determine if there exists one which is more suitable for the situation presented at Turf Tank.

Fixed Displacement Methods

The first method for velocity estimation that will be introduced is called fixed displacement. The method is introduced because of its ability to estimate low speed more accurately [7, 8]. The fixed displacement method estimates the velocity with the following equation:

$$\omega_e \approx \frac{\Theta}{t_e - t_{e-1}} \tag{3.10}$$

where ω_e is the velocity estimated from the most recent encoder edge event e, Θ is the encoder quantisation, t_e is the time for the most recent encoder edge event and t_{e-1} is the time for the previous encoder edge event.

The fixed displacement method should have a higher accuracy at low-speed operation because it can approximate velocities infinitely close to zero [7, 8]. This is because the velocity estimate is only updated when an encoder edge event has occurred, and the time between encoder edge events is measured. This removes the quantisation noise inherent to the fixed time methods, because sampling is only performed at quantisation boundaries.

However, this also introduces some weaknesses for the estimate, being that it has variable phase, and the phase increases significantly at lower speeds due to the time between encoder events. The estimate is also not able to represent zero velocity on its own, as no new encoder events would be received, and the velocity would therefore never be updated. Another downside comes with the implementation of the estimate. If the velocity is to be updated every time an encoder edge event occurs, as stated by the fixed displacement method, a μC's central processing unit (CPU) has to be interrupted at each encoder edge event. The rate of interrupts becomes higher the faster the encoder is rotated. This can eventually become a problem because too many interrupts can overload the CPU. As stated earlier, the magnetic angle position sensor (MAPS) attached to the Turf Tank Two robot's wheels has 16.384 counts per revolution (CPR) when utilising quadrature decoding. When performing line marking, the robot reaches a max speed of 2,4 rev/s. This equates to just above 39.000 interrupts each second, which is problematic when all other functionalities of the robot have to be maintained. As a result, the fixed displacement method is not viable as a velocity estimate if the velocity is updated at every encoder edge event.

Hardware solutions, however, exist that avoid interrupts at each encoder edge event. The velocity estimation is still based on Eqn. (3.10), but the velocity is not updated at each encoder edge event but instead at each motor control loop. This is done by storing the encoder edge event time and position data in memory without CPU intervention. With the data stored in the μC memory, the velocity can be updated at each control loop. An example of this is seen in Figure 3.5.

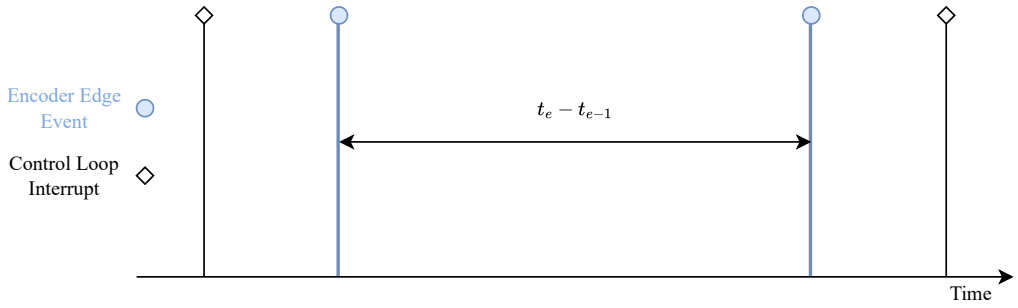

Figure 3.5
Fixed displacement method with data stored in memory without CPU intervention.

Here, two encoder edge events marked with a blue line can be seen between two control loop times. The two encoder events and their corresponding time is saved in the μC memory between the two control loops. The velocity estimate can then be updated at the time of the new control loop by using Eqn. (3.10).

With the fixed displacement method explained, the next method, called the combined method, will be explained in the next section.

Combined Method

There also exists a method that combines the variable component from the fixed displacement method and the fixed time method, called the combined method [9, 10]. Here, both the position and time can vary. Similarly to the fixed displacement method, the combined method can also be implemented without updating the velocity estimate on an interrupt basis. The velocity is estimated from the newest position and time from the current and previous control loops using the following formula:

$$\omega \approx \frac{\theta_c - \theta_p}{t_c - t_p} \tag{3.11}$$

Where c and p are short for current, previous. The method is also illustrated in Figure 3.6.

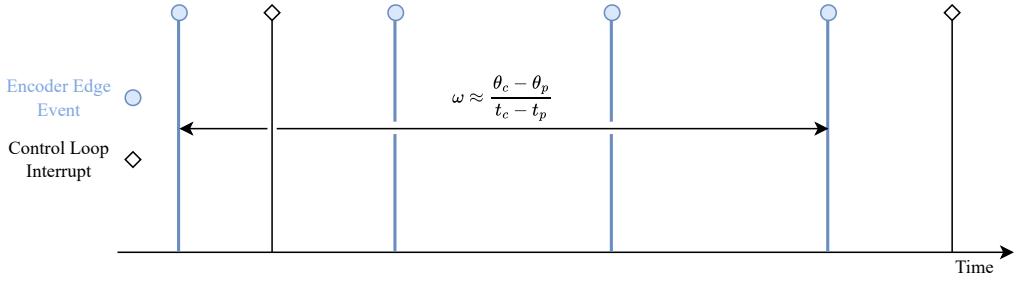

Figure 3.6

Combined method for velocity estimation with data stored in memory and the velocity being updated in each motor control loop.

The velocity estimate is updated each motor control loop if a minimum of one encoder edge event has occurred. The position and time for each encoder edge event are stored in memory. The position and time difference is calculated between the newest encoder edge event in the last motor control loop and the newest encoder edge event in the current motor control loop. In Figure 3.6, there are three new encoder edge events in the current motor control loop. The resulting position and time difference used for the velocity estimation are shown.

The difference between the fixed displacement method and the combined method comes when there is more than one encoder edge event in each motor control loop. Here, the combined method results in an averaged velocity over multiple encoder edge events. This has its upsides and downsides. The downside is that averaging will introduce some phase to the velocity estimate and still cannot represent zero velocity. The upside being that the averaging will smooth the velocity estimate.

Model Dependent Methods

While the former method groups focus on creating a suitable velocity estimate directly from the encoder position data available, the model-based methods try to estimate the velocity of the system by using the available data as well as knowledge about the physical system. There exists several different versions of these estimators, some of the most well-known being Luenberger observers and Kalman filters. Since these methods utilise a model of the system to create their estimates, there needs to be a model with a certain level of detail. This is complicated with the Turf Tank robot, since friction can change, and the mass of the robot changes as it works, by the paint canister slowly being emptied. Furthermore, traction loss significantly alters the inertia of the system and would be very difficult to capture in a model. In addition to that, model-based methods are also unsuited due to their poor behaviour when fed quantised data, as the encoder data [11]. There exists methods for getting around this problem, but it increases the complexity of the implementation. Therefore, the earlier introduced and simpler methods are explored initially.

With the proposed methods introduced, the methods will be evaluated in relation to the hardware on the Turf Tank Two robot. This is done with the goal of aiding in the selection of a velocity estimation method.

Evaluating Velocity Estimation Methods in Relation to Hardware

With model-based methods initially not being selected, the fixed displacement method and the combined method will be further evaluated. This will be done by considering the available hardware and the effect it has on the

velocity estimation method. For the velocity estimation, it is the MAPS and timer hardware on the Turf Tank Two robot that is used. The MAPS effect will first be analysed.

The MAPS has an edge-to-edge differential non-linearity (DNL) error from their production that affects the accuracy of the velocity estimate. The MAPS on the Turf Tank Two robot has a maximum DNL error of ±0,01° at 2500 pulses per revolution (PPR), the behaviour of this can be seen in [3, p. 7]. No information is given on the DNL error at the setting of 4096 PPR. It is therefore assumed to be the same. When utilising quadrature decoding, the PPR is raised to 16384. The angular step size at this resolution is 0,022°. The MAPS DNL error can then be divided by its angular step size to find the maximum absolute DNL error.

$$\frac{0{,}01^\circ}{0{,}022^\circ} = 46\,\% \tag{3.12}$$

The maximum absolute DNL error is then equal to ±46 %. The effects of the DNL error increase with the velocity. This is because the DNL error is an absolute error that has a greater effect the smaller the time difference is. Here, the combined method has an advantage because it averages over multiple encoder events, which will lower the effect of the MAPS DNL error.

Tolerances in crystal oscillator frequency also introduce error to the velocity estimate, as the clock can run slower or faster than nominal. The Turf Tank Two robot uses an STM32F446ZE μC [12]. From the unused timers on the Turf Tank Two robot μC, a maximum clock frequency of 90 MHz can be used. This clock is driven by a crystal with an accuracy of ±5 ppm. The frequency error introduces the largest absolute velocity error, the higher the velocity of the robot is. At the line marking robots maximum velocity of 1,5 m/s the maximum error introduced is $\pm 0{,}8 \cdot 10^{-3}$ m/s. This introduces a very small absolute error that will have a negligible effect on the velocity estimate.

An error is also introduced because the encoder edge event will almost always occur between two timer ticks. This is shown in Figure 3.7 where an encoder edge event is shown in between two timer ticks.

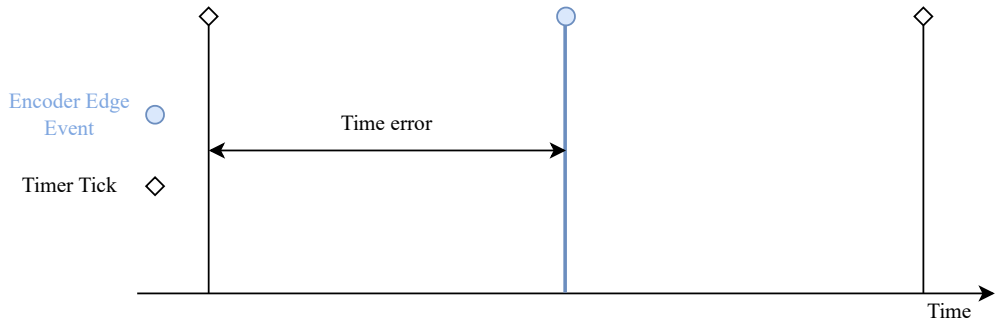

Figure 3.7

Illustration showing the timer error that can occur due to encoder events happening between timer ticks.

The timestamping error is shown in the figure as the time between the first timer tick and the encoder edge event. The maximum error introduced will be equal to one timer tick. The timer resolution can then be multiplied by the worst-case the timestamping error:

$$\frac{1}{90\,\text{MHz}}\,(1 + 5\,\text{ppm}) = 11{,}1\,\text{ns} \tag{3.13}$$

The maximum timestamping error is then 11,1 ns.

When again considering the worst-case scenario, which is the maximum velocity of the robot, the introduced velocity error can be evaluated. At maximum velocity, the robot wheels are turning at 15 rad/s, from this, the number of timer ticks between encoder events can be calculated to determine the maximum velocity error with the following formula.

$$N_{T_{step}} = \frac{\Theta}{\omega T_{step}} \tag{3.14}$$

This is calculated to 22802 timer ticks while driving at maximum velocity. The worst case for this error is when a full timestep is added to the correct time, which will result in a velocity error of 44 ppm, which is also deemed negligible. As a result of this, it can be stated that it is the DNL error from the encoder that has the biggest influence on the velocity error. The combined method has the lowest sensitivity to DNL of the two methods, due to the averaging over multiple encoder edge events. Since the control has not been unstable, the introduced phase of the combined method is deemed acceptable. The methods' low speed performance are also identical as long as one or less encoder edge events happen per sample. Based on this, it is decided to implement the combined method. The implementation of the combined method will then be described in the next section, starting with configuring the hardware for data collection without CPU interrupts.

Facilitating Collection of Encoder Data in Hardware

With the combined method, it is necessary to collect both position and time data for the encoder edge events. The current position data is acquired through the A and B edges coming from the incremental encoder μC as can be seen in Figure 3.8.

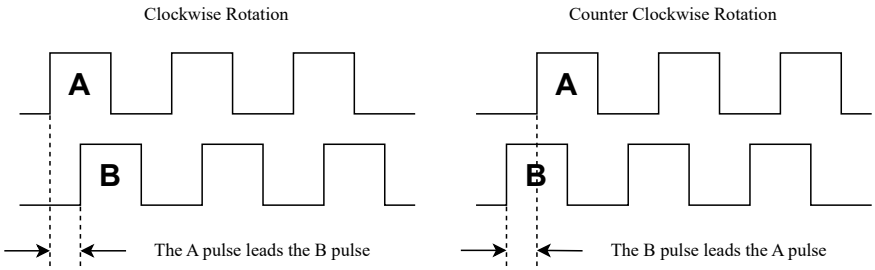

Figure 3.8
Examples of incremental encoder edge trains for clockwise and counter-clockwise rotation.

These are processed by a timer module on the μC setup in encoder mode. Encoder mode configures the timer to capture the encoder edges on its capture compare registers (CCRs) and then, based on the sequence in which they arrive, the direction bit is changed accordingly and the counter is incremented or decremented. The timer is setup to count from 0 to the encoders max range, it will then overflow or underflow if either limit is reached. By utilising an extra free-running timer, which will be referred to as the timestamping timer, it is possible to generate timestamps for every rising edge on the A channel, an illustration of this setup can be seen in Figure 3.9. This is not ideal, as it limits the resolution of the available encoder data by 1/4. There exists a way to setup the hardware that permits timestamping of every encoder edge, however this requires alterations to the current pin setup, and is therefore not viable.

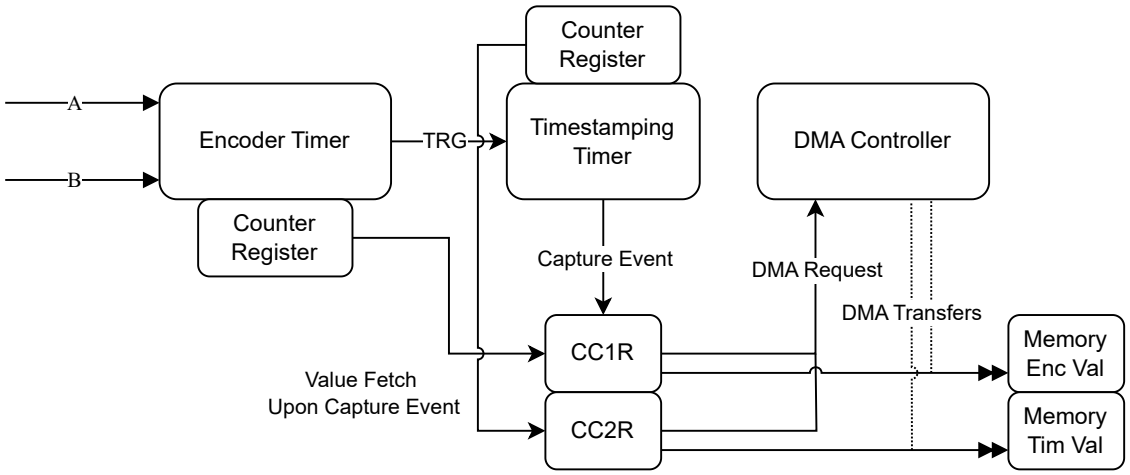

Figure 3.9

Illustration showcasing the hardware setup to facilitate collection of encoder and time data.

The timestamping is done by enabling the generation of trigger signals upon a change in the state of the capture compare 1 interrupt flag (CC1IF) in the encoder timer, this is a flag that is raised when the chip detects a change in value in its CCR1. This signal can then be used to trigger an event on the time stamping timer, which captures the encoder value from the encoder timer and the time value from its own counter register, into its CCR's. These can then start separate direct memory access (DMA) request which transfer the data from the time stamping timers CCR's into arrays defined in code, designed to hold the captured data until later processing. The DMA is setup to run in circular mode which means once it reaches the end of the data array its assigned to, it will start overwriting the old data at the start of the array with new data and so on. An illustration of this can be seen in Figure 3.10 were the arrows shows the transfer of data to memory for each encoder edge event.

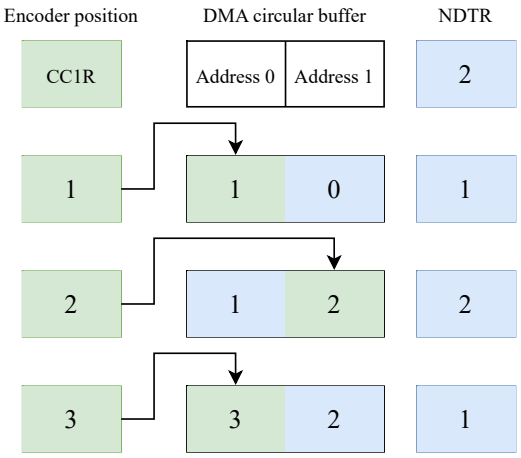

Figure 3.10

Figure illustrating the functionality of the DMA circular buffer.

The DMA buffer has a number of data to be transferred (NDTR) register that points to the address where the DMA will transfer data to the next time an encoder event occurs. This is shown in Figure 3.10 with the blue boxes. The NDTR value is 2 for the DMA circular buffer address 0 and 1 for address 1. This functionality becomes important for tracking where the newest value is in the assigned data array, which is needed in the implementation of the velocity estimate.

With position and timestamp data available in memory without interrupting the CPU of the μC the implementation of the combined method can be explained next.

Implementation of Combined Method

In the following section the implementation of the combined method will be explained. This will initially be done using a flowchart that can be seen in Figure 3.11. The implementation will be done on the STM32F446ZE μC the Turf Tank Two robot uses [12]. The flow chart show the overall steps involved in updating the velocity at each motor control loop interrupt.

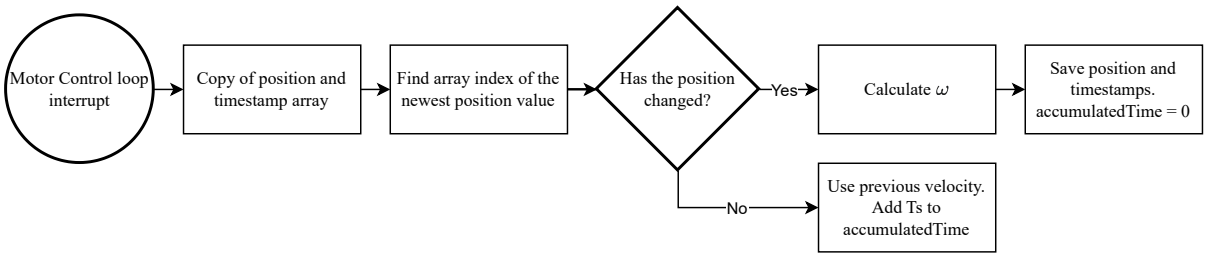

Figure 3.11

Flow chart describing the overall implementation of the velocity estimate.

The flow chart in Figure 3.11 start out in the left circle with the arrows showing the flow of the program. Initially, the logic starts when an interrupt is generated by the motor control timer. The first task handled is then copying the time and position data from the arrays which the DMA has transferred data to. The data is copied to two new arrays ensuring the data cannot be overwritten by the DMA while the logic is running. Since the DMA transfers data in a circular manner as described in Section 3.3, it is necessary to determine which index contains the newest value, as the index of the newest data changes every time the DMA transfers data. This is done in the next block, trough the DMA's NDTR register, which contains information on which address the DMA will write to next. With this information its possible to determine which address the DMA wrote to last, which will then be the newest value, the index of this value is then saved. The newest index value is found through the following equation:

$$newestValueIndex = (bufferSize - NDTR) - 1 \tag{3.15}$$

As can be seen from Eqn. (3.15), the newest value index (NVI) will return a negative value when the DMA is set to transfer to the first entry in the array. It is necessary to catch this condition and set the NVI equal to the length of the array minus one. After determining the index of the newest value, the logic enters an if statement that determines whether the position has changed since the last sample. This is done simply by comparing the new position value with the value from the last motor control loop. If the position has not changed, the if statement returns false, and the velocity estimate is simply reused from the last sample. If the if statement returns true, the new velocity estimate is calculated using Eqn. (3.11). When determining the change in position between two data points, the encoder position overflow or underflow has to be accounted for. In Figure 3.12, a flowchart of the logic for handling this overflow can be seen.

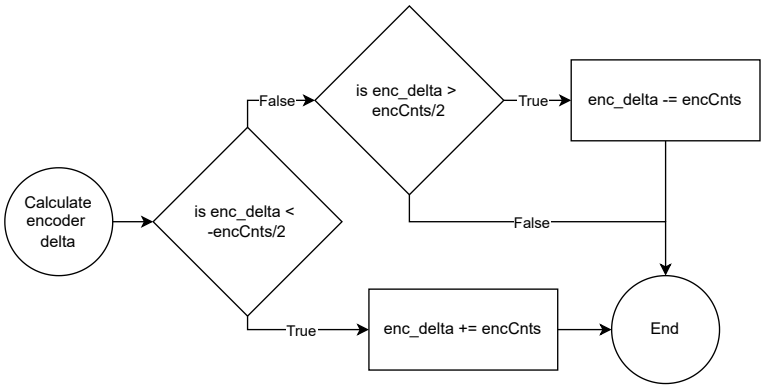

Figure 3.12

Flow chart describing handling of encoder under/overflow.

First, the encoder delta is calculated, and it is then compared if its less than negative the total encoder counts divided by 2. In the case that it is, the corrected delta is found by adding the total number of encoder counts to the calculated delta. If its not another if statement checks whether the encoder delta is larger than the total encoder counts divided by two. If this returns true the encoder delta is corrected by subtracting the total number of encoder counts, if it returns false the initially calculated encoder delta does not need correction and can be used as is.

When calculating $t_c - t_p$ from Eqn. (3.11), overflow of the timestamp timer has to be handled to calculate the correct time between timestamps. This is relevant when the timestamp timer overflows in between two encoder edge events as can be seen in Figure 3.13. More than one overflow cannot happen within a control loop interrupt due to the sampling rate, which simplifies the calculations. To aid in the handling of this overflow a variable called accumulatedTime is introduced in the code. If no new encoder data is received since the last control loop interrupt, one sample time is added to the variable

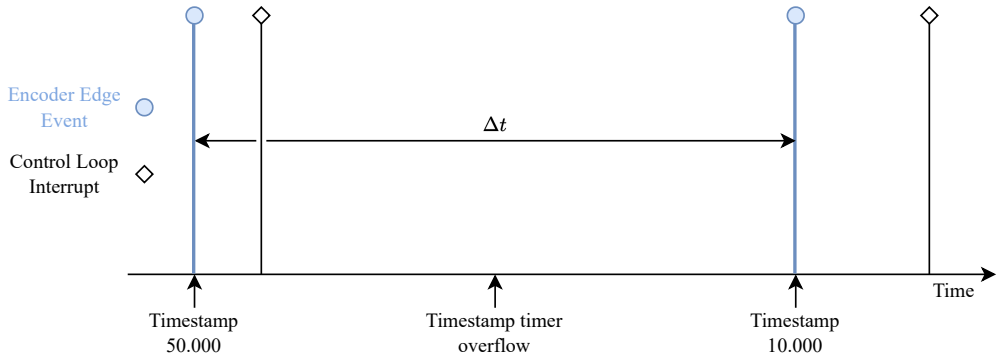

Figure 3.13

Example of timestamp timer overflowing between encoder events.

Here, the timestamp of the first encoder edge event is 50,000 and 10,000 of the second, meaning the timer has overflowed. The timestamp timer is a 16 b timer, meaning it will overflow after 65536 timer ticks. If $t_c - t_p$ is calculated the wrong Δt is calculated. In the example below, the accumulatedTime variable is set to zero, meaning that there was an encoder edge event in the last motor control loop.

$$10{,}000 - 50{,}000 = -40{,}000 \tag{3.16}$$

The overflow situation is handled with an if statement that checks if $t_p > t_c$ is true. If this condition is true Δt

is calculated with the following formula:

$$\Delta t = 65.536 - t_p + t_c + accumulatedTime \tag{3.17}$$

Otherwise Δt is calculated normally by $t_c - t_p + accumulatedTime$.

After calculating the velocity, the logic ends with saving the position and time data used in this iteration, so it can be used for comparison in the next sample, and the accumulatedTime is set to zero. The implementation of the combined method velocity estimate will now be tested in the following section.

Initial Testing and Problems

With the combined method velocity estimate, implemented tests can be run to check the performance. The initial test consists of turning a wheel by hand and seeing what velocity the method estimates. The results of this can be seen in Figure 3.14.

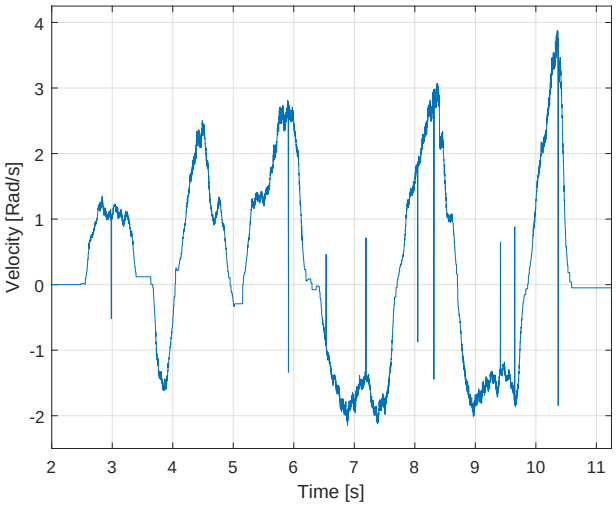

Figure 3.14

Plot showing initial results from the combined method velocity estimate, race conditions are seen causing velocity spikes.

As can be seen in Figure 3.14, there is a problem with the estimate, random significant velocity spikes show across the estimate. An example is the spike in velocity just before 6 s. Here the velocity spikes from approximately 2,5 rad/s to −1,3 rad/s and back again. This error turns out to be caused by race conditions happening when the data from the DMA target arrays is being copied. Data within the array changes while it is being copied, causing mismatches. This is unwanted behaviour as spikes from race conditions will cause added tracking error. Additionally, the effect of the combined method not being able to represent a velocity of zero is also visible. This can be seen at approximately 10,5 s where the velocity crosses zero and stays at a constant velocity even though the wheel is stationary. How this behaviour is improved and how race conditions are handled will be described in the next two sections.

Handling of Race Conditions

In the following section, an introduction to race conditions will first be given, followed by the implementations made to handle race conditions.

Race conditions happen as a result of the DMA position and timestamp stream transferring data to its target memory locations while the motor control loop is copying data from the same memory locations. This will happen if an encoder edge event occurs when the position and timestamp data are being copied during a motor control loop. This can result in a mismatch of new and old position and timestamp data in the copied array at the index of the newest value. This ends up giving race condition spikes that can be seen i Figure 3.14. Two types of race conditions can happen in the program. The first one is when a new position and an old timestamp are copied, and vice versa. Both equate to wrong velocity estimates that should be avoided.

The implementations made to handle race conditions will be explained using the flowchart in Figure 3.15. The flowchart describes the program structure of the combined method with race condition handling implemented.

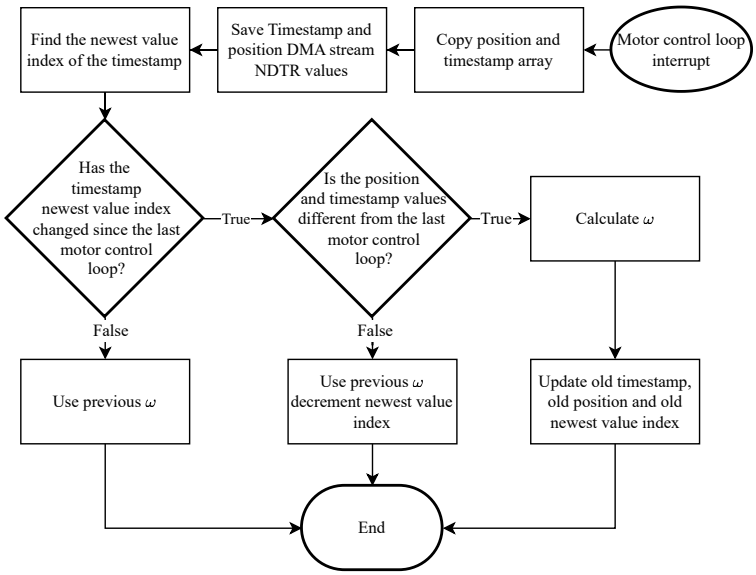

Figure 3.15
Flowchart showcasing the handling procedure for race conditions.

The flowchart starts in the motor control loop interrupt at the top of Figure 3.15. The program then starts out copying the position and timestamp array. Then the NDTR value for the timestamp and position DMA stream is saved. The timestamp timer NDTR value is then used to find the array index of the newest value. With the first three code blocks executed, sufficient data is obtained to detect the two types of race conditions explained earlier. This is done in the following parts of Figure 3.15 with if statements. The if statement checks if the NVI has changed for the timestamp array, meaning a new encoder edge event has occurred. If this is false, no new timestamp is available, and a new velocity cannot be calculated. The previous velocity estimate is then used, and the motor control loop is ended. If it is true that the NVI has changed since the last motor control loop, the code goes to the next if statement in Figure 3.15. Here, it is checked if both the position and timestamp have changed since the last motor control loop. If this statement is false, a race condition has happened, and the previous velocity estimate is used. The NVI variable is also decremented, ensuring that the correct position and timestamp values are compared in the next motor control loop. If both the position and timestamp value have changed, a new velocity estimate is calculated. Then the old timestamp, old position and old NVI are updated for comparison in the next motor control loop. With the implementation of race condition handling described the implementations made to enable the combined method to estimate zero velocity will be described next. Afterwards, both the race condition handling and zero velocity estimation will be tested and concluded upon.

Velocity Decay

As mentioned in Section 3.3, the velocity estimate is not able to reach zero velocity on its own. This is because in the transition from some small velocity to zero velocity, encoder events stop occurring, and the velocity will get stuck at the last small velocity. To solve this issue, velocity decay is introduced. This lets the velocity decay towards zero when new encoder data is not present. It functions by utilising the earlier defined variable

accumulatedTime, which, if no new encoder data is received since the last control loop interrupt, one sample time is added to the variable. If this variable's value goes above the previous time between the last two encoder events, the code starts updating the velocity according to Eqn. (3.18).

$$v = \frac{\Delta x}{accumulatedTime + th} \tag{3.18}$$

Where th is the time from the last encoder event up to the interrupt that happened within. This method lets the velocity decay towards zero when no new data is received and represents a theoretical maximum possible velocity. It is also a reliable estimation of the current velocity until the next encoder event is received.

Test After Race Condition Handling and Velocity Decay is Implemented

With implementations made to handle race conditions such that large velocity estimation spikes do not occur, and velocity decay also being implemented, a test is performed again. The same test as in Section 3.3 is performed where the motor is turned by hand. The resulting velocity estimate can be seen in Figure 3.16.

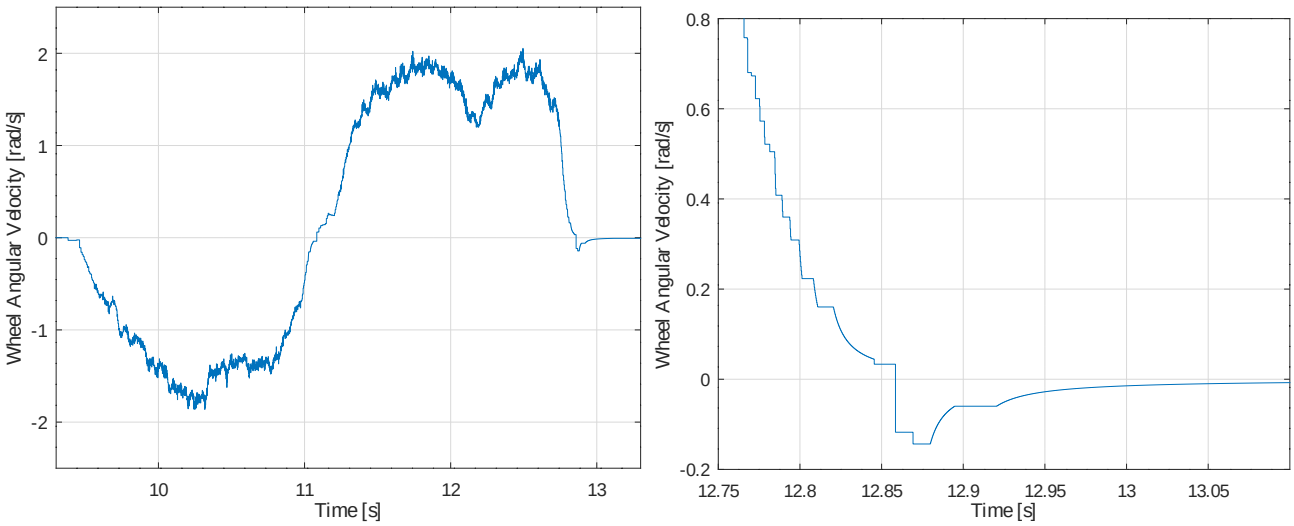

(a) *New velocity estimate free of velocity spikes.*

(b) *A zoom in showcasing the velocity decay functioning.*

Figure 3.16

Free wheel test of combined method velocity estimate after implementing race condition handling and velocity decay.

Here, it is seen that there are no large velocity spikes because race conditions have been handled. The implementation of velocity decay can also be seen working in Figure 3.16b. The velocity can be seen decaying at around 12,83 s. When the next encoder event happens, only a small correction is needed. This behaviour is an improvement because it is a better representation of the real velocity. The velocity is now also able to decay towards zero as seen from around 12,93 s and onwards. It can also be seen that the sample rate is lower the closer to zero the velocity becomes, and until no updates happen. The is a result of the combined method. The velocity estimate is still noisy, which is unwanted. This is expected to be primarily because of the MAPS DNL as investigated earlier in Section 3.3. This is because the noise intensity rises as the velocity rises. A solution to lower the noise will, as a result, be investigated in the next section.

Addition of Low Pass Filter to Combined Method Velocity Estimate

It is observed in the previous section that the combined method's velocity estimate is noisy. To lower the noise in the velocity estimate, a LPF is implemented. The LPF's cut-off frequency is set to 45 Hz, which is the same

as Turf Tanks HPF. This means that they have the same bandwidth. This is chosen because it has not been observed that the phase it introduces is the limiting factor. It has always been the excitation of the robot chassis' resonance frequencies. A new test is performed where the robot wheel is rotated by hand. Here, the combined method velocity estimate with and without the LPF is plotted in Figure 3.17a. Here it is seen that the noise intensity is lowered from the blue line and to the yellow as expected. The combined method velocity estimate is also compared with the originally used HPF in Figure 3.17b.

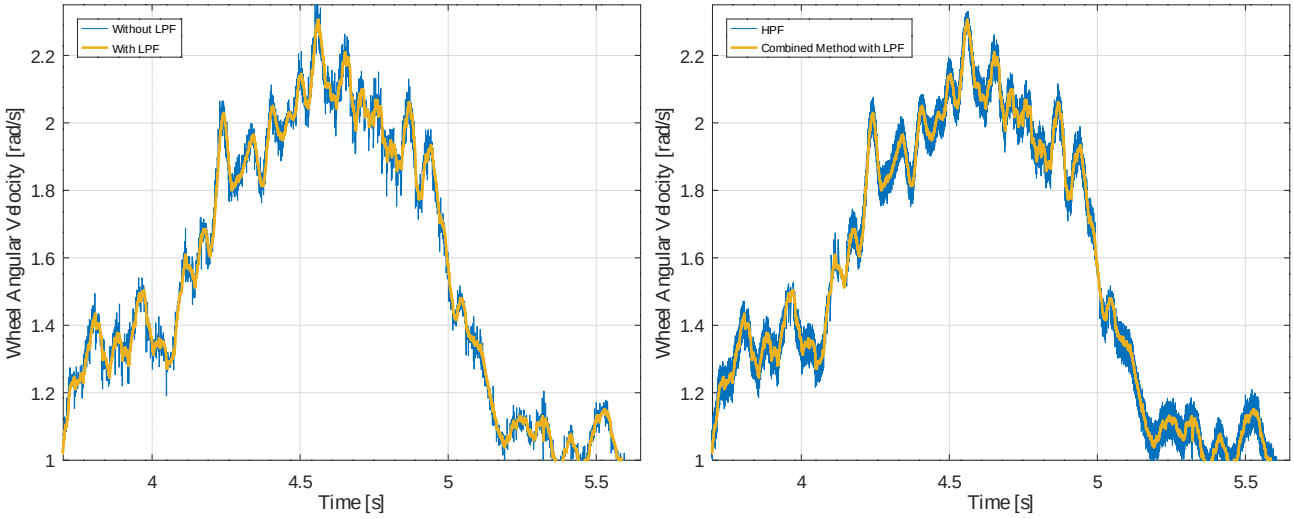

(a) *Comparison of combined method velocity estimate with and without LPF.*

(b) *Comparison between the combined method velocity estimate with an LPF and the old HPF velocity estimate.*

Figure 3.17

From this, a couple of observations are made. The first is that the combined method velocity estimate with the LPF, which is the yellow line in Figure 3.17b, has a lower noise intensity. The second observation is that the combined method velocity estimate can estimate the same velocity as the HPF. This means that it is working correctly. The new velocity estimate is, as a result, deemed to have a better performance than Turf Tanks HPF. With the new velocity estimate implemented and tested, the PI velocity controller will be tuned and tested with Turf tanks validation trajectory in the next section.

Performance Evaluation after Implementation of Velocity Estimate

The velocity controller with the new velocity estimate implemented is tuned following the same procedure of raising the gains as much as possible without the robot making audible noise. This ended up with PI controller gains of 1,5 and 18,75 which is higher than then detuned controller solution PI controller gains of 1 and 12,5. With the controller tuned the validation trajectory is again performed. From analysing the CTE data the same behaviour regarding outliers in CTE is observed as in all the previous performed validation trajectory tests. The largest outliers in CTE occur when transitioning from a line to an arc and vice versa. This is both when driving forward and backwards but worst backwards. The resulting MACTE and RMSCTE are improved by 13 % and 21 %. The improvement in performance is very reminiscent of the first proposed solution where the controller is detuned. The performance in MACTE and RMSCTE is only improved by 2 %pt and 3 %pt compared to the detuned controller. It is suspected that the negligible performance gain is due to the the robot controller remaining unaltered and that the added disturbance rejection had minimal impact. To investigate if a further improvements can be made to the velocity controllers bandwidth, filtering methods to remove the resonance

frequencies from the estimate are investigated in the next sections.

3.4 The Resonance Problem

As described in Section 2.2, it is concluded that the primary cause of noise problems on the robot is resonance in the robot chassis. The resonance in the chassis would then cause oscillations in the velocity estimate, further exciting the natural frequencies in the system. In the previous sections, different attempts at reducing the audible noise problems have been made, including designing a new improved velocity estimate with reduced noise and tuning the controller to have a first-order response. These solutions have improved the performance concerning the wishes, but it is expected that further improvements regarding MACTE, RMSCTE and bandwidth are still possible. The next solution will be focused on attenuating the resonant frequencies in the velocity estimate to further reduce the vibrational content in the motor.

Removing the Resonant Frequencies from the Velocity Estimate

There exist several ways of removing frequencies from a signal by filtering. A filtering solution could be a Butterworth low-pass, low-pass or notch filters to attenuate the resonant frequencies in the velocity estimate. Common for these is that they come with a phase delay of varying degrees depending on the amount of filtering, which is undesired. Therefore, it becomes a compromise between achieving the needed attenuation while keeping sufficient phase at the operating frequencies of the system. The LPF in Eqn. (3.19).

$$H(s) = \frac{\omega_c}{s + \omega_c} \tag{3.19}$$

It is already used in smoothing the velocity estimate, and possesses characteristics as shown in Figure 3.18, The figure is also shown characteristics for a second and fourth order Butterworth filter with the general form Eqn. (3.20).

$$H(s) = G_0 \prod_{k=1}^{n} \frac{\omega_c}{s - \omega_c \epsilon^{\frac{j(2k+n-1)\pi}{2n}}} \tag{3.20}$$

Where G_0 is the DC-gain, n is the filter order, and ω_c is the cut-off frequency.

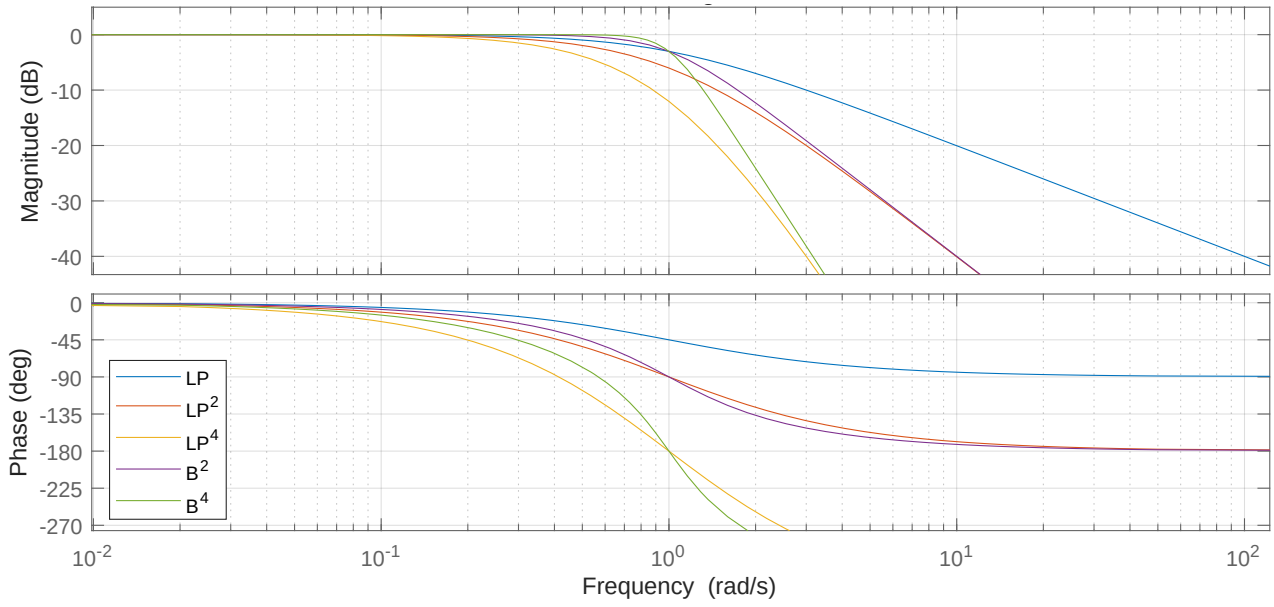

Figure 3.18

Frequency response of low-pass and Butterworth filters.

The first order LPF LP in Figure 3.18 has −20 dB of attenuation per decade after the cut off frequency, increasing to −40 dB and so on for higher order filters, as seen from LP^2 and LP^4 in Figure 3.18. Furthermore, the filter reaches −45° of phase at its cut-off frequency, with the phase loss starting at least one decade before the cut-off frequency. The Butterworth filter has a steeper roll-off on the attenuation, meaning it attenuates less before the cut-off frequency, which is desirable. The phase response is also slightly more favourable, with less phase loss occurring before the cut-off frequency.

The velocity control loop has a bandwidth of 2 Hz to 4 Hz and the velocity estimate around 45 Hz with its initial low-pass filtering. With the first resonant frequency being around 150 Hz, this puts about a decade and a half between the resonant frequency and bandwidth of the velocity control. Looking at Figure 3.18 it can be seen that even for fourth-order low-pass and Butterworth filters, the phase loss is very minimal a decade and a half from the cut-off frequency. This, in theory, makes the two suitable for attenuating the wanted frequencies. A solution could be placing a fourth-order Butterworth filter at 300 rad/s as shown in Figure 3.19.

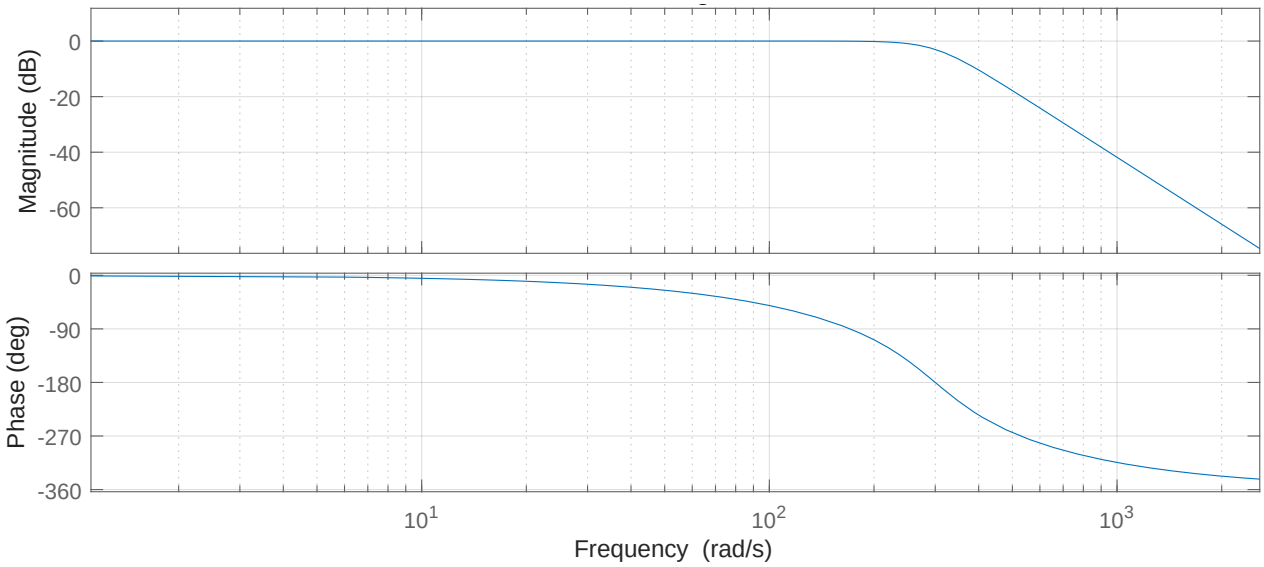

Figure 3.19

Frequency response of fourth order Butterworth filter with 300 rad/s *cut-off frequency.*

Here it is possible to achieve around −40 dB of attenuation at the desired frequency of 150 Hz, while only losing 14° of phase at the operating frequency of around 4 Hz. Whether this specific amount of attenuation is enough or too much is not clear, and experimentation will have to be performed to see what is necessary. Furthermore, while the phase loss is minimal, it is also not known fully if it will bring problems, this will also need to be tested. Ideally, the needed gain is lower than what is achieved here, as this would also permit further lowering the phase loss by moving the cut-off frequency forward. A fourth-order low-pass filter would be able to achieve a lot of the same as the Butterworth, but with worse phase characteristics and attenuation before the wanted frequencies. Based on this, it makes most sense to utilise the Butterworth filter. The Butterworth filter seems suitable in theory, but complications may arise in the implementation process. This will be discussed next. Discretising the fourth-order Butterworth filter using the bilinear transform gives the discrete transfer function in Eqn. (3.21).

$$H(z) = \frac{1{,}796 \cdot 10^{-6} z^4 + 7{,}185 \cdot 10^{-6} z^3 + 1{,}078 \cdot 10^{-5} z^2 + 7{,}185 \cdot 10^{-6} z + 1{,}796 \cdot 10^{-6}}{z^4 - 3{,}804 z^3 + 5{,}431 z^2 - 3{,}449 z + 0{,}822} \tag{3.21}$$

It quickly becomes apparent that the majority of the numerator coefficients are floating point numbers with

factor 10^{-6}, while the denominator coefficients are all at 10^{0}. This large difference between coefficients creates problems due to the limits of floating point precision, in this case causing small numbers to be lost in calculations due to truncation. The discretised Butterworth filter is therefore not immediately usable as it is. Solutions could be separating the filter up into several lower-order filters in series, or lowering the sample frequency to reduce the difference between the numerator and denominator coefficients. Granted that the implementation of the Butterworth filter is complicated by floating point limitations, other filters will be considered.

The notch filter is a different type of filter that only attenuates a small band of frequencies, and has 0 dB gain elsewhere. A notch filter can be created from two second-order system denominators as in Eqn. (3.22).

$$H(s) = \frac{s^2 + 2\xi_n \omega s + \omega^2}{s^2 + 2\xi_d \omega s + \omega^2} \tag{3.22}$$

Where ω is the target frequency, and the width and attenuation of the filter is then tuned by altering the damping ratio of the numerator and denominator. In Figure 3.20, the frequency response of notch filters with varying damping ratios can be seen.

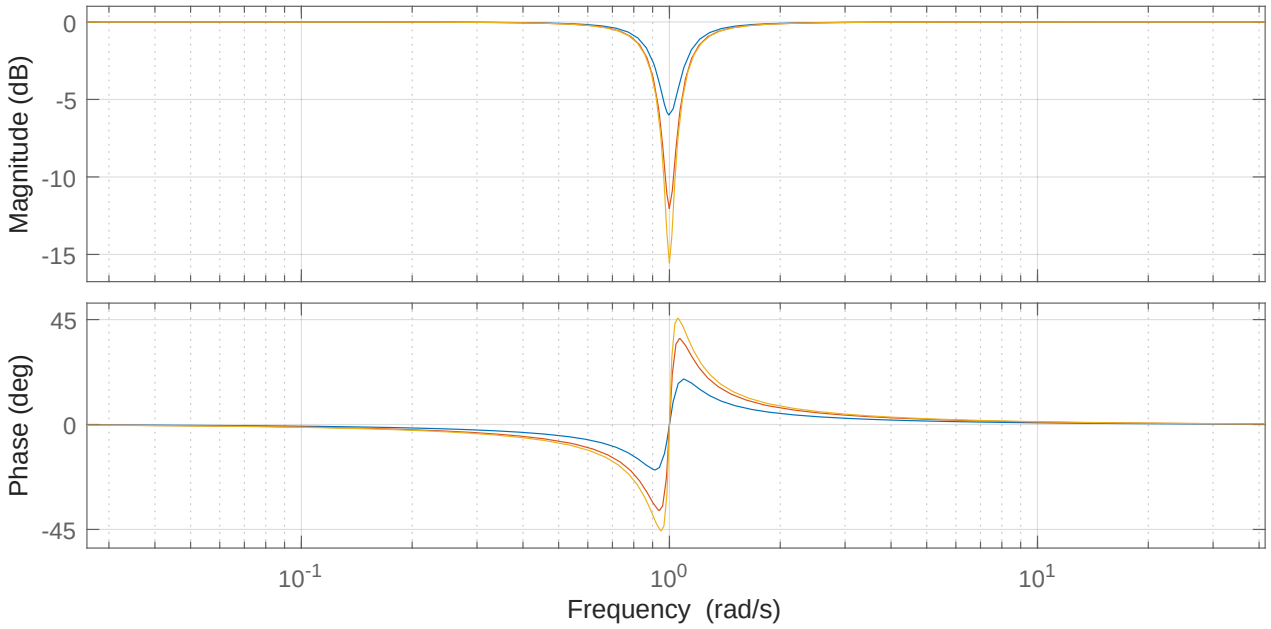

Figure 3.20

Frequency response of notch filters with varying damping ratio.

From this, it can be observed that the notch filter can achieve significant attenuation while retaining a decent phase close to the attenuated frequencies. Looking at the notch filter with the highest ratio between denominator and numerator damping, at least −15 dB of attenuation is achieved, with a total phase loss of 45° at the target frequency. Furthermore, only a decade out from the target frequency, the phase loss is kept at a minimum, losing close to 0°. Even further out, around the bandwidth of the velocity controller, the phase loss would be effectively 0°. Designing a notch filter for the specific case at hand, the target frequency is set at 180 Hz, the numerator damping at 0,0043633 and the denominator damping at 0,25. This creates a filter with the frequency response seen in Figure 3.21.

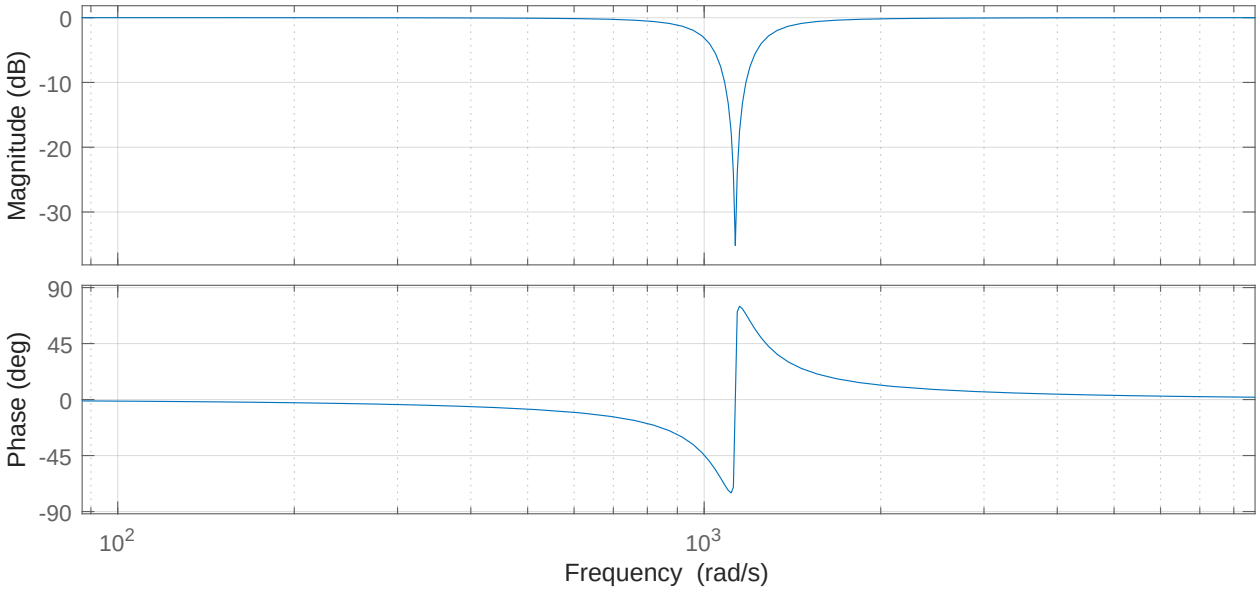

Figure 3.21
Frequency response of 180 Hz *target frequency notch filter.*

This filter reaches −35 dB at the target frequency, while only losing 0,385° of phase at the operating frequency of the velocity control. The attenuation is on par with the performance of the Butterworth filter, but at a lower phase loss. A weakness of the notch filter is the attenuation is only focused around one frequency. This is a problem as the natural frequencies can vary from robot to robot, so one specific notch filter most likely will not solve the issue for all robots. Ideally, anything above the operating frequency would be attenuated. It might be favourable to utilise several notch filters placed at each resonant frequency of the system, but this would also increase phase loss at the operating frequency. The currently implemented LPF with a cut-off frequency at 45 Hz could provide the higher frequency attenuation.

Looking at Eqn. (3.23) the discretised notch filter can be seen.

$$H(z) = \frac{0{,}967z^2 - 1{,}86z + 0{,}966}{z^2 - 1{,}86z + 0{,}933} \tag{3.23}$$

Here, it is clear that the size differences between the numerator and denominator coefficients are insignificant concerning floating-point precision. This means the notch filter can easily be implemented without further changes being made to the code structure of the robot. Based on the observation of the notch filter's potential performance and its ease of implementation, this is initially tested as a solution to the resonance problem of the robot. The LPF with a cut-off frequency at 45 Hz is also kept.

Performance test of proposed solution

To test if the notch filter makes a difference, the gains are increased to a K_p of 2 and the $\frac{K_i}{K_p}$ ratio is maintained at 4,650, ensuring a first-order response. The robot now does not make audible noise at speeds above 0,5 rad/s but a new problem is encountered below 0,5 rad/s. The system starts oscillating and makes audible noise when on the ground, and even higher noises when the wheels are not on the ground. In Figure 3.22, the oscillations can be seen when the robot is not on the ground. The same oscillations happen when on the ground, with the only difference being that the amplitude is lower.

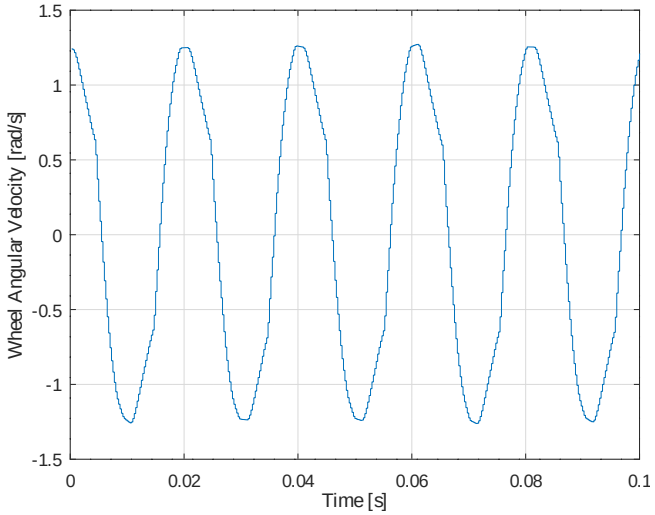

Figure 3.22

Velocity oscillations with a 0 velocity reference. The velocity controller PI gains are set to 2 *P-gain with the* $\frac{K_i}{K_p}$ *ratio set to* 4,650*.*

In Figure 3.22 it can be seen that the velocity oscillates at a frequency of 50 Hz, unlike earlier, where it was 180 Hz. It is also observed during the test that it is mostly the wheels that oscillate, while the chassis's natural frequencies are not excited. This problem is deemed to be a limit cycle. This is because the closer the velocity comes to zero, the less feedback the MAPS provides. This results in a higher phase the closer the velocity is to zero, due to the effectively lower sample rate. The velocity controller is thereby unstable in a region around zero velocity, but becomes stable again when outside of this band because the feedback rate is higher. Raising the PI velocity controller gains enlarged this instability band to a point where it resulted in audible noise. This is even worse for the robot when it is not in contact with the ground because the stability margin is lowered in this configuration as described in Table 3.2. Solutions to prevent the limit cycle with and without contact with the ground from making audible noise will be investigated in the next section.

3.5 Fourth Solution: Current Controller & Bumpless Transfer

Earlier in Section 3.2, a model was developed which showed that the mechanical and electrical dynamics become complex conjugated when there is no ground contact. This causes the system to oscillate in this situation. This explains why the audible noise and the amplitude of the velocity oscillation are highest in this situation. It is therefore of interest to make the electrical pole faster, such that the mechanical and electrical systems do not merge and oscillate. A method to move the electrical pole further away from the mechanical pole is to introduce a current feedback gain K_{iq}. The structure can be seen in Figure 3.23.

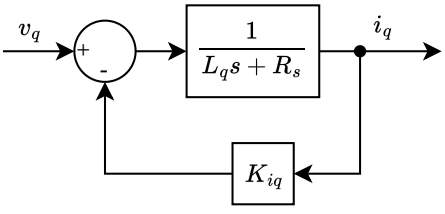

Figure 3.23

Current feedback.

Closing the loop with the feedback formula results in the dynamics in Eqn. (3.24)

$$\frac{1}{L_q s + R_s + K_{iq}} = \frac{\frac{1}{L_q}}{s + \frac{R_s + K_{iq}}{L_q}} \tag{3.24}$$

To design K_{iq}, a desired closed-loop characteristic equation Λ_d is defined and can be seen in Eqn. (3.25).

$$\Lambda_d = s + \omega_d \tag{3.25}$$

Where ω_d is the desired pole location.

The denominator of Eqn. (3.24) is equated to Eqn. (3.25) and the equation is solved for K_{iq} in Eqn. (3.26).

$$\frac{R_s + K_{iq}}{L_q} = \omega_d \Rightarrow K_{iq} = \omega_d L_q - R_s \tag{3.26}$$

A pole location of $-150 \cdot 2\pi$ is chosen, this results in the following open-loop poles:

$$\text{Ground contact: } s = -940{,}4 \ \& \ -2{,}063, \qquad \text{No ground concact: } s = -885{,}5 \ \& \ -56{,}98 \tag{3.27}$$

The slow system pole has now moved closer to the origin when the wheel is not slipping, meaning the velocity controller $\frac{K_i}{K_p}$ will need to be adjusted to maintain the approximate first-order response. The poles are also no longer complex-conjugated when the wheel is lifted off the ground. To summarise, the full control system is now pictured in Figure 3.24.

As seen in Figure 3.24, the change compared to Figure 2.5 is the addition of the current gain and the new velocity estimation and filtering.

After the introduction of the current gain, the velocity controller is retuned, such that the dominating pole is at $\approx -8{,}5$ with ground contact. This was achieved with a K_p of 2,25 and K_i of $2{,}063K_p$. The system poles and with and without ground contact, can be seen in Table 3.3.

Contact poles	**Contact zeros**	**No contact poles**	**No contact zeros**
−943,88	−282,7	−974,1	−282,7
−270,8	−2,063	−124,7+237,4i	−2,063
−8,473		−124,7−237,4i	
−2,063		−1,659	

Table 3.3

Closed loop system poles with and without the wheel having contact with the surface, with the current controller.

Comparing this to Table 3.2, the angle of the complex conjugate pole pair at no ground contact has decreased, where the angle from the negative real axis is now ≈62° instead of ≈71°. The introduction of the current feedback thereby had the intended effect.

More tuning is done, which resulted in K_p of 5 and K_i of $2{,}063K_p$ without audible noise. The resulting system zeros and poles can be seen in Table 3.4.

Contact poles	**Contact zeros**	**No contact poles**	**No contact zeros**
−948,0	−282,7	−1.050	−282,7
−255,2	−2,063	−86,89+353,1i	−2,063
−19,89		−86,89−353,1i	
−2,063		−1,659	

Table 3.4

Closed loop system poles with and without the wheel having contact with the surface, with the current controller.

The dominating pole is now located at ≈ -20, leading to a time constant of $\approx 0{,}05$ s. This will be verified later.

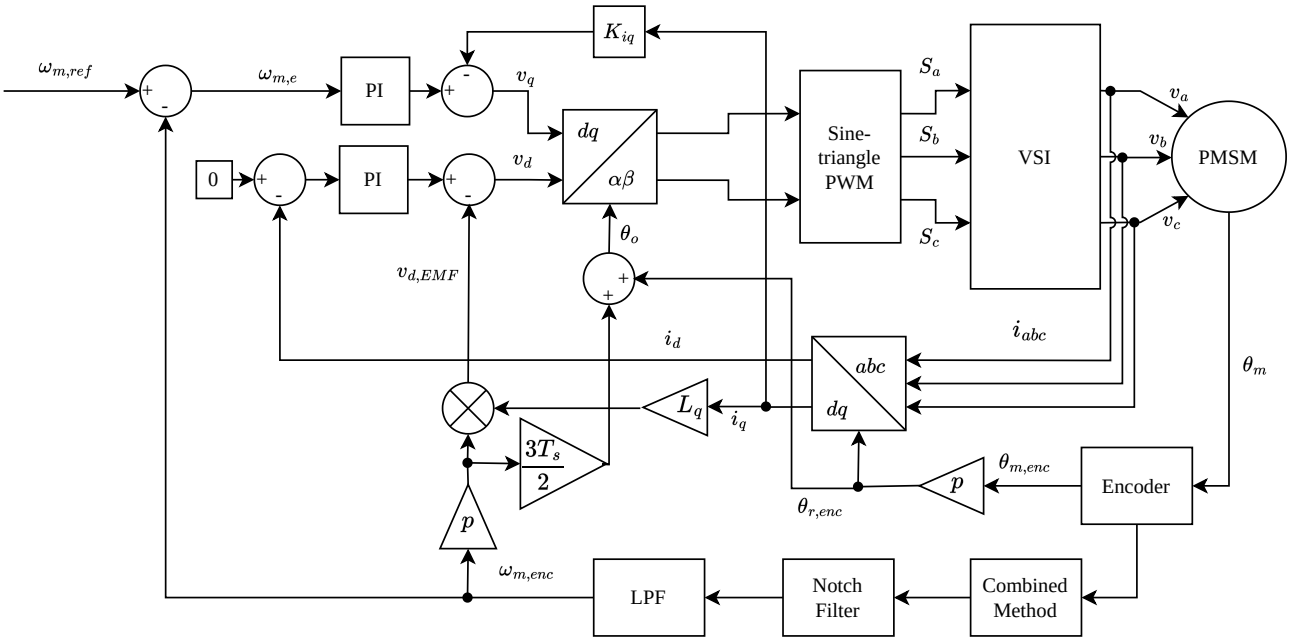

Figure 3.24

Final individual wheel control structure.

The audible noise made by the robot while not in contact with the ground is reduced, but is still present. The controller still has the limit cycle problem at velocities close to zero but to a lesser degree than before. To fully remove the audible noise, while keeping the performance at higher velocities, a bumpless transfer to another set of lower gains will be performed when the reference enters the range of ±0,75 rad/s. The lower gains consist of a K_p of 3 and K_i of $2{,}063K_p$. How this bumpless transfer is achieved will be explained in the next section.

Bumpless Transfer

A bumpless transfer between two sets of controller gains is achieved when the control output stays continuous in the transition. To ensure the transfer is bumpless, Eqn. (3.28) must be fulfilled.

$$K_{p,1}e + I_{e,1} = K_{p,2}e + I_{e,2} \tag{3.28}$$

Where $K_{p,1}$ is the current proportional gain, e is the error, $I_{e,1}$ is the current error integrator state, $K_{p,2}$ is the new proportional gain and $I_{e,2}$ is the error integrator state after the transfer.

To fulfil this requirement, the following procedure in Eqn. (3.29) is implemented.

$$\Delta u = \left(K_{p,1} - K_{p,2}\right) e \tag{3.29}$$

$$I_{e,2} = I_{e,1} + \Delta u \tag{3.30}$$

First, the change in output from changing the proportional gain is computed. This is then added to the integrator state. After this, the new controller gains can safely be applied.

The performance of the system with this new controller structure and bumpless transfer will now be examined.

Performance Evaluation of Velocity Controller with Notch Filter, Current Controller & Bumpless Transfer

With the notch filter, current controller feedback gain and bumpless transfer implemented, the controller gains ended up being a K_p of 5 and K_i of $2{,}063K_p$. The lower gains at the bumpless transfer at ±0,75 rad/s is K_p of 3 and K_i of $2{,}063K_p$. These gains ensured no audible noise. The velocity control is once again tested with Turf Tanks validation trajectory to evaluate trajectory tracking performance. From analysing the CTE data the same behaviour regarding outliers in CTE is observed as in all the previous performed validation trajectory tests. The largest outliers in CTE occur when transitioning from a line to an arc and vice versa. This is both when driving forward and backwards, but worst backwards. The resulting MACTE and RMSCTE are improved by 15 % and 19 % relative to the baseline test of Turf Tank 120° commutation control. When comparing performance to the solution proposed, with a new velocity estimate implemented, an improvement of 2 %pt in MACTE is obtained, but the RMSCTE is reduced by 2 %pt. To evaluate the performance concerning the wishes, a linear velocity step response is performed which is seen in Figure 3.25.

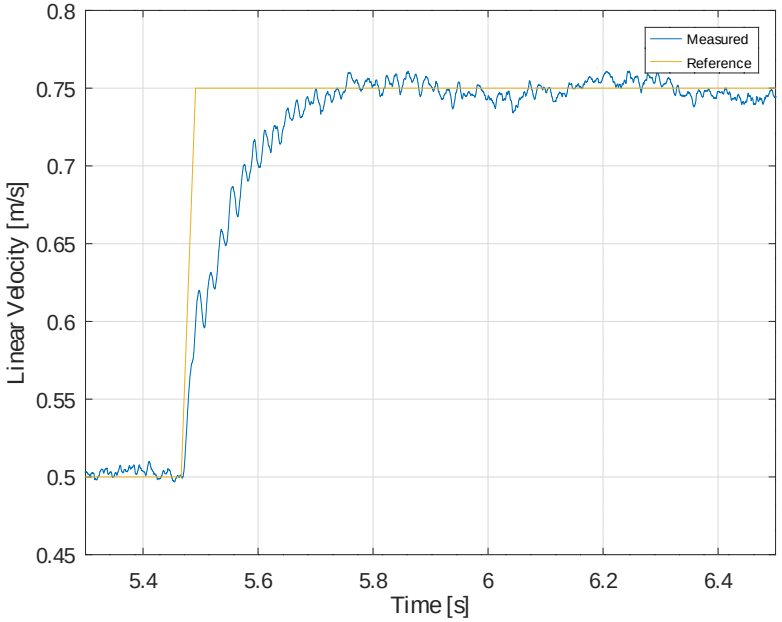

Figure 3.25
Linear step response of the same controller.

Here, it is seen that an approximate first-order response is achieved. The wish for linear and decoupled first-order linear and angular velocity dynamics is still only partially fulfilled because linear first-order linear velocity dynamics are only achieved with zero angular velocity. The time constant is approximated from the data to be 0,054 s. This fits well with the time constant calculated from the dominating pole of 19,89 rad/s to 0,05 s. The velocity controller bandwidth is thereby improved. The changes introduced in this fourth solution led to negligible changes in performance. This is deemed to be because the robot controller is remained unaltered throughout all tests.

With all four solutions presented, a conclusion on the analysis and solutions for the line marking robot will be performed.

4 | Conclusion on Analysis & Solutions for Line Marking Robot

It has been investigated how can a software solution utilising FOC be developed for the line marking robots, such that it can perform line marking without audible excitation of the robot's natural frequencies while obtaining equivalent or better trajectory tracking performance to the currently in use 120° commutation control.

Initially, a thorough problem analysis is performed, through which it is discovered that the primary cause of the audible noise problems is low natural frequencies in the robot chassis getting excited by the motor control. For the line marking robot, it is preferable to create a software solution, avoiding the expensive process of altering hardware on the many hundreds of robots already in service. Four software solutions are introduced with three of them being viable solutions meaning they fulfil the requirements stated earlier in Section 2.7. Wishes are also introduced for the velocity control as they are expected to improve the line marking robots trajectory tracking performance. As a result more than one solution is introduced because it is of interest to investigate if the trajectory tracking performance can be improved.

Turf Tanks motor control and the four developed solutions are put through the same trajectory tracking test to evaluate their trajectory tracking performance. In the test the line marking robot follows a validation trajectory developed by Turf Tank that puts the robot through most of the manoeuvres it can encounter when performing line marking for customers. The same robot and test location is used for all tests. Performance on other field surfaces is, as a result, unknown. Only one test is performed for Turf Tanks motor control and the four developed solutions but is not deemed to invalidate the results. The trajectory is approximately 150 m long and it is therefore deemed that the MACTE and RMSCTE can represents the solutions trajectory tracking performance.

The coupling between the motor control and the robot controller complicates performance comparisons. Because the robot controller and the model on which it is based remain unchanged during all tests, the observed performance trends, when changing the motor control, are not necessarily representative of potential performance. When the motor control changes, the accuracy of the model in the robot controller changes, which also affects the trajectory tracking performance. To observe the actual performance difference, one would have to adjust the model and retune the robot controller for each solution. Regardless of the robot controller tuning, a better model fit, along with an increased bandwidth, is expected to increase the potential trajectory tracking performance, by increased accuracy of the robot controller predictions and a reduction in robot controller control effort.

The four developed solutions will now be concluded upon with regards to the requirements and wishes stated in Section 2.7. This will be done individually for each of the four solutions.

Solution 1: Detuned Turf Tank Controller

The first proposed solutions consist of detuning Turf Tank's version of the controller until the audible noise is gone. Turf Tanks controller referenced here is their controller that causes the robots natural frequencies to be excited in their implementation of FOC. It is not their controller for their currently in use commutated control. Here the P-gain is lowered from 1,5 to 1 and the I-gain from 18,75 to 12,5.

The detuned controller fulfils all requirements. The robots natural frequencies are not excited such that is causes audible noise. The velocity control is stable when the wheels are not in contact with the ground and the MACTE and RMSCTE are 11 % and 18 % lower than the baseline of Turf Tanks currently used commutated control.

In terms of the wishes, performance has not improved. The velocity controller bandwidth is lowered compared to Turf Tank's tuned controller because the controller has been detuned to fulfil the requirements, and the linear and angular step response is not first-order.

Controller with First-Order Linear Velocity Response

The second proposed solution consists of a controller tuned to have a first-order linear velocity step response with the condition that the angular velocity is zero. In comparison to the detuned Turf Tank controller the I-gain is further lowered from 12,5 to 4,65.

The controller fulfils the first two requirements by not exciting the robot's natural frequencies, causing audible noise and by being stable when the wheels are not in contact with the ground. The controller, however, does not fulfil the MACTE and RMSCTE requirements as the values are 8,7 % and 12 % higher than the baseline of Turf Tanks currently used commutated control.

In terms of the wishes, the velocity controller bandwidth is further lowered because of the reduction in I-gain compared to the detuned controller. A first-order linear step response is, however, obtained under the condition that the angular velocity is zero. The first-order linear step response wish is thereby sometimes met, but not the wish of a first-order angular step response.

Controller with Combined Method Velocity Estimator

The third proposed solution consists of using another velocity estimation method introduced as the combined method. This method reduced the noise in the velocity estimate, enabling the P-gain and I-gain to be raised to 1,5 and 18,75.

This controller fulfils all of the requirements. The robot's natural frequencies are not excited such that is causes audible noise. The velocity control is stable when the wheels are not in contact with the ground and the MACTE and RMSCTE are 13 % and 21 % lower than the baseline of Turf Tanks currently used commutated control.

In terms of the wishes, the velocity controller bandwidth is improved as the P-gain and I-gain are raised compared to the two previous solutions. The wishes of first-order linear and angular step responses are, however, not met.

Controller with Notch Filter, Current Controller, Bumpless Transfer & First-order Linear Velocity Response

The fourth proposed solution consists of a combination of the aforementioned solutions as well as multiple additions made to raise the velocity control bandwidth. The first addition is a notch filter with its target frequency placed at 180 Hz as this is the frequency with the largest observed amplitude of the audible noise. A feedback gain is added to the q-axis current controller to aid in fulfilling the requirement stating that the velocity control must be stable with the wheels not in contact with a surface. To aid in fulfilling the same requirement and stop audible noise from occurring, a bumpless transfer between two controllers is added. At velocity references below ±0,75 rad/s, a controller with lower P-gain of 3 and I-gain of $2{,}063K_p$ is used. The gains for the controller above velocity references of ±0,75 rad/s have a P-gain of 5 and an I-gain of $2{,}063K_p$. Lastly, the controller is again tuned to have a first-order linear step response under the condition that the angular velocity is zero.

This controller fulfils all of the requirements. The robot's natural frequencies are not excited such that is causes audible noise. The velocity control is stable when the wheels are not in contact with the ground and the MACTE and RMSCTE are 15 % and 19 % lower than the baseline of Turf Tanks currently used commutated control. It is, however, not certain that the requirements will be fulfilled if the developed control is tested on several line marking robots. This is because the natural frequencies differ between robots. The notch filter is, as a result, not a very robust solution to the problem.

In terms of the wishes, the bandwidth of the velocity controller is further improved compared to the previous solutions. The wish of a first-order linear step response is obtained under the condition that the angular velocity is zero. The wish of a first-order angular step response is not met.

It is also observed that there is no noticeable improvement in trajectory tracking performance even though the velocity control bandwidth is raised. This is expected to be because the robot controller remained unchanged throughout all of the tests. As a result, it is deemed that the robot controller is the limiting factor for the trajectory tracking performance during testing.

The findings made in this initial analysis and solution search have provided valuable knowledge, which will be utilised in the development of the mower prototype.

5 | Technical Analysis for Mower Prototype

As mentioned in Chapter 1, Turf Tank has expressed an interest in a mower prototype capable of operating on terrain which is too challenging for their own mower in development. The root causes of Turf Tank's problem with audible noise and unacceptable terrain surface damage with their line marking robots have been treated in the previous chapters. The insights gained here will be used in the mower design process such that the same problems should not occur. This chapter will start with defining requirements and wishes for the mower prototype. These will be formulated in collaboration with Turf Tank and representatives from one of Turf Tanks customers being Aalborg Golf Club. The definition of requirements and wishes is then followed by a technical analysis investigating relevant vehicle and terrain theory. The goal of the technical analysis is to obtain knowledge to make educated mechanical design choices for the mower prototype in later chapters. This should heighten the possibility of the mower prototype fulfilling the requirements and wishes.

5.1 Requirements & Wishes

The requirements and wishes are derived through meetings and discussions with representatives from Turf Tank and Aalborg Golf Club, measurements made at Aalborg Golf Club and the insights gained from working with the line marking robot. The requirements and wishes will be listed, followed by a clarification if deemed necessary. Arrows are placed at the end of requirements if there is a desired direction of improvement. For example, if the mower can drive faster than 2 m/s, the performance is deemed better. This requirement is then given an arrow pointing upwards. Requirements regarding cutting quality are primarily based on Aalborg Golf Club's needs, as it is expected that if these can be fulfilled, the quality should be satisfactory for the rest of the possible customer base. This is because greenkeepers are expected to demand the highest cut quality within the customer base. The resulting requirements will be listed next.

General Functionality

- **Requirements**
  1. The mower's natural frequencies must not be excited such that it causes audible noise
  2. Must cut edges of grass areas (for example around a bunker on a golf course)
  3. Must be outfitted with one 24 cm cutting head
  4. Must have an adjustable cutting height of 10 mm to 70 mm with 1 mm increments
  5. Must have a cut tolerance of 3 mm on fairways when measured against the primary contour, where grass is cut to a length between 12 mm to 14 mm. Only valid within the limits specified in Section 5.1-Cutting Quality Limits ↓
  6. Must have a cut tolerance of 10 mm on first-cut and semi-rough, when measured against the primary contour, where the grass is cut to lengths of 32 mm and 38 mm to 44 mm respectively. Only valid within the limits specified in Section 5.1-Cutting Quality Limits ↓
  7. Outside the limits specified in Section 5.1-Cutting Quality Limits the field must not be scalped and have a cutting tolerance of 20 mm on fairway and 50 mm on first-cut and semi-rough ↓

8. The cutting head must be mounted directly to the mower chassis
9. Must utilise wheels for traction
10. The mower must not be wider than 45 cm ↓

- **Wishes**
  11. Should be as compact as allowed by the required functionality

Mobility

- **Requirements**
  12. Must be able to maintain a speed of 2 m/s while operating on grades up to 5 % ↑
  13. Must be able to achieve an acceleration of 0,5 m/s^2 on flat terrain ↑
  14. Must have a minimum turning radius of 0, around an axis within the mowers top down outline
  15. Must be able to climb grades of 80 % ↑
  16. The mower must be able to traverse a 5 cm tall obstacle, such as a curb ↑
  17. Traverse an Ø15 cm sprinkler hole ↑

Electrical

- **Requirements**
  18. The mower must have an emergency stop button
  19. Must use electric motors for propulsion

Field Strain

- **Requirements**
  20. Must not damage the terrain it drives upon, meaning dirt patches must not be visible after the mower has driven over the grass
  21. The mower wheels must not slip
- **Wishes**
  22. The wheels of the mower should be within the diameter of the cutting head to minimise visible wheel tracks on the grass

Some of the requirements will now be explained in greater detail. the first requirement needing clarification is requirement 3. Turf Tank has already designed a 24 cm cutting head, which they want to reuse. Therefore, the mower will be designed with this limitation in mind.

Requirement 16 states that the mower should be able to traverse an obstacle of 5 cm or less. This is because the mower should be able to drive over, for example, little sticks or a curb when transitioning between mowing areas. The customer must not be forced into altering their landscape to enable the mower to operate. Thereby, if the mower can traverse a 5 cm obstacle, it should be able to handle most obstacles it is expected to encounter.

In requirements 5, 6 and 7 the terms primary contour and cutting quality limits are mentioned for the first time. These terms will now be defined.

Primary Contour

The primary contour is introduced in the requirements stated in 5.1 in regard to measuring the cut grass. The goal of the cut when cutting grass, especially on golf courses is creating a smooth surface where the golf ball rolls consistently. The soil structure under the grass is not a smooth surface but rather a surface with varying degrees of bumpiness and roughness. If one were to cut the grass to a smooth surface and measure the length of the cut directly from the top of the soil, the length of the cut grass would vary regardless of the top of the turf being one smooth surface. From this stems a wish for a definition of a baseline which can be measured against, that corresponds to the smooth surface the top of the grass should have. This baseline is referred to as the primary contour and will now be defined. At the golf course grass length is measured using a device called a grass prism as seen in Figure 5.1.

(a) *Grass prism used by Aalborg Golf Club to check the quality of the cut grass.*

(b) *The mirror on the grass prism where the grass and scale are seen.*

Figure 5.1

Grass Prism used for measuring the cut grass.

The grass prism rests on the ground and defines the primary contour. If the grass prism is moved over a grass field, the centre of it defines a point on the primary contour. This is illustrated in Figure 5.2 by the black lines representing the grass prism where the red dots on the lines are its centre, which lies on the primary contour.

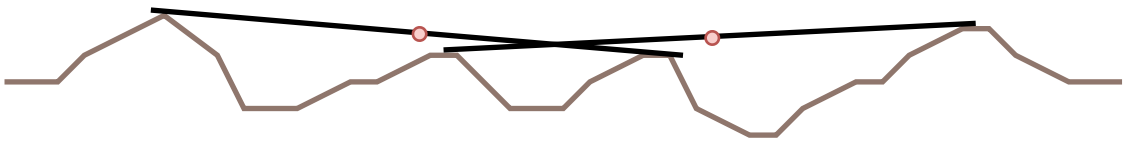

Figure 5.2

Illustration of the grass prism placed on a brown terrain. The black line is the grass prism, and the red dot on the line is the centre of the grass prism. The centre of the grass prism is a point on the primary contour.

If the grass prism is then dragged across the entire surface and the red dot is traced, the primary contour is formed. In Figure 5.3, an example of a contour and its accompanying primary contour can be seen.

Figure 5.3
Primary contour generated for a longer section of terrain as the red line, and the brown line is the terrain.

As seen in the Figure 5.3, the primary contour creates a smooth curve which lies on top of the peaks of the underlying structure of the soil. With the primary contour described, the limits for when the cutting quality requirements should be fulfilled will be described next.

Cutting Quality Limits

In requirement 5 to 7, a limit for when the requirements should be fulfilled is mentioned. This limit stems from meetings with Turf Tank representatives and Aalborg Golf Club greenkeepers, where it became clear that if the terrain is too challenging, the cut quality requirements are not the same. This is, for example, if a large, sudden change in the primary contour is present. This could be in the form of sprinkler holes, a sunken area, tree roots, larger bumps or similar. The common factor being no contour deviations larger than ±3 cm from a 50 cm line whose ends are placed on the primary contour. This is shown in Figure 5.4.

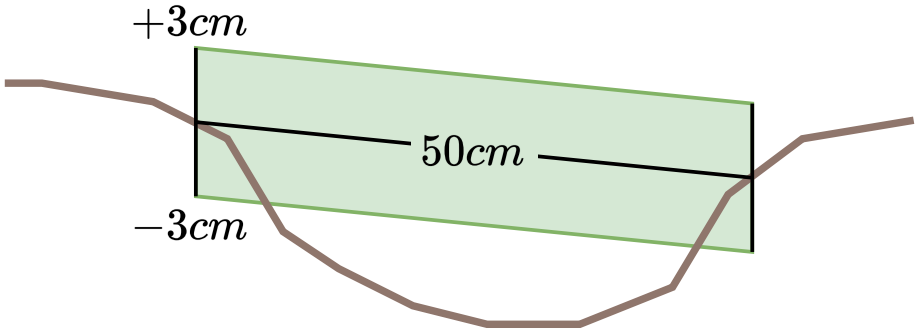

Figure 5.4
The bounding box for the terrain that defines the limit at which the cutting quality requirements must be fulfilled.

To easily identify if the cutting quality requirement should be fulfilled in a given field, a measuring device is designed. This device can be seen in Figure 5.5 as the black line. It has two 3 cm tall arms going perpendicular to the longer black line. Both have feet with square plates mounted. The plates have the size of the longest dimension of the grass prism, which is 16 cm. This is done such that the device sits on the primary contour. The length of the device is 50 cm as this length is appropriate to detect too large changes in the primary contour, and the length of the legs is 3 cm. The distance from the horizontal beam to the primary contour is then measured along the device. If the distance from the beam exceeds 6 cm or if the terrain contacts the beam, the requirements for cutting quality do not have to be fulfilled. An example of this can be seen in Figure 5.5.

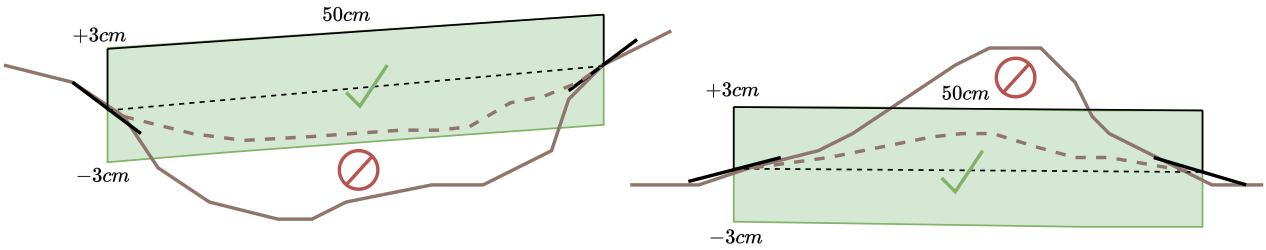

Figure 5.5

An illustration showcasing acceptable and unacceptable terrain features with regards to cutting requirements.

In the left illustration, the terrain is too challenging because there is more than 6 cm from the beam down to the ground. In the right illustration, the terrain is too challenging because the ground contacts and rises above the beam. In both illustrations, a dashed line is drawn that shows how the terrain could look if the requirements should be fulfilled.

With all the requirements listed and some of them clarified, a technical analysis of off-road theory will be performed next to obtain knowledge on off-road vehicle design.

5.2 Off-Road Vehicle Theory

As an important part of the development of a new mower prototype for Turf Tank, a thorough understanding of what makes a good off-road platform must first be acquired. Secondly, it is also important to investigate the challenges the terrain Turf Tank wants to operate on introduces. The performance of off-road vehicles is categorised by their ability to develop drawbar pull, negotiate grades or in general overcome difficult terrain. Drawbar pull is defined as the excess of force a vehicle can generate, taking all losses into account [13]. For the problem stated by Turf Tank, the important factor is the ability to traverse terrain as defined in the requirements. This should be done without damaging the terrain. Furthermore, it needs to traverse bumpy terrain without transferring the bumps to the cut height. In this chapter, the different vehicle parameters that affect the performance of an off-road vehicle are researched. The gathered knowledge can then later be used to make educated decisions on platform design. This process will start with a characterisation of the terrain that Turf Tanks wants the mower to operate on.

Characterisation of Terrain

The development of an off-road mower platform and its performance are influenced by the terrain it is designed to operate on. The terrain the mower will be operating on will primarily be grassy fields of varying smoothness. This will primarily be in the form of grass sports fields like the ones at Turf Tank's existing customers, along with fairway and semi-rough at golf courses. Therefore, the following analysis will focus on the characteristics of these types of terrain. Further analysis of the specific terrain characteristics will be performed later in this section.

The characteristics of grass fields are dependent on the presence of grass and the soil composition [13]. Soil is the combination of sand, clay and silt and is often portrayed in a triangle of soil as seen in Figure 5.6.

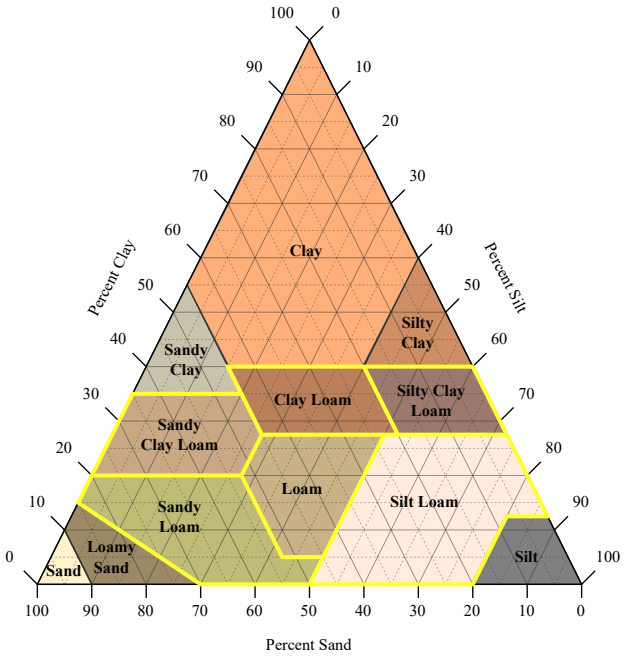

Figure 5.6

Triangle of soil composition and the corresponding soil type. The soil types found on golf courses are highlighted in yellow.

The soil compositions of grass fields, fairways and semi-roughs are sandy loam, sandy clay loam, clay loam, silty clay loam, silt loam and loam as highlighted in Figure 5.6 [14].

Two properties are generally used to describe the mechanical behaviour of soil: cohesion and angle of internal friction. Here, generally, the higher the cohesion and angle of internal friction, the easier the terrain is to traverse. The cohesion and angle of internal friction are mechanical properties of the soil related to how well the soil can hold its shape and at what angle the soil will fail under a shearing load. In Figure 5.7, two soil samples can be seen, one grassy soil with high cohesion that easily holds its shape if a sample is cut from the ground. The other sample represents dry sand, which possesses very little cohesion and will quickly lose its shape if a square sample is lifted from the terrain.

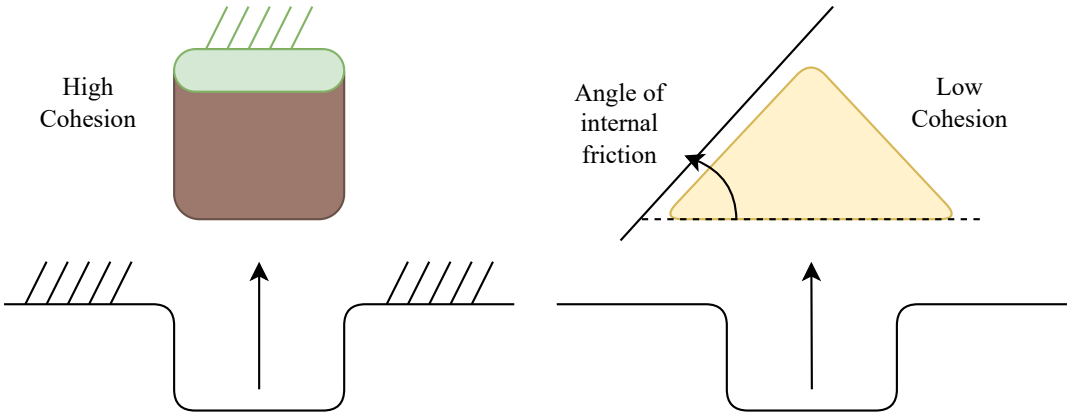

Figure 5.7

An illustration showing the effects of cohesion and angle of internal friction in a soil.

The angle formed between the side of the now triangular sample of sand and the horizontal represents the angle of internal friction. From [13], cohesion and angle of internal friction can be listed for some of the selected soil

compositions in Table 5.1. The limited number of soil compositions stems from the availability of sources.

Terrain Type	Cohesion c	Angle of Internal Friction ϕ
clayey loam	6,2 kPa	30,3°
Sandy Loam	1,72 kPa	29°
Regular Loam	3,1 kPa	29,8°

Table 5.1

Cohesion and angle of internal friction of soil types the mower can encounter. The parameters listed are from [13].

Here, it is seen that sandy loam is the soil type with the lowest cohesion and angle of internal friction and is thereby the most challenging soil type. The mower is expected to only operate on soils with grass. In [15], it is stated that the presence of grass in soil increases the cohesion and angle of internal friction of the soil. Specific numbers for these depend on the type of grass, the age of the grass and more, and therefore they are not easily available. Due to the increasing effect, sandy loam with no grass is considered a worst-case scenario. By designing the mower so that it should be able to traverse sandy loam, it is then expected that it will be able to traverse all possible soil and grass combinations it is expected to encounter.

With the terrain introduced, the major external forces acting on a wheeled vehicle will be investigated next.

Major External Forces Acting on a Wheeled Vehicle

It is important to investigate the major forces acting on a wheeled vehicle as they dictate its movement. The major forces acting on a wheeled vehicle are shown in Figure 5.8 [13].

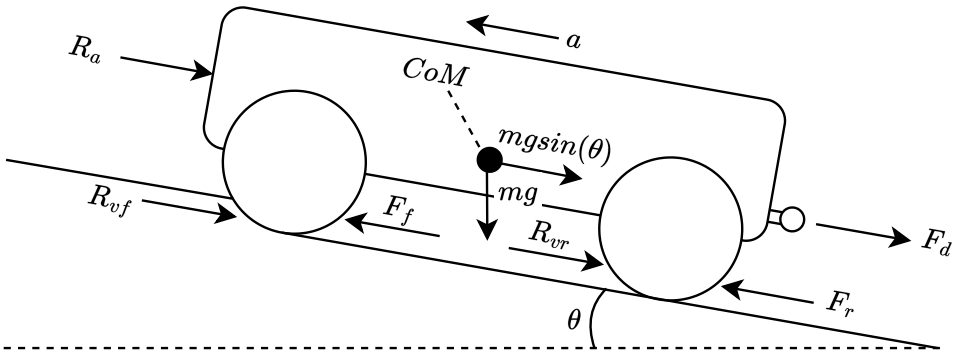

Figure 5.8

Figure showing the different forces that act upon an off-road vehicle in motion.

In Figure 5.8, the arrows show the forces acting on the vehicle and their direction. Based on Figure 5.8, the equation of motion (EoM) is formulated in Eqn. (5.1).

$$ma = F_f + F_r - R_a - R_{vf} - R_{vr} - F_d - mg\sin(\theta) \tag{5.1}$$

Where m is the mass of the vehicle and a is the linear acceleration of the vehicle's CoM. F_f and F_r are the thrust forces propelling the vehicle forward. The thrust generated is limited by the torque the motor can output and the amount of force the wheels can successfully transfer to the terrain. Thereby, an increase in either motor torque or wheel traction can lead to an increase in thrust, depending on which is the limiting factor. The drag force R_a

is the aerodynamic resistance. The size of the drag force is highly dependent on the vehicle's speed relative to the wind speed. According to [13], the drag force of off-road vehicles operating under 48 km/h is usually not a significant factor. Turf Tank wants to operate the mower at a maximum speed of 2 m/s = 7,2 km/h. As a result, the size of the drag force will be negligible. In case of storms generating wind speeds high enough to have a noticeable aerodynamic effect, the mower is not expected to operate. The forces R_{vf} and R_{vr} are the motion resistance from each wheel. This force is generated by wheel-terrain interactions and drivetrain resistances. The force F_d is the drawbar force from, for example, a trailer mounted to the vehicle. In a Turf Tank context, the drawbar force will be zero. The last term $mg \sin(\theta_s)$ is the gravitational force.

The motion resistance forces R_{vf} and R_{vr}, collectively referred to as R_v, need further investigation into what their size is influenced by. A deeper investigation of the motion resistance will therefore be performed next.

Sources of Motion Resistance

The motion resistance R_v is composed of several different aspects in off-road operation [13]. This involves obstacle resistance R_{ob}, internal resistance of drivetrain R_{in} and resistance due to compaction of the terrain R_t.

The first type of motion resistance is obstacle resistance, which comes from the vehicle's wheels encountering objects such as rocks, stumps, roots, holes and bumps in the terrain and likewise. The severity of the resistance depends on the size, shape and more of the obstacle. An example of a wheel meeting an obstacle in the form of a rock formation can be seen in Figure 5.9a.

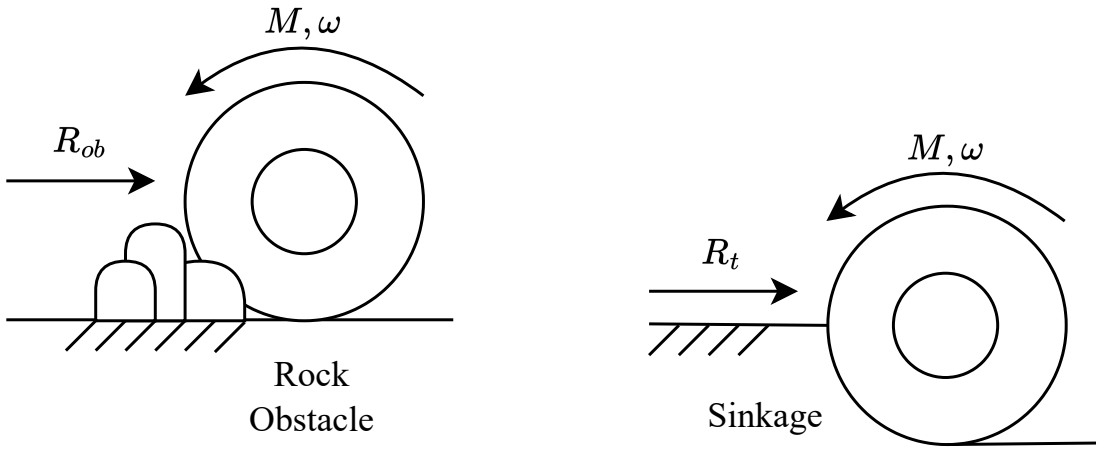

(a) *A wheel experiencing resistance by encountering an obstacle.*

(b) *A wheel experiencing compaction resistance due to sinkage.*

Figure 5.9

The terrain Turf Tank wants to operate on generally does not have that many obstacles. (Søren Elton Mark, Turf Tank, Personal Communication, 16/10-24). The obstacles that do find their way onto the fields, be it sports fields or golf courses, mainly consist of bumps, holes and various plant matter. The severity of bumps, holes and other obstacles on the terrain is generally not large and not often present, as the areas are often well maintained, granted that it would otherwise affect the functionality of the areas negatively (Søren Elton Mark, Turf Tank, Personal Communication, 16/10-24).

The next source of motion resistance is the internal resistance R_{in} of the drivetrain. This refers to the friction present in the mechanical assembly of the drivetrain, which the motor has to overcome to generate forward rotation. Since the resistance is dependent on the design of the drivetrain, it is not possible to determine the magnitude of this resistance currently. It can only be stated that it should be the aim to minimise this resistance in the design.

The last source of motion resistance considered is the resistance R_t created by the interaction between the wheels and the terrain. This resistance will primarily present itself due to sinkage of the tyre when operating on softer terrains [13]. An illustration of sinkage is shown in Figure 5.9b. If the sinkage becomes excessive or if small mounds of material are present which can fit between the wheelbase of the mower, belly drag could also become a factor to consider. Belly drag is when the bottom of a vehicle comes in contact with the terrain. Belly drag introduces significantly more resistance and would severely reduce drawbar pull, and should therefore be avoided [13]. In the next section it will be analysed how different vehicle parameters affect it's ability to develop drawbar pull.

Generation of Drawbar Pull

In this section, trends in drawbar pull when altering design parameters of the wheel and the mass of the mower will be analysed. This is of interest since it will enable intelligent choices regarding wheel dimensions and mass later in the design process. The thrust is the propelling force of the vehicle and is as mentioned earlier, provided in unison by the vehicles motor, and the traction available between the wheels and terrain. The maximum thrust is then limited by the lesser of the two properties. In this the traction is in most cases the limiting factor in the generation of thrust [13]. Apart from the possible thrust that can be generated by the vehicle and the wheel terrain interaction, there is also limits for how much thrust the terrain can support before it breaks apart. Generally the possible thrust a terrain can support can be estimated by Eqn. (5.2) assuming the contact area is known and that the pressure on the contact patch is uniform [13].

$$F_{max} = cA + F_N \tan(\phi) \tag{5.2}$$

Here, c is the cohesion of a certain terrain, A is the contact area between the tyres of the vehicle and the terrain, F_N is the normal force. In [13] the contact area is determined experimentally, by measuring the contact area at different wheel loadings. This is not possible at this stage of the development process since nothing is known about wheel type, size and so on.

It is known from [16, p. 2] that the contact area for a tyre is primarily dependent on the wheel loading and the tyre pressure. Assuming the tyre pressure is significantly larger than the pressure stemming from the tyre carcass stiffness. This is true for modern tyres inflated at rated pressures. Given this, changes in diameter and width contribute to a change in the shape of the contact area but not the size of the area. Therefore the contact area in the calculations will be kept at a constant value. The accuracy of the chosen contact area has lesser importance as it is constant throughout the calculations and therefore does not contribute to any changes in the tendencies observed.

When using Eqn. (5.2) it is seen that in a cohesively dominated soil such as wet clay [13], higher thrust may primarily be obtained by an increase in contact area. On the other end of the spectrum in a frictionally dominated terrain such as dry sand [13], higher thrust is primarily obtained by an increase in vehicle mass. This does not however mean that for a vehicle operating on frictional terrains, that it is in interest to increase the vehicle mass

indefinitely. While an increase in mass may result in an increase in possible thrust, it also increases the ground pressure of the vehicle and in turn the sinkage of the vehicle into the soil. The sinkage of a vehicle causes resistance towards movement as mentioned in Section 5.2 due to compaction of the soil, this resistance can for a rigid tyre be described by Eqn. (5.3) [17]. A rigid tyre is defined by the sum of the tyre's inflation pressure and carcass pressure being larger than the ground pressure. The difference between a rigid and elastic tyre is that in the latter the contact area is dependent on inflation pressure. An elastic tyre will generally induce less compaction resistance, as the lower pressure increases the tyre's footprint, distributing the load over a larger area, reducing sinkage [17]. Based on this, rigid tyres are expected to be the worst-case scenario in terms of compaction resistance. The equations describing rigid tyres are also simpler than for elastic tyres and as such will be used for this initial analysis.

$$R_c = \frac{1}{s(n+1)b^{\frac{1}{2n+1}}} \left(\frac{3F_N}{\sqrt{D}} \right)^{\frac{2n+2}{2n+1}} \tag{5.3}$$

Here n is the exponent of soil deformation, a terrain parameter attained empirically and s is defined as seen in Eqn. (5.4) [17].

$$s = (3-n)^{\frac{2n+2}{2n+1}} \left(\frac{k_c}{b} + k_\phi \right)^{\frac{1}{2n+1}} \tag{5.4}$$

Where k_c and k_ϕ are cohesive and frictional pressure sinkage parameters for the terrain, these parameters are coefficients that describe the sinkage of a plate with a certain contact area due to a pressure being applied. They are determined empirically through tests. The difference between the possible thrust and the compaction resistance provides the available drawbar pull as seen in Eqn. (5.5) [17], assuming the remaining resistive terms from Eqn. (5.1) are 0.

$$DP = F_{max} - R_c - mg\sin(\theta) \tag{5.5}$$

This is, as described earlier, an expression of the amount of excess force a vehicle has available for movement and pulling loads. If the available drawbar pull evaluates to zero or less, or is less than the required drawbar pull based on the other factors, the vehicle will be unable to move. Additionally, sinkage is also calculated from Eqn. (5.6) [17], as excessive sinkage is expected to increase the chance of terrain damage.

$$z = \left(\frac{3F_N}{b(3-n)(\frac{k_c}{b} + k_\phi)\sqrt{D}} \right)^{\frac{2}{2n+1}} \tag{5.6}$$

As mentioned earlier, there exist modified equations which incorporate the effects of deformed tyres with regards to sinkage, compaction resistance and losses specific to deformation of the tyre. These can be included in the coming chapters if elastic wheels are to be used in designs to be defined later. It should also be noted that these equations assume the wheels have uninterrupted contact with the soil, meaning no slip can be present and the wheels never lose contact with the terrain. If contact is lost with the terrain the ability to generate thrust is lost which is undesired. It should therefore be the goal to maintain contact with the terrain surface. For now, the theory behind rigid wheels will be used to gain an insight into how vehicle mass and wheel dimensions affect vehicle performance.

In the following calculations, drawbar pull has been evaluated for a small vehicle with four wheels, where all 4 wheels are driven. As every single wheel of a vehicle has some potential of transferring thrust to the terrain it is necessary for all wheels to be driven, to utilise the available thrust to its full potential. The calculations have been made for sandy loam as it is expected to be the most challenging terrain the mower should operate

on. Calculations have been made to determine the effects of changing vehicle mass, vehicle mass on an 80 % grade, tyre widths and tyre diameters. For all calculations, only one variable is changed at a time, the mass variation calculations have fixed tyre parameters and vice versa. The standard set of variable values used for the first calculations is 5 cm tyre width, 20 cm tyre diameter and a vehicle mass of 20 kg, this is chosen based on parameters from existing mowers operating in the same market from Husqvarna and MAMMOTION [18, 19]. In Table 5.2, the terrain parameters for the calculations can be seen.

Terrain Type	n	k_c	k_ϕ	c	ϕ
Sandy Loam	0,7	5,27 kN/m^{n+1}	1.515,04 kN/m^{n+2}	1,72 kPa	29°

Table 5.2

Terrain values for sandy loam used in analysis [13] [17].

On the graphs seen in figures 5.10a and 5.10b, the effects of changing vehicle mass on flat and sloped terrain can be seen.

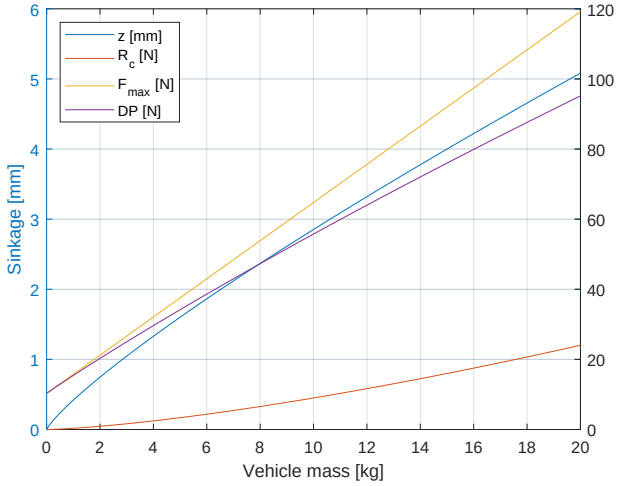

(a) *Sinkage, compaction resistance, maximum possible force and drawbar pull plotted with the mass of the vehicle being the parameter that is changed on flat ground.*

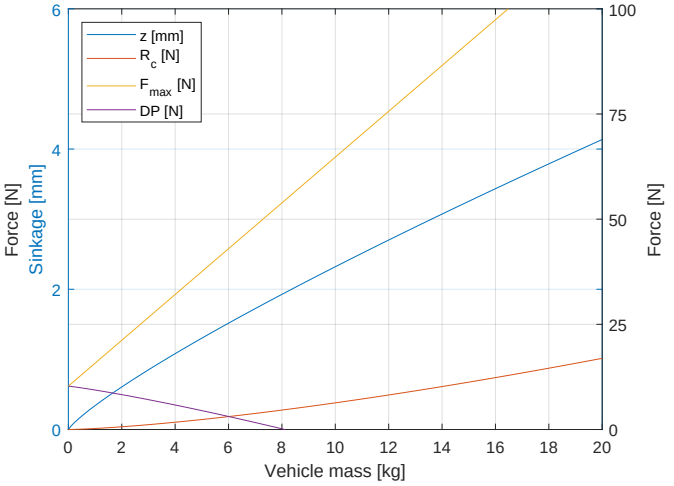

(b) *Sinkage, compaction resistance, maximum possible force and drawbar pull plotted with the mass of the vehicle being the parameter that is changed on an 80 % grade.*

Figure 5.10

When looking at Figure 5.10a it can be seen that the drawbar pull shown as the purple line increases as the mass is increased. It can also be observed that the possible thrust starts above 0 N, this is because it is evaluated based on what the terrain can support and not what the vehicle can transfer to the terrain. And as seen Eqn. (5.2) the possible thrust a terrain can support is partly determined by cohesion and contact area, regardless of the weight on it. It is also interesting to note that the slope of the drawbar pull curve is declining and that the slope of the compaction resistance R_c is rising. If the mass continues to be increased eventually the drawbar pull will go negative and the vehicle will no longer be able to drive forward. When the maximum grade of 80 %, set in the requirements, and its effects are added to the calculation, the result can be seen in Figure 5.10b. Here, the drawbar pull decreases as the mass of the vehicle is increased. When looking at adding mass to increase the vehicles off-road characteristics the trend on flat ground is that adding mass gives more drawbar pull but it has a diminishing return the higher the mass is. On the 80 % grade the trend is that adding mass only negatively affects the vehicles off-road characteristics. It is also important to note that the sinkage increases as the mass increases. This is expected to increase the chance of unacceptable field damage. Next tyre width and diameter

are varied and the results are shown in Figure 5.11. The width ranges from 2 cm to 10 cm and diameter ranges from 5 cm to 40 cm.

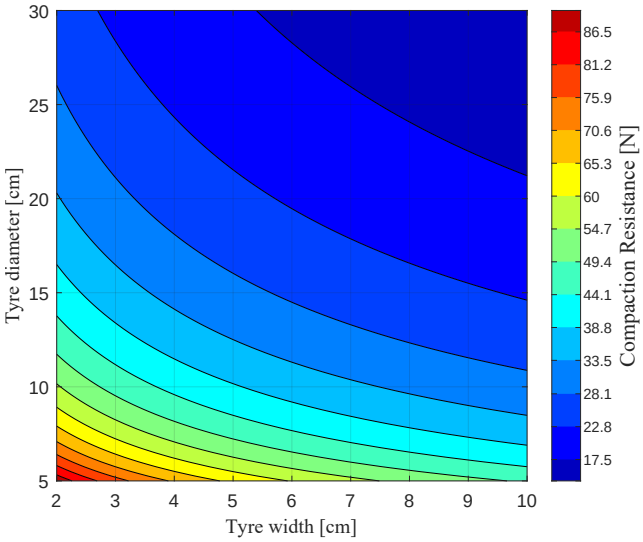

(a) *Compaction resistance as a function of tyre width and diameter.*

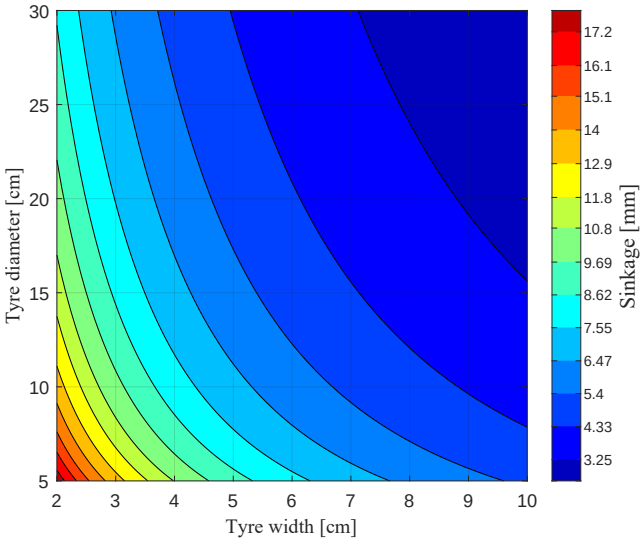

(b) *Sinkage as a function of tyre width and diameter.*

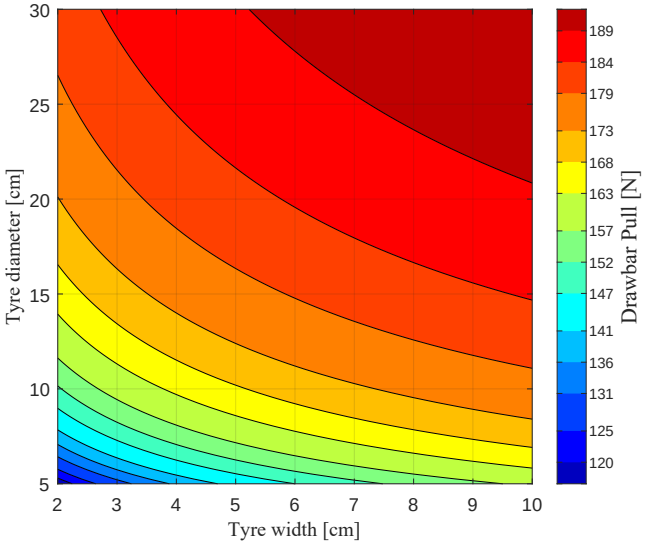

(c) *Drawbar pull as a function of tyre width and diameter.*

Figure 5.11

Plot contour lines are aligned with the ticks on the colour bars.

Figure 5.11 discloses that increasing tyre width and diameter affect all parameters positively. It reduces compaction resistance, sinkage and increases drawbar pull, though with diminishing returns. The diminishing returns of increasing dimensions would also be reflected in increased mass, diminishing the returns further and potentially removing them completely. Inspecting figures 5.11a and 5.11c, it is beneficial for compaction resistance and drawbar pull to have a diameter larger than the width. This is opposed to Figure 5.11b where increasing tyre width is more beneficial than increasing the diameter. Tyre dimensioning will therefore be a trade-off between sinkage, drawbar pull and limited by realistic wheel dimensions.

In the above analysis, it has been determined how different vehicle parameters affect the amount of trust the terrain can support. It has however not been analysed if it is possible to transfer the thrust from the wheels to

the terrain. If the thrust is to be generated by static friction between the wheel and terrain, the static friction coefficient has to be high enough. Driving up terrain with a 80 % grade is deemed to be the most challenging terrain from a traction perspective. The friction force and normal force changes with the grade and as a result the required static friction coefficient. It is the ratio between these forces that determine the required static friction coefficient. The required friction coefficient can then be expressed as:

$$\frac{F_f}{F_N} = \frac{mg\sin(\theta)}{mg\cos(\theta)} = \tan(\theta) \tag{5.7}$$

If the maximum grade of 80 % is inputted in the above equation, the required static friction coefficient becomes 0,8. This is the required friction coefficient to remain stationary on a grade. As a result an even higher static friction coefficient is required to maintain a velocity or to accelerate. From [20] the static friction coefficient between a car tyre and grass is in the range from 0,59 to 0,80, depending on the grass type and whether the grass is wet or not. Generation of thrust purely from friction is as a result not sufficient to obtain the required mobility. Other methods to improve the thrust generation must therefore be analysed. This will be done in the next section.

Tyre Lugs

One way to obtain additional traction can come in the form of lugs placed on the tyre surface. Tyre lugs are also utilised by earlier introduced existing mowers from Husqvarna and MAMMOTION. Tyre lugs can dig into the soil and utilise more of the possible thrust the soil can withstand. The different parameters that effect tyre lugs performance will be introduced in the following section. The goal is to investigate if the addition of tyre lugs can make a large enough traction contribution to increase the chance of the mower fulfilling the mobility requirements.

It is of interest to perform calculations on the possible contribution to thrust tyre lugs can make. From [13] it is stated that the possible thrust a lug can develop is given by Eqn. (5.8). To aid in the description of Eqn. (5.8) figures 5.12a and 5.12b are introduced.

$$F_p = b(\frac{1}{2}\gamma_s h_b^2 N_\phi + q h_b N_\phi + 2c h_b N_\phi) \tag{5.8}$$

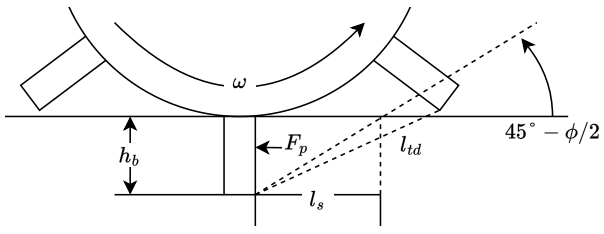

(a) *tyre with lugs showing lug depth h_b, lug thrust F_p, rupture distance l_s and lug tip distance l_{td}.*

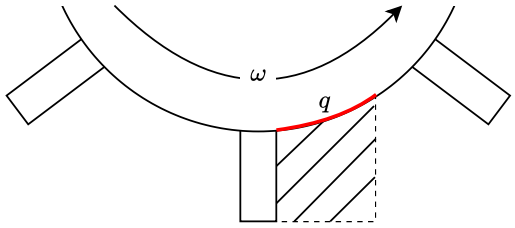

(b) *Tyre with lugs showing surcharge and where its pressure is applied a the red line.*

Figure 5.12

In Eqn. (5.8) F_p is the increase in possible thrust, due to the addition of a single tyre lug, b is the width of the tyre lug, γ_s is the bulk unit weight of the soil defined by the density of the soil times the gravitational acceleration, h_b is the penetration depth of the lug, N_ϕ is the flow value of the soil and is defined as:

$$N_\phi = \tan(45 - \phi/2)^2 \tag{5.9}$$

where ϕ is the angle of internal friction illustrated earlier in Figure 5.7. In Eqn. (5.8) q is the surcharge which is the pressure applied to the soil behind the lug by the tyre. This is illustrated in Figure 5.12b as the pressure applied to the ground marked with the red line. Lastly, c is the cohesion of the soil.

Eqn. (5.8) is based on some assumptions about the tyre dimensions. This involves width of the lug being relatively wider than the penetration depth of the lug, lug width equal to rim width, a smooth and flat lug surface and a lug tip distance larger than the rupture distance l_s of the terrain defined in Eqn. (5.10).

$$l_s = \frac{h_b}{\tan(45 - \phi/2)} \tag{5.10}$$

Rupture distance is a measure for the minimum needed distance between two lug tips, to allow the soil in between to fail in a manner where the soil is able to support thrust. If the lug tip distance is smaller than the rupture distance, the soil will fail at the lug tips, and the lugs will instead have caused an increase in effective tyre diameter and not an increase in possible thrust [13].

Purely from looking at Eqn. (5.8) an increase in penetration depth h_b equates to a greater increase in possible thrust compared to increasing the width b of the tyre lugs. The penetration depth is, however, only achievable if the vehicle mass is large enough for the lug to penetrate the terrain. Penetration into the terrain can be troublesome when considering the requirement regarding field strain. The requirement states that the mower must not damage the terrain it drives upon, meaning dirt patches must not be visible after the mower has driven over the grass. If the tyre lugs penetrate too deeply into the grass, there must come a point where the damage is unacceptable.

To investigate if tyre lugs should be added to the mower design, calculations are made with Eqn. (5.8) to see how much thrust lugs can add. In Figure 5.13, the lug traction is shown as a function of lug depth and width as a contour plot.

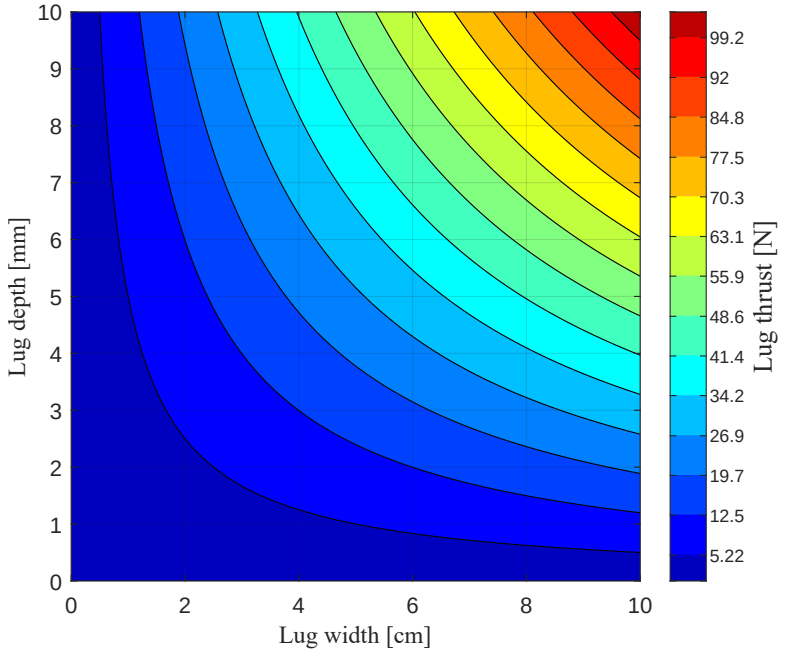

Figure 5.13

Contour plot showing lug thrust as a function of lug width and lug depth.

If a realistic lug dimension is considered of 5 cm width and 7,5 mm depth based on earlier mentioned existing

mowers form Husqvarva and MAMMOTION [18, 19] the produced lug thrust of a single lug is approximately 37 N. With four wheels in total the tyre lug thrust ads significant thrust. The force pulling down a vehicle of 15 kg on an 80 % grade is about 100 N. This means lugs alone here would be able to generate the necessary force, without being dependent on the friction between tyre and terrain. Ultimately correctly designed tyre lugs can improve the off-road capabilities of the mower, however they may pose challenges with regards to terrain damage. It is however expected that if lug size is kept similar to or smaller than the existing products, any possible terrain damage will be insignificant as Husqvarna and MAMMOTION otherwise would have problems with their products.

5.3 Suspension

As mentioned in Section 5.2 before, thrust can be generated from a surface; it is vital to maintain contact with the surface. Suspension can aid in doing this, by keeping the tyres in contact with the terrain as the vehicle traverses it [17]. If a vehicle has no suspension, the bumpiness of the terrain will be transferred directly to the chassis, causing the chassis to bump around. In the mower context, this results in the cutting head jumping around, compromising its ability to maintain the desired cutting height, resulting in an unevenly cut grass field. By introducing suspension, the vehicle should be better able to absorb the smaller bumps in the terrain, allowing the chassis and cutting head to smoothly follow the primary contour of the terrain.

To evaluate the effects suspension could have on the performance of the vehicle, a longitudinal half-car suspension model will be created. The half-car model is chosen over a quarter-car model since it enables the simulation of pitch in the vehicle. It also enables simulating placing the cutting head in different positions along the length of the vehicle and seeing how this affects the cutting quality. This can be used to simulate how the vehicle will react while driving over a surface with various suspension setups, as well as no suspension. This enables comparison between various setups, with the information gained then being used to determine if suspension should be included in the final design, and also allowing for tuning of an eventual suspension setup that may be included in the design. A full car suspension model is not chosen as it is not expected to provide important insights that the half car model cannot provide, therefore, the added complexity is not desired. The development of a half-car model will be introduced in the next section.

Half Car Suspension Model

The half-car suspension model is based on the following setup as seen in Figure 5.14 and is cross-checked with [21]. Based on this model validation will not be performed for the full model here, as it has already been proven by others.

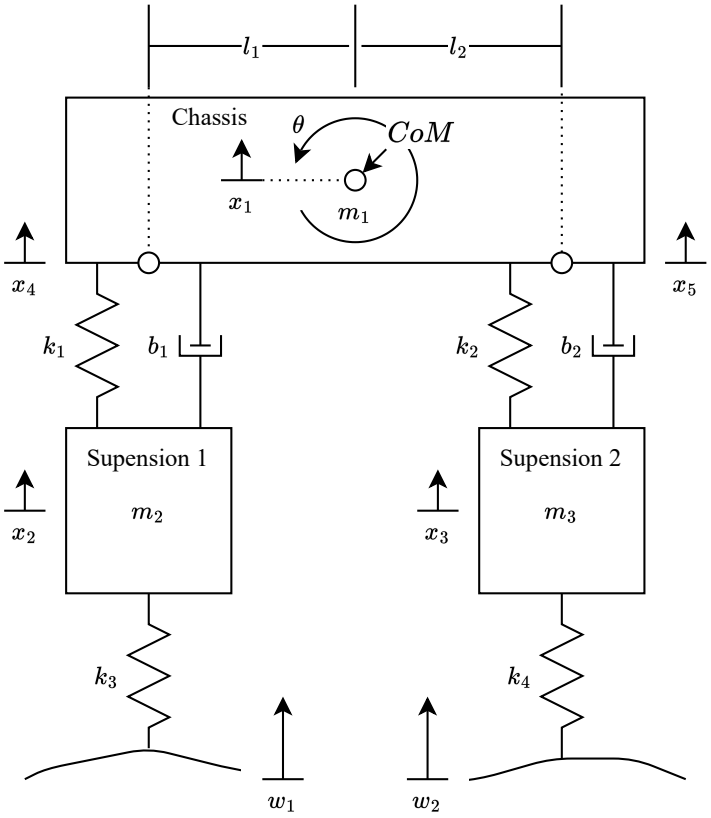

Figure 5.14
Half car suspension model.

The model consists of a chassis with two degrees of freedom (DoF), which are coupled to two suspension assemblies each with one DoF. The coupling is modelled as a spring and damper system. Further down the connection between the wheels and ground is modelled as a spring only. From Figure 5.14, the EoM for the system are formulated:

$$J\ddot{\theta} = -l_1(k_1(x_2 - x_4) + b_1(\dot{x}_2 - \dot{x}_4)) + l_2(k_2(x_3 - x_5) + b_2(\dot{x}_3 - \dot{x}_5)) \tag{5.11}$$

$$m_1\ddot{x}_1 = k_1(x_2 - x_4) + b_1(\dot{x}_2 - \dot{x}_4) + k_2(x_3 - x_5) + b_2(\dot{x}_3 - \dot{x}_5) - m_1 g \tag{5.12}$$

$$m_2\ddot{x}_2 = \begin{cases} k_1(x_4 - x_2) + b_1(\dot{x}_4 - \dot{x}_2) + k_3(w_1 - x_2) - m_2 g, & \text{if } w_1 >= x_2 \\ k_1(x_4 - x_2) + b_1(\dot{x}_4 - \dot{x}_2) - m_2 g, & \text{if } w_1 < x_2 \end{cases} \tag{5.13}$$

$$m_3\ddot{x}_3 = \begin{cases} k_2(x_5 - x_3) + b_2(\dot{x}_5 - \dot{x}_3) + k_4(w_2 - x_3) - m_3 g, & \text{if } w_2 >= x_3 \\ k_2(x_5 - x_3) + b_2(\dot{x}_5 - \dot{x}_3) - m_3 g, & \text{if } w_3 < x_3 \end{cases} \tag{5.14}$$

Where l_1 and l_2 are the lengths from the chassis CoM to the suspension attachment points, and x_4 and x_5 are the vertical positions of the suspension attachments points. x_4 and x_5 are described as follows:

$$x_4 = -l_1\theta + x_1 \tag{5.15}$$

$$x_5 = l_2\theta + x_1 \tag{5.16}$$

The system has eight states θ, $\dot{\theta}$, x_1, $\dot{x}_1$, x_2, $\dot{x}_2$, x_3 and $\dot{x}_3$ corresponding to the DoF and their derivates. Additionally, there are two inputs w_1, the terrain height for the rear wheel and w_2, the terrain height for the front

wheel. If the suspension is above the terrain height, for example $w_1 < x_2$, the input for that suspension, w_1, has no effect. This reflects real-world behaviour, where the terrain cannot pull on the tyre. It is achieved through a separate EoM for each case. In reality, there is only one input, the terrain profile, which can then be mapped to the two individual inputs. First, the terrain profile $w(x)$ is mapped into a time domain function $w(t)$ by defining a longitudinal velocity v.

$$w(t) = w(x), \quad x = vt \tag{5.17}$$

The front wheel input is then time-delayed by τ to obtain the rear wheel input

$$w_1(t) = w_2(t - \tau), \qquad \tau = \frac{l_1 + l_2}{v} \tag{5.18}$$

The small angle approximation is used and the suspension attachment points are thereby assumed to only move vertically. Additionally, the suspension always moves vertically, no matter the chassis angle θ, which is also only accurate at small angles. The inputs will therefore only contain small grades to account for this inaccuracy.

The parameters for the model are selected from existing products on the market, from Husqvarna and Mammotion [19, 22]. The parameters can be seen in Table 5.3. The stiffness of the tyres was determined by pressing on the tyres while on a scale and noting the deflection, this method is of low precision. However throughout the simulations doubling the tyre stiffness was done as an experiment to see how much it affects the performance. Here insignificant change was observed and as such the estimated tyre stiffness was deemed okay, regardless of the precision of the measuring method being low.

Model Parameter	**Value**	**Unit**
Body Height	0,2	m
l_1,l_2	0,4	m
m_1	7	kg
m_2,m_3	1	kg
k_3,k_4	15000	N/m
Wheel Diameter	0,2	m

Table 5.3

Body height, l_1 and l_2 are the lengths from the suspension attachment points to the body CoM, m_1 half body mass, m_2 and m_3 are the wheel masses and k_3 and k_4 are the tyre stiffnesses.

The model is given step inputs to verify its behaviour, the inputs can be seen in Figure 5.15

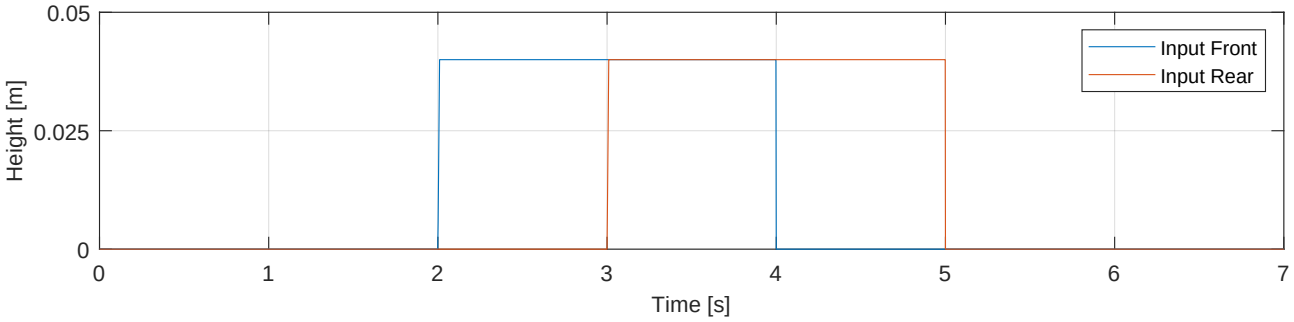

Figure 5.15

The step inputs fed to the model to verify its behaviour.

The resulting trajectories of the positions x_1, x_2 and x_3 are plotted Figure 5.16.

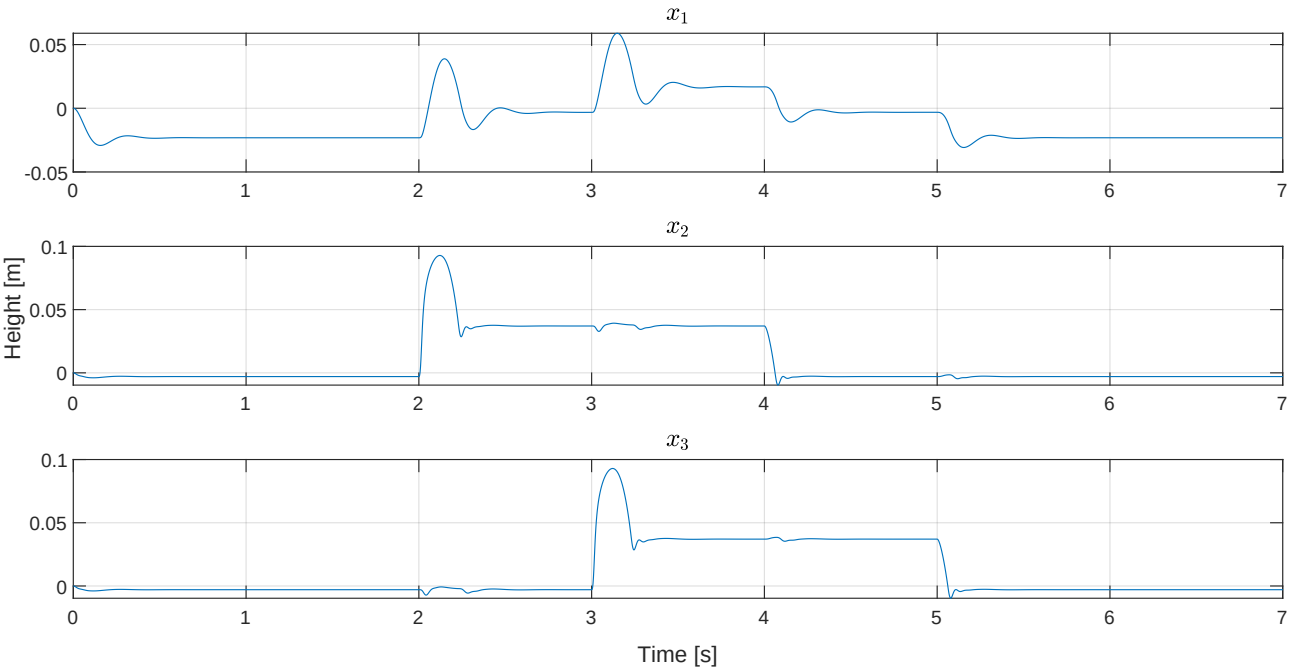

Figure 5.16

Model velocity response to input seen in Figure 5.15.

From this, it is confirmed that the model sags initially and reaches steady state at a certain amount of suspension sag, with the characteristics of the response defined by the spring rate, damping and mass of the system. The step response of the model shows that the amplitude of the chassis' reaction is less than the wheels due to the lower spring stiffness and added damping, compared to that of the tyre stiffness with no damping, which determines the wheels' response. In Figure 5.17, the acceleration of the wheels can be seen.

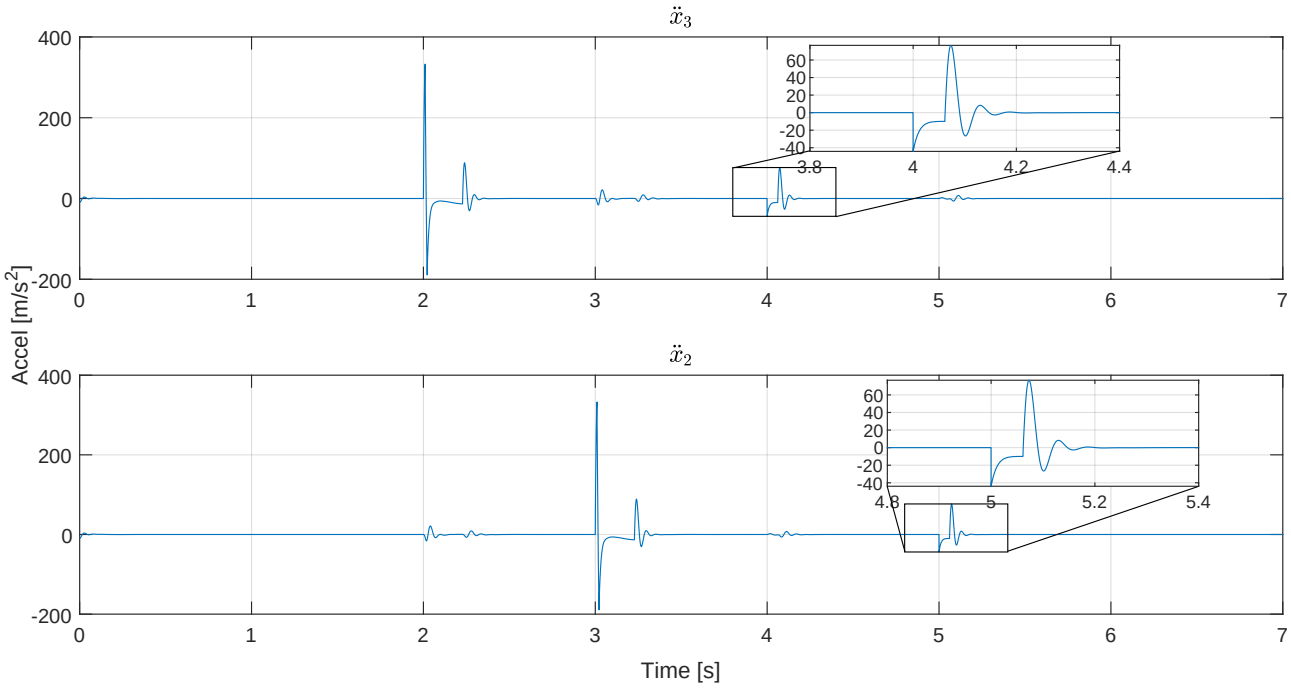

Figure 5.17

Model acceleration response to input seen in Figure 5.15.

Looking at the falling behaviour of the wheels in the zoomed in sections, the acceleration of the movement is around $-40\,\mathrm{m/s^2}$ initially, tapering off to gravitational acceleration at around gravitational acceleration of $-9{,}82\,\mathrm{m/s^2}$. This shows that the ground is indeed unable to pull on the wheel since the acceleration would otherwise be significantly higher due to the stiffness of the tyre. With this, the model is confirmed to be behaving as expected.

Terrain Data

Before the suspension model can be used to make decisions on solutions for the final prototype, proper terrain data must first be acquired. To do this it is decided to construct a measuring device which can measure the contour of a given length of terrain, so it can be used as an input to the suspension model. A design is made and the 3D model of it can be seen in Figure 5.18. Some data processing is necessary due to the design of the device, the details of this can be seen in Appendix A.4.

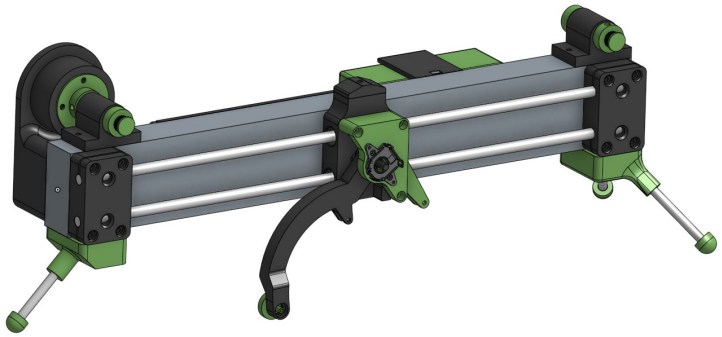

Figure 5.18
The 3D model of the terrain measuring device.

The device is built around a 40 × 80 mm aluminium extrusion. On the front, two linear rods are mounted with two brackets on either end. The rods are 60 cm long, and the brackets are 5 cm wide each. This gives the device a total usable measuring length of 44 cm when also factoring in the carriage width of 6 cm. The carriage is mounted on the linear rods with four linear bearings. The head has an arm mounted in two bearings, with an encoder to measure the angle of the arm. The encoder has a 14 b resolution. At the end of the arm is a wheel with a diameter of 25 mm. This wheel is then rolled across the terrain when a measurement is made, transferring the contour changes into rotation of the arm, which is then measured by the encoder. The wheel size is made as small as possible while keeping the measuring arm from contacting the terrain if larger terrain changes occur besides that wheel. A small wheel is preferable to get as high a level of detail of the terrain as possible. This is because a wheel performs some filtering of the terrain it rolls across. The arm is pulled towards the terrain using a spring. The carriage is moved by the motor mounted at the far left end in Figure 5.18. On this, a pulley is mounted which accepts a GT2 belt, this is then looped down around the opposite side pulley, and the two ends finally fasten to the carriage. A 13-bit encoder is mounted on the motor to allow for position control of the motor, and to log the position of the carriage for each height measurement as they are made. Lastly, the device is driven using an STM32 board, an ODrive Pro motor driver and is powered by a five-cell Lithium-Ion Polymer (LiPo) battery. The STM32 board is used for everything except performing the motor control, which the ODrive Pro board is used for. Data points are logged at a rate of 500 Hz and stored on an SD card.

In Figure 5.19a and Figure 5.19b, the final assembled device can be seen.

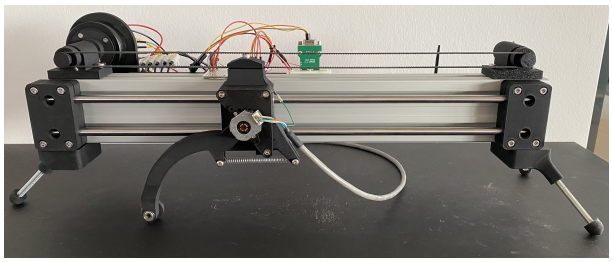

(a) *Front of produced terrain tester.*

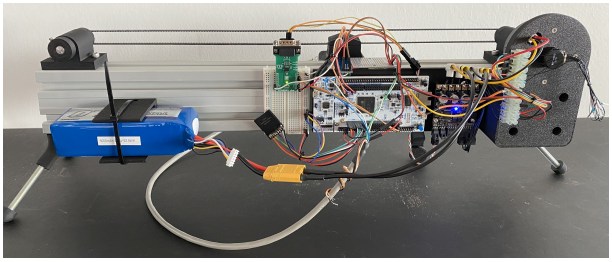

(b) *Back of produced terrain tester.*

Figure 5.19

Verifying Performance

With the device assembled, it is necessary to verify its performance before any testing can occur. To do this, a test terrain is made in computer-aided design (CAD). This has known heights and grades, and can be 3D printed, after which the device can attempt to measure it. The measured data can then be compared to the known contour of the test terrain to verify the performance of the device. A graph showcasing the test terrain is seen in Figure 5.20a, and the 3D printed terrain is shown in Figure 5.20b. The 3D printed terrain is dimensionally accurate to within 0,02 mm to 0,13 mm depending on where it is measured. The measurements are performed with a digital calliper with an advertised accuracy of ±0,02 mm. The terrain shown in the plot, which is used for comparison with the measured data, has been corrected with the errors in dimension found in the 3D print.

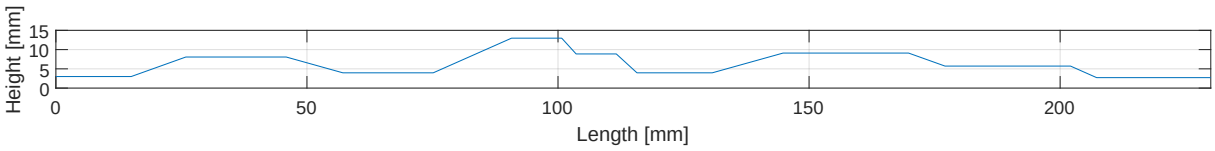

(a) *Graph showing the test terrain for validation of measurement device.*

(b) *3D printed terrain used for validation.*

Figure 5.20

In the printed terrain part, fillets with a 25 mm radius are added to the first three valleys. The 25 mm wheel should roll nicely across these and capture them in the measurement. Because a wheel is being rolled over the terrain and not a small tip, there will be some changes to the terrain as it is seen by the wheel. The wheel is unable to capture corners or valleys with radii or widths smaller than its radius or diameter, respectively. Because of this, the measurement and test terrain contour can not be compared directly, first, a wheel filter must be applied to the test terrain. This filter generates a new curve as it would be seen if a wheel of a certain diameter were rolled across it while tracing the wheel's centre. This curve is referred to as the diluted terrain. The diluted terrain can then be compared to the measured data. In Figure 5.21, this can be seen.

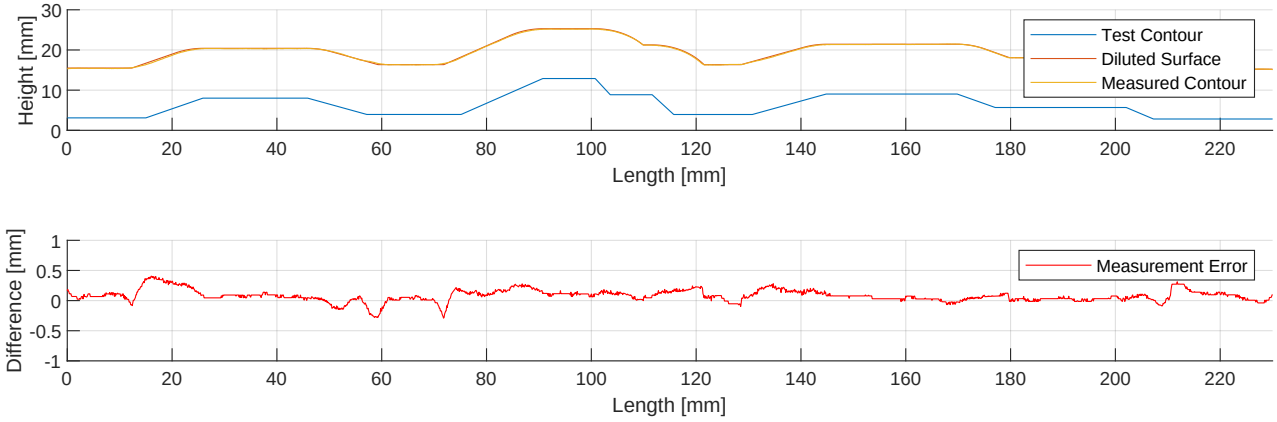

Figure 5.21

Graph showing the test terrain, measured terrain, diluted terrain and measurement error.

In the figure, the original test terrain can be seen as the blue line. It is defined without the radii applied to the first three valleys in the 3D printed part, so some discrepancy between the measured data and the defined data is expected here. The test terrain diluted by a wheel filter is seen by the orange line, and the measured data is then seen as the yellow line. As can be seen in the figure, the two follow each other closely. Underneath, the measurement error is plotted. From this, it can be seen that the maximum deviation is roughly 0,4 mm found at the first valley, so here a higher deviation is expected because of the lack of fillet in the defined test terrain. Looking at the flat sections, the deviation is in the range 0,05 mm to 0,15 mm.

Based on this test, the accuracy of the measurement device is found to be satisfactory. So it can now be used for gathering terrain data for use in the suspension model. Terrain data is gathered at Aalborg Golf Club on the fields where the mower is expected to be operating. This is done on fairway and semi-rough. On each terrain type, several measurements are made, which can then be strung together into one longer terrain section. The sections can then be fed to the simulation model, and from there, suspension tuning can take place.

Evaluation of Suspensions Impact

With the half-car suspension model completed and proper terrain data acquired, it is now possible to simulate and test the effects suspension has on the performance of a vehicle. Performance is seen as the ability to maintain wheel contact with the terrain and maintain the set cut height. These will be expressed as the percentage contact time, root mean square cut error (RMSCE) and mean absolute cut error (MACE). The percentage contact time is calculated as the percentage of wheel data points where the y-position is equal to or lower than the terrain data. The RMSCE and MACE and very similar to the metrics RMSCTE and MACTE used for evaluating the performance of the line marking robot. The RMSCE is calculated as the root mean square (RMS) value of the difference between the y-position of the chassis CoM and the primary contour. The MACE is calculated as the mean absolute value of the difference between the y-position of the chassis CoM and the primary contour. Initially, it is of interest to see what behaviour a vehicle presents with and without suspension. This behaviour is approximated by making the suspension very stiff and with minimal damping. The spring stiffness is set to 5.000 kN/m and the damping 2 N s/m. The other physical properties of the vehicle are chosen to be the same as derived earlier in Section 5.3 based on existing mowers from Husqvarna and MAMMOTION [19, 22]. The resulting parameters are again listed in Table 5.3. The input terrain used for the simulations is created from semi-rough terrain measurements made with the terrain measurement device introduced in Section 5.3. Each

measurement has a length of around 40 cm. To obtain a longer test terrain, randomly selected terrain measurements are appended to obtain an input terrain with a length of approximately 22 m. Each terrain measurement is rotated by a small angle between ±1° given by $\sin\left(P\frac{\pi}{6}\right)°$, where P is a different integer for each measurement. This is done to make some low-frequency, larger contour changes in the primary contour that the mower should follow, which is of interest as the mower should be able to follow these contours without bottoming out in the suspension. The terrain is also filtered by the wheel filter with the specified wheel diameter for the model, as explained in regards to the terrain tester, before being fed to the model. The resulting input terrain is seen in Figure 5.22.

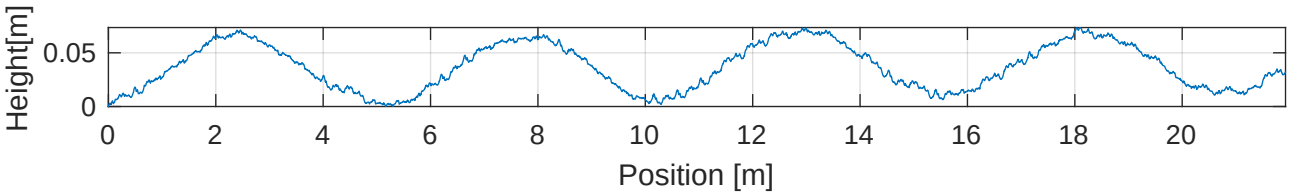

Figure 5.22

Long terrain generated from terrain measurements with rotations performed on each terrain measurement to generate changes in the primary contour.

The result from the first simulation of no suspension on the semi-rough terrain can be seen in figures 5.23a and 5.23b.

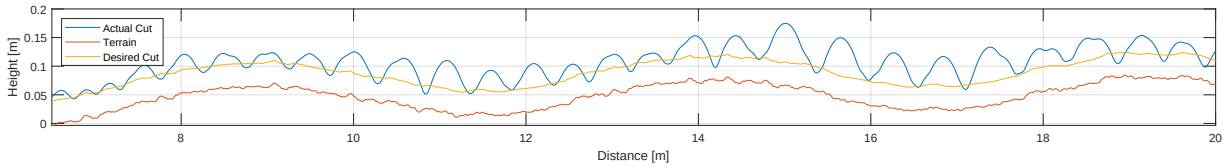

(a) *Simulation result showing the semi-rough terrain as the red line, the desired cutting height as the yellow line and the actual cut grass as the blue line without suspension.*

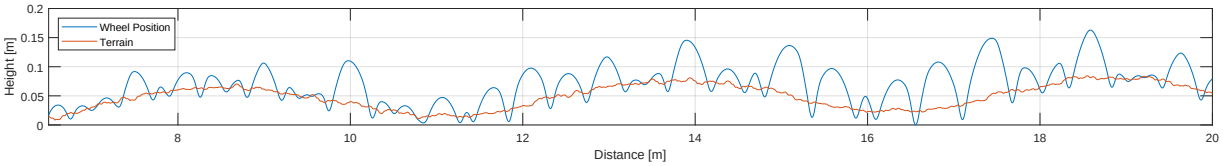

(b) *Simulation result showing the semi-rough terrain as the red line and the front wheel position as the blue line without suspension.*

Figure 5.23

In Figure 5.23a, the yellow line is the desired cut, offset by 40 mm from the primary contour and the red line is the terrain. The yellow line represents the ideal cut line if the mower can perform the cut perfectly. The blue line then represents the actual cut produced by the position of the cutting head, as the mower traverses the terrain. In Figure 5.23b, the wheel position is skipping along the terrain, due to the lack of suspension. This translates to a cutting head which is also bouncing around in Figure 5.23a, ultimately affecting the cutting performance negatively. From this initial test, the percent contact time is found to be 27,4 %, the MACE 19,5 mm and the RMSCE 26,8 mm. This acts as the baseline upon which improvements should be made. These baseline simulation results are expected to be a worst-case scenario as the terrain is rigid in the simulation. It is expected that the terrain will add damping in real life and compress under the contact pressure of the vehicle, resulting in the vehicle jumping less and having a higher contact percentage.

To examine whether suspension can improve the performance, suspension is now tuned by trial and error in the half-car model, and new simulations are performed to see if it provides better performance. The tests can be seen in figures 5.24a and 5.24b.

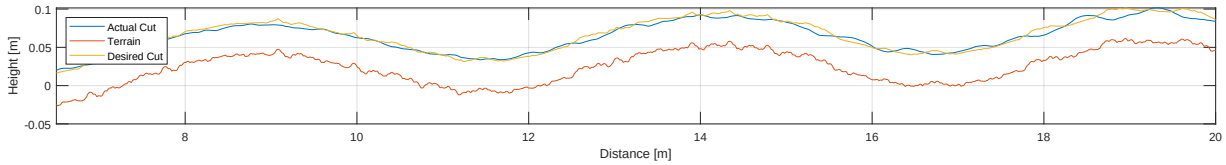

(a) *Simulation result showing the semi-rough terrain as the red line, the desired cutting height as the yellow line and the actual cut grass as the blue line with suspension.*

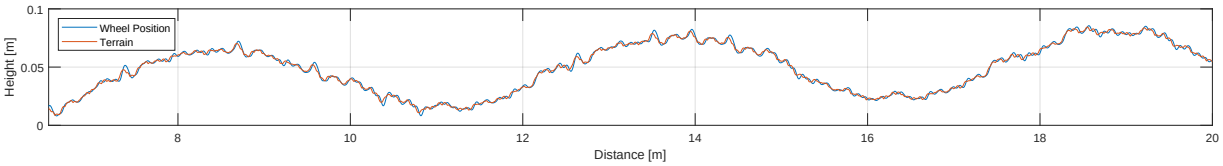

(b) *Simulation result showing the semi-rough terrain as the red line and the front wheel position as the blue line with suspension.*

Figure 5.24

This time, the blue and yellow lines follow each other much closer, indicating that cutting performance should be improved. Furthermore, looking at the second figure, it is seen that the wheel remains in close contact with the terrain for a significantly larger percentage of the time. Specifically the contact time percentage is now 52,1 %, the MACE 3,8 mm and the RMSCE 5,3 mm. It is observed that the largest cutting errors occur when the vehicle wheels are placed on the peaks or in the valleys of the terrain. An example from the simulation where this is prominent is seen in Figure 5.25.

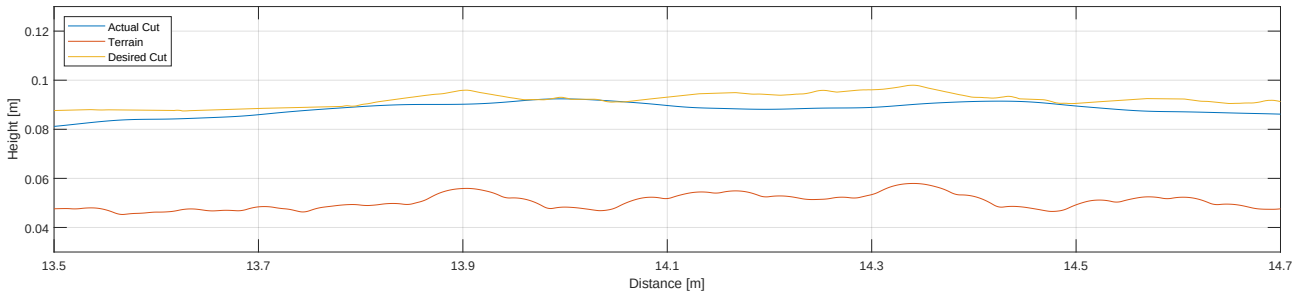

Figure 5.25

Cut out from simulation result showing the semi-rough terrain as the red line, the desired cutting height as the yellow line and the actual cut grass as the blue line with suspension. The cutting error is largest when the terrain has peaks because of the central cutting head placement.

Here, the cutting error is large at 13,9 m and around 14,1 m to 14,4 m where there are peaks in the terrain. The wheelbase is 0,8 m. This error occurs because the cutting head is placed in the centre and, as a result, will cut the grass lower at these peaks. The contribution to the cutting error caused by the cutting head placement cannot be removed with suspension. The determining factor is the cutting head placement, and the effect is thereby minimised by moving the cutting head closer to a wheel axle. Through the process of tuning the suspension, it was found to be a compromise between contact time and cutting error. Softer suspension had a positive effect on contact time, but at a point it starts affecting the cutting error negatively, as the vehicle gets closer to bottoming out when grades change.

To determine the difference between driving on semi-rough and fairway, similar simulations are performed to

the ones above with fairway data, with and without suspension. The results are listed in Table 5.4.

Performance Parameter	Without Suspension	With Suspension
Contact Time Percentage	39,6 %	51 %
RMSCE	6,4 mm	4,3 mm
MACE	4,8 mm	2,8 mm

Table 5.4

Results from simulating the half car model on fairway terrain with and without suspension.

When looking at the performance parameters from simulating on fairway terrain, the suspension again improves the performance. The improvement in contact percentage is similar. The improvement in MACE and RMSCE are, however, smaller. This is expected to be because the fairway terrain is smoother and causes the vehicle to bounce less without suspension.

These simulations showcase the need for suspension in the given example. Adding suspension shows improvements both in regard to contact with the terrain and maintaining cutting tolerances. The effects are greatest on semi-rough terrain, where the improvement is significant.

5.4 Insights from Technical Analysis for Off-road Mower Platform

With the technical analysis completed a summary will now be presented. Summarising the relevant findings done throughout the analysis. These will help steer the design in the correct direction in the following chapters.

Earlier, it was determined that the mower will primarily drive on different soil compositions with grass, but can encounter soil without grass. Grass generally improves the ground's ability to withstand forces from a vehicle's wheels without getting damaged. The worst-case scenario is thereby deemed to be sandy loam without grass. This is because sandy loam is the soil composition with the worst physical properties that is used at golf courses. With the most challenging terrain, determined calculations are performed with sandy loam. Here, the mobility of the vehicle is analysed when varying design parameters such as wheel dimensions and vehicle mass. The thrust generated in the calculations is based on what the terrain can withstand. The insights gained suggest that the wheel and ground contact area should be maximised from a mobility perspective. The positive effect on mobility when enlarging the contact area has a diminishing effect. The second insight gained is that the weight of the vehicle should be minimised. This insight comes from calculations of the vehicle driving up a 80 % grade where the weight has a large effect on the mobility. The last insight gained from the calculations is that traction generated purely from the friction between the tyre and sandy loam, with and without grass, is not enough to fulfil the mobility requirements. Additional traction is therefore needed. Here, wheel lugs are investigated as an example of a method of obtaining additional traction. Wheel lug sizes equivalent to competitors on the market are analysed. Calculations show that approximately 150 N of thrust can be obtained with wheel lugs. This is already significant compared to the force pulling down on a vehicle of 15 kg, which was about a 100 N. Even higher thrust should be possible if the wheel lug dimensions are enlarged. Especially, the lug depth is shown to have a large impact on the possible thrust. The design challenge then becomes to dimension wheel lugs to generate as much thrust as possible without introducing unacceptable field surface damage.

The thrust calculations are based on the wheels having contact with the ground, and being driven for them to

be able to generate the thrust. Based on this all wheel drive is desired. No thrust can be generated if contact is not maintained. A known method to improve contact with the ground is suspension. Therefore, the effects of adding suspension are investigated to evaluate its effect on ground contact and cutting quality. For the analysis, a half-car model is developed. Calculations are made with and without suspension. The tuning of the suspension in the half-car model is shown to be a compromise between ground contact and cutting quality. This is because the ground contact is improved the softer the suspension is. The same goes for the cutting error, but at some point, the cutting error starts rising again if the suspension is further softened. The insight gained then suggests that suspension should therefore be added to the design of the mower and that the tuning of the suspension is a compromise to best meet the requirements. It is also observed that the cutting head placement has an effect on the cutting quality. The insight gained is that the cutting head should be placed as close to a wheel axle as possible. This is because the vehicle wheels can be placed between peaks and valleys in the terrain, causing the cutting head to cut too short on peaks and vice versa.

In summary, seven insights are gained:

- The contact area between wheel and ground should be maximised
- The mower weight should be minimised
- The friction coefficient between tyre and ground should be maximised
- Wheel lugs should be added to the tyre design
- Suspension should be added
- The cutting head should be placed as close to a wheel axle as possible
- All wheels should be driven

With the technical analysis performed the solution design process for the mower will be explained next.

6 | Solution Design for Mower Prototype

With the technical analysis completed for a mower platform in the prior section, the design process will be started next. Here, the insights gained in the technical analysis will be used. First, a concept generation will be performed for the mower. The selection of a mower concept will be based on the requirements defined in Section 5.1 and the insights gained in the technical analysis. Following the selection of a mower concept, the development process of the final solution will be presented. This will involve the design of the drive unit, suspension, electronics, control and programming. Once the mower has been produced, final tests are performed. This is done to enable evaluation of the requirements and wishes.

6.1 Mower Concept Generation

In the following section, the concept generation for the mower will be presented. The goal is to investigate possible concepts and evaluate them, leading to the selection of a concept that is expected to fulfil and have the best performance concerning the requirements stated in Section 5.1. The concept generation that will be presented will focus on the process of selecting a steering concept, placement of the cutting head, drive unit concept and suspension concept. The steering concepts will all have all wheel drive (AWD) and suspension. These two decisions are based on the conclusions made in Section 5.4-Insights from Technical Analysis for Off-road Mower Platform. In the concept generation process, existing mowers on the market will be investigated for inspiration.

Steering Concepts

The concept generation for the steering concept is first performed. The concept generation process led to four viable solutions that will be presented and discussed. All concepts are with AWD as insights from the technical analysis in Section 5.2 highlighted that this is favourable for utilising traction. Existing mowers on the market are deemed viable if they are branded as highly mobile in terms of traction abilities and can zero-turn. Here two mowers are deemed as viable. The first is from Husqvarna and is called Husqvarna Automower 535 AWD EPOS [18]. The steering concept of this mower can be seen in figures 6.1a and 6.1b with alterations made to the cutting head placement.

Here, the rear end of the mower has an articulation joint that allows the rear axle to rotate ±90°, allowing zero turn. Husqvarna has the cutting head placed between the two front wheels. To fulfil the requirement of edge cutting, the two introduced concepts have the cutting head placed to the side or in front of the mower. The side position allows continuous edge cutting, whereas the front position does not. If, for example, the edge of a golf course bunker has to be cut, the mower has to drive front-first towards the edge and manoeuvre around to cut the next section of the edge. Another downside to the front mounting position is, when transitioning from flat terrain to a grade. Here, the cutting head can end up colliding with the terrain because it is the first component to encounter the grade. Here, additional solutions must be made to solve this problem. The downside of the side placement is that the mower has to be longer because the rotating rear end has to clear the cutting head. As

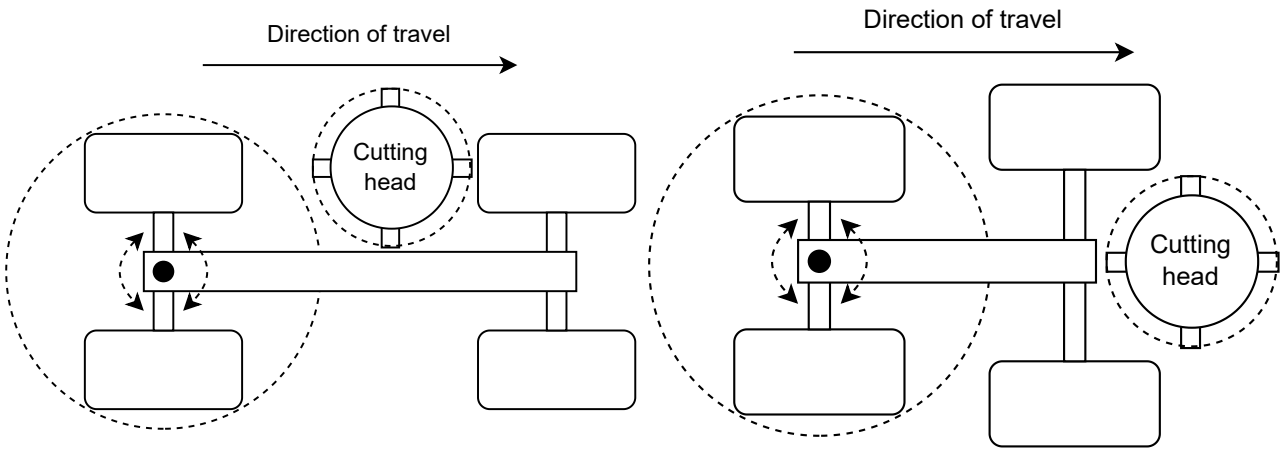

(a) *Husqvarna Automower 535 AWD EPOS inspired steering concept with the cutting head placed to the left side of the mower.*

(b) *Husqvarna Automower 535 AWD EPOS inspired steering concept with the cutting head placed in front of the mower.*

Figure 6.1

a result of these considerations, the concept with the cutting head placed to the side is deemed favourable. The second mower on the market deemed viable is from MAMMOTION and is called LUBA 2 AWD [19]. This concept can be seen in Figure 6.2a with an alteration made to the type of omni-wheel chosen.

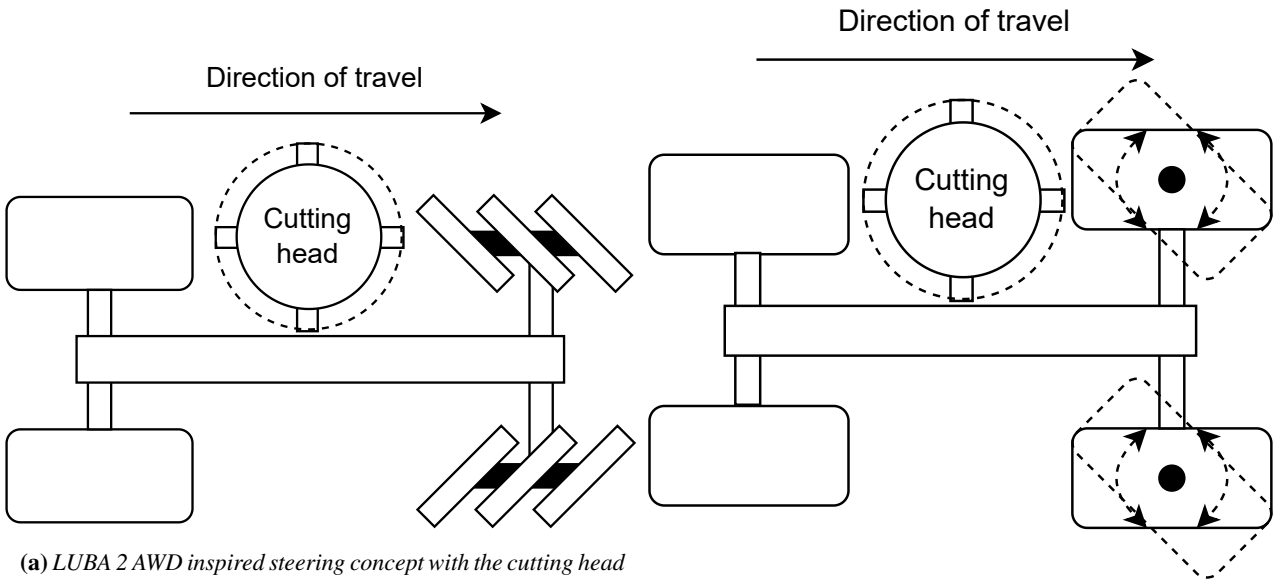

(a) *LUBA 2 AWD inspired steering concept with the cutting head placed to the left side of the mower. The omni wheel rollers are placed at* 45°.

(b) *Steering concept where the front the wheels can rotate* ±90° *with Ackerman steering. The cutting head is placed to the left side of the mower.*

Figure 6.2

In this concept, the two front wheels are omni wheels, and the cutting head is again mounted on one side. Omni wheels allow the mower to perform zero turns without the need for an additional joint like the concepts in figures 6.1a and 6.1b. The LUBA 2 AWD has omni wheels with rollers mounted at 90°, unlike in Figure 6.2a where the rollers are mounted at 45°. This alteration is made because of the situation where the mower traverses a grade. Here, the 90° omni wheels of the LUBA 2 AWD will not help in maintaining the direction. In this situation, the two rear motors have to produce an additional torque to maintain the direction, increasing the requirements for traction. With 45° omni wheels, the front wheels will also be able to aid in maintaining the

mower's direction. It is, however, expected that the tread designs omni-wheels allow will lead to lower possible traction than traditional wheels. For that reason, concept Figure 6.1a is still deemed to be the best. The last concept to be introduced is the one in Figure 6.2b. Here, the front wheels can rotate in the same manner as a car with Ackerman steering, but with a larger steering range of ±90° relative to a normal car, allowing zero turn. The cutting head is once again placed to the side of the mower. This concept is deemed to have a higher complexity in the steering concept compared to that of the concept in Figure 6.1a, it is also deemed to complicate suspension design. The steering is deemed more complex as one or two additional actuators are required to enable the Ackerman steering. The steering concept is, however, expected to require less available traction to steer the mower because traction is not needed to rotate the rear end like the concept in Figure 6.1a. The added complexity of the steering concept is, however, deemed unwanted compared to the possible improvements in mobility. As a result steering concept and cutting head placement in Figure 6.1a is selected.

Suspension Concepts

The next part of the mower concept to select is the suspension concept. When analysing the selected existing mowers on the market from MAMMOTION and Husqvarna [18, 19] it is only the LUBA 2 AWD mower that has suspension. This is expected to be because these two mowers' maximum operation velocity is 0,6 m/s and the need for suspension is lower. The LUBA 2 AWD has a roll joint on the front axle. This concept can be seen in Figure 6.3 with the addition of damping, which the LUBA 2 AWD does not have.

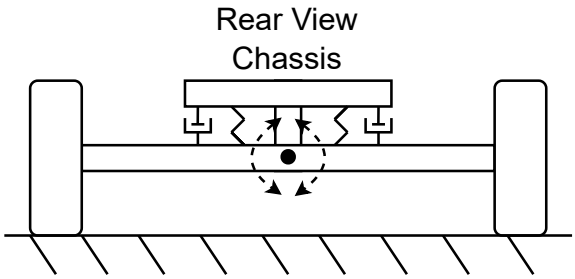

Figure 6.3

LUBA 2 AWD inspired suspension with a solid axle that can rotate about the centre. The alteration made is the addition of dampers.

Here, the front axle can roll about the axle centre with a set of springs and dampers mounted. This suspension concept can be added to both the front and rear axles. This concept has a couple of downsides. The first being that the concept only allows the axle centre to roll, and the axle centre thereby cannot travel vertically. If, for example, both wheels encounter a bump, all compliance is lost. Another downside is that the unsprung mass of the suspension concept becomes high because of the added axle mass and rotational inertia, limiting the dynamic performance. The first upside for the concept is that it is mechanically simple because it only requires one roll joint and a set of springs and dampers. The second upside is that the suspension roll enables the mower wheels to maintain contact with a double curved surface. This is, however, only possible as long as the suspension roll is not maxed out, as with all suspension types. Apart from the suspension concept inspired by the LUBA 2 AWD mower, two more concepts are introduced. These consist of a type of solid axle suspension concept and individual suspension, as can be seen in figures 6.4a and 6.4b.

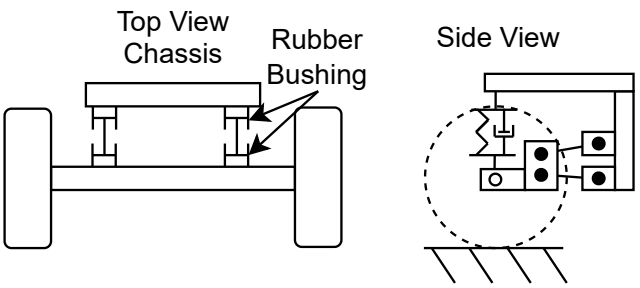

(a) *Solid axle suspension concept that allows roll and vertical travel of the axle's roll centre. Rubber bushings are used to allow some twist in the joints that enables axle roll. Two sets of springs and dampers are mounted between the axle and chassis. A top view and a side view are shown.*

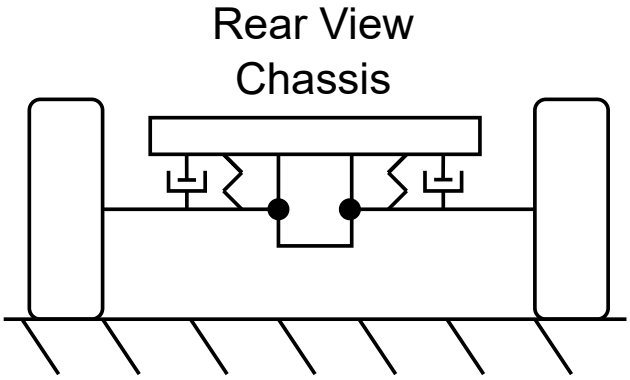

(b) *Individual wheel suspension concept that can rotate about a joint on the chassis. A spring and damper is mounted between each wheel and the chassis.*

Figure 6.4

The solid axle suspension concept is introduced because it enables both roll and vertical travel of the axle. This type of suspension is often utilised on off-road vehicles because of its ability to provide very large roll angles. The vertical travel is achieved as it can hinge at the chassis and axle fixture points. Rubber bushings are used that allow some compliance in the mounting, enabling suspension roll. The downsides of the solid axle concept are added mechanical complexity compared to the Luba 2 AWD concept, as well as a similar high unsprung mass. The last concept in Figure 6.4b is individual wheel suspension. Here, each wheel is connected to the chassis through a separate linkage, allowing it to move independently of the others. A spring and a damper are mounted between the wheel and chassis. This concept is introduced because it has lower unsprung mass and causes less chassis movement [23] compared to the solid axle concept. The downside is that the mechanical complexity is higher because it requires more components. Overall, the individual suspension concept is expected to have the best ability to maintain contact with the terrain. Furthermore, the generally small variations in terrain height, do not require the extreme roll angles the solid axle suspension can provide. The individual suspension also generally imposes less body roll, which is seen as a positive from a cutting quality perspective. As a bonus, the lowered unsprung mass is expected to enable the suspension to better absorb frequent, smaller bumps, compared to the higher mass of the solid axle system. It is, as a result, the suspension concept that will be selected for the mower.

Drive Unit concepts

The last part of the mower concept generation is to select the drive unit concept. The selected concept has AWD and therefore four electric motors must be placed on the mower. A gearbox will also be connected to each motor. This choice stems from several reasons. It is experienced earlier in Section 3.3 that encoder quantisation introduces noise into a fixed time velocity estimate. A gearing also decreases position quantisation, thereby reducing the noise in the velocity estimate. A gearing will also allow the size of the motor to be smaller and thereby lighter. A drive unit will then consist of a motor and a gearbox, and how it is connected to the wheels. From the drive unit concept generation, two concepts will be presented and one selected. The two concepts can be seen in figures 6.5a and 6.5b.

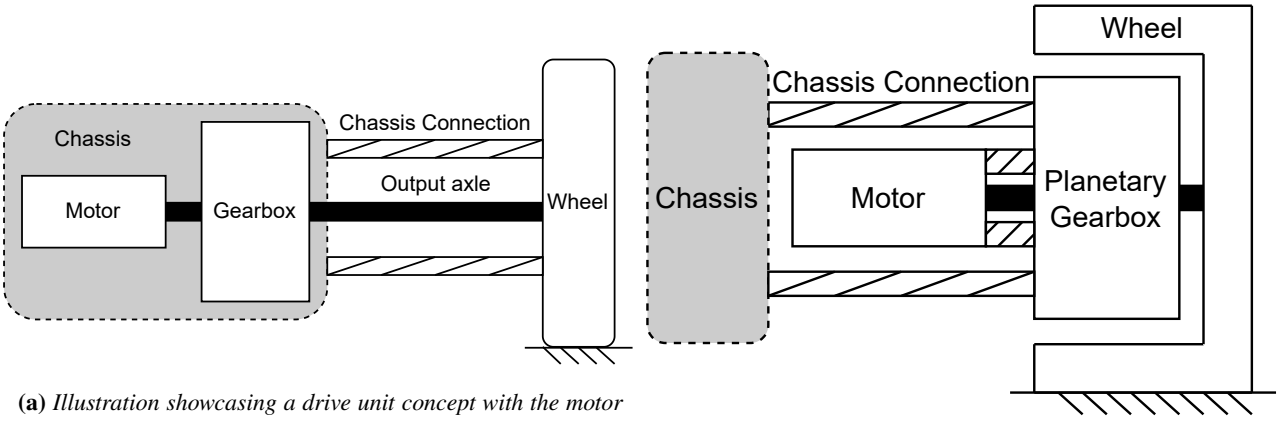

(a) *Illustration showcasing a drive unit concept with the motor and gearbox mounted inboard on the vehicle.*

(b) *Illustration showcasing a drive unit concept with the motor and gearbox mounted outboard in the rim of the wheel.*

Figure 6.5

The first concept in Figure 6.5a has the motor and gearbox mounted to the mower chassis. Here, an output axle connects the gearbox and wheel. By placing the motor and gearbox on the chassis, the unsprung mass is reduced, which gives better conditions for the suspension. One of the downsides is the need for an output axle and the joints that must enable it to move during suspension travel. Having to place the motor and gearbox on the chassis is also expected to lead to a wider mower. This is because the space within the wheels and suspension is not utilised. A wider rear axle is especially unwanted as it leads to a longer mower. This is because the cutting head needs to clear the rotation rear. Because of these downsides, the concept in Figure 6.5b is introduced. This drive unit concept places the gearbox inside the wheel. Here, a planetary gearbox is chosen because of the compact cylindrical shape, which allows it to fit within a wheel. The motor can then be mounted to the outside of the planetary gearbox. This concept is deemed to enable a narrower axle width. The downsides are that the unsprung mass will be higher and the suspension geometries will be more limited compared to the concept in Figure 6.5a. It is, however, known from [17] that minimisation of unsprung mass becomes more important the faster the vehicle drives. The mower has a low operation velocity of 2 m/s compared to regular road cars. Unsprung mass is not as big a limiting factor at lower velocities, and as such the increase from outboard motor and gearbox is not expected to be a problem. However it should still be the goal to minimise it, as it only contributes positively to performance. As a result of these considerations, the drive unit concept in Figure 6.5b is selected.

With the primary concept choices made for the mower the detailed design of the mower can be introduced. This will start with the detailed design of the drive unit.

6.2 Drive Unit

From the concept generation, a general design was picked for the drive unit. This consists of an in-wheel mounted gearbox and motor setup. This section will now address the component selection and design process of the mower's drive unit. The drive unit is designed as one of the first components, as it is one of the core components of the vehicle. Later suspension, frame and so on will be designed around the drive units.

Initial Considerations

To be able to correctly dimension and design the drive unit, certain parameters must first be known, most importantly, the torque that the mower must be able to output at the wheels. This becomes relevant when selecting a motor. The defining factor in regards to the torque is the mass of the mower, the 80 % grade it is set to climb and some excess for acceleration and resistance. The torque required to climb the grade is defined by both the mass and the wheel size of the mower. The mass is not yet fully known, however, it is expected to be around 20 kg, which is around the mass of existing mowers on the market from Husqvarna and Mammotion [18, 19]. The wheel size is expected to be around 20 cm as this is found to give good performance in Section 5.2, while not chasing diminishing returns, and it is considered to be a realistic size for the mower's intended size. It is also similar to existing products and larger than a sprinkler hole of 15 cm as per the requirements. To calculate the required torque for maintaining a set velocity on an 80 % grade, simple calculations can be made.

$$F = mg \sin(\theta_s) \tag{6.1}$$

The force is found to be 120,8 N for the mower, equalling 30,2 N per wheel. The required torque is then given by the force per wheel times the wheel radius and is found to be 3 Nm. As this is the torque required for maintaining a set velocity with no resistance, some overhead should be added to allow for acceleration as well as overcoming various resistances. Earlier in Section 5.2 in Figure 5.11a compaction resistance is plotted for varying tyre dimensions, and at a mass of 20 kg. These parameters are similar to those expected for the mower design, and it is seen that for a tyre diameter of 20 cm the compaction resistance can be expected to be between 17,5 N to 33,5 N for varying tyre widths. This likely means 10 % to 30 % should be added to the torque value to compensate for compaction resistance. As it is known that the design will feature a gearbox, the efficiency loss from this should also be considered. From [24] it is stated that a planetary gearbox stage is approximately 97 % efficient. It is desired to keep the gearbox at a single stage due to compactness, therefore, the efficiency loss should be small. It is, however, expected that 3D printing will further reduce efficiency due to bad tolerances, so a total reduction of 15 % is considered. Based on this the torque value is increased by 45 % to account for resistances and gearbox efficiency, giving a torque requirement of around 4,35 Nm. It should also be ensured that the mower can accelerate as defined in the requirements, here it is stated that it should achieve at least 0,5 m/s^2. Based on the mower's mass and this acceleration, a force of 10 N is required. This is lower compared to the force the mower is already required to output for it to climb the 80 % grade. With this in mind, the mower will have plenty of torque for accelerating on flat terrain. On grades, any overhead will enable it to accelerate sufficiently, as there are no requirements for acceleration there. Due to the uncertainty coupled with these estimations, a motor with a large excess of torque that, without a doubt, will be able to perform as needed is desired. It is therefore decided to add 50 % extra to the torque requirement, resulting in a torque value of 6,75 Nm. Next, the motor selection will be considered.

Motor Selection

Based on the final concept selected in Section 6.1, it is known that the drive unit will consist of an in-wheel gearbox with a motor attached. The motor for this setup will now be selected based on various considerations. Due to the motor being mounted on the wheel and thereby being a part of the unsprung mass, it is of interest to keep the mass low. This is because it allows the suspension to accelerate quicker, which improves its ability to stay in contact with the terrain [13]. It should also be able to provide the 6,75 Nm, granted that a gearing will be present. Due to the desire for a single-stage gearbox as mentioned earlier, the gearing is limited to a maximum

of 1:10, as this is the recommended upper limit of gearing for a single-stage planetary gearbox [25]. Therefore, the motor should fulfil the requirements at a gearing of maximum 1:10, as this is the best case, the motor should also be able to perform at lower gearings. A bigger motor will, as a result, be selected later to account for some of the uncertainty in the realisable gearing ratio. The final consideration is the availability of the motor. Due to the limited time frame of the project, the motor should be readily available for order. With these considerations in mind, different motors are considered, with the choice landing on a Turnigy Aerodrive SK3-6364 190Kv [26]. A picture of the motor can be seen in Figure 6.6.

Figure 6.6
An image showing the selected drive motor for the mower [26].

The motor has a line-to-line KV rating of 190 RPM/V, from which a q-axis current torque constant of 0,0435 Nm/A is calculated. This calculation can be seen in Appendix A.5. Based on this and a gearing of 1:10, the motor can provide the required torque at 15,5 A q-axis current. This is acceptable, as the motor is rated for up to 65 A RMS phase currents. This also leaves plenty of overhead in case the gearing ends up being lower. This overhead is quite significant, and as such, a smaller motor would have been better in terms of mass. However, the next step down in motor size resulted in a higher KV rating, making it impractical to deliver the desired wheel torque with the same gearing. Based on this and the fact that the mower is a prototype, it was decided to go with the larger motor. Next, the wheel design will be considered, as the inner dimensions of the rim will constrain the outer dimensions of the planetary gearbox.

Wheel Design

The primary goals of the mower wheels are housing the gearbox and creating a mounting interface for a 3D printed tyre. It should be sufficiently strong not to crack or break while operating, but the material thickness must also not be so large that the dimensions of the gearbox become too constrained. Ideally, finite element analyses (FEAs) should be conducted for proper design. However, as the design will be 3D printed, there are a lot of uncertainties in the geometry due to the slicer and in strength, due to layer adhesion and as such FEAs cannot provide useful results. Based on this, dimensioning is based on intuition and aims to be on the safe side concerning strength. As mentioned earlier in Section 6.2 the wheel diameter is set to be 20 cm, the wheel width is set at 5 cm as it was found in Section 5.2 that going much above this, the performance gains quickly diminishes. First, a design is created for the rim, this can be seen in figures 6.7a and 6.7b.

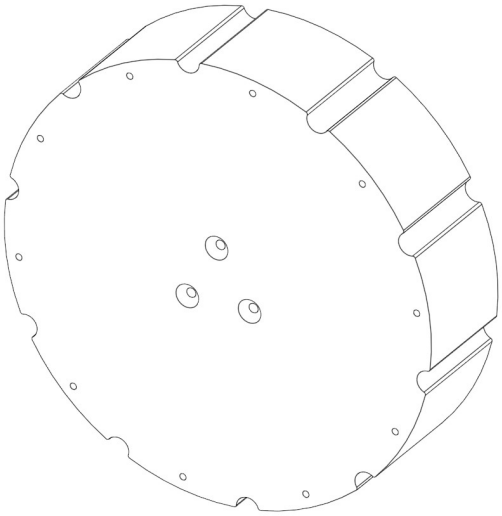

(a) *The mower rim seen from the front.*

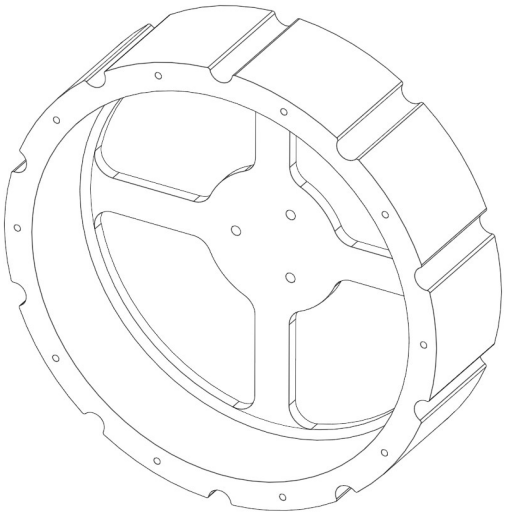

(b) *The mower rim seen from the rear.*

Figure 6.7

The rim features a closed front to prevent dirt and debris from entering. A set of four spokes is raised from the front surface, raising the spokes adds extra stiffness and strength while also adding a mounting surface for the gearbox to the rim. On the outer diameter are several valleys, which act as mechanical locking devices for the tyre to be mounted. Lastly, several small holes are placed alongside the outer diameter on both front and rear faces. These allow for mounting bead locks to keep the tyres in place once they are mounted to the rim. The tyres will be printed in thermoplastic polyurethane (TPU) and as such will not have as good frictional properties as was it rubber. Ideally, rubber tyres would have been used, but with the available production methods and within the time frame, this was not possible. From Section 5.2 it is known that friction alone will not be enough to climb grades of 80 % even with rubber. Therefore, wheel lugs will be added to the tyre as they were analysed to be able to provide the additional thrust needed. Based on these observations, a tyre is modelled, which can be seen in Figure 6.8a.

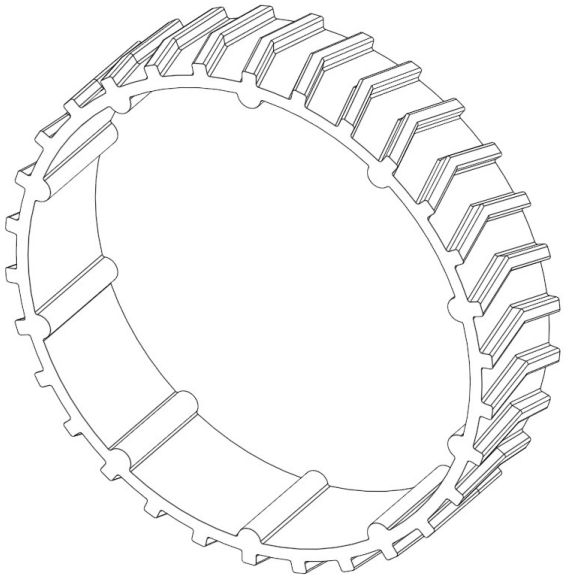

(a) *The TPU tyre for the mower, with lugs.*

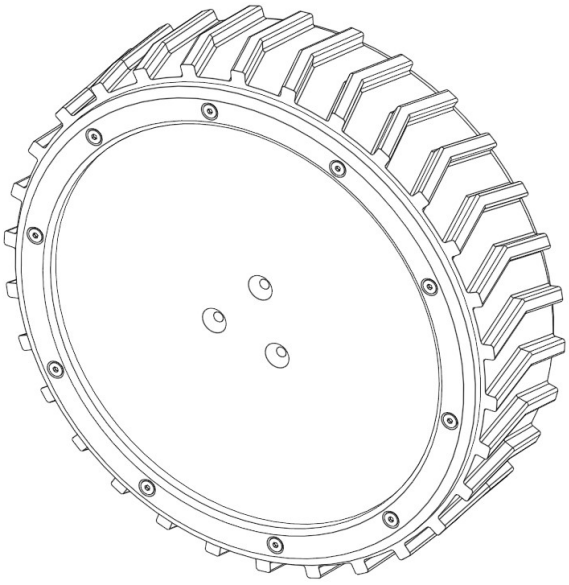

(b) *The full wheel assembly.*

Figure 6.8

The tyre is made to be airless since a 3D printed rim and tyre will not be airtight. With this the tyre is printed to be fairly rigid so that it can hold its shape on its own. This also means that the insights gained from Section 5.2 are applicable as the analysis in that section took offset in rigid tyres. Lugs are added as discussed, these have an arrow-like shape to aid in the vehicle not sliding sideways when going across the length of a grade. The traction the lugs will be able to produce can be estimated from eqns. (5.8) and (5.10). From Eqn. (5.10) the rupture distance is found to be 8,5 mm with a lug height of 5 mm, this is less than the lug tip distance of 18 mm of the tyre. The equation is based on straight lugs so there is some uncertainty regarding the results. From Eqn. (5.8) the available thrust from a single lug is then estimated to be 15 N to 30 N depending on the size of the contact patch, which is hard to estimate precisely. The contact patch is defined by the tyre's width and the length of the contact patch. The width is known as it was set at 5 cm, the length is then an estimate, and it is here varied from 2 cm to 4 cm to see how it affects the performance. Considering all four wheels together, this should create mechanical traction of 45 N to 90 N. Granted that the force pulling the mower down is around 120 N when parked on a 80 % grade as found earlier in this section, the lower value of 45 N may be too low, when also considering an approximate frictional coefficient range of 0,3 to 0,4 between grass and TPU. This range is based on the earlier found friction coefficient range in Section 5.2 between grass and rubber. It is expected to be worse between TPU and grass, and to be conservative, it is halved. With this low friction, less than half of the required force can be generated through friction, and as such, the lugs should contribute slightly more than half of the required force. If the contact patch turns out to be on the lower end, the lug depth can be increased to compensate. The lug dimensions chosen are slightly smaller than those of the MAMMOTION and Husqvarna mowers, which do not seem to damage terrain, and therefore, the designed lugs are expected to be fine with regards to terrain damage. To finalise the wheel design, bead locks are added to the assembly, locking the tyre on the rim. The final complete assembly can be seen in Figure 6.8b. With the wheel completed, the focus can now shift towards the design of the in-wheel gearbox.

Gearbox Design

As described in Section 6.1, it is decided that the gearbox should be housed in the rim of the wheel. This is to try and keep the system compact by utilising the space in the wheel. As well as trying to keep the mechanical system simpler by eliminating the need for axles and the joints needed for those to work. When choosing which style of gearbox to implement, the important factor is the fitment in the rim to maximise the use of the available space, therefore, it is decided to utilise a planetary gearbox. These can be made completely circular and therefore lend themselves well to the task at hand.

From a motor point of view, a higher gearing is favourable due to being able to run the motor at higher speeds, increasing sensor feedback and thereby improving the foundation for control. How close the resulting gear ratio gets to 1:10 is a compromise between what is possible to fit in the rim and how small a gear module is used. As the gearbox is to be 3D printed, it is necessary to be liberal with the module of the gears. It is difficult and unreliable to do strength calculations on 3D printed parts, and therefore, it is decided to make everything as large as will fit within the rim. This will provide the maximum potential for strength, but also weigh more than a properly sized gearbox. As this mower is a prototype, this is deemed acceptable, and the gearbox could then be optimised later in a production design.

Initial considerations are made about the layout of the gearbox. The sun gear will be the input, and as such, it will be fastened to the motor axle. Then both the carrier and ring gear can be the output. If the ring gear is

chosen as the output, sealing the gearbox is expected to be difficult. It would likely either require a dynamic seal or a very large bearing around the size of the ring gear, this could quickly become very expensive. Based on these factors, it is chosen that the carrier should be the output. With this, it is possible to make the ring gear a part of the enclosure of the gearbox, making sealing easier, as it can now come from a more reasonably sized bearing, which the carrier will be supported by.

With various factors considered, the gearbox design itself can begin. It is initially chosen to make the ring gear the largest outer diameter the rim will allow. This is found to be 159 mm based on the inner diameter of the rim and some clearance to allow for deflection of the rim without contacting the gearbox. A tooth module of 1,5 mm is picked as a compromise between allowing for a large number of teeth, while also making them large enough for 3D printing. It is wanted to have 8 mm of wall in the ring gear, for strength purposes and for making room for bolts to assemble the gear housing. Based on this, the root diameter of the ring gear becomes 143 mm. From this and the module, the pitch diameter is calculated to be:

$$d = d_f - 2{,}5m = 143\,\text{mm} - 2{,}5\,\text{mm} \cdot 1{,}5\,\text{mm} = 139{,}25\,\text{mm} \tag{6.2}$$

The teeth count is then found:

$$z = \frac{d}{m} = \frac{139{,}25\,\text{mm}}{1{,}5\,\text{mm}} = 92{,}83 \tag{6.3}$$

Based on this, the number of teeth on the ring gear will be 93 [27]. Next, the sun gear is set to have as few teeth as possible to allow for the highest gearing. Normally, it is ill advised to go below 14 teeth on a gear [28], in this case, the teeth number is set at 15 as 14 would have required a non-integer number of teeth for the planets, which is not possible. With this combination of ring and sun gear teeth, the planets require 39 teeth. Finally, the gearing of this combination is found to be:

$$gearing = \frac{zc}{za} + 1 = \frac{93}{15} + 1 = 7{,}2 \tag{6.4}$$

A gearing of 1:7,2 is less than the 1:10 considered in the motor selection, but as the motor had plenty of overhead, it should still be sufficient. With this gearing 21,56 A of q-axis current is required to provide the needed torque.

With the design of the gearing sorted, the mechanical design of the gearbox itself can begin. Initially, the ring gear is designed, and the front and rear of it can be seen in figures 6.9a and 6.9b.

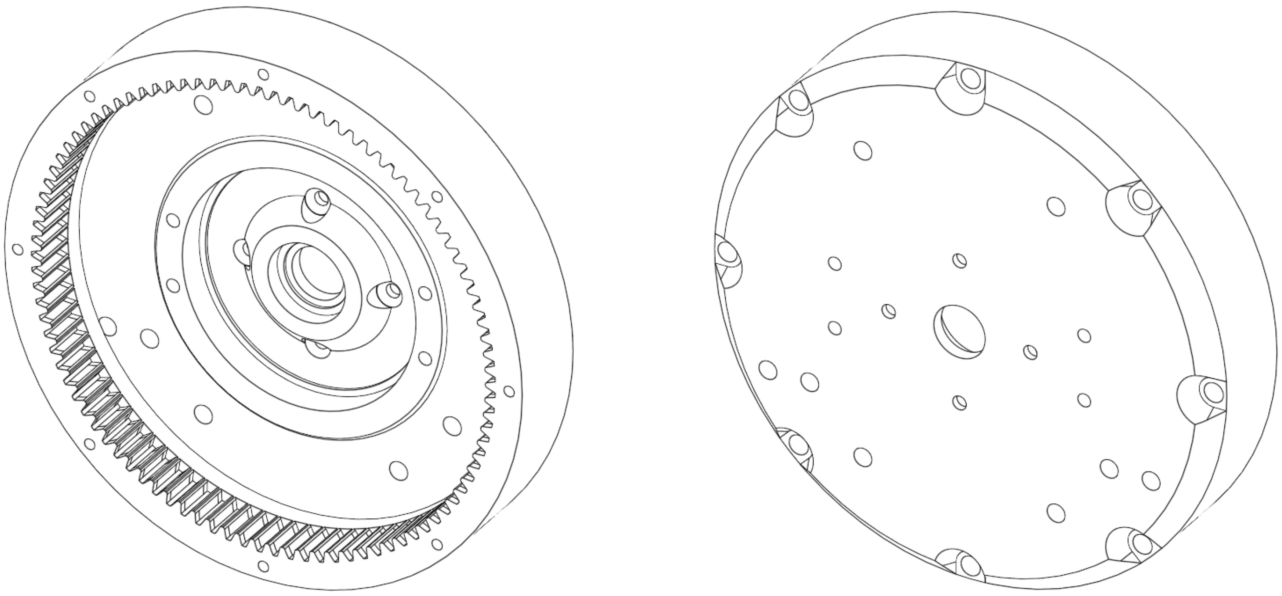

(a) *The ring gear integrated in the gearbox housing seen from the front.*

(b) *The ring gear and gearbox housing with various mounting holes seen from the rear.*

Figure 6.9

The ring gear is integrated in the input side housing for the gearbox, along with the mounting interface for motor which is the four screw holes seen around the centre opening, suspension brackets and encoder mounting which are the other holes which can be seen on the rear of the housing. Bearing seats are added to accommodate the sun gear and planet carrier bearings. Finally 12 holes are added around the perimeter of the housing which accommodate assembly screws for joining the input and output side housing later. Next, the motor, sun and planet carrier mounting in the input side housing can be seen in Figure 6.10.

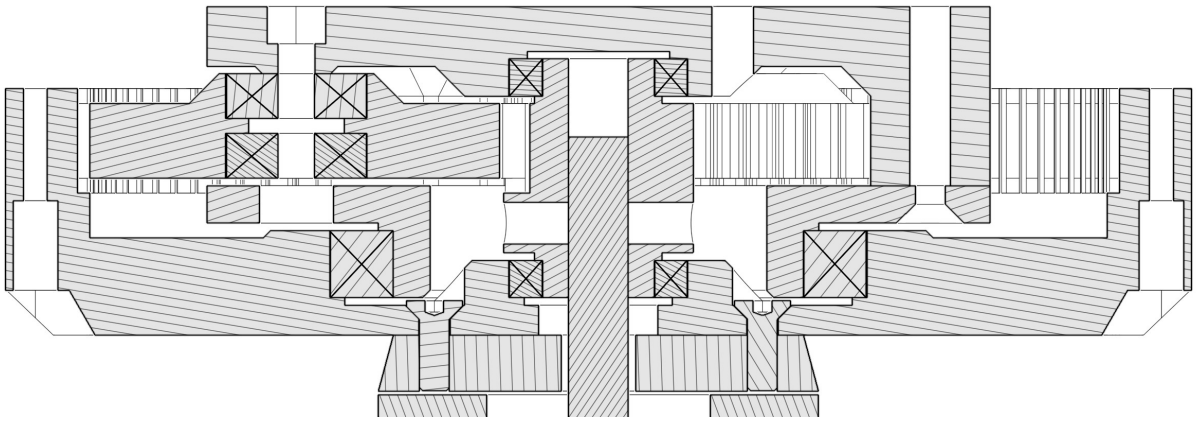

Figure 6.10

Section view showcasing the sun, carrier and planets mounted in the ring gear and housing.

The motor is mounted on the rear of the housing with four screws coming through from the inside, as can be seen in the bottom of Figure 6.10. The motor shaft then passes through the centre opening of the housing and connects with the sun gear. The sun gear is supported by both the motor axle, a bearing in the centre of the input side housing, as well as a bearing seated in the output side of the carrier. This is the smallest bearing which can be seen at the top of Figure 6.10. In the two holes which can be seen on either side of the sun gear at its bottom, threaded inserts are mounted. Using these the sun gear is then fastened to the motor axle using set

screws, with thread locking compound to prevent loosening even with the vibration of the gearbox operating. As mentioned, the carrier mounting in the input side housing is also shown in Figure 6.10. The carrier is composed of two separate sections, referred to as the input and output sides, which sandwich the planets. It is mounted in the input side housing on a larger bearing seated around the small bearing, which holds the sun gear. It can be seen at the bottom of Figure 6.10. The bearing size was chosen based on it being the largest easily available bearing, which was also cheap. It is reused in the output side housing to support the output side of the carrier. In figures 6.11a and 6.11b images of the carrier and planet assembly alone can be seen.

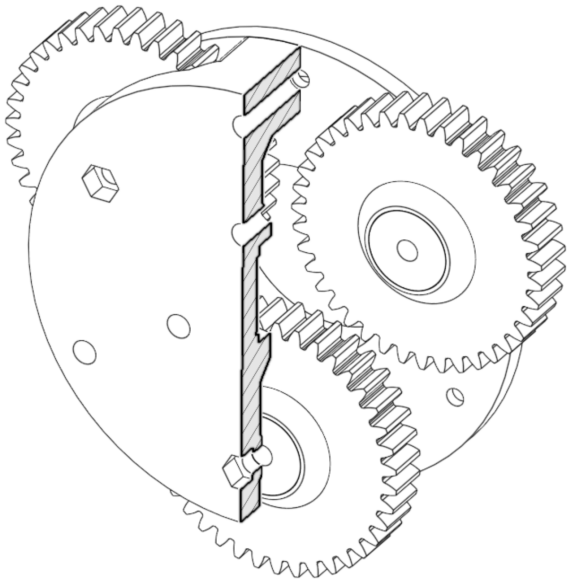

(a) *View from the front of the planets and carrier, with a section cut out of the output side carrier to better show the mounting of the planets.*

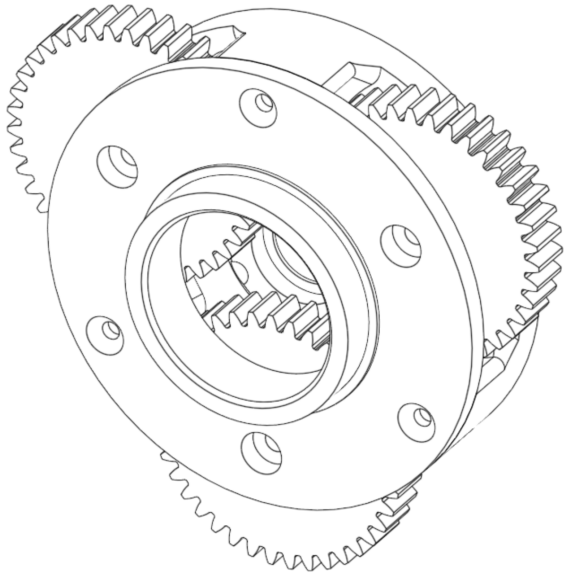

(b) *View of the rear of the planet carrier assembly, where the large bearing interface can be seen on the rear carrier.*

Figure 6.11

Here, the two parts of the carrier are clearly seen. The input side carrier can be seen in Figure 6.11b here the bearing interface is also seen, along with three countersunk holes which are for connecting the input and output side of the carrier. A further three holes are seen, these are to give clearance to the bolts which mount the planets to the output side of the carrier. In Figure 6.11a, a hexagonal hole can be seen on the left side, which is for seating a nylon lock nut. The planets are then mounted on the output side carrier half by a bolt passing through two bearings seated in each planet gear to the nylon lock nut. This can be seen in Figure 6.10 on the left. The lock nut is used to prevent the planets from loosening during operation. Furthermore, the output side carrier has a small raised section, so it only contacts the inner ring of the bearing in the planet, allowing it to spin without rubbing the seal. Images of the full gearbox assembly with and without the output side housing can be seen in Figure 6.12.

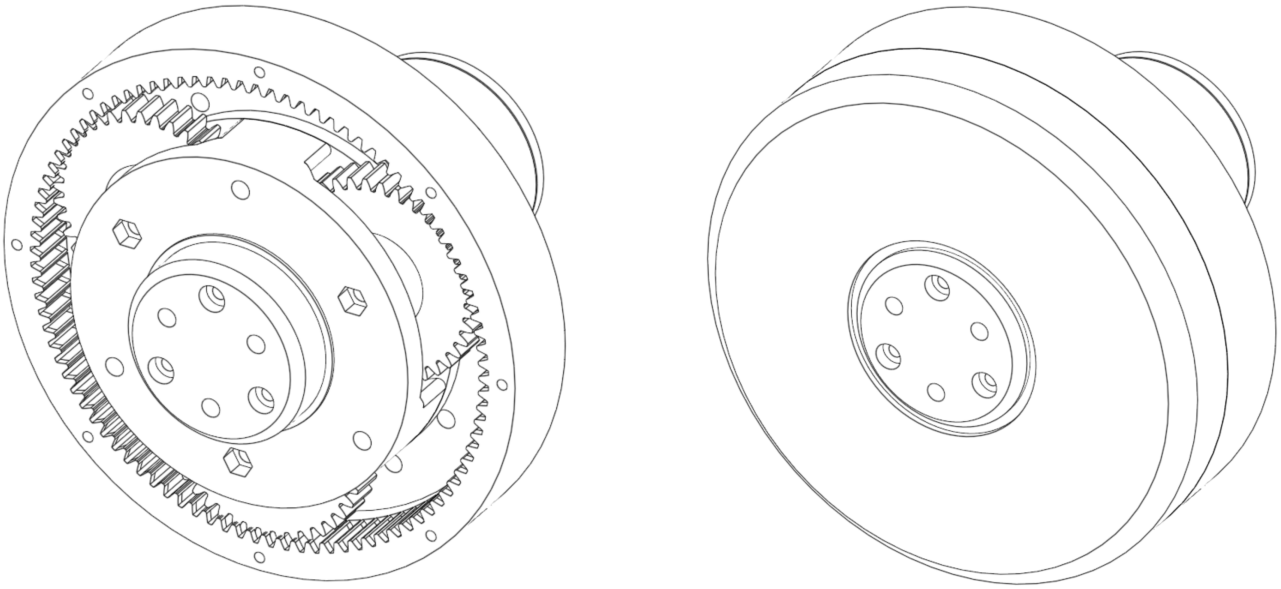

(a) *Image of the planet carrier with output flange mounted in the ring gear housing.*

(b) *Image of the fully assembled gearbox.*

Figure 6.12

In this Figure 6.12a, it is shown how the full carrier assembly is mounted in the input side housing. The output flange is now also seen mounted to the output side of the carrier. This flange mounts to the carrier with three bolts and has a further three holes in which threaded inserts are mounted, allowing for the mounting of the wheel rim. The output flange also acts as the second bearing interface on the carrier. This then sits in the bearing mounted in the output side housing, making the carrier supported from both sides, increasing the stiffness of the assembly. Finally, in Figure 6.12b, the full assembled gearbox can be seen, where primarily the two housing parts are showcased, but the output flange can also be seen in the middle protruding out slightly, as well as the end of the motor can be seen in the rear.

With this, the planetary gearbox is completed and ready for installation in the wheel, and as such, the drive unit has been completed. The final design resulted in a gearing of 1:7,2, the motor can output the required torque at 21,56 A q-axis current and a wheel diameter of 20 cm with tyre lugs to generate the thrust required for climbing grades of 80 %. Next in the process, the suspension design will be presented.

6.3 Suspension Design

From the concept generation performed in Section 6.1 an individual suspension concept is selected. In the following section, the detailed design of the mower's individual suspension will be presented. Given a larger time frame and more resources, the suspension design process following the terrain research performed in Section 5.3 would ideally start by thoroughly investigating different suspension geometries and their characteristics. Based on this, decisions could be made on which suspension geometries would be most suitable. Expanded suspension models could then be created based on these geometries, thereby allowing simulation for verifying and investigating the individual performance of each of the possible solutions. This should then lead to a decision on a single specific suspension setup that is deemed most suitable, which would then be designed mechanically and eventually produced.

Due to time limitations, limited production methods and capacity. A simpler approach is chosen, which is considered the ideal given the circumstances of the project. There are several reasons behind this choice of approach. The chosen production method for the mower is primarily based on 3D printing because of its fast production time, the part designs it allows and price. The availability of Turf Tank's 3D-printing capacity is severely limited later in the timeline of the project. Therefore, it is important to quickly arrive at a solution which can be put in production to ensure the completion of the mechanical assembly. Taking this approach enables completing and testing the full mechanical and electrical system of the mower within the project's time frame. Dedicating a large part of the project time to suspension design would therefore be putting the goal of the project at risk.

Mechanical suspension design

Based on the approach described in the introduction to this section, a suspension design direction is chosen for the individual suspension concept selected in Section 6.1. The goal of the suspension geometry is to get as close to a linear spring/damper characteristic as possible. This is because it will have a better correlation with the simulation results from the earlier developed half car model in Section 5.3. It is also a wish to keep the complexity of the suspension low. This will be in the form of as few unique parts as possible and low complexity mountings between the mower chassis and wheels. The reason for wanting a few unique parts is that if parts break during testing, they will be easier to replace and require less occupation of Turf Tanks 3D-printers.

With the design direction established, the suspension will be designed next. As introduced Section 6.2, the drive unit has been designed. This puts some limitations on how the suspension can be designed. The motor takes up a lot of the space where suspension could be placed. One type of suspension design that can provide space for the motor and the suspension travel is a double wishbone design. The implementation of a double wishbone suspension can be seen in Figure 6.13.

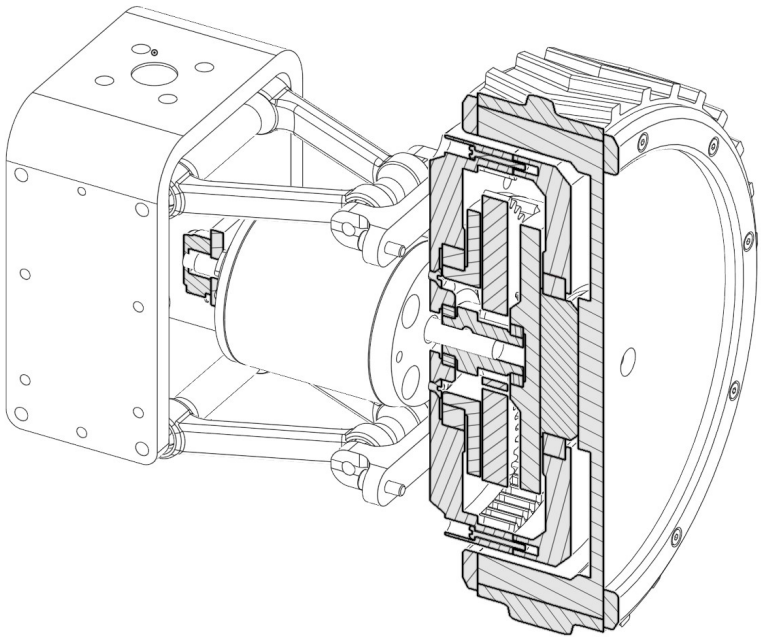

Figure 6.13
Double wishbone design connecting the chassis and drive unit.

The hole in the centre of the wishbone allows space for the motor and 42 mm suspension travel. In Figure 6.13,

the length of the wishbones is chosen to be equal. If the length ratio between them is altered, positive and negative camber can be introduced [17]. Because the tyre is flat, camber is unwanted. This is because camber will lower the contact area between the tyre and the ground and raise the stress applied to the soil. Camber is thereby expected to lower the possible traction and heighten the possibility of field surface damage. This explains the chosen wishbone length ratio. The selection of a wishbone suspension design is also in line with the chosen design direction. This is because wishbones have a low complexity and can be easily mounted to the mower chassis and gearbox. The equal wishbone length also results in the need for only one type of wishbone. Based on the above consideration, a double wishbone design will be chosen for the suspension design.

Next, the placement of spring and damper will be considered. For the mower it is decided to utilise a strut assembly which is a spring and damper already assembled in one collective unit. The strut is going to be mounted between the centre bracket connecting the left and right suspension assemblies, and the bracket on each drive unit meant for suspension mounting. To let the strut clear the chassis and centre bracket of the mower, a bracket is designed and mounted on the centre bracket. The mounting can be seen in Figure 6.14.

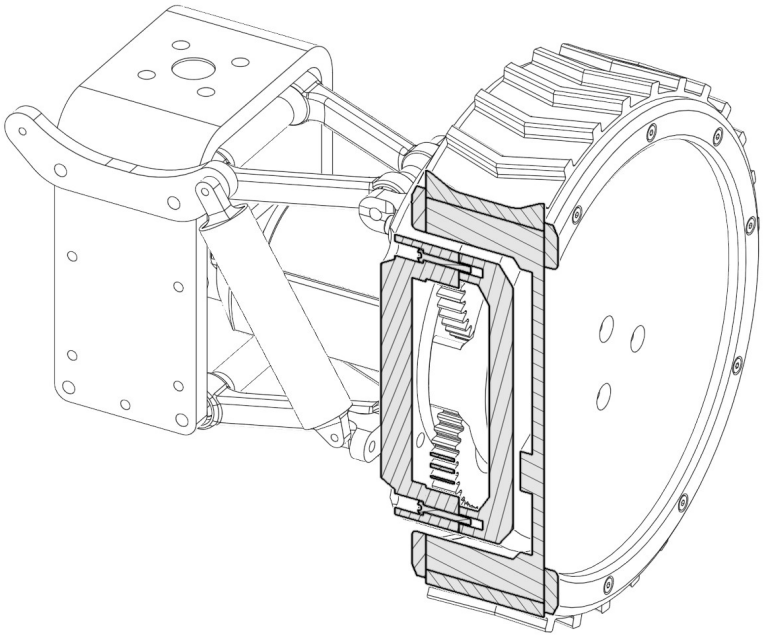

Figure 6.14

Placement of strut in the suspension design and the two brackets needed to mount it.

As can be seen, this results in the strut being mounted at an angle to the suspension. This introduces non-linearities to the spring and damper characteristics. The effect on the characteristics is of interest to analyse to decide if the introduced non-linearities are acceptable. To analyse the effects, the strut dimensions have to be chosen. Struts available for purchase are evaluated, and a radio control (RC)-car strut is selected that is made for a 1/10 scale off-road RC-car. The strut has 38 mm of travel. The suspension CAD model is used to obtain data points for wheel travel and corresponding strut travel. In Figure 6.15, data points for strut travel are shown as a function of the wheel travel.

Here, it is seen that the strut travel is lower than the wheel travel. This means that the equivalent strut stiffness and damping coefficient are reduced. The non-linearity introduced is not significant.

Apart from the reduction in equivalent spring stiffness and damping, there is also a change in the vertical force component produced by the strut throughout the suspension travel. This is caused by the strut angle changing

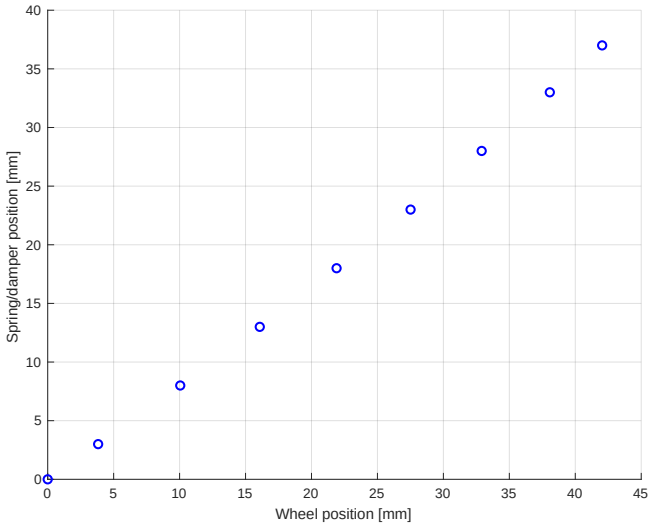

Figure 6.15

Plot of wheel position and corresponding strut position.

during travel. This will be analysed similarly by calculating the percentage of the maximum vertical force component for each of the data points plotted in Figure 6.15. The percentage of the maximum vertical force component throughout the suspension travel can be seen in Figure 6.16.

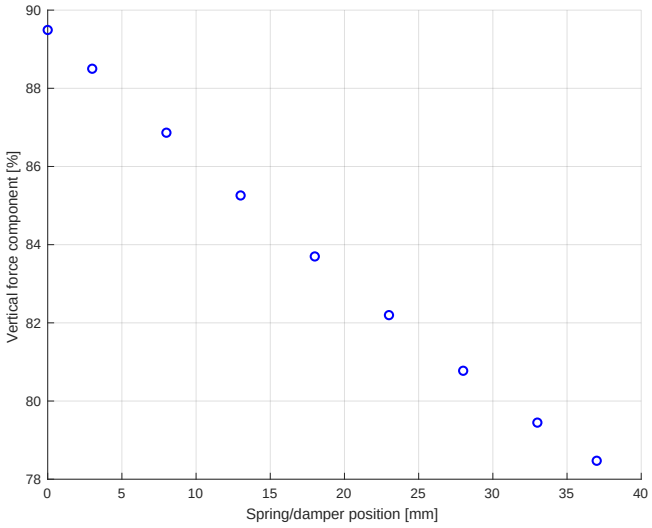

Figure 6.16

Plot of strut position and corresponding vertical force component.

The vertical force component is 89,5 % in full extension and goes down to 78,5 % in full compression. This causes the suspension to have a degressive characteristic and overall reduction in stiffness. The change in the vertical force component is also not linear, but the introduced non-linearity is not that large. The suspension strut characteristic is deemed acceptable. The strut mounting location is therefore kept, and the introduced non-linearities will be added to the half-car model later in this section. The chosen RC-car strut is also selected for the suspension design. The spring stiffness and damping coefficient are unknown from the supplier. The spring and oil in the damper can, however, be changed. It is therefore of interest to tune the suspension dynamics in the earlier developed half-car model to improve the performance of the mower. Then a new set of springs can be bought with the designed spring stiffness, and the oil in the damper can be changed to get the designed damping coefficient.

Half-Car Model Validation

It is the goal to tune the designed suspension to maximise ground contact and minimise cutting error. For this, the earlier developed half-car model will be used for the tuning process. The result will be a spring stiffness and damping coefficient. A new spring can then be bought for the RC-car strut, and the oil in the damper can be changed to get the wanted damping coefficient. However, before the half-car model can be used, its ability to depict the mower's suspension dynamics has to be validated.

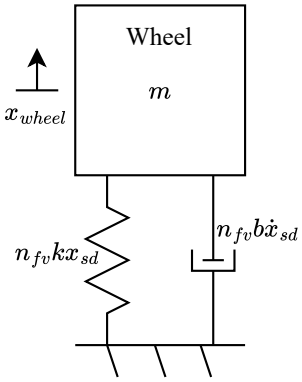

Figure 6.17
Suspended mass model used for half car model validation. It consists of a wheel mass, a spring and a damper from the bought RC-car strut.

Earlier in Section 5.3, the half car model's behaviour is deemed to be physically correct, along with the system equations being cross-checked with [21]. Validation of the model's ability to depict the mower's suspension behaviour needs to be performed. This is because there are uncertainties in the model parameters, such as the suspension damping or possible unknown dynamics not included in the model. An experimental setup to validate the full half-car model will not be developed. Instead, a new simulation model is developed consisting of a suspended mass with a spring and a damper. This model is chosen because an experiment can be performed with the produced mower that isolates this system. This is done by flipping the mower upside down and dropping the wheel while recording the response. It is expected that if the dynamics of the suspended mass model can represent the response from the experiment, then the half-car model can also be validated. This is because the primary differences between the models are the rigid chassis connecting the front and rear suspension along with the tyres, spring and damper. The uncertainties related to the chassis connection are low, as a rod is used as an approximation. The primary uncertainty in the half-car model is expected to be the suspension parameters. The suspended mass system is shown in Figure 6.17.

For the suspended mass model, the EoM:

$$m\ddot{x}_{wheel} = n_{fv}(kx_{sd} - b\dot{x}_{sd} + F_{preload}) - mg \tag{6.5}$$

Here m is the suspension mass of 1,95 kg determined from weighing a produced suspension, k of 520 N/m is the spring stiffness, which is measured from the bought struts spring, b is the damping coefficient, x_{sd} is the position of the strut, $\dot{x}_{sd}$ is the velocity of the strut, n_fv is the vertical component of the strut force, $F_preload$ is the spring preload added to ensure the strut does not bottom out and mg is the gravitational force acting on the suspended mass.

The strut position x_{sd} is obtained by using a second-order polynomial that maps the wheel position x_{wheel} to the strut position x_{sd}. The second-order polynomial is obtained by curve fitting to the data points introduced earlier in Figure 6.15. The polynomial has an R^2 value of 0,99. The strut velocity $\dot{x}_{sd}$ is obtained by using a polynomial that transforms the wheel velocity to strut velocity. The polynomial is obtained by taking the derivative of the polynomial that transforms wheel position to strut position. The polynomial n_{fv} that transforms the spring, damping and preload force to its vertical component is obtained by curve fitting a second-order polynomial to the earlier introduced data points in Figure 6.16. The polynomial also has an R^2 value of 0,99.

With the non-linearities added to the suspended mass model, its response is ready to be compared with the

produced suspension. The produced suspension response is obtained by performing video analysis. The mower is flipped upside down, where the wheel is lifted such that the suspension is fully extended and then dropped. A feature on the wheel is then tracked to obtain the dynamic response of the suspension. The data handling process will not be elaborated further. The script developed for the video analysis can be seen in Appendix A.6. The resulting suspension is compared to the response from the suspended mass model. The damping coefficient is manually fitted to the response since it is unknown. The two responses can be seen in Figure 6.18.

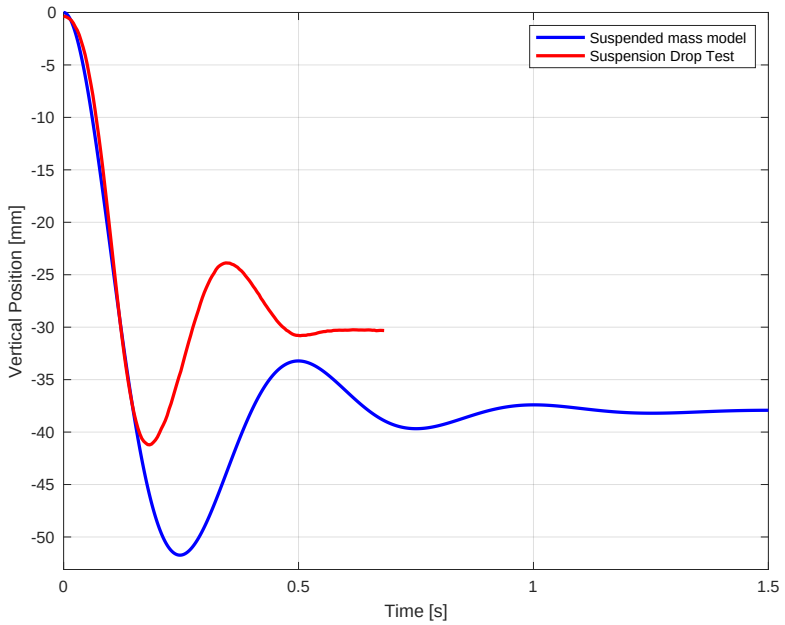

Figure 6.18

Response from dropping the wheel from full suspension travel shown as the red curve and the response from the suspended mass model given the same initial conditions shown as the blue curve.

Here, it can be seen that the suspended mass model is not able to replicate the response of the produced suspension. The primary differences are that the model dynamics are slower, the settling position is different, and the produced suspension has some static and Coulomb friction, causing the oscillations to stop sooner. The slower dynamics and lower settling position are expected to be because the model has a lower spring stiffness than the produced suspension. There is, however, little uncertainty in the measured spring stiffness, as it has been determined experimentally, and polynomials are used in the calculation of spring force. As a result, it is expected that some unknown spring stiffness is affecting the suspension. After some investigation, it is discovered that the bought RC-car strut compresses the air within the cylinder. This works as an air spring and can be the cause of the added spring stiffness. An air spring is then added to the suspended mass system, as can be seen in Figure 6.19.

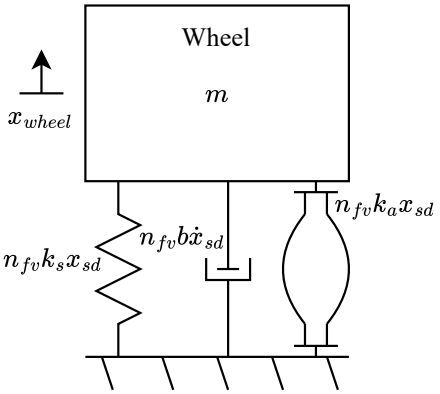

Figure 6.19

Suspended mass model used for half car model validation. It consists of a wheel mass, a spring and a damper from the bought RC-car strut and an air spring caused by the compression of the air volume inside the RC-car damper.

Here, the air spring stiffness k_a has to be determined. The air spring force comes from the pressure in the cylinder chamber acting on both sides of the piston with unequal areas. It is therefore of interest to calculate the increase in pressure with the piston stroke and the resulting force acting on the suspension.

The compression of the air is assumed to be an adiabatic process, due to its higher speed relative to heat exchange with the surroundings. The pressure before and after an adiabatic compression is given by:

$$p_i V_i^\kappa = pV^\kappa => p = \frac{p_i V_i^\kappa}{V^\kappa} \tag{6.6}$$

Here p_i is the initial pressure, V_i is the initial volume, κ is the adiabatic constant equal to 1,4 for air, p is the pressure at a given piston stroke, and V is the air volume at the same given piston stroke. The dimensions of the RC-car damper are measured to obtain the initial air volume and change in volume with piston stroke. The air spring force can then be calculated by the following equation:

$$F_{air} = (p - p_i)(A_{piston} - (A_{piston} - A_{rod})) => F_{air} = (p - p_i)A_{rod} \tag{6.7}$$

Here, F_{air} is the air spring force, A_{piston} is the area of the piston, and A_{rod} is the area of the piston rod. The difference in area on each side of the piston equals the piston rod area. The equation is thereby simplified. The expression for the air spring force is then added to the suspended mass model, and the system equation then becomes:

$$m\ddot{x}_{wheel} = n_{fv}(kx_{sd} - b\dot{x}_{sd} + F_{preload} + F_{air}) - mg \tag{6.8}$$

With the addition of the air spring force, the suspended mass model response is once again compared to the response of the produced suspension as can be seen in Figure 6.20.

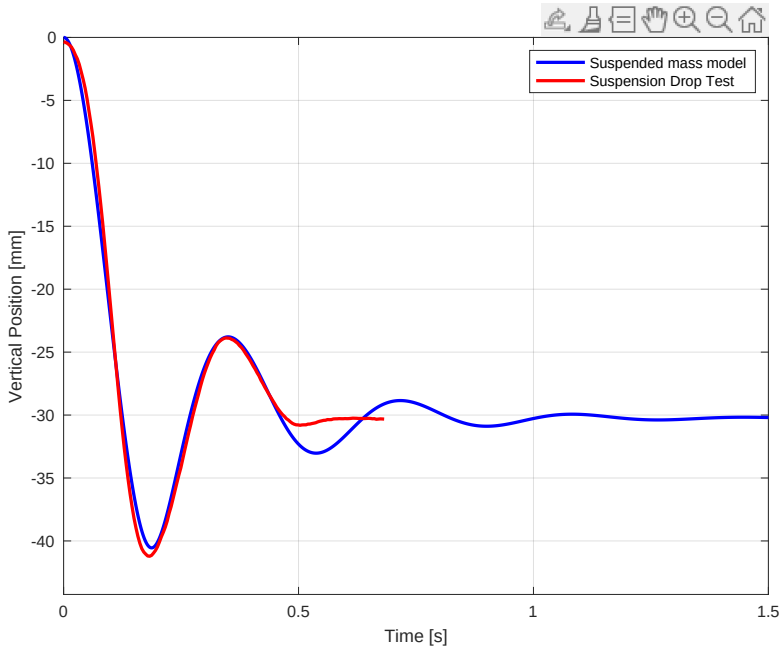

Figure 6.20

Response from dropping the wheel from full suspension travel shown as the red curve and the response from the suspended mass model given the same initial conditions shown as the blue curve. An air spring has been added to the suspended mass model.

The dynamic response of the model now fits well, and the primary difference now seems to be caused by static and Coulomb friction. The damping coefficient is fitted to be 21 N s/m. The suspended mass model's ability to replicate the produced suspension is deemed acceptable, and the half-car model is, as a result, also deemed to be validated. The new additions to model the effects of suspension geometry, air spring force and preload are added to the half-car model. The half-car model is thereby ready to tune the mower's suspension such that a new set of springs can be bought and the oil in the damper can be changed.

Suspension tuning

In this section, the suspension for the mower will be tuned. This will be done to minimise the RMSCE and MACE, as well as to maximise the percentage contact time. These performance parameters were introduced earlier in Section 5.3. The terrain for the simulations will be the same as used and described in Section 5.3. With the input terrain defined, the mower parameters from the produced mower are input to the model. The air spring is kept equal to the one used earlier in the half-car suspension model validation. The parameters can be seen in Table 6.1.

With the input terrain, model parameters and tuning goals determined, the suspension can be tuned. This is done through an iterative process. The spring stiffnesses tested in the simulation are available for purchase with spring dimensions that fit the bought strut. The resulting spring stiffness is 1.460 N/m and damping coefficient is 30 N s/m. This led to a RMSCE of 5,5 mm, MACE of 4,2 mm and a percentage contact time of 49,7 %. In the tuning process, it is experienced that the same level of performance cannot be obtained as earlier with the linear half-car model. The RMSCE is 0,2 mm higher, the MACE is 0,4 mm higher and the percentage contact is 3,4 % lower. The reason behind this is due to the non-linearities added to the model. This is highlighted when the same vehicle parameters are used, where the same performance cannot be obtained. The added non-linearities are thereby unwanted, but the reduction in performance is deemed acceptable.

Model Parameter	Value	Unit
Body Height	0,2	m
l_1	0,591	m
l_2	0,357	m
m_1	3,765	kg
m_2,m_3	1,95	kg
k_3,k_4	15000	N/m
Wheel Diameter	0.2	m

Table 6.1

Body height, l_1 and l_2 are the lengths from the suspension attachment points to the body CoM, m_1 half body mass, m_2 and m_3 are the wheel masses and k_3 and k_4 are the tyre stiffnesses.

To test if the right damping coefficient is obtained with the change of oil, a video analysis experiment will again be performed. This experiment is equivalent to the one performed earlier, where the mower is turned upside down and the wheel is dropped from the suspension's fully extended position. The suspension response where the damping has been tuned to fit the response can be seen in Figure 6.21.

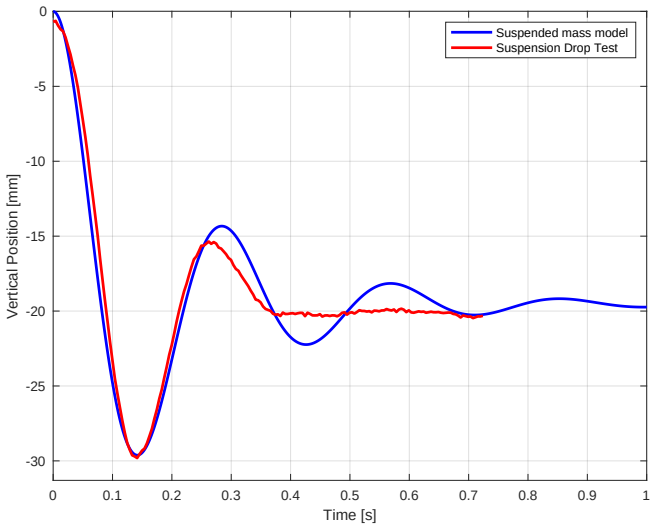

Figure 6.21

Response comparison between the suspension and suspended mass model. The suspension response is after changing springs and the damper oil. The suspended mass model response is after tuning the damping to fit the response.

The damping coefficient is fitted to be 27 N s/m that is 3 N s/m lower than wanted. The difference in amplitude at around 0,28 s and the difference in settling position are deemed to be because of static friction and Coulomb friction, not included in the model. To test if the lower damping is acceptable in terms of performance, a simulation is performed with the damping coefficient set to 27 N s/m. This results in no change in the RMSCE, the MACE being 0,1 mm higher and the percentage contact being 0,65 %pt lower. The reduction in performance is deemed acceptable, and the new oil is kept.

6.4 Remaining Mechanical Design

With the drive unit and suspension completed, it is time to connect the different parts into a final full mower. For this to happen, a few parts are missing, namely brackets for mounting the suspension, the articulation joint for the rear end, some form of chassis, a mounting solution for electronics, as well as mounting for the cutting head. Most of these are simple and, as such, will only be presented without going into detail about the design and process. Afterwards, the design of the rotating rear end will be explained in more detail. During the process of connecting the different parts of the mower, efforts are made to prevent resonance in the chassis. This is done as it was observed with the line marking robot to result in audible noise problems. It has primarily been achieved by avoiding making large flat thin surfaces, such as the chassis of the line marking robot. This aids in keeping the natural frequencies higher and preventing resonance. It has also been a consideration to keep mass as close to the ground as possible, to keep the centre of gravity low, aiding in preventing the mower from tipping over on steep grades. This has been achieved by placing the remaining components such as electronics and batteries as low as possible. In figures 6.22 and 6.23, a CAD model of the fully designed mower can be seen from both sides.

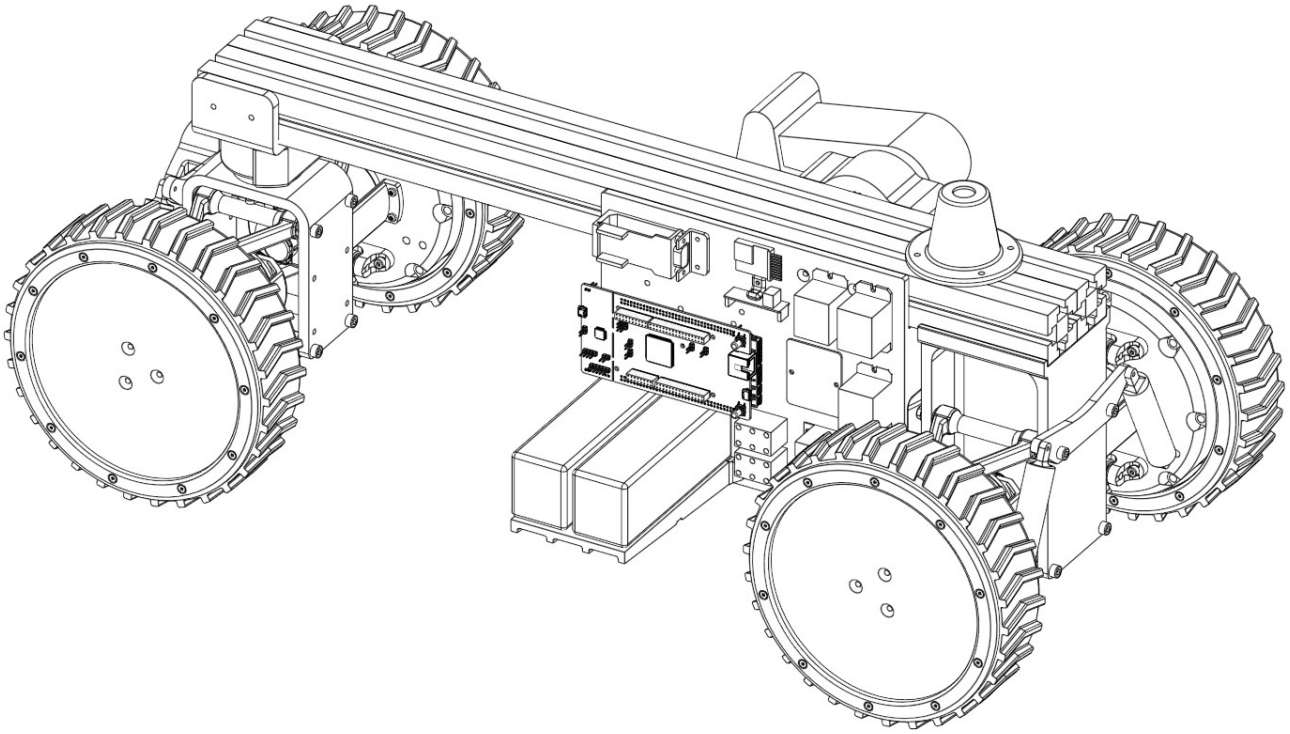

Figure 6.22

Picture of the fully designed mower seen from its right side.

The front bracket is a simple construction made only as a connection point for the front suspension assemblies. On the left side of the mower are the electrical components laid out on a plate. This plate is mounted to the side of a 40 × 80 mm aluminium extrusion, which acts as a chassis for the mower. The batteries are also mounted on this plate, on top of a supporting platform. On the opposite side of the chassis, the cutting head is mounted. The cutting head is mounted in a bracket fastened to the aluminium extrusion. The cutting head can be mounted on this bracket in various positions, allowing for adjustment of the cutting height. It is however only possible to adjust the cutting height in fairly large increments, this does not fulfil the functionality described in the requirements, which states 1 mm increments. The setup does allow for setting a cut height which is within the limits of both semi-rough and fairway, based on this and time limitations the solution is accepted regardless

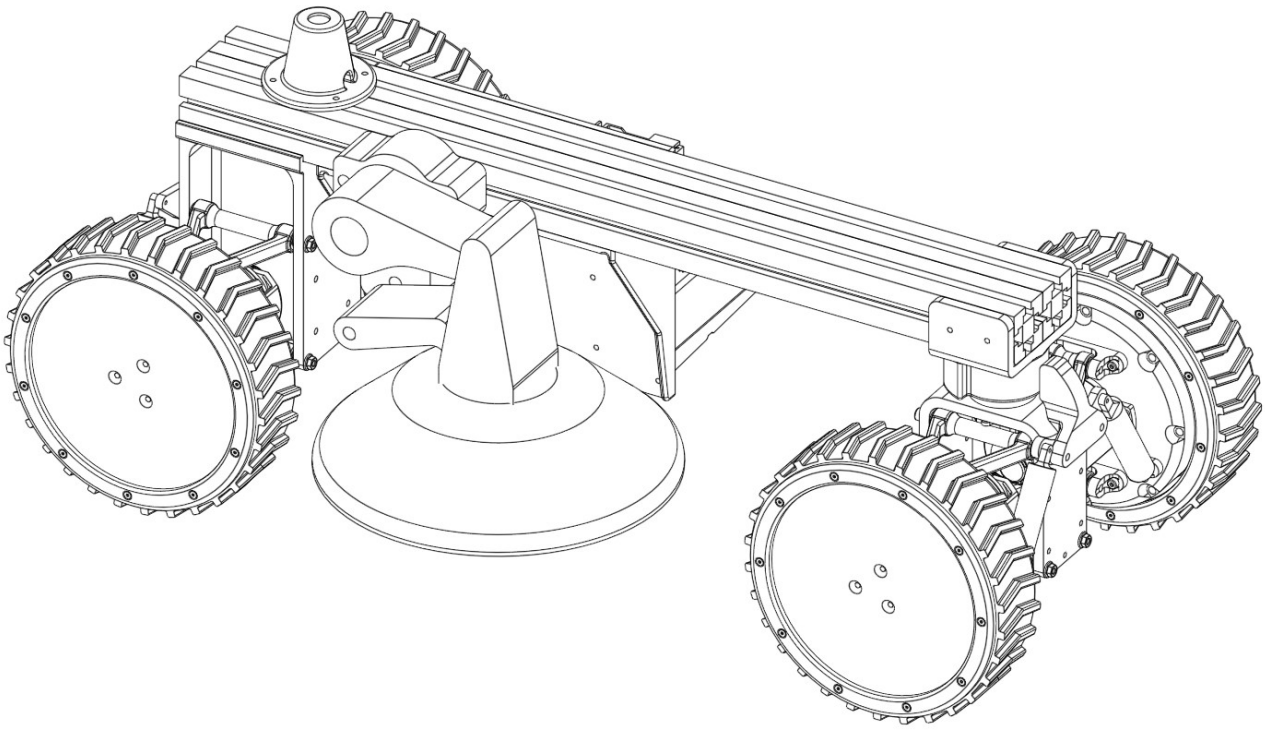

Figure 6.23
Picture of the fully designed mower seen from its left side.

of its inability to fulfil the requirement completely. The important factor for the prototype mower is to test the cutting ability, and the full functionality of the cutting height adjustment does not need to be there for this to happen.

The rear section houses the functionality of the articulation joint, as described in the Section 6.1 and will be presented next. The complete rear assembly can be seen in Figure 6.24.

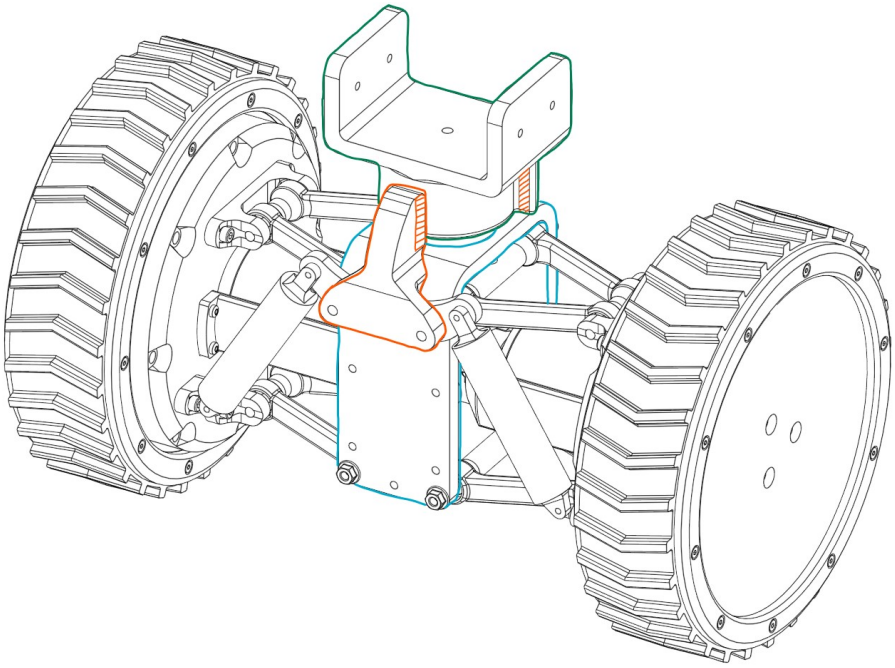

Figure 6.24
The complete rear assembly shown, with rear bracket highlighted in blue, mechanical bump stop highlighted in orange, and the rear articulation joint highlighted in green.

The new parts not discussed in earlier sections are highlighted in the figure. In blue is the rear bracket connecting the suspension assemblies to the articulation joint, which allows the rear end to rotate about its central axis. In green is the articulation bracket, which is mounted on the 40 × 80 mm extrusion mentioned above. The articulation joint is implemented between the rear bracket and the articulation bracket. In orange is highlighted a mechanical bump stop, implemented to prevent the rear end from turning more than 95° in either direction. The contacting surfaces are highlighted with orange hatching. Next, on Figure 6.25, a section view of the articulation joint can be seen.

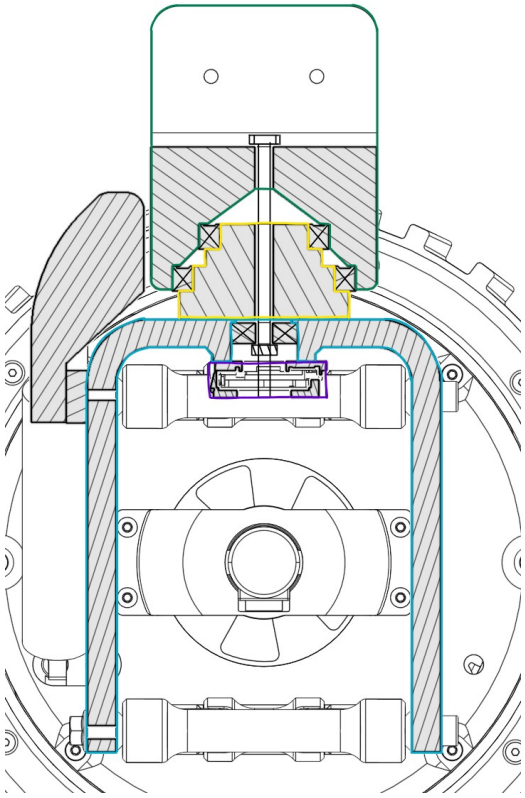

Figure 6.25

A section view of the rear articulation joint. The rear bracket is highlighted in blue, the articulation bracket in green, the encoder in purple, and the bearing pedestal in yellow.

Here, the interface between the rear bracket and the articulation bracket is shown in detail. A bearing pedestal highlighted in yellow, is mounted on the top of the rear bracket using four screws. On this, two bearings are seated on which the articulation bracket sits. There is one additional bearing underneath the rear bracket. This allows the rear bracket to articulate even when a bolt is passed through the entire assembly and used to clamp the assembly together. This staggering of several bearings is done to improve the stiffness of the joint. It has the goal of strengthening the joint as well as minimising the flex of the joint as it bears the load from the torque the wheels apply to the ground. All bearings are marked with a cross in Figure 6.25. Lastly, an encoder is mounted on the underside of the rear bracket. This connects to a fixed bolt passing through the assembly. And as such, the angle of the rear bracket can be measured as it articulates.

With this, the design of the mower is completed. Afterwards, the mower is produced and fully assembled. The majority of parts are 3D printed, making the production process fairly quick. Some iteration is done on specific parts to get tolerances within reason. The result is a functioning gear train and, in general, good functionality of all parts. A picture of the produced mower can be seen in Figure 6.26.

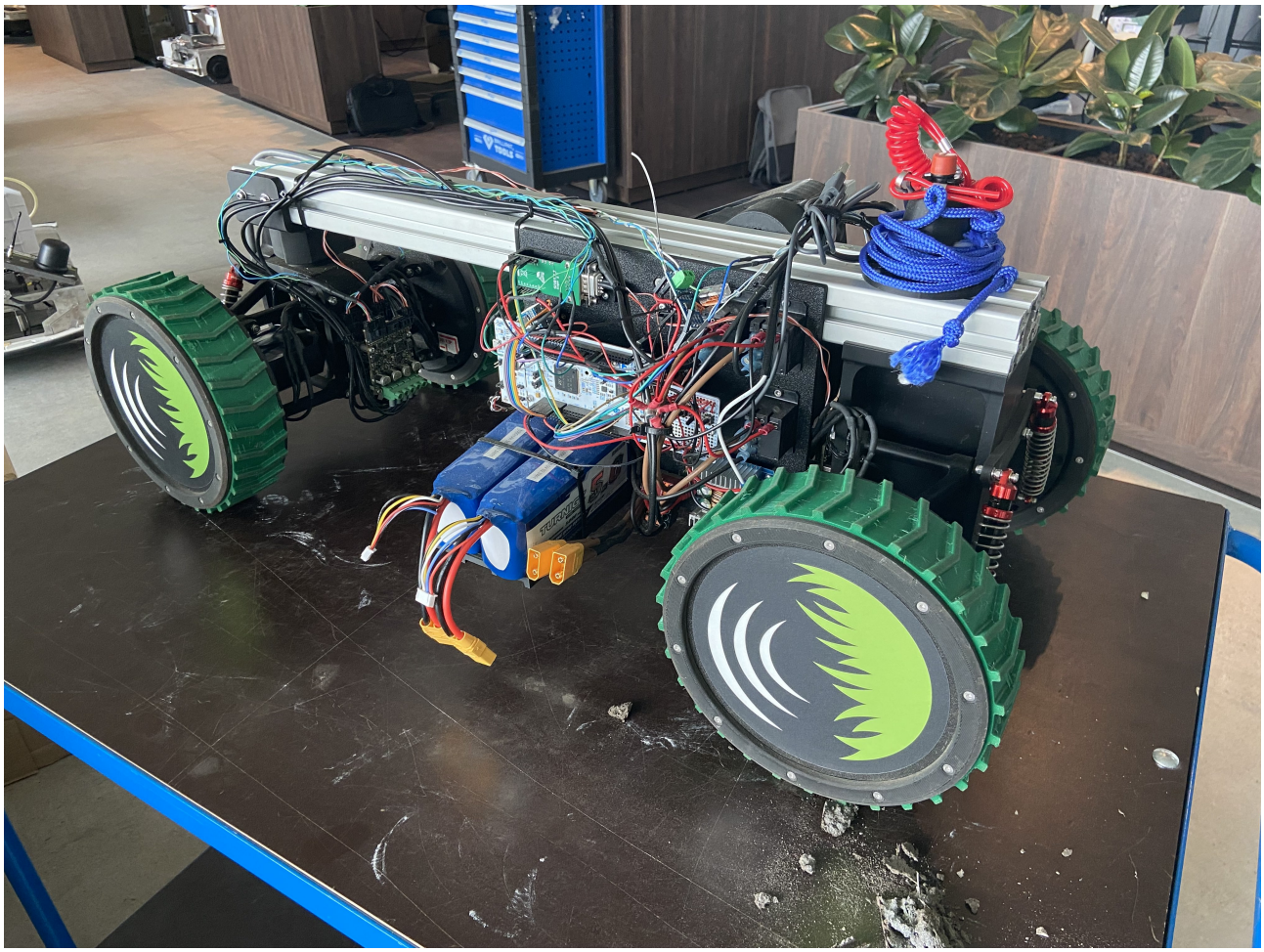

Figure 6.26
A picture of the fully assembled mower.

In the next section, the electronic circuit design for the mower will be presented.

6.5 Electronics

An electronic system needs to be designed to control the newly designed mower. First, an overview of the overall system architecture will be given, after which some specific decisions ensuring safety and robustness will be highlighted. The full schematic can be found in Appendix A.7.

The system will be designed around a Turf Tank supplied STM NUCLEO-F429ZI development board [29], which will handle initialisation, control, data logging and an individual drive for each of the five motors. And as the mower is a mobile platform, the power supply will be based around a battery. The battery chosen is a five-cell LiPo with a nominal voltage of 18,5 V and a capacity of 5 Ah. Two of these batteries are parallelised to double the capacity and increase the runtime. The battery also has a continuous discharge rating of 30 C = 30 A/(A h). With the two packs parallelised, the batteries can approximately supply a continuous power of:

$$2 \cdot 30\,\mathrm{C} \cdot 5\,\mathrm{A\,h} \cdot 18{,}5\,\mathrm{V} \approx 5{,}5\,\mathrm{kW} \tag{6.9}$$

Which should be more than enough for all operating scenarios. Additionally, the STM development board requires a 5 V supply. This will be provided by stepping down the battery voltage using a buck converter.

To measure the articulation angle and motor positions, encoders are used. For the articulation joint, a 14-bit absolute encoder is used to avoid a calibration procedure at startup. For the motors, 13-bit incremental encoders are used, the outputs of which are routed to both the μC and the drives. This is done to minimise latency on all measurements, as the drives would otherwise have to transfer the data to the μC through some sort of digital communication.

With the overall system architecture explained, the decisions ensuring safety and robustness will be explained next

Safety

In case the system becomes unstable or an error occurs, power to the drives should be easy to cut remotely to avoid potential accidents. Additionally, to avoid errors from faulty programming, the system should be completely electromechanical. Based on these requirements, the following safety circuit in Figure 6.27 is designed.

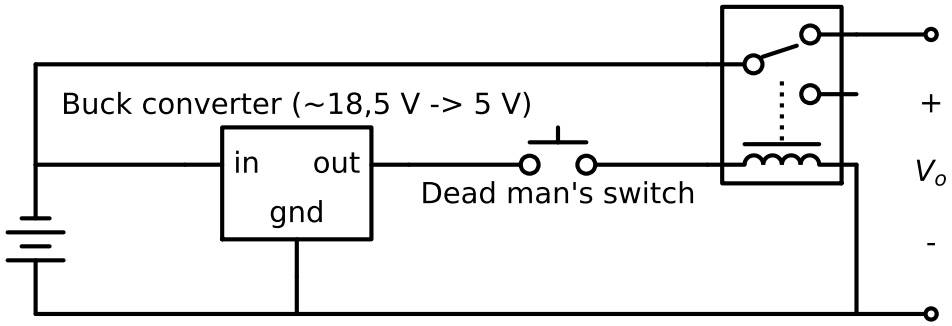

Figure 6.27
The state of the safety circuit when the dead man's key is present.

The battery supply to the drives is routed through a relay, which is controlled by a switch. A dead man's switch is chosen to facilitate remote operation. When the dead man's key is inserted, the dead man's switch is open and the relays are not energised. In this state, which is the one shown in Figure 6.27, the batteries are connected to the drives. When the dead man's key is removed by pulling the string, the relays are energised and the drives are disconnected from the battery.

The drives themselves are also chosen with safety in mind. The choice falls on ODrives [30], as they provide built-in motor and DC-bus current limiting, protecting the motors and batteries and runtime error checking, such that they stop if an encoder is disconnected, etc.. They also facilitate easy setup and debugging through Python and a graphical user interface (GUI).

To communicate between the ODrives and the μC controller area network bus (CAN bus) is used. ODrive recommends this method, and the μC has a built-in CAN bus peripheral, simplifying the implementation and removing additional responsibilities from the software. CAN bus is also a differential protocol, making it more noise resistant.

Control

To control the mower, a 2-channel radio transmitter-receiver combo for an RC-car will be used. The RC-transmitter can be seen in Figure 6.28 respectively.

Figure 6.28
RC-transmitter.

The wireless communication between the two units is set up from the factory, such that the transmitter just needs four AA-batteries and the receiver a 5 V supply. The receiver then outputs two 60 Hz PWM signals with duty cycles from ≈ 6 % to 12 % depending on the position of the trigger and wheel.

Data logging

Data logging is needed on the mower. Without data logging, debugging becomes difficult, and presentation and analysis of data and performance become complicated. The data logging frequency should follow the control loop frequency to be able to visualise the control dynamics. This is expected to lie in the range of 250 Hz to 1.000 Hz. It is also important that the data logging is not limited to a timespan that is too short. It is expected that tests up to one hour in duration will be performed. The extraction of data should also not be too time-consuming. With these wishes stated, a data logging method is selected next.

It is not possible to log data directly to a computer through serial communication, as this requires a physical connection between the μC and the computer, which is undesirable for a mobile platform. As a result, the data needs to either be transmitted wirelessly or locally saved on the mower and extracted later. The second approach is chosen due to a lack of knowledge on wireless communication and possible reliability problems. The local storage on the μC is very limited, though, as it only has 2 MiB of flash memory and 256 KiB of random-access memory (RAM), some of which will be taken up by the program itself. Assuming 16 32 b values are logged each control loop iteration, this results in a total of 16.384 sample points with 2 MiB of storage. With a sample rate of 250 Hz, this amounts to ≈ 65,5 s. This is a very short time and would require very frequent data extraction, which is inconvenient outside a fixed test bench. The storage is thereby expanded with a 32 GiB SD card using the μC's built-in SD card peripheral and an SD card slot.

This newly designed electronic system will be utilised to control the mower, but first, a model and controller have to be derived. This will be done in the next section.

6.6 In-plane Dynamic Model & Control

The goal for the control is to simplify and facilitate potential future autonomous integration into the existing Turf Tank robot control system explained in Section 2.1, which will also include development of a new MPC. However, in this project, the control will receive references from the RC transmitter mentioned in Section 6.5 operated by a user manually, as automation is outside the scope of the project.

The overall goal for the resulting closed-loop dynamics is decoupling and linearity. These goals stem from the currently used MPC robot controller implemented on the Turf Tank Two/Light, also explained in Section 2.1, where it simplifies the control problem by reducing the model error. Currently, Turf Tank uses individual wheel velocity control on the Turf Tank Two/Light, but this does not result in linear and decoupled dynamics regardless of the current linear and angular robot velocity as seen in Figure 3.1. Due to this, a centralised control structure will be utilised to compensate for system non-linearities and coupling. This controller should also result in linear closed-loop dynamics.

Due to the requirements 20 and 21, concerning terrain damage and wheel slip, a slip controller will be added to reduce the chances of terrain damage and excessive slip. This will not completely prevent slip, as no direct measurement of vehicle velocity is available, and the actual slip is therefore not measurable. A simpler model-based approach will therefore be taken. Ideally, slip would be completely eliminated, but this is sometimes not physically possible. If the mower is immobilised due to insufficient traction, it should stop trying to climb the grade, as it can only result in slip and terrain damage. This would be achieved with some automation logic, which will not be covered.

To facilitate designing the controller, a state-space model of the mower will be derived. The derivation will follow the Lagrangian method used in [5]. The method starts by formulating the constraints and the kinematics on matrix-vector form. The energies are then formulated and constrained EoM can be formulated. The system is then order-reduced by unconstraining it using the kinematics. The unconstrained EoM can then be manipulated to achieve their state-space form. The derivation is based on the simplified top-down diagram of the mower seen in Figure 6.29.

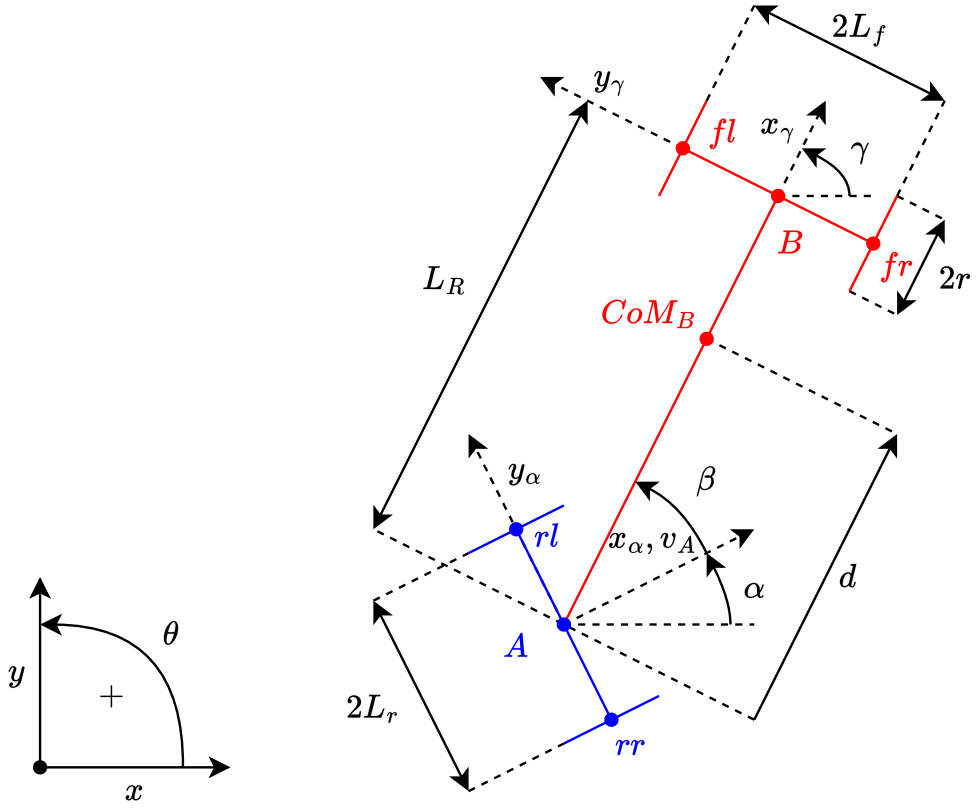

Figure 6.29

L_R is the wheelbase of the robot, $2L_r$ is the rear track width, $2L_f$ is the front track width, r is the wheel radius, point A and B are the centre points of each axle, d is offset of the CoM of body B from point A, points rl, rr, fl, fr are the contact points for each wheel, α is the orientation angle of the rear body in a fixed reference frame, γ is the orientation of the front body in the same fixed reference frame and β is the articulation angle.

Before modelling, some simplifying assumptions are made:

- Pure rolling/no longitudinal slip
- No lateral movement of each axle/no lateral slip
- Wheels are assumed perfectly circular and infinitesimally thin, such that the contact line/patch reduces to a point and the radius doesn't vary with the angle

- CoM_A is located at A
- CoM_B is not offset laterally
- Wheel CoMs are located above their contact points
- No damping

The assumptions of no lateral and longitudinal slip will not be fulfilled in all cases, but they will be fulfilled in the majority of cases, and the controller will therefore build on this assumption. The control should not become unstable in the case of slip, though. The CoM assumptions will reduce the number of model parameters and simplify the model. This should be accurate, as this has been accounted for in the drive unit design in Section 6.2. Lastly, no damping is assumed due to the large uncertainty and variation over time and because the model will be used for controller design and not an accurate simulation. It will therefore be a disturbance that the controller should handle.

The desired variables for control and thereby also the model formulation, are the linear velocity of point A, v_A, and the articulation angle β. v_A is chosen as the means to control the velocity of the mower, and β is chosen to control the turning radius. The model will initially be formulated in eight generalised coordinates, along with the constraints, after which it will be reduced to an unconstrained formulation only in the control variables. These generalised coordinates are listed below.

$$\mathbf{q} = \begin{bmatrix} x_A & y_A & \alpha & \gamma & \phi_{rl} & \phi_{rr} & \phi_{fl} & \phi_{fr} \end{bmatrix}^T \tag{6.10}$$

Where x_A and y_A are the coordinates of A in a fixed reference frame, α is the orientation of body A, γ is the orientation of body B and ϕ_{xx}, $xx = \begin{bmatrix} rl & rr & fl & fr \end{bmatrix}$ are the wheel rotation angles.

To express the constraints, the coordinates of A, B, rl, rr, fl, fr in the fixed reference frame are expressed as a function of the generalised coordinates.

$$\mathbf{r}_A = \begin{bmatrix} x_A & y_A \end{bmatrix}^T \tag{6.11}$$

$$\mathbf{r}_{rl} = \mathbf{r}_A + \mathbf{R}_1 \begin{bmatrix} 0 & L_r \end{bmatrix}^T \tag{6.12}$$

$$\mathbf{r}_{rr} = \mathbf{r}_A + \mathbf{R}_1 \begin{bmatrix} 0 & -L_r \end{bmatrix}^T \tag{6.13}$$

$$\mathbf{r}_B = \mathbf{r}_A + \mathbf{R}_2 \begin{bmatrix} L_R & 0 \end{bmatrix}^T \tag{6.14}$$

$$\mathbf{r}_{fl} = \mathbf{r}_A + \mathbf{R}_2 \begin{bmatrix} L_R & L_f \end{bmatrix}^T \tag{6.15}$$

$$\mathbf{r}_{fr} = \mathbf{r}_A + \mathbf{R}_2 \begin{bmatrix} L_R & -L_f \end{bmatrix}^T \tag{6.16}$$

Where

$$\mathbf{R}_1 = \begin{bmatrix} \cos(\alpha) & -\sin(\alpha) \\ \sin(\alpha) & \cos(\alpha) \end{bmatrix} \tag{6.17}$$

$$\mathbf{R}_2 = \begin{bmatrix} \cos(\gamma) & -\sin(\gamma) \\ \sin(\gamma) & \cos(\gamma) \end{bmatrix} \tag{6.18}$$

These positions are then differentiated wrt. time to get the velocity of each point expressed in the generalised coordinates $\dot{\mathbf{r}}_A$, $\dot{\mathbf{r}}_{rl}$, $\dot{\mathbf{r}}_{rr}$, $\dot{\mathbf{r}}_B$, $\dot{\mathbf{r}}_{fl}$, $\dot{\mathbf{r}}_{fr}$. Additionally, some unit vectors are defined to represent the x and y

directions in the two local body frames represented by eqns. (6.17) and (6.18).

$$\mathbf{x}_\alpha = \begin{bmatrix} \cos(\alpha) & \sin(\alpha) \end{bmatrix}^T \tag{6.19}$$

$$\mathbf{y}_\alpha = \begin{bmatrix} -\sin(\alpha) & \cos(\alpha) \end{bmatrix}^T \tag{6.20}$$

$$\mathbf{x}_\gamma = \begin{bmatrix} \cos(\gamma) & \sin(\gamma) \end{bmatrix}^T \tag{6.21}$$

$$\mathbf{y}_\gamma = \begin{bmatrix} -\sin(\gamma) & \cos(\gamma) \end{bmatrix}^T \tag{6.22}$$

These will be utilised to express the no longitudinal and lateral slip constraints.

The lateral movement constraint means that point A cannot move in the direction of $\mathbf{y}_\alpha$ and similarly, point B in the direction of $\mathbf{y}_\gamma$. This is expressed via a dot product between the point's velocity and a vector perpendicular to the corresponding body's orientation.

$$\dot{\mathbf{r}}_A \cdot \mathbf{y}_\alpha = 0 \tag{6.23}$$

$$\dot{\mathbf{r}}_B \cdot \mathbf{y}_\gamma = 0 \tag{6.24}$$

Similarly, the pure rolling constraints can also be expressed as the dot product between the velocity of the wheel's contact point and a vector in the orientation of the body on which the wheel is mounted. This quantity is equal to the wheel's angular velocity multiplied by the radius.

$$\begin{aligned} \dot{\mathbf{r}}_{xx} \cdot \mathbf{x}_\alpha = r\dot{\phi}_{xx} \Leftrightarrow \dot{\mathbf{r}}_{xx} \cdot \mathbf{x}_\alpha - r\dot{\phi}_{xx} = 0, \qquad xx = rl, rr \\ \dot{\mathbf{r}}_{xx} \cdot \mathbf{x}_\gamma = r\dot{\phi}_{xx} \Leftrightarrow \dot{\mathbf{r}}_{xx} \cdot \mathbf{x}_\gamma - r\dot{\phi}_{xx} = 0, \qquad xx = fl, fr \end{aligned} \tag{6.25}$$

Resulting in a total of six constraints.

As all these constraints are linear in the generalised velocities, they can be expressed in the following form.

$$\mathbf{\Lambda}\dot{\mathbf{q}} = 0 \tag{6.26}$$

$$\mathbf{\Lambda} = \begin{bmatrix} -\sin(\alpha) & \cos(\alpha) & 0 & 0 & 0 & 0 & 0 & 0 \\ -\sin(\gamma) & \cos(\gamma) & 0 & L_R & 0 & 0 & 0 & 0 \\ \cos(\alpha) & \sin(\alpha) & -L_r & 0 & -r & 0 & 0 & 0 \\ \cos(\alpha) & \sin(\alpha) & L_r & 0 & 0 & -r & 0 & 0 \\ \cos(\gamma) & \sin(\gamma) & 0 & -L_f & 0 & 0 & -r & 0 \\ \cos(\gamma) & \sin(\gamma) & 0 & L_f & 0 & 0 & 0 & -r \end{bmatrix} \tag{6.27}$$

Due to these six constraints, it is also possible to express all the generalised velocities with a reduced set of velocities. These velocities are chosen based on the desired control variables v_A and β to be $\boldsymbol{\eta} = \begin{bmatrix} v_A & \dot{\beta} \end{bmatrix}^T$.

The generalised velocities $\dot{\mathbf{q}}$ can then be expressed in the following manner

$$\dot{\mathbf{q}} = \mathbf{S}\boldsymbol{\eta} \tag{6.28}$$

$$\begin{bmatrix} \dot{x}_A \\ \dot{y}_A \\ \dot{\alpha} \\ \dot{\gamma} \\ \dot{\phi}_{rl} \\ \dot{\phi}_{rr} \\ \dot{\phi}_{fl} \\ \dot{\phi}_{fr} \end{bmatrix} = \begin{bmatrix} \cos(\alpha) & 0 \\ \sin(\alpha) & 0 \\ \frac{\sin(\gamma-\alpha)}{L_R} & -1 \\ \frac{\sin(\gamma-\alpha)}{L_R} & 0 \\ \frac{1}{r} - \frac{L_r \sin(\gamma-\alpha)}{L_R r} & \frac{L_r}{r} \\ \frac{1}{r} + \frac{L_r \sin(\gamma-\alpha)}{L_R r} & -\frac{L_r}{r} \\ \frac{\cos(\gamma-\alpha)}{r} - \frac{L_f \sin(\gamma-\alpha)}{L_R r} & 0 \\ \frac{\cos(\gamma-\alpha)}{r} + \frac{L_f \sin(\gamma-\alpha)}{L_R r} & 0 \end{bmatrix} \begin{bmatrix} v_A \\ \dot{\beta} \end{bmatrix}$$

The $\mathbf{S}$ matrix represents the kinematics of the mower. The derivation is explained in Appendix A.8.

It can also be shown that the matrix $\mathbf{S}$ is in the null space of $\boldsymbol{\Lambda}$, meaning $\boldsymbol{\Lambda}\mathbf{S} = \mathbf{S}^T\boldsymbol{\Lambda}^T = 0$. This property will be used later to transform the constrained EoM to an unconstrained form by eliminating the constraint term $\boldsymbol{\Lambda}\dot{\mathbf{q}}$.

To derive the EoM, a Lagrangian approach will be taken. Lagrange's equations of motion with generalised forces and torques, and constraints are given by:

$$\begin{aligned} \frac{\mathrm{d}}{\mathrm{d}t}\left(\frac{\partial L}{\partial \dot{\mathbf{q}}}\right) - \frac{\partial L}{\partial \mathbf{q}} &= \mathbf{p} - \boldsymbol{\Lambda}^T\boldsymbol{\lambda} \\ \mathbf{p} &= \begin{bmatrix} 0 & 0 & 0 & 0 & \mathcal{T}_{rl} & \mathcal{T}_{rr} & \mathcal{T}_{fl} & \mathcal{T}_{fr} \end{bmatrix}^T \end{aligned} \tag{6.29}$$

Where $L = T - V$, T is the total kinetic energy, V is the total potential energy, $\boldsymbol{\lambda}$ is the vector of Lagrange multipliers with one for each constraint, representing the force from each constraint and $\mathcal{T}_{xx}$ are the wheel torques. Due to the assumption of in-plane movement, there is no change in potential energy during operation and therefore $L = T$.

The kinetic energy will now be expressed, starting with the wheels

$$T_{xx} = \frac{1}{2}\left(m_w \dot{\mathbf{r}}_{xx}^T \dot{\mathbf{r}}_{xx} + I_m \dot{\alpha}^2 + I_w \dot{\phi}_{xx}^2\right), \qquad xx = rl, rr \tag{6.30}$$

$$T_{xx} = \frac{1}{2}\left(m_w \dot{\mathbf{r}}_{xx}^T \dot{\mathbf{r}}_{xx} + I_m \dot{\gamma}^2 + I_w \dot{\phi}_{xx}^2\right), \qquad xx = fl, fr \tag{6.31}$$

Where m_w is the total mass of the wheel including the gearbox and motor, I_m is their MoI about an axis through the diameter and I_w is their rotational MoI.

Next, the kinetic energy of the rear body

$$T_r = \frac{1}{2}\left(m_r \dot{\mathbf{r}}_A^T \dot{\mathbf{r}}_A + I_r \dot{\alpha}^2\right) \tag{6.32}$$

Where m_r is the mass of the rear body and I_r is its' MoI about its' CoM.

Lastly, the front body. To express the kinetic energy, a vector to the front body CoM is defined.

$$\mathbf{r}_c = \mathbf{r}_A + \mathbf{R}_2 \begin{bmatrix} d & 0 \end{bmatrix}^T \tag{6.33}$$

The kinetic energy can then be expressed as

$$T_f = \frac{1}{2}\left(m_f \dot{\mathbf{r}}_c^T \dot{\mathbf{r}}_c + I_f \dot{\gamma}^2\right) \tag{6.34}$$

Where m_f is the mass of the front body and I_r is its' MoI about its' CoM.

The total energy is then the sum of all these individual energies

$$T = T_r + T_f + T_{rl} + T_{rr} + T_{fl} + T_{fr} \tag{6.35}$$

$$= \left(\frac{m_f}{2} + \frac{m_r}{2} + 2m_w\right)\left(\dot{x}_A^2 + y_A^2\right) + \frac{I_w}{2}\left(\dot{\phi}_{rl}^2 + \dot{\phi}_{rr}^2 + \dot{\phi}_{fl}^2 + \dot{\phi}_{fr}^2\right) \tag{6.35a}$$

$$-\left(2L_R m_w + dm_f\right)\sin(\gamma)\,\dot{x}_A\dot{\gamma} + \left(2L_R m_w + dm_f\right)\cos(\gamma)\,\dot{y}_A\dot{\gamma} \tag{6.35b}$$

$$+\left(m_w {L_r}^2 + I_m + \frac{I_r}{2}\right)\dot{\alpha}^2 + \left(m_w L_R^2 + m_w {L_f}^2 + \frac{m_f d^2}{2} + \frac{I_f}{2} + I_m\right)\dot{\gamma}^2 \tag{6.35c}$$

Utilising Eqn. (6.29) the constrained EoM become

$$m\ddot{x}_A - m_d\left(\sin(\gamma)\,\ddot{\gamma} + \cos(\gamma)\,\dot{\gamma}^2\right) = \lambda_1\sin(\alpha) + \lambda_2\sin(\gamma) - \cos(\alpha)\left(\lambda_3 + \lambda_4\right) - \cos(\gamma)\left(\lambda_5 + \lambda_6\right) \tag{6.36}$$

$$m\ddot{y}_A + m_d\left(\cos(\gamma)\,\ddot{\gamma} - \sin(\gamma)\,\dot{\gamma}^2\right) = -\lambda_1\cos(\alpha) - \lambda_2\cos(\gamma) - \sin(\alpha)\left(\lambda_3 + \lambda_4\right) - \sin(\gamma)\left(\lambda_5 + \lambda_6\right) \tag{6.37}$$

$$I_A\ddot{\alpha} = L_r\left(\lambda_3 - \lambda_4\right) \tag{6.38}$$

$$m_d\left(-\sin(\gamma)\,\ddot{x}_A + \cos(\gamma)\,\ddot{y}_A\right) + I_B\ddot{\gamma} = L_f\left(\lambda_5 - \lambda_6\right) - L_R\lambda_2 \tag{6.39}$$

$$I_w\ddot{\phi}_{rl} = \mathcal{T}_{rl} + \lambda_3 r \tag{6.40}$$

$$I_w\ddot{\phi}_{rr} = \mathcal{T}_{rr} + \lambda_4 r \tag{6.41}$$

$$I_w\ddot{\phi}_{fl} = \mathcal{T}_{fl} + \lambda_5 r \tag{6.42}$$

$$I_w\ddot{\phi}_{fr} = \mathcal{T}_{fr} + \lambda_6 r \tag{6.43}$$

Where $m = m_f + m_r + 4m_w$, $m_d = 2L_R m_w + dm_f$, $I_A = 2m_w {L_r}^2 + 2I_m + I_r$ and $I_B = 2m_w {L_R}^2 + 2m_w {L_f}^2 + m_f d^2 + I_f + 2I_m$.

The EoM are put on the following matrix-vector equation form, which will be used for reformulation:

$$\mathbf{H}\ddot{\mathbf{q}} + \mathbf{V}\dot{\mathbf{q}} = \mathbf{E}\mathbf{u} - \mathbf{\Lambda}^T\boldsymbol{\lambda} \tag{6.44}$$

To reduce the equations, they are first pre-multiplied by $\mathbf{S}^T$ to eliminate the constraint term $\mathbf{\Lambda}^T\dot{\mathbf{q}}$, due to $\mathbf{S}$ being in the null space of $\mathbf{\Lambda}$, as explained earlier. Then $\ddot{\mathbf{q}}$ is substituted for $\frac{\mathrm{d}}{\mathrm{d}t}(\mathbf{S}\eta)$ and $\dot{\mathbf{q}}$ for $\mathbf{S}\eta$. Utilising this allows the EoM to be put on unconstrained form:

$$\bar{\mathbf{H}}\dot{\boldsymbol{\eta}} + \bar{\mathbf{V}}\boldsymbol{\eta} = \bar{\mathbf{E}}\mathbf{u} \tag{6.45}$$

$$\bar{\mathbf{H}} = \mathbf{S}^T\mathbf{H}\mathbf{S}, \quad \bar{\mathbf{V}} = \mathbf{S}^T\left(\mathbf{H}\dot{\mathbf{S}} + \mathbf{V}\mathbf{S}\right), \quad \bar{\mathbf{E}} = \mathbf{S}^T\mathbf{E}$$

This also reduced the system to just two equations from the previous eight.

These equations are then solved for $\dot{\boldsymbol{\eta}}$ and put on the form $\dot{\boldsymbol{\eta}} = \mathbf{f}(\boldsymbol{\eta},\beta,\mathbf{u})$, utilising that $\beta = \gamma - \alpha$ and $\dot{\beta} = \dot{\gamma} - \dot{\alpha}$.

$$\dot{\boldsymbol{\eta}} = \mathbf{f}(\boldsymbol{\eta},\beta,\mathbf{u}) = -\bar{\mathbf{H}}^{-1}\bar{\mathbf{V}}\boldsymbol{\eta} + \bar{\mathbf{H}}^{-1}\bar{\mathbf{E}}\mathbf{u} \tag{6.46}$$

$$-\bar{\mathbf{H}}^{-1}\bar{\mathbf{V}}\boldsymbol{\eta} = \begin{bmatrix} -\frac{N_{v_A}(\beta)}{D(\beta)} v_A\dot{\beta} \\ \frac{N_{\dot{\beta}}(\beta)}{D(\beta)} v_A\dot{\beta} \end{bmatrix} \tag{6.47}$$

The system dynamics represented by $-\bar{\mathbf{H}}^{-1}\bar{\mathbf{V}}\boldsymbol{\eta}$ depend on v_A, $\dot{\beta}$ and β, while the input effects $\bar{\mathbf{H}}^{-1}\bar{\mathbf{E}}$ only depends on β. The full explicit equations can be viewed by running the MATLAB script in Appendix A.9

Lastly, an integrator is added to include β as a state in the model, such that the model can be put on general non-linear state space form $\dot{\mathbf{x}} = \mathbf{f}(\mathbf{x},\mathbf{u})$, where $\mathbf{x} = \begin{bmatrix} v_A & \dot{\beta} & \beta \end{bmatrix}^T$. This model can also be written on $\dot{\mathbf{x}} = \mathbf{A}(\mathbf{x})\mathbf{x} + \mathbf{B}(\mathbf{x})\mathbf{u}$ form which will be used for controller design.

Before a controller is designed, it is desired to validate the model. A simulation is performed first to check if the model is energy-conserving, which it should be since no damping is included. This is verified to be the case. Actual validation of the model is complicated, though for multiple reasons. Firstly, the mower is difficult to control safely in open loop, due to its unconstrained nature. Secondly, because the system behaves chaotically. During testing, the system trajectory was observed to be extremely sensitive to initial conditions and slight differences in input amplitudes, making it very difficult to compare measurements with simulation results. A controller will therefore be designed first. The model will then be validated by checking if the desired dynamics match the observed dynamics.

Control

Another problem also needs to be addressed before a controller can be designed. As mentioned earlier, there are only two control variables, but four inputs, meaning the system is over-actuated. This means the control problem is underdetermined, and infinite combinations of the inputs can produce the same output. This problem can be solved using multiple methods, like optimisation or defining a map from two variables to the four inputs. The latter is chosen for its' relative simplicity. The pseudo-input vector $\mathbf{o}$ with two entries, along with a map from the pseudo-inputs to the wheel torques, is defined.

$$\mathbf{u} = \mathbf{M}\mathbf{o}$$
$$= \begin{bmatrix} \frac{1}{r} - \frac{L_r \sin(\beta)}{L_R r} & \frac{L_r}{r} \\ \frac{1}{r} + \frac{L_r \sin(\beta)}{L_R r} & -\frac{L_r}{r} \\ \frac{\cos(\beta)}{r} - \frac{L_f \sin(\beta)}{L_R r} & 0 \\ \frac{\cos(\beta)}{r} + \frac{L_f \sin(\beta)}{L_R r} & 0 \end{bmatrix} \begin{bmatrix} \dot{v}_u \\ \ddot{\beta}_u \end{bmatrix} \tag{6.48}$$

The first pseudo-input $\dot{v}_u$ is a sort of net drive force, which is distributed based on each wheel's distance from the instantaneous centre of rotation (ICR), which is defined by β. The second pseudo-input is the torque about the articulation joint. The mapping is derived from the wheel velocity kinematics described in Eqn. (6.28). Whether this mapping is optimal in any way or simplifies the system in any regard is unknown. This map results in a new input matrix $\mathbf{B_o}$ given by $\mathbf{BM}$. With these new pseudo-inputs, the system now only has two inputs and is no longer over-actuated. A controller can thereby be designed.

To design the controller, a physically motivated feedback linearisation approach will be utilised. This approach is inspired by [31] and is implemented successfully in [11]. The method derives a potentially non-linear state-dependent controller that results in decoupled linear closed-loop dynamics. The motor dynamics are ignored in the controller design, as the drives are tuned to have a current control bandwidth of 1.000 rad/s, which is more than an order of magnitude larger than the desired system bandwidths. Whether this is valid will be evaluated later.

Before the controller is designed, an error integrator is added to each control variable to remove steady-state error and compensate for disturbances. The structure of the resulting open-loop system can be seen in Eqn. (6.49).

$$\begin{aligned}\dot{\mathbf{x}}_z &= \mathbf{A}_z\mathbf{x}_z + \mathbf{B}_z\mathbf{o} + \mathbf{Z}\mathbf{r} \\ &= \begin{bmatrix} A_{11} & 0 & 0 & 0 & 0 \\ A_{21} & 0 & 0 & 0 & 0 \\ 0 & 1 & 0 & 0 & 0 \\ -1 & 0 & 0 & 0 & 0 \\ 0 & 0 & -1 & 0 & 0 \end{bmatrix} \begin{bmatrix} v_A \\ \dot{\beta} \\ \beta \\ z_{v_A} \\ z_\beta \end{bmatrix} + \begin{bmatrix} B_{11} & B_{12} \\ B_{21} & B_{22} \\ 0 & 0 \\ 0 & 0 \\ 0 & 0 \end{bmatrix} \begin{bmatrix} \dot{v}_u \\ \ddot{\beta}_u \end{bmatrix} + \begin{bmatrix} 0 & 0 \\ 0 & 0 \\ 0 & 0 \\ 1 & 0 \\ 0 & 1 \end{bmatrix} \begin{bmatrix} r_{v_A} \\ r_\beta \end{bmatrix} \\ \mathbf{A}_z = \begin{bmatrix} \mathbf{A} & \mathbf{0} \\ -\mathbf{C} & \mathbf{0} \end{bmatrix}, \quad \mathbf{C} &= \begin{bmatrix} 1 & 0 & 0 \\ 0 & 0 & 1 \end{bmatrix}, \quad \mathbf{B}_z = \begin{bmatrix} \mathbf{B}\mathbf{M} \\ \mathbf{0} \end{bmatrix}\end{aligned} \tag{6.49}$$

Where subscript z indicates extended due to the integrators. z_{v_A} and z_β are the control variable integrator states and $\mathbf{r}$ is the reference vector.

The coefficients A_{11}, A_{21}, B_{11}, B_{12}, B_{21} and B_{22} are all state-dependent, but this dependency is ignored during the controller design as part of the method.

The following control law is then used to close the loop:

$$\mathbf{o} = \mathbf{F}\mathbf{r} - \mathbf{K}\mathbf{x}_z \tag{6.50}$$

Where $\mathbf{r}$ is the reference vector, $\mathbf{F}$ is the 2×2 reference gain matrix and $\mathbf{K}$ is the 2×5 feedback gain matrix. The total number of controller parameters is therefore 14.

This results in the following closed-loop system:

$$\dot{\mathbf{x}}_z = \mathbf{A}_{cl}\mathbf{x}_z + \mathbf{B}_{cl}\mathbf{r}, \qquad \mathbf{A}_{cl} = \mathbf{A}_z - \mathbf{B}_z\mathbf{K}, \qquad \mathbf{B}_{cl} = \mathbf{B}_z\mathbf{F} + \mathbf{Z} \tag{6.51}$$

$$\dot{\mathbf{x}}_z = \begin{bmatrix} A_{cl,11} & A_{cl,12} & A_{cl,13} & A_{cl,14} & A_{cl,15} \\ A_{cl,21} & A_{cl,22} & A_{cl,23} & A_{cl,24} & A_{cl,25} \\ 0 & 1 & 0 & 0 & 0 \\ -1 & 0 & 0 & 0 & 0 \\ 0 & 0 & -1 & 0 & 0 \end{bmatrix} \begin{bmatrix} v_A \\ \dot{\beta} \\ \beta \\ z_{v_A} \\ z_\beta \end{bmatrix} + \begin{bmatrix} B_{cl,11} & B_{cl,12} \\ B_{cl,21} & B_{cl,22} \\ 0 & 0 \\ 1 & 0 \\ 0 & 1 \end{bmatrix} \begin{bmatrix} r_{v_A} \\ r_\beta \end{bmatrix} \tag{6.52}$$

To decouple the two control variables v_A and β, there should be no gain from β and its' integrals and derivates to $\dot{v}_A$, therefore $A_{cl,12}$, $A_{cl,13}$ and $A_{cl,15}$ should be zero. The same goes the other way round, and therefore $A_{cl,21}$ and $A_{cl,24}$ should also be zero. Lastly, the reference for each control variable should only influence the control variable and its derivatives, therefore $B_{cl,12}$ and $B_{cl,21}$ should also be zero. This leads to a total of seven equations and the following system:

$$\dot{\mathbf{x}}_z = \begin{bmatrix} A_{cl,11} & 0 & 0 & A_{cl,14} & 0 \\ 0 & A_{cl,22} & A_{cl,23} & 0 & A_{cl,25} \\ 0 & 1 & 0 & 0 & 0 \\ -1 & 0 & 0 & 0 & 0 \\ 0 & 0 & -1 & 0 & 0 \end{bmatrix} \begin{bmatrix} v_A \\ \dot{\beta} \\ \beta \\ z_{v_A} \\ z_\beta \end{bmatrix} + \begin{bmatrix} B_{cl,11} & 0 \\ 0 & B_{cl,22} \\ 0 & 0 \\ 1 & 0 \\ 0 & 1 \end{bmatrix} \begin{bmatrix} r_{v_A} \\ r_\beta \end{bmatrix} \tag{6.53}$$

The controller has 14 DoF, meaning seven additional equations are needed to solve the problem. These will be generated by pole placement for the two decoupled systems. First, the order of the closed-loop dynamics will be determined by generating the closed-loop transfer function matrix

$$\mathbf{G}_{cl} = \mathbf{C}_z \left(s\mathbf{I} - \mathbf{A}_{cl}\right)^{-1} \mathbf{B}_{cl}, \qquad \mathbf{C}_z = \begin{bmatrix} 1 & 0 & 0 & 0 & 0 \\ 0 & 0 & 1 & 0 & 0 \end{bmatrix}$$
$$\mathbf{G}_{cl} = \begin{bmatrix} \frac{(F_{11}B_{11}+F_{21}B_{12})s-K_{14}B_{11}-K_{24}B_{12}}{s^2+(K_{11}B_{11}-A_{11}+K_{21}B_{12})s-K_{14}B_{11}-K_{24}B_{12}} & 0 \\ 0 & \frac{(F_{12}B_{21}+F_{22}B_{22})s-K_{15}B_{21}-K_{25}B_{22}}{s^3+(K_{12}B_{21}+K_{22}B_{22})s^2+(K_{13}B_{21}+K_{23}B_{22})s-K_{15}B_{21}-K_{25}B_{22}} \end{bmatrix} \tag{6.54}$$

Where s is the Laplace variable.

As evident by the diagonal transfer function matrix, decoupling was achieved by setting the entries previously mentioned to zero. It is seen that G_{11}, the transfer function from $r_{v_A} \rightarrow v_A$, is 2nd order and has one zero and that G_{22}, the transfer function from $r_\beta \rightarrow \beta$, is 3rd order and also has one zero. To minimise the number of parameters defining the controller, a single pole/zero location is used for each transfer function, ω_{v_A} for G_{11} and ω_β for G_{22}. Therefore, the zero in each transfer function will cancel one of the poles. The desired closed-loop transfer functions are then:

$$G_{v_A} = \frac{\omega_{v_A}}{s+\omega_{v_A}} = \frac{\omega_{v_A}s + \omega_{v_A}^2}{s^2 + 2\omega_{v_A}s + \omega_{v_A}^2} \tag{6.55a}$$

$$G_\beta = \frac{\omega_\beta^2}{s^2 + 2\omega_\beta s + \omega_\beta^2} = \frac{\omega_\beta^2 s + \omega_\beta^3}{s^3 + 3\omega_\beta s^2 + \omega_\beta^2 s + \omega_\beta^3} \tag{6.55b}$$

This leads to seven additional equations, as the coefficients of the characteristic and numerator polynomials in each transfer function have to match the desired coefficients. Summing up, the 14 equations can be seen on the left in Eqn. (6.56) and the solution on the right in Eqn. (6.57).

$$\begin{aligned}
-K_{12}B_{11} - K_{22}B_{12} &= 0 \\
-K_{13}B_{11} - K_{23}B_{12} &= 0 \\
-K_{15}B_{11} - K_{25}B_{12} &= 0 \\
A_{21} - K_{11}B_{21} - K_{21}B_{22} &= 0 \\
-K_{14}B_{21} - K_{24}B_{22} &= 0 \\
F_{12}B_{11} + F_{22}B_{12} &= 0 \\
F_{11}B_{21} + F_{21}B_{22} &= 0 \\
-\omega_{v_A}^2 - K_{14}B_{11} - K_{24}B_{12} &= 0 \\
K_{11}B_{11} - 2\omega_{v_A} - A_{11} + K_{21}B_{12} &= 0 \\
-\omega_\beta^3 - K_{15}B_{21} - K_{25}B_{22} &= 0 \\
-3\omega_\beta^2 + K_{13}B_{21} + K_{23}B_{22} &= 0 \\
K_{12}B_{21} - 3\omega_\beta + K_{22}B_{22} &= 0 \\
F_{11}B_{11} - \omega_{v_A} + F_{21}B_{12} &= 0 \\
-\omega_\beta^2 + F_{12}B_{21} + F_{22}B_{22} &= 0
\end{aligned} \tag{6.56}$$

$$\begin{aligned}
K_{11} &= \frac{A_{11}B_{22}-A_{21}B_{12}+2B_{22}\omega_v}{B_{11}B_{22}-B_{12}B_{21}} \\
K_{12} &= -\frac{3B_{12}\omega_\beta}{B_{11}B_{22}-B_{12}B_{21}} \\
K_{13} &= -\frac{3B_{12}{\omega_\beta}^2}{B_{11}B_{22}-B_{12}B_{21}} \\
K_{14} &= -\frac{B_{22}{\omega_v}^2}{B_{11}B_{22}-B_{12}B_{21}} \\
K_{15} &= \frac{B_{12}{\omega_\beta}^3}{B_{11}B_{22}-B_{12}B_{21}} \\
K_{21} &= -\frac{A_{11}B_{21}-A_{21}B_{11}+2B_{21}\omega_v}{B_{11}B_{22}-B_{12}B_{21}} \\
K_{22} &= \frac{3B_{11}\omega_\beta}{B_{11}B_{22}-B_{12}B_{21}} \\
K_{23} &= \frac{3B_{11}{\omega_\beta}^2}{B_{11}B_{22}-B_{12}B_{21}} \\
K_{24} &= \frac{B_{21}{\omega_v}^2}{B_{11}B_{22}-B_{12}B_{21}} \\
K_{25} &= -\frac{B_{11}{\omega_\beta}^3}{B_{11}B_{22}-B_{12}B_{21}} \\
F_{11} &= \frac{B_{22}\omega_v}{B_{11}B_{22}-B_{12}B_{21}} \\
F_{12} &= -\frac{B_{12}{\omega_\beta}^2}{B_{11}B_{22}-B_{12}B_{21}} \\
F_{21} &= -\frac{B_{21}\omega_v}{B_{11}B_{22}-B_{12}B_{21}} \\
F_{22} &= \frac{B_{11}{\omega_\beta}^2}{B_{11}B_{22}-B_{12}B_{21}}
\end{aligned} \tag{6.57}$$

Substituting the state-dependent model coefficients found in Section 6.6 into the solution and applying the controller to the system model derived in Section 6.6 confirms that the dynamics match Eqn. (6.55). Initially, ω_{v_A} is

chosen to 2 Hz and ω_β to 1,5 Hz, whether this is sufficient will be evaluated after testing. The model parameters used for the controller are gathered from CAD and are listed in Table A.1 in Appendix A.10.

Before the controller can be implemented, some practicalities need to be solved, because a μC is used for implementation. The treatment of the sensor inputs, velocity estimation and the RC-transmitter will be explained next.

Implementation

The controller is implemented on a μC and therefore needs to be discretised. The bilinear transformation is used in all cases where discretisation is necessary. Some of the model states are also not directly measured, specifically v_A and $\dot{\beta}$. These need to be estimated based on the other measurements. The available measurements are β and the motor angles $\phi_{m,xx}, xx = \begin{bmatrix} rl & rr & fl & fr \end{bmatrix}$. $\dot{\beta}$ will be estimated using a 25 Hz HPF on the measured β, the formulation can be found in Appendix A.3. Due to gearing between the motor and wheels, the quantisation noise has been reduced drastically, allowing the use of a simpler fixed-time velocity estimate. To estimate v_A, the wheel velocities are first estimated by applying four 25 Hz HPFs to the motor angles and then dividing by the gearbox gear ratio. v_A is then computed using a least-squares error-based estimator on the kinematics described in Eqn. (6.28) and used for torque distribution in Eqn. (6.48). The cost function for the problem is thereby:

$$f = \frac{1}{2} \left(\mathbf{M}\boldsymbol{\eta} - \dot{\boldsymbol{\phi}} \right)^T \left(\mathbf{M}\boldsymbol{\eta} - \dot{\boldsymbol{\phi}} \right) \tag{6.58}$$

Where $\dot{\boldsymbol{\phi}}$ is the vector of measured wheel velocities.

The problem variables are v_A and $\dot{\beta}$. The estimator is found by solving $\nabla f = 0$. The estimate for v_A is then:

$$\begin{gathered} v_A = \frac{{L_R}^2 r}{\sigma}\dot{\phi}_{rl} + \frac{{L_R}^2 r}{\sigma}\dot{\phi}_{rr} + \frac{{L_R}^2 r\cos(\beta) - L_R L_f r \sin(\beta)}{\sigma}\dot{\phi}_{fl} + \frac{{L_R}^2 r\cos(\beta) + L_R L_f r \sin(\beta)}{\sigma}\dot{\phi}_{fr} \\ \sigma = 2{L_R}^2 \cos(\beta)^2 + 2{L_R}^2 + 2{L_f}^2 \sin(\beta)^2 \end{gathered} \tag{6.59}$$

Following this, all model states are now estimated, and the state-dependent gains can then be calculated as necessitated by Eqn. (6.57).

The two references are generated using the two DoF handheld RC-transmitter mentioned in Section 6.5. The trigger is used to generate r_{v_A}, with the range ±2 m/s and the wheel is used to generate r_β in the range $\pm\frac{\pi}{2}$ rad. The exact mapping is non-linear to improve driveability and is available in Figure A.5 in Appendix A.11. To reduce wheel slip and avoid integrator wind-up, both references are rate-limited. r_{v_A} to 4 m/s^2 and r_β to $\frac{\pi}{2}$ rad/s. Additional control of slip will also be implemented, but first, the main controller functionality is tested.

Test of Control

All elements are now ready, and the controller can be started. An initial sample rate of 500 Hz is used. To verify performance and validate the model, the mower is driven around using the RC-transmitter on asphalt and a grass field. The references are also input to Eqn. (6.55), called the trackers. If the trackers match the response, the desired dynamics have been obtained. A section of these comparisons can be seen below in figures 6.30 and 6.31.

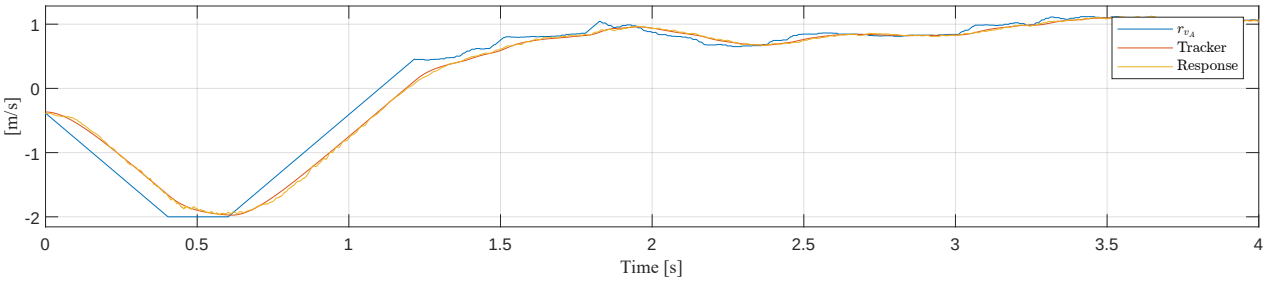

(a) r_{v_A}, *tracking response and actual response.*

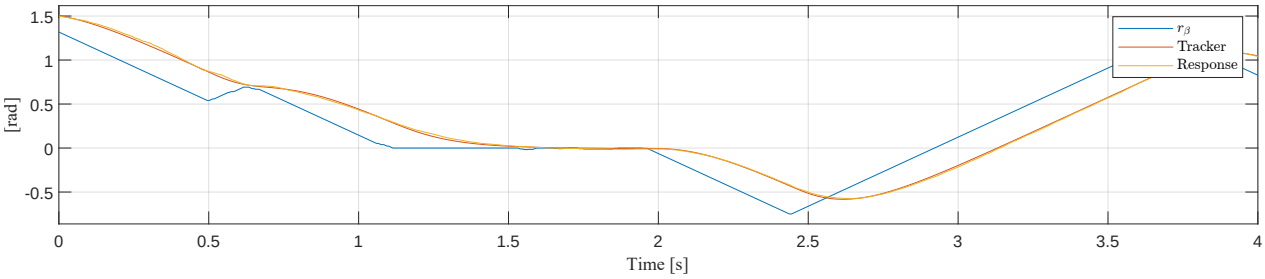

(b) r_β, *tracking response and actual response*

Figure 6.30

Comparison on asphalt.

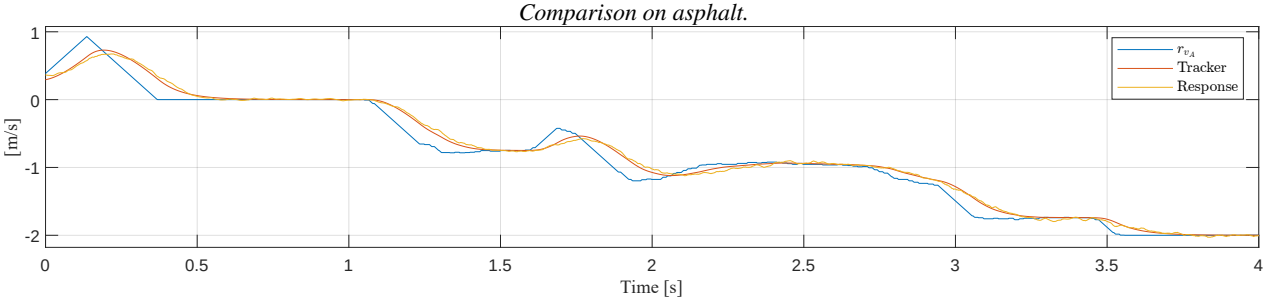

(a) r_{v_A}, *tracking response and actual response.*

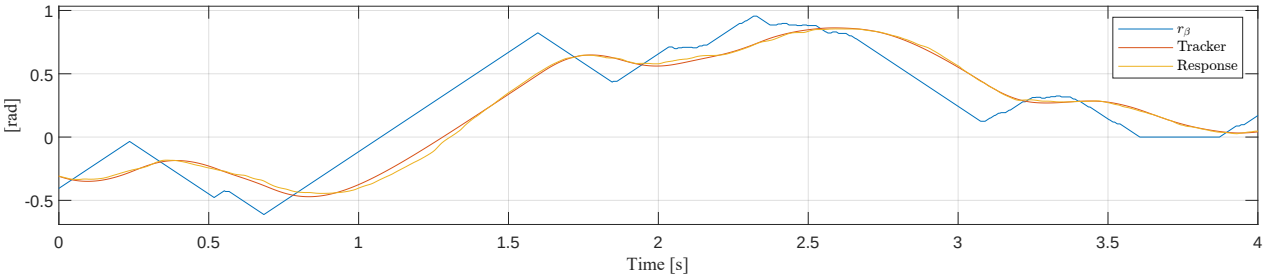

(b) r_β, *tracking response and actual response*

Figure 6.31

Comparison on grass.

As seen in both figures 6.30 and 6.31, the desired dynamics are generally very closely matched on both surfaces, also when both references are changing simultaneously. β has larger deviations from the desired dynamics on grass, probably caused by the additional disturbance of the many small bumps and lumps, which are not present on asphalt. The neglect of the motor current dynamics is also validated based on this. From this, performance, decoupling and the chosen poles/zeros are deemed satisfactory, and the main controller will not be tuned further. Requirement 13 for acceleration is also fulfilled, as the mower accelerates faster than 0,5 m/s^2 in figures 6.30a and 6.31a. A test for requirement 12 is also performed, this time on Kristian Rytter ApS' field. 5 s of the reference and response can be seen in Figure 6.32.

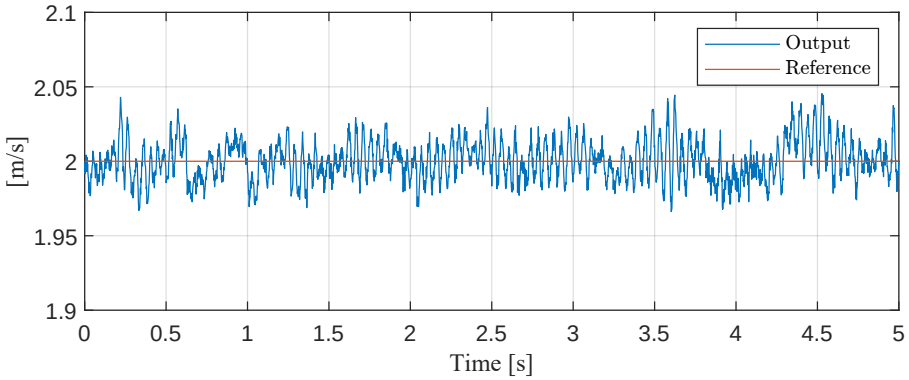

Figure 6.32

Velocity and velocity reference from driving on Kristan Rytter's field.

The mower maintains a velocity of 2 m/s as required, with some additional noise due to the roughness of the field.

However, on grades above 50 % to 60 % or slippery surfaces, the controller tended to result in one wheel slipping and the mower getting stuck. This is expected as no traction control has been implemented yet. But before implementing traction control, it is interesting to analyse how the mower ends up making wheel slip first. One wheel slips due to the varying traction and friction for all the wheels and because the controller does not redistribute torque. One wheel starts spinning, and the controller then thinks the mower is going too fast due to the vehicle velocity estimator in Eqn. (6.59). It then reduces the torque on all wheels, and the mower is stuck. In steady state, the result is one wheel slipping while it is spinning four times faster than nominal, while the other three wheels are stationary. The v_A error is zero in this scenario, again because of the estimator in Eqn. (6.59). This scenario is pictured in Figure 6.33, along with a reference wheel velocities based on the reference linear velocity and the wheel torques.

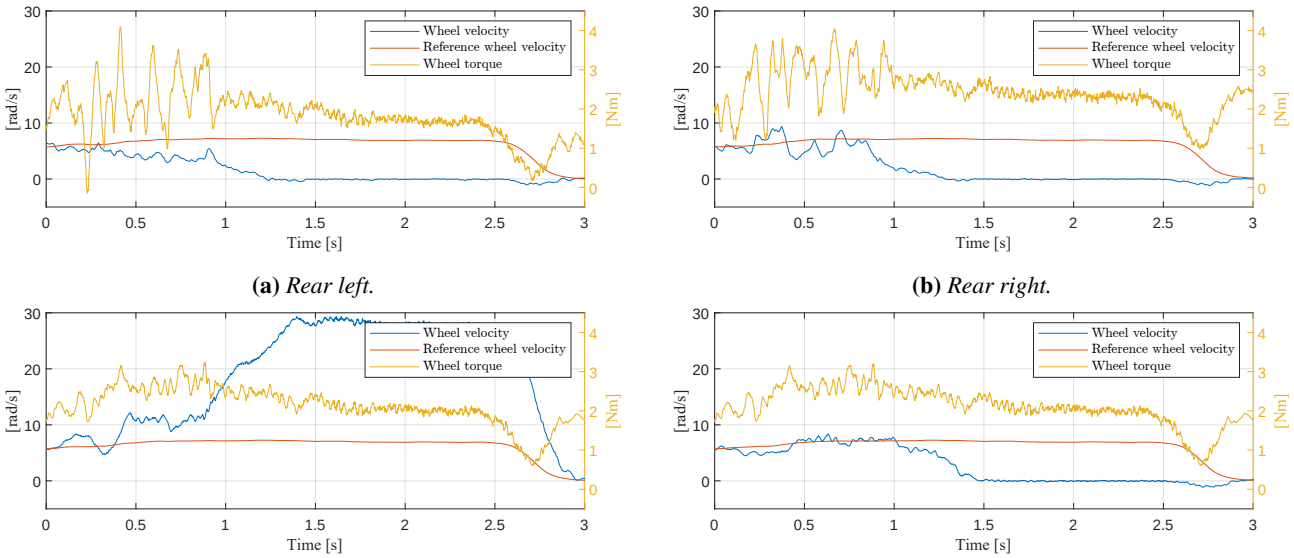

(a) *Rear left.*

(b) *Rear right.*

(c) *Front left.*

(d) *Front right.*

Figure 6.33

Wheel velocities, reference wheel velocities and wheel torques for all wheels while the mower is stuck with one wheel slipping.

This behaviour is undesired both concerning requirements 20 and 21 and from a control and mobility perspective. To control the slip from becoming excessive and gain some more mobility, an additional traction controller is added to each wheel. The reference for these controllers will be nominal wheel velocities, generated based on

the desired dynamics. The details of this will now be explained.

Traction Control

It is not possible to implement real traction control, as no sensor for vehicle velocity is present, and observability of the vehicle velocity is thereby lost during four-wheel slip. This situation is very unlikely, unless the surface is ice or similar. To obtain a vehicle velocity estimate which is less affected by slip, the vehicle velocity is instead calculated on a per axle basis, and the numerically smallest value is chosen for the feedback. The per-axle estimates are also based on a least-squares error approach like Eqn. (6.59) and can be found in Appendix A.8. A single wheel slipping will then not throw off the vehicle velocity estimate, as the calculation for the other axle would be used instead. An individual-wheel estimate would be desirable, but is not mathematically or practically realisable. For example, one wheel is sometimes stationary, at a specific turning radius, making the estimate sensitive to noise and impractical.

Above in Section 6.6-Implementation, it was concluded that the mower follows the desired dynamics closely while no slip is present. This fact will be used to design a per-wheel model following controller inspired by a method presented in [32].

For a set of v_A, $\dot{\beta}$ and β, all wheel velocities are given through Eqn. (6.28), provided no slip is present. Therefore, an expected v_A and $\dot{\beta}$ must be generated to compute expected wheel velocities. The expected wheel velocities always need to correspond to the currently measured β, therefore, no expected value is generated for β. To generate the expected value of v_A, r_{v_A} is passed through Eqn. (6.55a). Additionally, it is filtered with a 25 Hz LPF to match the phase of the wheel velocity estimates generated with the 25 Hz HPFs. To generate the expected value of $\dot{\beta}$, an alternate formulation of a second-order system is utilised. The formulation can be seen in Figure 6.34.

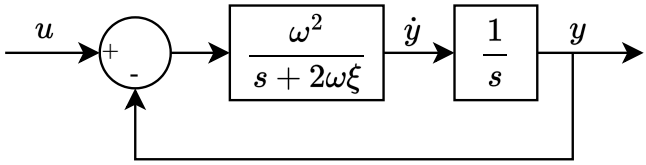

Figure 6.34

Second-order system formulated as a first-order system and an integrator with negative feedback.

Here, the input-output error is passed through a first-order system to get the output derivative. This principle will be used with Eqn. (6.55b) to generate the expected $\dot{\beta}$ from r_β and β. The system can be seen in the Figure 6.35.

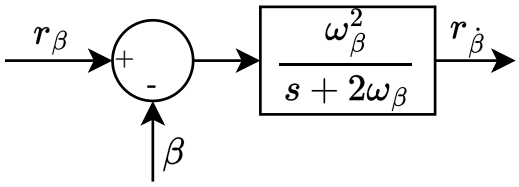

Figure 6.35

System for generating $r_{\dot{\beta}}$.

This value is also similarly low-pass filtered with the same 25 Hz cutoff frequency.

These expected values can now be used to calculate the expected wheel velocities using the kinematics in Eqn. (6.28). A proportional-derivative (PD) controller is then applied to the error between the expected and measured wheel velocity to generate an additional wheel torque for each wheel, to get it in line with the expected velocity. The proportional term is intended to control the error in steady-state slip, while the derivative term

is for preventing slip in the first place. A 25 Hz HPF is used to approximate the derivative. The structure can be seen in Figure 6.36.

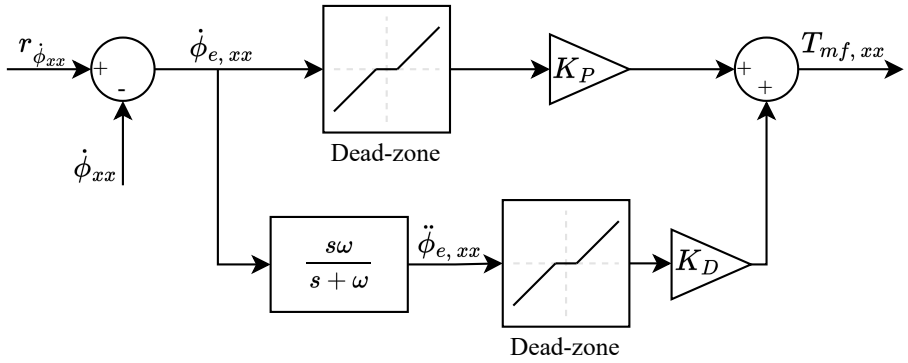

Figure 6.36

Individual-wheel model following controller.

It is not desired to follow these expected wheel velocities exactly, as the calculation assumes no disturbances. There is an offset error in the β measurement, and suspension movement and terrain curvature will also affect the real no-slip wheel velocities. Dead zones are therefore implemented on velocity error and the acceleration error, such that the controller only acts when the error is outside a tolerance. The tolerances and gains were tuned iteratively until a satisfactory result was obtained, resulting in the following values seen in Table 6.2

Variable	Tolerance	Gain
$\dot{\phi}_{e_{xx}}$	±2 rad/s	0,6 Nm/(rad/s)
$\ddot{\phi}_{e_{xx}}$	±2 rad/s^2	0,025 Nm/(rad/s^2)

Table 6.2

Slip controller parameters.

A before and after the implementation of the new vehicle velocity estimate and slip controller comparison of the wheel velocities and torques while climbing an 80 % grade, can be seen in Figure 6.37.

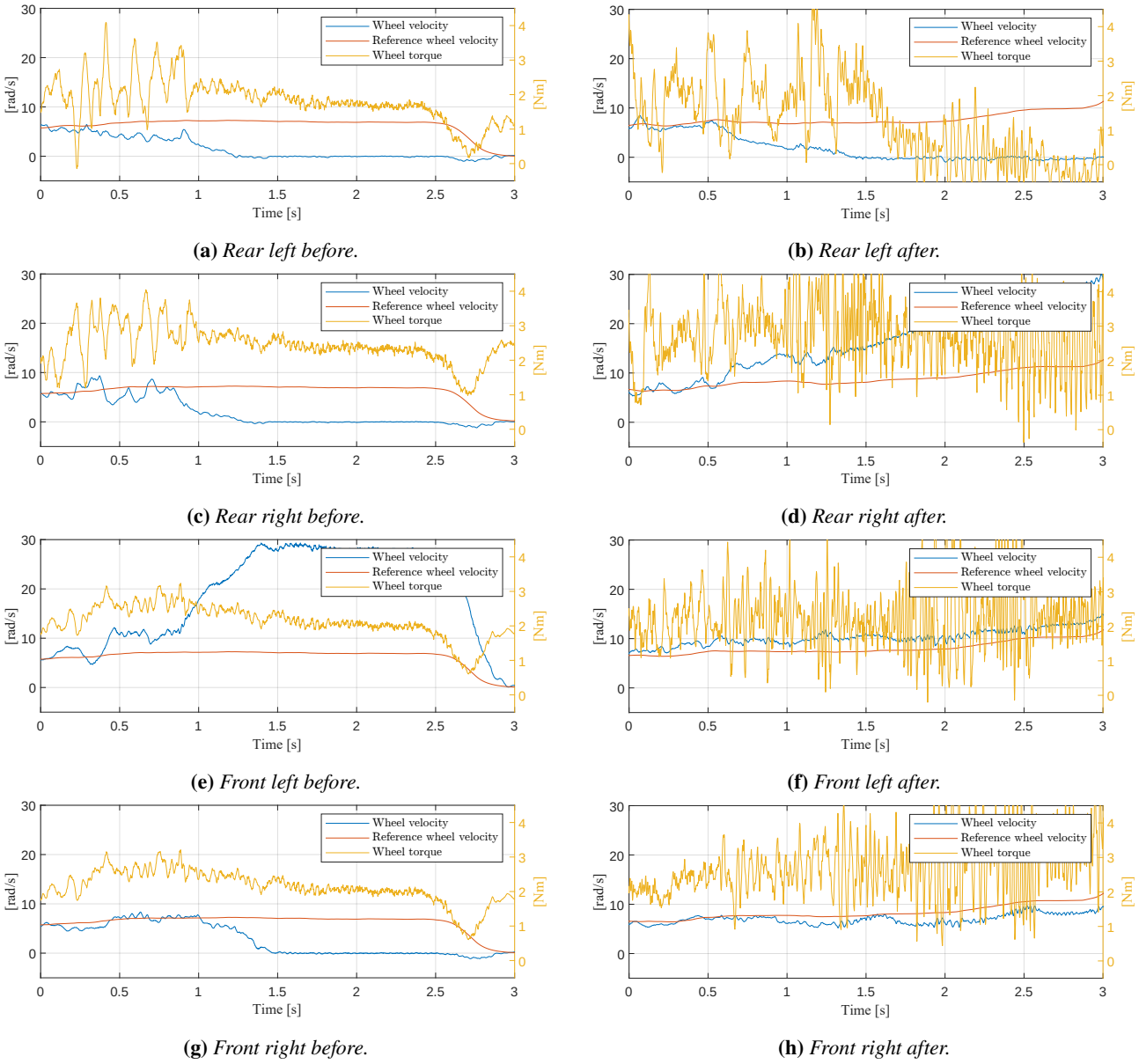

(a) *Rear left before.*

(b) *Rear left after.*

(c) *Rear right before.*

(d) *Rear right after.*

(e) *Front left before.*

(f) *Front left after.*

(g) *Front right before.*

(h) *Front right after.*

Figure 6.37

Wheel velocity comparison before and after the addition of slip control. Axes are the same on all plots too ease comparison.

In the before scenario on the left, the mower gets stuck with only the front left wheel slipping as seen in Figure 6.37e, and the torque for all wheels is approximately identical. This is the scenario also mentioned earlier. After the implementation of the additional individual-wheel PD model-following controllers, the mower manages to climb the 80 % grade and torque is redistributed such that three wheels are now slipping and following their respective reference velocities more closely. A downside is additional noise on the output in these scenarios, but this could probably be addressed through additional tuning. The problem of wheel slip is not resolved though, the results of which will be shown in Section 7.1.

6.7 Programming

The goal for the program is consistent behaviour and reliable data logging. In previous projects, unreliable data logging specifically has always been the cause of many problems. Without reliable data, debugging the control

implementation and presenting and proving performance becomes complicated, as also stated in Section 6.5. The decisions made to ensure reliable data logging and consistent behaviour will be explained, following an overview of the complete program flow.

A flowchart of the program can be seen in Figure 6.38

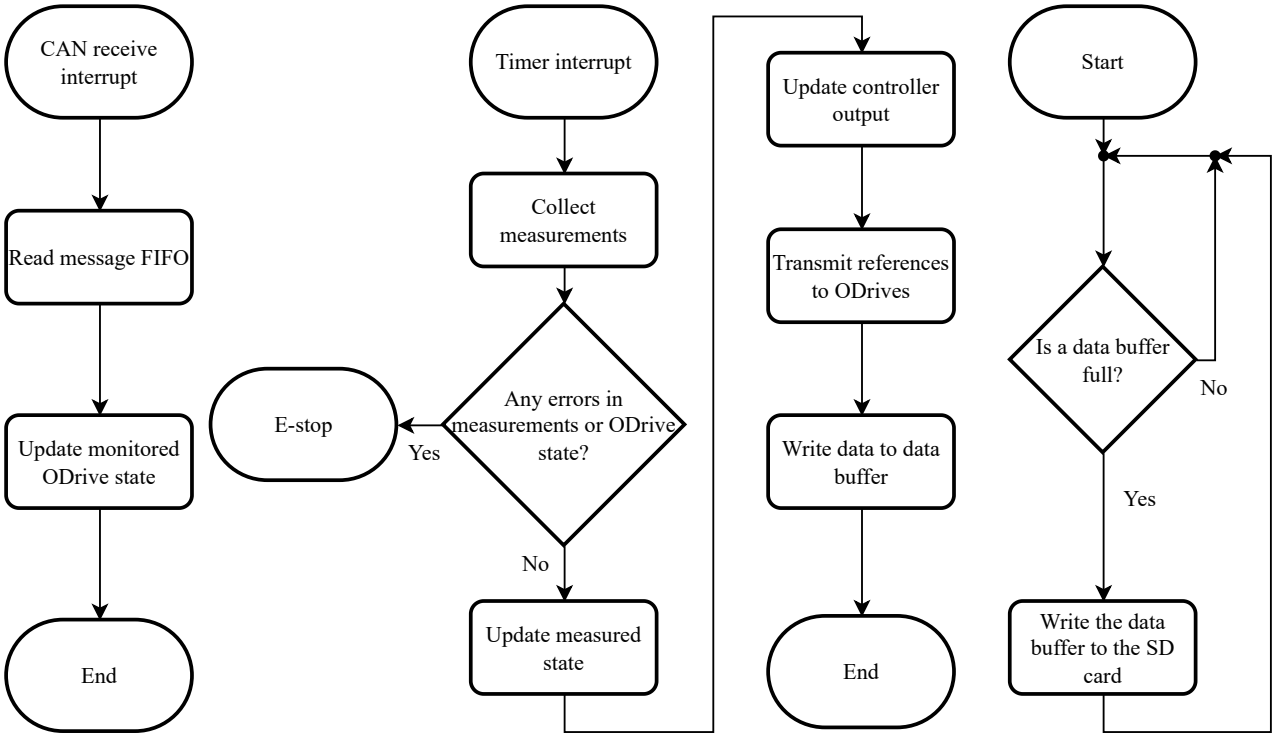

Figure 6.38

Each thread represented with its different flows.

Most of the program is event-based, where the events are the interrupts. Three ”threads” are running concurrently: the CAN bus receive interrupt on the left, the periodic timer interrupt in the middle and the infinite loop on the right.

The CAN bus receive interrupt's only purpose is to handle the received messages from the drives. Handling a message consists of reading the header, which contains a device ID and a message ID, and updating the appropriate variables depending on the device and message ID. An example is updating the currently stored state of the front left wheel ODrive when a heartbeat message is received from the corresponding ODrive.

The 500 Hz timer interrupt is the main part of the program. First, measurements are collected, and safety and error checks are done. If errors are detected, an E-stop message is broadcast to all ODrives and the program is halted. If no errors are detected, the velocity estimates and integrators are updated, and the new desired torques are computed. These new torque references are then transmitted to each ODrive, after which, the sample counter and selected data are written to the data buffer, and a full buffer flag is raised. The sample counter functions as a timestamp for each data point. If there is a discontinuity in the data, it is easily detectable by checking the sample counter. Faulty data can thereby be detected. In the infinite loop, the buffer full flag is then repeatedly checked. And whenever it is raised, the data is written to the SD card.

The overall program structure is a common case for real-time embedded systems, which usually have a real-time operating system (RTOS) for non-timing critical tasks and higher priority interrupts for timing critical tasks.

Which interrupt priorities are used, why they are used, and how they contribute to achieving deterministic and reliable behaviour will be explained next.

Consistent Behaviour

The STM32F429ZI implements two types of interrupt priorities: pre-emption priority and sub-priority. If an interrupt has a higher pre-emption priority than the current process, the current process will be interrupted and the corresponding interrupt service routine (ISR) will be executed. After executing the ISR, the program returns to the previously interrupted process. If the interrupts instead had the same pre-emption priority, they would be queued by their respective sub-priorities. The CAN bus receive and timer interrupts have been configured with the same maximum pre-emption priority. The timer interrupt is more timing critical than the CAN bus receive interrupt. But because of the CAN bus receive ISR's short execution time and the CAN bus peripheral's limited hardware FIFO, the same pre-emption priority is used to ensure that each message is handled in its entirety, without interruptions. Instead, the timer interrupt has a higher sub-priority. The result is visualised in Figure 6.39.

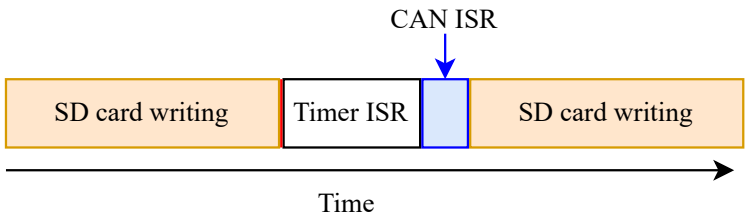

Figure 6.39
At the red line between SD card writing and the Timer ISR, both a CAN bus receive and a timer interrupt are received simultaneously.

Here, a CAN bus receive and a timer interrupt are triggered simultaneously. The SD card write process is pre-empted and the ISRs are executed in the order of their subpriorities.

The maximum delay before execution of the timer ISR, which would occur if a CAN bus receive interrupt is received just before a timer interrupt, is thereby given by the execution time of the CAN bus receive ISR. This computation time is only 4,2 µs, which is 0,2 % of the control loop period of 2 ms.

How robustness towards these interruptions is achieved for the data logging will be explained next.

Data Logging

In Section 6.5, an SD card is chosen for data logging. Specifics relevant for effective and reliable usage of SD cards will therefore be researched to achieve reliable data logging.

The smallest unit, which can be read from or written to, on an SD card is called a sector. To write a value smaller than the sector size, the sector first has to be read, modified and then rewritten. Therefore, the chunks of data to write should be aligned at the sector boundaries to avoid the read and modify operations to achieve maximum bandwidth. The SD card is default formatted, resulting in a sector size of 512 B. Therefore, the data chunks should have a size which is an integer multiple of 512 B. Larger transfers are generally also faster, due to the avoidance of repeat tasks at the start and end of transfers. Based on this, a data buffer size of 65 KiB is selected. This allows a total of 16.384 4 B values like standard floating point numbers and integers. This buffer

takes up 25 % of the μC's 256 KiB RAM, which is deemed acceptable, as the memory requirements for the rest of the program are small in comparison. With logging of 32 4 B values each cycle at the sample frequency of 500 Hz, the buffer will be filled every 1,024 s. To continue logging data while the previous data is being written to the SD card, an additional buffer is allocated. Every time a buffer is filled, a boolean value, representing the selected buffer, is toggled, and the previously mentioned buffer full flag is raised. This flag is then checked in the infinite loop, and a transfer of the currently not selected buffer is started.

To decrease the involvement of software and the chance for errors because of the interrupts, DMA is used for handling the transfers. This introduces additional interrupts into the program, which raise some flags used for the logic and tracking of progress during the transfers. These all have a lower pre-emption priority than the CAN bus receive and timer interrupts, and the timing explained previously will therefore not be affected.

When putting it all together, a transfer takes 16,7 ms while also handling the timer and CAN bus receive interrupts, resulting in an effective bandwidth of 3,9 MB/s. Last, the additional safety features achieved through software are explained.

Safety

In addition to the electro-mechanical safety with the dead man's switch introduced in Section 6.5, automated safety features are also added to the program. This consists of monitoring the time between each received heartbeat from each ODrive, enabling a watchdog on the ODrives, ensuring the RC-transmitter is connected and checking the digital communication with the absolute encoder for error.

To ensure all ODrives operate as intended, they are tracked with an individual heartbeat timer and counter. The ODrives transmit heartbeats at 10 Hz. The heartbeat timers are updated in the timer ISR, while the heartbeat counter is incremented and the heartbeat timer is reset in the CAN bus receive ISR. The timers are also checked during the timer ISR, and if one of them exceeds 200 ms, an E-stop message is broadcast to all ODrives and the program is terminated. A similar mechanism is also active on all the ODrives in closed-loop control mode. If they do not receive a reference for 1 s, they automatically exit closed-loop control and return to idle. Lastly, if an error occurs on a single ODrive, the rest are also stopped.

The 14 b absolute encoder sends two additional bits in addition to the 14 b position data [33]. These two bits represent a checksum of the position data. These checksum bits are also computed based on the received position data using the same method as the encoder and compared to the received checksum bits. If they are not identical, the measurement is considered invalid, and the control loop position is not updated. If two invalid measurements are received in a row, E-stop is broadcast, and the program is terminated.

Lastly, the RC-transmitter connection is also monitored. It is observed during testing that the RC-receiver stops outputting PWM signals when the RC-transmitter is disconnected. The PWM signals are captured using a timer peripheral on the μC. In this peripheral, a flag is raised each time an edge is detected on the input. This is utilised to detect whether the RC-transmitter is connected, by checking this flag in the timer ISR. If the flag has not been raised for a time corresponding to three periods of PWM signals, E-stop is broadcast and the program is terminated.

With programming completed, the mower is now fully functional. The concepts for the steering, drive unit and suspension were chosen in Section 6.1 and they were designed in sections 6.2 to 6.4. To facilitate the con-

trol, an electronic system was designed in Section 6.5, after which, the controller was designed in Section 6.6. Everything is then implemented on a μC as just described. The source code is included in a directory named "Code" in Appendix A.12, and a video of the mower driving can be seen in Appendix A.12 named MowerClimbingHill.MOV. The mower is now ready for testing and conclusions concerning the requirements in Section 5.1.

7 | Test and Conclusion of Mower Prototype

In the following chapter, the mower will first be tested to gain insight into its performance regarding the requirements. This will be followed by a conclusion on the mower's ability to fulfil the requirements and wishes.

7.1 Testing of Mower Prototype

With the completion of the mower design, the mower will be tested in the following section. The purpose of the tests is to determine if the mower fulfils the requirements that only can be concluded upon by performing tests. This involves the following requirements from Section 5.1:

5. Must have a cut tolerance of 3 mm on fairways when measured against the primary contour, where grass is cut to a length between 12 mm to 14 mm. Only valid within the limits specified in Section 5.1-Cutting Quality Limits
6. Must have a cut tolerance of 10 mm on first cut and semi rough, when measured against the primary contour, where the grass is cut to lengths of 32 mm and 38 mm to 44 mm respectively. Only valid within the limits specified in Section 5.1-Cutting Quality Limits
7. Outside the limits specified in Section 5.1-Cutting Quality Limits, the field must not be scalped and have a cutting tolerance of 20 mm on fairway and 50 mm on first cut and semi rough

15. Must be able to climb grades of 80 %
16. The mower must be able to traverse a 5 cm tall obstacle, such as a curb
17. Traverse an Ø15 cm sprinkler hole
20. Must not damage the terrain it drives upon, meaning dirt patches must not be visible after the mower has driven over the grass

Requirement 5, the first cut part of 6 will not be tested. Requirement 7 will not be tested at Aalborg golf course, but a test is performed at Kristian Rytter ApS' field which is deemed to a more challenging terrain and therefore representable for if the requirement is fulfilled. This is due to the mounting of the cutting deck which does not allow for continuos adjustment of the cutting height, it was not possible to set a cutting height which matched what the golf club was cutting their fairway to at the time. Based on this the mower was not allowed to cut on fairway and first cut. Requirement 7 is not tested because the golf course was very busy on the day of testing and as a result it was not prioritised. To be able to evaluate the performance in rougher terrain, a test will be performed on Kristian Rytter ApS' field which was also used for testing the line marking robot. This terrain is deemed to be outside the scope of requirement 5 and 6, and is also expected to be rougher than what could be met on the golf course which would fall under requirement 7. As such this test is expected to give insight into the mowers ability to fulfil requirement 7 at the golf course.

Several tests are performed to test the remaining requirements. The first test involves semi-rough in requirement 6. The test is performed at Aalborg Golf Club, where grass is cut in the semi-rough. The quality of the cut grass is evaluated with the grass prism. Initially, a section of grass is picked out, where the grass is uncut and higher

than the set cut height of the mower, which is 40 mm, a picture of this can be seen in Figure 7.1. The height of the grass cannot be determined from the pictures as it is hard to get the right point of view with the camera towards the prism. However, the grass length was measured in person at Aalborg Golf Club to be outside the range of the prism pre-cut meaning it was longer than 42 mm.

Figure 7.1

Semi-rough grass measurement using the grass prism. The picture is taken before the grass is cut with the mower.

After taking the picture, the same section of grass is cut. The mower is driven at 2 m/s while cutting. Next, a new measurement is made in the same location. The results can be seen in Figure 7.2.

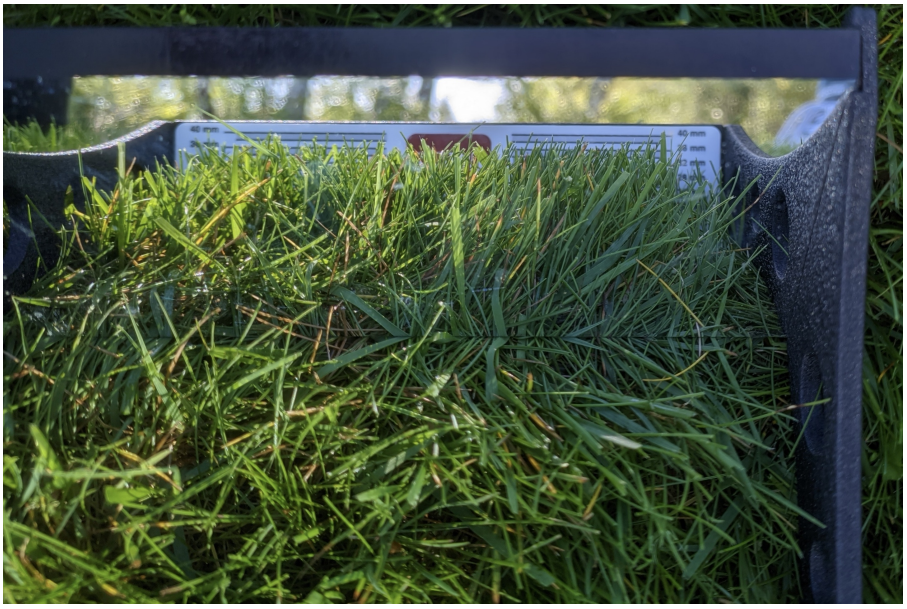

Figure 7.2

Semi-rough grass measurement using the grass prism. The picture is taken after the grass is cut with the mower.

The grass is cut cleanly and with good consistency. Only a few strands of grass stand out from the surroundings. These are expected to have been lying down and, as a result, did not come in contact with the cutter blades. The length of the cut cannot be determined from the picture because of the camera's point of view. However, measurements made in person at Aalborg golf course showed the cut to be around 40 mm to 41 mm. This means the cut has a tolerance of about 3 mm. It is expected that the tolerance is ±3 mm, but it is hard to see the shorter strands in the measurement as they disappear between the taller strands.

As mentioned earlier, tests are performed at Kristian Rytter ApS' field to replace the missing tests for requirement 7 at Aalborg golf course. Here grass is cut in the field at 2 m/s. The quality of the field is outside the limits specified in Section 5.1-Cutting Quality Limits. As a result, it is only requirement 7 and 21 the mower has to fulfil. The grass prism is not available for the test performed at Kristian Rytter ApS' field. A visual evaluation is thereby only performed, this is deemed sufficient as scalping or deviations of more than 50 mm is possible to evaluate visually. In figures 7.3a and 7.3b the cutting test performed at Kristian Rytter ApS' field can be seen.

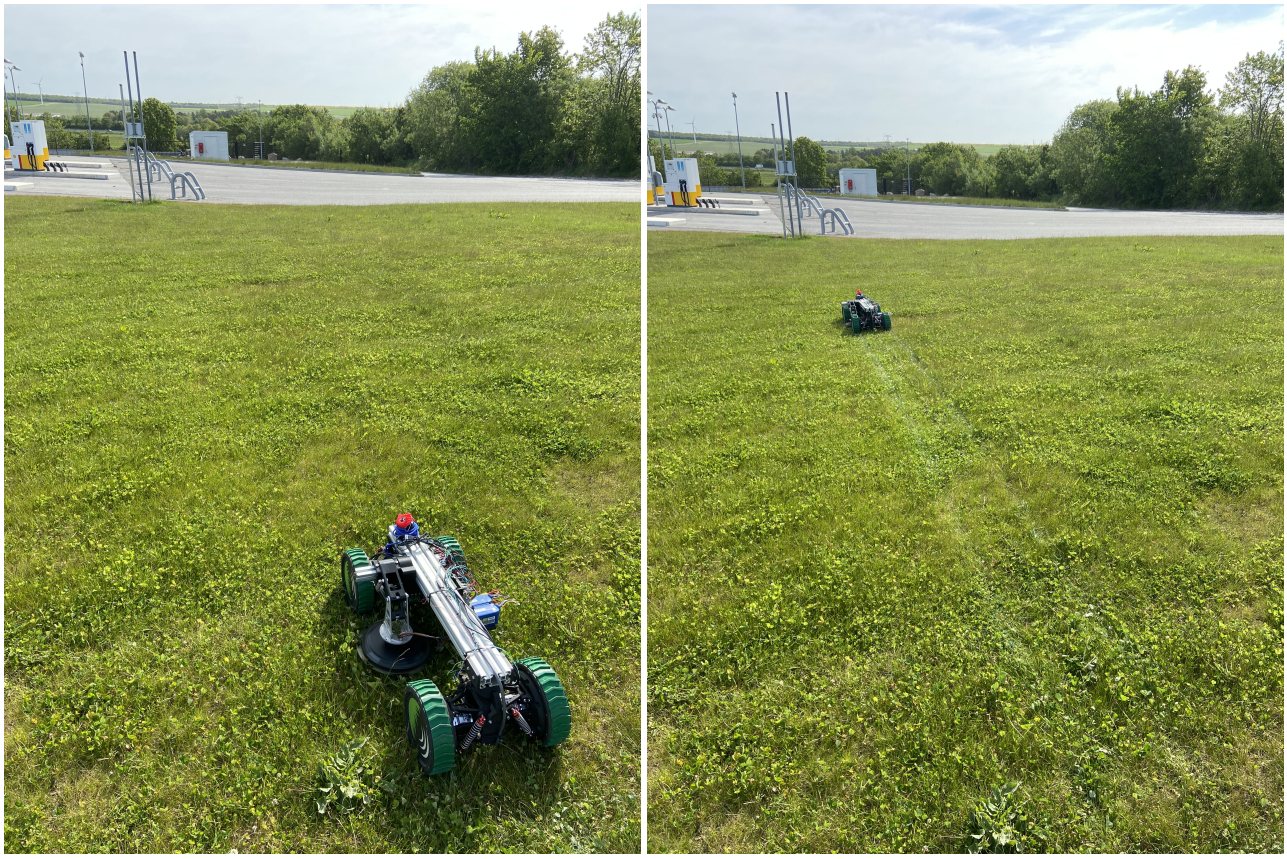

(a) *Test location at Kristian Rytter ApS' field before the grass is cut.*

(b) *Test location at Kristian Rytter ApS' field after the grass is cut.*

Figure 7.3

From this, the cutting quality is deemed to be within the limits. The grass field has not been scalped and from visual inspection the quality of the cut grass is deemed to fulfil requirement 7 and 21.

requirement 15 is tested at a small hill close to Turf Tank headquarters with a grade of approximately 80 %. The hill is composed primarily of loose soil without grass and as such is expected to be a good representation of sandy loam. In figures 7.4a and 7.4b images can be seen showcasing the angle of the grade as well as wheel

marks after the mower has driven up the small hill.

(a) *Grade of approximately* 80 % *at test location selected for the test of requirement 15.*

(b) *Wheel marks from the mower climbing the approximately* 80 % *grade successfully.*

Figure 7.4

The mower can climb the grade. Some wheel slip is present, but that is to be expected on loose soil without much cohesion and also because traction control is not implemented that fully prevents wheel slip.

For requirements 16 and 17, the mower is driven over a 5 cm curb and a sprinkler hole at Aalborg Golf Club. The mower can traverse both these types of obstacles. It is, however, hard to visualise the mower traversing the obstacles, and as a result, it will not be shown. The mower has AWD, a ground clearance above 5 cm and a 20 cm wheel diameter larger than the sprinkler holes 15 cm diameter. It is therefore not surprising that the requirements are fulfilled.

Requirement 20 is also deemed to be fulfilled. This is because no dirt patches are made in the grass by the mower during the 20 min to 30 min the mower drove around at Aalborg Golf Club and during the test at Kristian Rytter ApS' Field.

With the tests performed, a conclusion can be made in the next section.

7.2 Conclusion of Mower Prototype

In the following section, conclusions will be made on the investigation of how a robotic mower can be developed for operation on the terrain specified by Turf Tank. Here, a technical analysis was first performed to gain knowledge on which design parameters affect off-road vehicle performance. Following the technical analysis, a robotic mower prototype was developed and produced. A conclusion will then be made regarding the requirements and wishes formulated in Section 5.1.

Before the development of the mower prototype, Turf Tank's problems with their line marking robots were investigated. This was done to obtain knowledge on the root causes such that the same problems would not be carried over to the mower prototype. After highlighting the root causes for Turf Tank's audible noise problem and unacceptable field surface damage with their line marking robots, which is summarised in Section 2.5, four solutions to the audible noise problem were proposed. The main insights gained led to the formulation of two requirements for the mower prototype in Section 5.1. The two requirements are:

- 1. The mower's natural frequencies must not be excited such that they cause audible noise
- 21. The mower must not make wheel slip

Conclusions will now be made on the developed mower prototype concerning the requirements and wishes formulated in Section 5.1. Requirements and wishes will be written in italic.

General Functionality Requirements

The first requirement states that *the mower's natural frequencies must not be excited such that it causes audible noise*. This requirement is fulfilled as no audible noise caused by excitation of natural frequencies has been observed throughout all of the tests performed with the mower. requirement 2 states that *the mower must be able to cut the edges of grass areas*. This requirement is fulfilled as the mower's cutting head is placed to the side of the mower with its knives sticking further out to the side than the mower wheels, enabling the mower to drive around a golf course bunker without falling into the sand. requirement 3 states that *the mower must be outfitted with a* 24 cm *cutting head*. This is fulfilled as the mower has been outfitted with a 24 cm cutting head provided by Turf Tank. requirement 4 states that *the mower must have an adjustable cutting height of* 10 mm *to* 70 mm *with* 1 mm *increments*. This requirement is not fulfilled as only a few cut height settings in the range of 10 mm to 70 mm have been implemented. requirement 5 states that *the mower must have a cut tolerance of* 3 mm *on fairways when measured against the primary contour, where grass is cut to a length between* 12 mm *to* 14 mm. *Only valid within the limits specified in Section 5.1-Cutting Quality Limits*. This requirement is deemed to be fulfilled from tests performed at Aalborg golf club on semi-rough. The requirement is formulated regarding cutting grass on fairways, which has not been tested, but the results from cutting grass on semi-rough are deemed to provide insights into how the cutting quality will be on fairways. This is because the terrain is smoother on fairways, and the grades the mower can encounter are less steep. The cutting quality should therefore be better on fairway than on semi-rough terrain. On the semi-rough, the tests showed a cutting tolerance of approximately ±3 mm, which is within the tolerance stated in requirement 5. There were a few strands of grass that did not seem to have been cut each time a measurement was done with the grass prism. This is, however, deemed acceptable as the large majority of the grass had been cut within tolerance. requirement 6 states that *the mower must have a cut tolerance of* 10 mm *on first cut and semi-rough, when measured against the primary contour, where the grass is cut to lengths of* 32 mm *and* 38 mm *to* 44 mm *respectively. Only valid within the limits specified in*

Section 5.1-Cutting Quality Limits. This requirement is deemed to be fulfilled from the test performed on the semi-rough already mentioned. Grass has not been cut in the first cut, but the terrain in the first cut is equal to or easier to cut than semi-rough and the requirement is, as a result, deemed to be fulfilled. requirement 7 states that *outside the limits specified in Section 5.1-Cutting Quality Limits, the field must not be scalped and have a cutting tolerance of* 20 mm *on fairway and* 50 mm *on first cut and semi-rough*. This requirement has not been tested in fairway, first cut and semi-rough but results from cutting grass at Kristian Rytter ApS' field are deemed to give insight into the performance. Here the grass was not scalped and from visual inspection the cut grass was within the cutting tolerance of both fairway, first cut and semi-rough. requirement 8 states that *the cutting head must be mounted directly to the mower chassis*. This requirement is fulfilled. requirement 9 states that *the mower must use wheels for traction*, which is fulfilled. requirement 10 states that *the mower must not be wider than* 45 cm. This requirement is fulfilled as the mower is 39 cm wide. Wish number 11 states that *the mower should be as compact as allowed by the required functionality*. During the design process, the wish was primarily considered by attempting to make the mower as narrow and short as its functionality would permit.

Mobility Requirements

requirement 12 states that *the mower must be able to maintain a speed of* 2 m/s *while operating on grades up to* 5 %. This requirement is fulfilled as tests have been performed on Kristian Rytter ApS' field where the mower could maintain 2 m/s. requirement 13 states that *the mower must be able to achieve an acceleration of* 0,5 m/s^2 *on flat terrain*. This requirement is fulfilled as tests have been performed on flat asphalt and grass where an acceleration of 4 m/s^2 was achieved. requirement 14 states that *the mower must have a minimum turning radius of zero, around an axis within the mower's top-down outline*. This requirement is fulfilled as the mower's articulation joint allows the mower to turn around an axis in the middle of the front axle. requirement 15 states that *the mower must be able to climb grades of* 80 %. This requirement is fulfilled from a tests performed outside of Turf Tanks headquarters. requirement 16 states that *the mower must be able to traverse a* 5 cm *obstacle*, and requirement 17 states that *the mower must be able to traverse a* 15 cm *sprinkler hole*. Two tests were performed at Aalborg golf club, where a 5 cm obstacle and a 15 cm sprinkler hole were successfully traversed. Requirements 16 and 17 are, as a result, deemed to be fulfilled.

Electrical Requirements

requirement 18 states that *the mower must have an emergency stop button*. This requirement is fulfilled as a dead man's switch is implemented on the mower that, if pulled, disconnects the 18,5 V batteries from the drives. requirement 19 states that *the mower must use electric motors for propulsion*. This requirement is fulfilled.

Field Strain Requirements

requirement 20 states that *the mower must not damage the terrain it drives upon, meaning dirt patches must not be visible after the mower has driven over the grass*. During all tests on grass, the mower did not damage the terrain such that dirt patches were visible. No functionality is, however, implemented that prevents the mower's wheels from slipping if traction is lost. If continuous wheel slip is performed on the same spot of grass, visible dirt patches will be made. The requirement is, as a result, deemed not to be fulfilled as long as the mower's wheels can slip. requirement 21 states that *the mower must not make wheel slip*. This requirement is not fulfilled as the implemented traction control does not prevent wheel slip. Wish number 22 states that *the wheels of the mower should be within the diameter of the cutting head to minimise visible wheel tracks on the grass*. It is only

the left wheel of the mower that is within the diameter of the cutting head. It is, however, observed in tests that there is minimal difference in the visibility of the wheel tracks between the left and right wheels.

8 | Future Work

During the project, ideas for solutions to different problems have been thought of, but were abandoned due to not fitting within the scope of the project. However, many of these ideas would be interesting to spend more time researching in the future, and as such, they will now be presented.

In the initial stages of the project, the work revolved around removing the audible noise from the line marking robot, which was caused by resonance in the robot chassis. The resonance is a problem primarily due to the low stiffness of the chassis, as it is made of large flat plates of aluminium, as well as the hard mounting of the motors directly on the chassis plates. In the project, a software solution was required by Turf Tank, but a mechanical solution would likely offer better results and be more robust. Therefore, it would be interesting to look into what would be required mechanically to solve the problem. This could include changing the motor mounting to reduce the transfer of vibrations between chassis and motor, both reducing resonance and reducing vibrations in the feedback. It could be adding a form of damping in the chassis to reduce the amplitude of the resonance, or it could be changing the chassis to increase its stiffness. While exploring this solution field, it should be kept in mind that the solution should be possible to implement on existing robots by local technicians in a day's work.

In the initial stages, an alternative velocity estimate was developed which used timestamping. Due to hardware limitations, this caused the effective resolution of the wheel encoder to be only a quarter of its standard resolution. Based on this, it is expected that the estimate could be further improved if changes were made to the hardware, enabling full resolution while time stamping. Therefore, it would be interesting to explore what would be required for this to be possible. And afterwards, what performance increase could be achieved by it.

While trying to improve the trajectory tracking performance of the line marking robot by making alterations to the motor velocity control, only marginal improvements were made. These lacking results are expected to have two primary reasons. The first reason is that the robot controller was left unaltered for the test of each proposed solution. The second reason is that the proposed solutions, at best, only have a linear first-order step response with the condition that the angular velocity is zero. The robot controller model still does not match the dynamics in all other scenarios, where the robot actually has difficulties, as seen in Figure 2.4, which is in the transitions from line to arcs. Based on this, it would be of interest to implement a centralised control structure such that the cross-coupling between linear and angular velocity could be removed and a first-order linear and angular velocity dynamics could be obtained. This is also expected to improve the user experience of the line marking robots' manual control mode.

In the search for filtering methods for the line marking robot to solve the resonance problem, Butterworth filters were discussed. These showed promise but were discarded due to sensitivity to floating-point truncation error. They are, however, expected to give similar performance as the notch filter and with increased robustness as they attenuate everything after the cut-off frequency. It would be of interest to investigate a Butterworth filter implementation where the higher-order Butterworth filter is separated up into several lower-order filters in series. This is with the goal of reducing the sensitivity to floating-point truncation error.

In the mechanical design process of the prototype mower, it was shown through simulations that adding simple suspension could improve the cutting quality by reducing the cut height error. It is expected that the suspension could be further improved, giving even better performance. This could be in the form of optimised suspension geometry, as an example, alterations could be made to reduce track width change during the suspension stroke, anti-squat geometry could be implemented, or something more complex like decoupled heave and roll could be examined. Decoupled heave and roll would allow for tuning of the two parameters individually, so they could be fine-tuned based on what is best when cutting grass. Further more progressive springs could be tried, which could potentially reduce the amplitude of the cut error due to bottoming out in quick grade changes. Non-linear dampers could also be examined, it is expected that lower rebound damping would be better as it would allow the wheels to reach the terrain again faster after a bump, and as such, it should increase contact time.

Another part of the driveline that would be interesting to optimise and where significant performance gains may be found is in the tyres. Currently, the vehicle uses TPU tyres due to limited production time and methods. During testing, it has been found that these compromise the abilities of the mower, especially on sloped terrain, since the friction coefficient of TPU is too small. Instead of TPU it would be of interest to mould a set of rubber tyres to improve friction. It would also be of interest to spend more time researching lug design, so that these could be further optimised to generate more thrust but without damaging the fields surfaces.

Through the suspension simulations, it was found that the placement of the cutting head between the two wheel axles contributes to a portion of the cutting height error. This is caused by height changes in the terrain in between the axles, transferring directly to the cutting height as the distance between the cutting head and the terrain is suddenly altered. It was also found during testing that the cut is negatively affected when the wheel is directly in front of the cutting head. The cutting head is placed behind the wheel as border cutting was of interest, which restrains it to sitting outside the wheelbase of the vehicle. Here, the side-mounted position was considered the best possibility. However, with the significant drawbacks this placement is observed to introduce, and based on conversations with Aalborg golf course, where it was stated that border cutting was of lesser importance, as it only contributes to a small portion of their working time. It is expected that moving the cutting head up between the front wheels would be a better design, which should lead to increased performance in maintaining the set cut height. It would also be interesting to experiment with adding a second cutting head to increase the cutting capacity of the mower.

During the cutting test grass was cut nicely. However, if the grass was combed against the direction of the cut after cutting often a few strands of grass would stand out having not been cut. This is likely due to those strands having laid down before being cut, and as such, they did not come into contact with the blades of the mower. On traditional lawn mowers there is often a little bent part on the end of the blades acting as a little winglet, sucking the grass up into the blade [34]. This aids in making sure all strands of grass come into contact with the blades and get cut. Based on this, it would be of interest to experiment and research if an aerodynamic device could be added to for example the disc of the cutting head which the blades mount to. This device should create suction to raise up the strands of grass, but also be efficient so it does not drain the batteries of the mower to quickly for it to be viable.

In the project a traction control solution was implemented. This would reduce torque to the wheels that are slipping and increase torque on the wheels that are not slipping. This, however, did not completely eliminate slip. It would therefore be interesting to investigate if methods exits that can eliminate wheel slip with the current

sensors on the mower or if additional sensors would be required.

Literature

[1] *Turf Tank - Opstregningsrobot klarer alle sportsbaner*. URL: https://turftank.com/da/.

[2] Robert M Gray and David L Neuhoff. 'Quantization'. In: *IEEE TRANSACTIONS ON INFORMATION THEORY* 44.6 (Aug. 1998). URL: https://ieeexplore-ieee-org.zorac.aub.aau.dk/document/720541.

[3] MagnTek. *MT6825*. Jan. 2020. URL: https://images.chipyun.com/pdf/C879562_B4B237BF3FE7F221B49BA241A007BF51.pdf.

[4] Singiresu S. Rao. *Mechanical Vibrations*. Ed. by Subhasree Patra. 6th ed. Harlow: Pearson Education, 2018.

[5] Rached Dhaouadi and Ahmad Abu Hatab. 'Dynamic Modelling of Differential-Drive Mobile Robots using Lagrange and Newton-Euler Methodologies: A Unified Framework'. In: *Advances in Robotics & Automation* 2.2 (2013).

[6] Daniel Jeppesen et al. *Design of Torque Control for Asetek Direct Drive PMSM Wheelbase Project*. Tech. rep. Aalborg University, May 2024.

[7] Jason Sachs. 'How to Estimate Encoder Velocity Without Making Stupid Mistakes: Part 1'. In: *Embedded Related* (Dec. 2012). URL: https://www.embeddedrelated.com/showarticle/158.php.

[8] Dao Zhou. *Lecture 10 : Quadrature Encoders*. Mar. 2020. URL: https://www.moodle.aau.dk/pluginfile.php/3070645/mod_resource/content/6/Lect_10.pdf.

[9] Stefan Brock and Krzysztof Zawirski. 'Speed Measurement Method for Digital Control System'. In: (2001). DOI: 10.6084/m9.figshare.730619. URL: https://www.researchgate.net/profile/Stefan-Brock/publication/241279665_Speed_Measurement_Method_for_Digital_Control_System/links/00b4951c93f20a24f5000000/Speed-Measurement-Method-for-Digital-Control-System.pdf?_tp=eyJjb250ZXh0Ijp7ImZpcnN0UGFnZSI6InB1YmxpY2F0aW9uIiwicGFnZSI6InB1YmxpY2F0aW9uIn19.

[10] R. J.E. Merry, M. J.G. van de Molengraft and M. Steinbuch. 'Velocity and acceleration estimation for optical incremental encoders'. In: *Mechatronics* 20.1 (2010), pp. 20–26. ISSN: 09574158. DOI: 10.1016/j.mechatronics.2009.06.010.

[11] Jonas Kynde and Kristian Borg Hansen. 'Design of set-based observer structure for use with state-controllers in systems with quantized feedback'. Aalborg: Aalborg University, May 2024.

[12] ST. *STM32F446ZE - High-performance foundation line, Arm Cortex-M4 core with DSP and FPU, 512 Kbytes of Flash memory, 180 MHz CPU, ART Accelerator, Dual QSPI - STMicroelectronics*. URL: https://www.st.com/en/microcontrollers-microprocessors/stm32f446ze.html.

[13] Jo Wong. *Terramechanics and Off-Road Vehicle Engineering*. Vol. 2. Elsevier, 2010.

[14] TWL Irrigation and Tony Ware. *The Different Types of Golf Course Grass – TWL Irrigation*.

[15] Wentao He, Tatsuya Ishikawa and Binh T. Nguyen. 'Effect evaluation of grass roots on mechanical properties of unsaturated coarse-grained soil'. In: *Transportation Geotechnics* 38 (Jan. 2023). ISSN: 22143912. DOI: 10.1016/j.trgeo.2022.100912.

[16] National Highway Traffic Safety Administration. *The Pneumatic Tire*. Tech. rep. U.S Department of Transportation, Feb. 2006. URL: https://www.safetyresearch.net/Library/NHTSA_Pneu_Tire.pdf.

[17] Moustafa El-Gindy and Zeinab El-Sayegh. *Road and Off-Road Vehicle Dynamics*. Tech. rep. 2023.

[18] Husqvarna. *Automower® 535 AWD EPOS™-robotplæneklipper*. URL: https://www.husqvarna.com/dk/robotplaeneklippere/automower-535awd-epos/.

[19] Mammotion. *LUBA 2 AWD Robot Lawn Mower*. URL: https://eu.mammotion.com/products/luba-2-awd-robot-lawn-mower.

[20] N J Mclarin et al. 'Frictional Characteristics of Roadside Grass Types'. In: May 2005. URL: https://saferroadsconference.com/wp-content/uploads/2016/05/Peter-Cenek-Frictional-Characteristics-Roadside-Grass-Types.pdf.

[21] Vladimír Goga and Marian Kl'Účik. 'Optimization of vehicle suspension parameters with use of evolutionary computation'. In: *Procedia Engineering* 48 (2012), pp. 174–179. ISSN: 18777058. DOI: 10.1016/J.PROENG.2012.09.502. URL: https://www.researchgate.net/publication/257726035_Optimization_of_Vehicle_Suspension_Parameters_with_use_of_Evolutionary_Computation.

[22] Husqvarna. *Automower® 435X AWD NERA med kabelfri teknologi-robotplæneklipper*. URL: https://www.husqvarna.com/dk/robotplaeneklippere/automower-435x-awd-nera-med-kabelfri-teknologi/.

[23] Mark Williams and Mark Williams. *Tech Corner: Off-Road Suspension Setups, Independent vs Solid Axle - The Engine Block*.

[24] Dave Lally. 'Roller Chains and Planetary Gearboxes Yield Accurate, Efficient Motion Control'. In: *https://www.machinedesign.com/mechanical-motion-systems/article/21837300/roller-chains-and-planetary-gearboxes-yield-accurate-efficient-motion-control* ().

[25] Howard Horn. *Planetary gears — A review of basic design criteria and new options for sizing*. URL: https://www.machinedesign.com/motors-drives/article/21834575/planetary-gears-a-review-of-basic-design-criteria-and-new-options-for-sizing.

[26] *Turnigy Aerodrive SK3 - 6364-190KV Brushless Outrunner Motor*.

[27] *Basic Gear Terminology and Calculation*.

[28] *Know about parameters that determine gear shapes | KHK Gears*.

[29] ST. *STM32 Nucleo-144 development board with STM32F429ZI MCU, supports Arduino, ST Zio and morpho connectivity*. URL: https://www.st.com/en/evaluation-tools/nucleo-f429zi.html.

[30] ODrive. *ODrive*. URL: https://odriverobotics.com/.

[31] Lasse Schmidt. *Multivariable Control, Lecture 7*. Tech. rep. Aalborg University, Mar. 2024.

[32] Valentin Ivanov, Dzmitry Savitski and Barys Shyrokau. 'A Survey of Traction Control and Antilock Braking Systems of Full Electric Vehicles with Individually Controlled Electric Motors'. In: *IEEE Transactions on Vehicular Technology* 64.9 (Sept. 2015), pp. 3878–3896. ISSN: 00189545. DOI: 10.1109/TVT.2014.2361860.

[33] Same Sky. *Same Sky AMT213B-V Encoder*. URL: https://www.sameskydevices.com/product/resource/amt21.pdf.

[34] Foxy Gardens. *Types Of Lawnmower Blades: A Cutting-Edge Journey*.

A | Appendix

A.1 Derivation of Line Marking Robot Model

The DDMR model is based on the following assumptions

- Pure rolling/no longitudinal slip
- No lateral movement of each axle/no lateral slip
- Wheels are assumed perfectly circular and infinitesimally thin, such that the contact line/patch reduces to a point and the radius doesn't vary with the angle
- The CoM is not offset laterally
- Wheel CoMs are located above their contact points
- No damping

The desired variables for control and thereby also the model formulation, are the linear and angular velocity of the centerpoint on the axle v and ω The model will initially be formulated in five generalised coordinates, along with the constraints, after which it will be reduced to an unconstrained formulation only in the desired model v and ω variables. These generalised coordinates are listed below.

$$\mathbf{q} = \begin{bmatrix} x_A & y_A & \theta & \phi_l & \phi_r \end{bmatrix}^T \tag{A.1}$$

Where x_A and y_A are the coordinates of A in a fixed reference frame, θ is the orientation of the DDMR and ϕ_l and ϕ_r are the wheel rotation angles.

To express the constraints, the coordinates of A, B, rl, rr, fl, fr in the fixed reference frame are expressed as a function of the generalised coordinates.

$$\mathbf{r}_A = \begin{bmatrix} x_A & y_A \end{bmatrix}^T \tag{A.2}$$

$$\mathbf{r}_l = \mathbf{r}_A + \mathbf{R} \begin{bmatrix} 0 & L \end{bmatrix}^T \tag{A.3}$$

$$\mathbf{r}_r = \mathbf{r}_A + \mathbf{R} \begin{bmatrix} 0 & -L \end{bmatrix}^T \tag{A.4}$$

Where

$$\mathbf{R} = \begin{bmatrix} \cos(\theta) & -\sin(\theta) \\ \sin(\theta) & \cos(\theta) \end{bmatrix} \tag{A.5}$$

These positions are then differentiated wrt. time to get the velocity of each point expressed in the generalised coordinates $\dot{\mathbf{r}}_A$, $\dot{\mathbf{r}}_l$, $\dot{\mathbf{r}}_r$. Additionally, some unit vectors are defined to represent the x and y directions in the local body frame represented by Eqn. (A.5).

$$\mathbf{x}_\theta = \begin{bmatrix} \cos(\theta) & \sin(\theta) \end{bmatrix}^T \tag{A.6}$$

$$\mathbf{y}_\theta = \begin{bmatrix} -\sin(\theta) & \cos(\theta) \end{bmatrix}^T \tag{A.7}$$

These will be utilised to express the no longitudinal and lateral slip constraints.

The lateral movement constraint means that point A cannot move in the direction of $\mathbf{y}_\theta$. This is expressed via a dot product between the point's velocity and a vector perpendicular to the corresponding body's orientation.

$$\dot{\mathbf{r}}_A \cdot \mathbf{y}_\theta = 0 \tag{A.8}$$

Similarly, the pure rolling constraints can also be expressed as the dot product between the velocity of the wheel's contact point and a vector in the orientation of the robot. This quantity is equal to the wheel's angular velocity multiplied by the radius.

$$\begin{aligned} \dot{\mathbf{r}}_l \cdot \mathbf{x}_\theta = r\dot{\phi}_l \Leftrightarrow \dot{\mathbf{r}}_l \cdot \mathbf{x}_\theta - r\dot{\phi}_l = 0 \\ \dot{\mathbf{r}}_r \cdot \mathbf{x}_\theta = r\dot{\phi}_r \Leftrightarrow \dot{\mathbf{r}}_r \cdot \mathbf{x}_\theta - r\dot{\phi}_r = 0 \end{aligned} \tag{A.9}$$

Resulting in a total of three constraints.

As all these constraints are linear in the generalised velocities, they can be expressed in the following form.

$$\mathbf{\Lambda}\dot{\mathbf{q}} = 0 \tag{A.10}$$

$$\mathbf{\Lambda} = \begin{bmatrix} -\sin(\theta) & \cos(\theta) & 0 & 0 & 0 \\ \cos(\theta) & \sin(\theta) & -L & -r & 0 \\ \cos(\theta) & \sin(\theta) & L & 0 & -r \end{bmatrix} \tag{A.11}$$

Due to these three constraints, it is also possible to express all the generalised velocities with a reduced set of velocities. These velocities are chosen to be the desired model variables v and ω to be $\boldsymbol{\eta} = \begin{bmatrix} v & \omega \end{bmatrix}^T$. The generalised velocities $\dot{\mathbf{q}}$ can then be expressed in the following manner

$$\dot{\mathbf{q}} = \mathbf{S}\boldsymbol{\eta} \tag{A.12}$$

$$\begin{bmatrix} \dot{x}_A \\ \dot{y}_A \\ \dot{\theta} \\ \dot{\phi}_l \\ \dot{\phi}_r \end{bmatrix} = \begin{bmatrix} \cos(\theta) & 0 \\ \sin(\theta) & 0 \\ 0 & 1 \\ \frac{1}{r} & -\frac{L}{r} \\ \frac{1}{r} & \frac{L}{r} \end{bmatrix} \begin{bmatrix} v \\ \omega \end{bmatrix}$$

The $\mathbf{S}$ matrix represents the kinematics of the DDMR

It can also be shown that the matrix $\mathbf{S}$ is in the null space of $\mathbf{\Lambda}$, meaning $\mathbf{\Lambda S} = \mathbf{S}^T\mathbf{\Lambda}^T = 0$. This property will be used later to transform the constrained EoM to an unconstrained form by eliminating the constraint term $\mathbf{\Lambda}\dot{\mathbf{q}}$.

To derive the EoM, a Lagrangian approach will be taken. Lagrange's equations of motion with generalised forces and torques, and constraints are given by:

$$\begin{aligned} \frac{\mathrm{d}}{\mathrm{d}t}\left(\frac{\partial L}{\partial \mathbf{q}}\right) - \frac{\partial L}{\partial \mathbf{q}} = \mathbf{p} - \mathbf{\Lambda}^T\boldsymbol{\lambda} \\ \mathbf{p} = \begin{bmatrix} 0 & 0 & 0 & \mathcal{T}_l & \mathcal{T}_r \end{bmatrix}^T \end{aligned} \tag{A.13}$$

Where $L = T - V$, T is the total kinetic energy, V is the total potential energy, $\boldsymbol{\lambda}$ is the vector of Lagrange multipliers with one for each constraint, representing the force from each constraint and $\mathcal{T}_l$ and $\mathcal{T}_r$ are the wheel torques. Due to the assumption of in-plane movement, there is no change in potential energy during operation and therefore $L = T$.

The kinetic energy will now be expressed, starting with the wheels

$$T_l = \frac{1}{2}\left(m_w \dot{\mathbf{r}}_l^T \dot{\mathbf{r}}_l + I_m \dot{\theta}^2 + I_w \dot{\phi}_l^2\right) \tag{A.14}$$

$$T_r = \frac{1}{2}\left(m_w \dot{\mathbf{r}}_r^T \dot{\mathbf{r}}_r + I_m \dot{\theta}^2 + I_w \dot{\phi}_r^2\right) \tag{A.15}$$

Where m_w is the total mass of each wheel, I_m is their MoI about an axis through the diameter and I_w is their rotational MoI.

Lastly, the robot body. To express the kinetic energy, a vector CoM is defined.

$$\mathbf{r}_c = \mathbf{r}_A + \mathbf{R}\begin{bmatrix} d & 0 \end{bmatrix}^T \tag{A.16}$$

The kinetic energy can then be expressed as

$$T_f = \frac{1}{2}\left(m_c \dot{\mathbf{r}}_c^T \dot{\mathbf{r}}_c + I_c \dot{\theta}^2\right) \tag{A.17}$$

Where m_c is the mass of the robot and I_c is its MoI about its CoM.

Utilising Eqn. (A.13) the constrained EoM become

$$(m_c + 2m_w)\,\ddot{x}_A + (-dm_c \sin(\theta))\,\ddot{\theta} + (-dm_c \cos(\theta))\left(\dot{\theta}\right)^2 = \lambda_2 \cos(\theta) + \lambda_3 \cos(\theta) - \lambda_1 \sin(\theta) \tag{A.18}$$

$$(m_c + 2m_w)\,\ddot{y}_A + (dm_c \cos(\theta))\,\ddot{\theta} + (-dm_c \sin(\theta))\left(\dot{\theta}\right)^2 = \lambda_1 \cos(\theta) + \lambda_2 \sin(\theta) + \lambda_3 \sin(\theta) \tag{A.19}$$

$$(-dm_c \sin(\theta))\,\ddot{x}_A + (dm_c \cos(\theta))\,\ddot{y}_A + \left(2m_w L^2 + m_c d^2 + I_c + 2I_m\right)\ddot{\theta} = L\lambda_3 - L\lambda_2 \tag{A.20}$$

$$I_w \ddot{\phi}_l = t_l - \lambda_2 r \tag{A.21}$$

$$I_w \ddot{\phi}_r = t_r - \lambda_3 r \tag{A.22}$$

The EoM are put on the following matrix-vector equation form, which will be used for reformulation:

$$\mathbf{H}\ddot{\mathbf{q}} + \mathbf{V}\dot{\mathbf{q}} = \mathbf{E}\mathbf{u} - \boldsymbol{\Lambda}^T \boldsymbol{\lambda} \tag{A.23}$$

To reduce the equations, they are first pre-multiplied by $\mathbf{S}^T$ to eliminate the constraint term $\boldsymbol{\Lambda}^T \dot{\mathbf{q}}$, due to $\mathbf{S}$ being in the null space of $\boldsymbol{\Lambda}$, as explained earlier. Then $\ddot{\mathbf{q}}$ is substituted for $\frac{\mathrm{d}}{\mathrm{d}t}(\mathbf{S}\eta)$ and $\dot{\mathbf{q}}$ for $\mathbf{S}\eta$. Utilising this allows the EoM to be put on unconstrained form:

$$\bar{\mathbf{H}}\dot{\boldsymbol{\eta}} + \bar{\mathbf{V}}\boldsymbol{\eta} = \bar{\mathbf{E}}\mathbf{u} \tag{A.24}$$

$$\bar{\mathbf{H}} = \mathbf{S}^T\mathbf{H}\mathbf{S}, \quad \bar{\mathbf{V}} = \mathbf{S}^T\left(\mathbf{H}\dot{\mathbf{S}} + \mathbf{V}\mathbf{S}\right), \quad \bar{\mathbf{E}} = \mathbf{S}^T\mathbf{E}$$

This also reduced the system to just two equations

A and **B** can then be determined:

$$\mathbf{A} = -\bar{\mathbf{H}}^{-1}\bar{\mathbf{V}}, \qquad \mathbf{B} = \bar{\mathbf{H}}^{-1}\bar{\mathbf{E}} \tag{A.25}$$

$$\mathbf{A} = \begin{bmatrix} 0 & \frac{dm_c r^2 \omega}{2I_w + m_c r^2 + 2m_w r^2} \\ -\frac{dm_c r^2 \omega}{2I_w L^2 + I_c r^2 + 2I_m r^2 + 2L^2 m_w r^2 + d^2 m_c r^2} & 0 \end{bmatrix} \tag{A.26}$$

$$\mathbf{B} = \begin{bmatrix} \frac{r}{2I_w + m_c r^2 + 2m_w r^2} & \frac{r}{2I_w + m_c r^2 + 2m_w r^2} \\ -\frac{Lr}{2I_w L^2 + I_c r^2 + 2I_m r^2 + 2L^2 m_w r^2 + d^2 m_c r^2} & \frac{Lr}{2I_w L^2 + I_c r^2 + 2I_m r^2 + 2L^2 m_w r^2 + d^2 m_c r^2} \end{bmatrix} \tag{A.27}$$

The exact formulation in Eqn. (3.1) can be achieved using the substitution described just below the presentation of the model.

A.2 Justification for Undamped Model

Figure A.1 is used to justify the undamped model

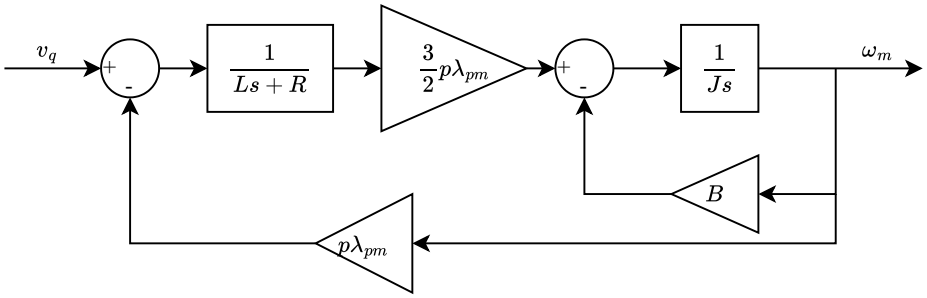

Figure A.1
Block diagram of the simplified linear model.

Inspecting, two feedback mechanisms reduce the effective output torque. The first is normal viscous friction B. The second is a sort of electrical damping due to back-EMF. This damping can be calculated by following the feedback path:

$$B_{elec} = \frac{3p^2\lambda_{pm}^2}{2R} \tag{A.28}$$

Evaluating, this becomes 0,5 Nm s/rad

This is way higher than any mechanical friction in the system and thereby dominates the gain from $v_q \rightarrow \omega_m$.

A.3 Discretisation of HPF

The continuous form of the HPF is:

$$\frac{Y(s)}{U(s)} = \frac{s\omega}{s+\omega} \tag{A.29}$$

The bilinear transform approximates the Laplace operator s as $\frac{2(z-1)}{T_s(z+1)}$. Inserting and simplifying:

$$\frac{Y(z)}{U(z)} = \frac{2\omega\,(z-1)}{(T_s\omega+2)\,z + T_s\omega - 2} \tag{A.30}$$

Multiplying by $\frac{z^{-1}}{z^{-1}}$ to shift back by one sample:

$$\frac{Y(z)}{U(z)} = \frac{2\omega\left(1-z^{-1}\right)}{T_s\omega + 2 + (T_s\omega-2)\,z^{-1}} \tag{A.31}$$

Multiplying across

$$Y(z)\left(T_s\omega + 2 + (T_s\omega-2)\,z^{-1}\right) = U(z)\left(2\omega\left(1-z^{-1}\right)\right) \tag{A.32}$$

Substituting $Y(z)$ for y_k and $Y(z)z^{-1}$ for y_{k-1} etc. the difference equation becomes:

$$y_k\,(T_s\omega+2) + y_{k-1}\,(T_s\omega-2) = 2\omega\,(u_k - u_{k-1}) \tag{A.33}$$

Isolating for y_k, the following result is obtained:

$$y_k = \frac{2\omega}{T_s\omega+2}\,(u_k - u_{k-1}) - \frac{T_s\omega-2}{T_s\omega+2}y_{k-1} \tag{A.34}$$

A.4 Terrain Tester Data Processing

Because the terrain height is measured through rotation of the measuring arm, the minimum increment of the measurement varies with the angle of the arm from vertical. This variation is shown in Figure A.2.

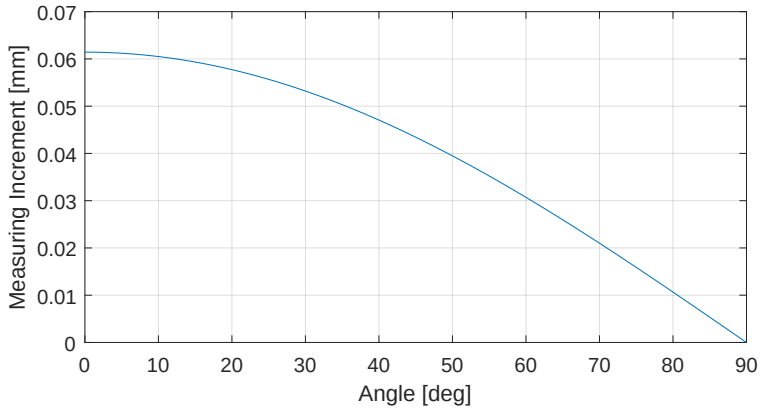

Figure A.2

Measurement increment as a function of arm angle starting from a vertical position.

This shows that the measuring increment is smallest when the arm moves closer to horizontal. However, the largest increment at vertical is still below the requirement of 0,5 mm tolerance so the resolution should be sufficient for the tolerance requirement. The device is designed so that the arm is at 45 degrees when placed on a flat surface. This allows equal amounts of travel both into holes in the contour as well as over bumps. During a measurement, the device is run slowly enough that any dynamics which could be introduced by the spring putting tension on the measurement arm can be neglected.

For each data point, the position of the carriage is logged along with the angular position of the measuring arm. This data has to be converted to the x and y positions of the wheel centre for each data point to get the correct measurement of the terrain. Here, the x-position is the horizontal location along the linear rods and y is the vertical location perpendicular to the linear rods. The y-position of the wheel centre from the encoder reading is calculated with the following equation:

$$y = L\,(1 - \cos(\theta)) \tag{A.35}$$

where y is the y-position of the wheel centre relative to a vertical reference position of the measuring arm, L is the length from the measuring arm's rotating centre to the centre of the wheel, and θ is the angle of the measuring arm. When the arm is resting in a vertical position, the angle is zero.

Because the wheel on the measuring arm rotates around a point, the x-position also changes when the measuring arm rotates. An example of this is shown in figures A.3a and A.3b where the same x-position of the wheel is achieved with two different carriage positions.

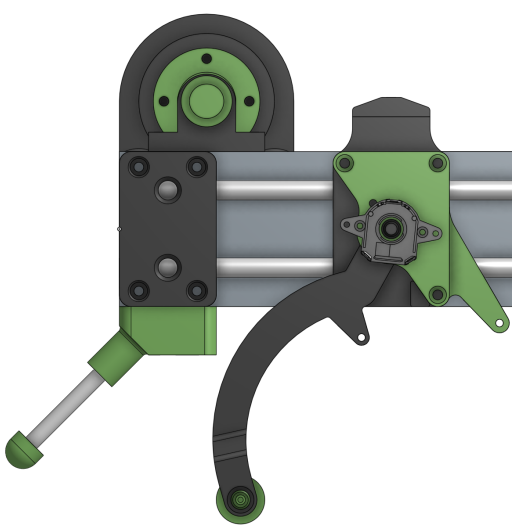

(a) *First position of the measuring arm.*

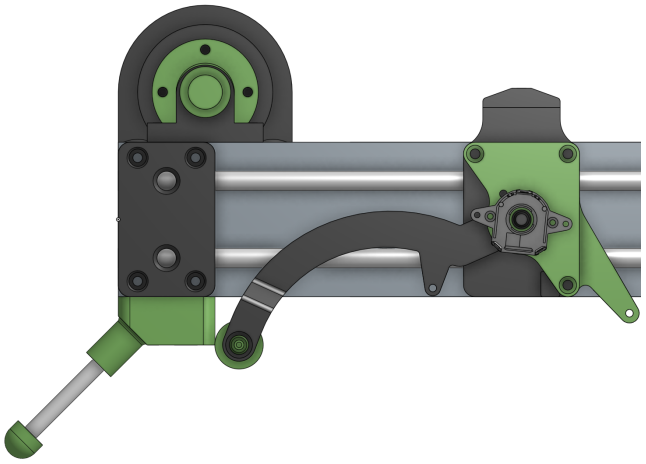

(b) *Second position of the measuring arm that shows that the same x-position of the wheel centre can be obtained with different carriage x-positions.*

Figure A.3

This offset in x-position for each data point is calculated with the following equation:

$$x = x_{carriage} - L\sin(\theta) \tag{A.36}$$

Where x is the wheel centre x-position, $x_{carriage}$ is the x-position of the carriage and θ is the angle of the measuring arm. When the arm is resting in a vertical position the angle is zero.

With the x-position offset implemented to calculate the wheel centre position, it is possible that multiple data points can have the same x-position. This is illustrated earlier in Appendix A.4. If this happens the first instance of the x-position and corresponding y-position is picked. The other data points with the same x-position is removed from the dataset. With the x and y position of the wheel centre obtained for each data point the accuracy and precision of the terrain tester will be evaluated next.

A.5 Conversion from KV to torque constant

The goal is to find the corresponding q-axis current torque constant, based on a KV value. KV is the resulting angular velocity for a given line-to-line voltage given in RPM/V. This is first converted to rad V/s by multiplication of $\frac{2\pi}{60}$. Then, the value is multiplied by $\sqrt{3}$ to convert from line-to-line to phase voltage. Reciprocating, $p\lambda_{pm}$ is obtained

$$p\lambda_{pm} = \frac{60}{2\pi \mathrm{KV}\sqrt{3}} \tag{A.37}$$

The torque constant can then be obtained by multiplication of $\frac{3}{2}$

$$K_T = \frac{3}{2} p\lambda_{pm} = \frac{3}{2} \frac{60}{2\pi \mathrm{KV}\sqrt{3}} \tag{A.38}$$

Evaluating the expression knowing that the motor has 7 pole pairs and a KV of 190 results in a torque constant of:

$$K_T = 190 \, \frac{\mathrm{Nm}}{\mathrm{A}} \tag{A.39}$$

A.6 Video Analysis Script

```
%% Load the Video
clear all
close all
vid = VideoReader('HydOilTest.mov');

% Read the first frame and display it
frame1 = readFrame(vid);
imshow(frame1);
title('Select the point to track');
hold on;

%% Manual Selection of Tracking Point
[x, y] = ginput(1); % User selects point
point = [x, y];

% Initialize the Point Tracker
tracker = vision.PointTracker('MaxBidirectionalError', 2);
initialize(tracker, point, frame1);

%% Track the Point and Show on Each Frame
positions = [];
time = [];
frame_idx = 1;

figure; % Create a figure for visualization

while hasFrame(vid)
    frame = readFrame(vid);
    [point, validity] = tracker(frame);

    if validity
        positions(frame_idx, :) = point;  % Store (x, y) position
    else
        positions(frame_idx, :) = [NaN, NaN]; % Handle lost tracking
    end

    time(frame_idx) = frame_idx / vid.FrameRate; % Compute time in
       seconds

    % Show the current frame with the tracked point
    imshow(frame);
```

```
    hold on;
    if validity
        plot(point(1), point(2), 'ro', 'MarkerSize', 10, 'LineWidth', 2);
            % Red circle at the tracked point
    end
    title(sprintf('Frame %d - Time %.2f s', frame_idx, time(frame_idx)));
    hold off;
    pause(1 / vid.FrameRate); % Play in real-time

    frame_idx = frame_idx + 1;
end

%% Scale Pixels to Real-World Units
% User selects two points on the ruler with a known real-world distance
imshow(frame1);
title('Select two points on the ruler');
[x_ruler, y_ruler] = ginput(2);

% Compute the pixel distance between the ruler points
pixel_length = sqrt((x_ruler(2) - x_ruler(1))^2 + (y_ruler(2) - y_ruler
    (1))^2);

% Define the known real-world length in mm (adjust as needed)
real_length_mm = 50;  % Example: 50 mm

% Compute scale factor (mm per pixel)
scale_factor = real_length_mm / pixel_length;

% Convert positions to real-world units (mm)
positions_real = positions * scale_factor;

% Offset data
positions_real(:,2) = positions_real(:,2)*(-1);
positions_real(:,2) = positions_real(:,2) - positions_real(1,2);

% Slo mo time correction for 240 fps video
time_real = time./8;
%% Plot Position Over Time
figure;
plot(time_real, positions_real(:,2), 'b-', 'LineWidth', 2);
xlabel('Time [s]');
ylabel('Vertical Position [mm]');
grid on;
```

```
xlim([0 max(time_real)])
ylim([min(positions_real(:,2))-2 max(positions_real(:,2))+2])
%% Save Data
data = [time', positions_real];
save('y-pos.mat', 'positions_real');
save('time_real.mat', 'time_real');

% Save plot
ax = gca;
exportgraphics(ax,'WheelDropResponse.pdf','ContentType','vector')
```

A.7 Electrical Schematic

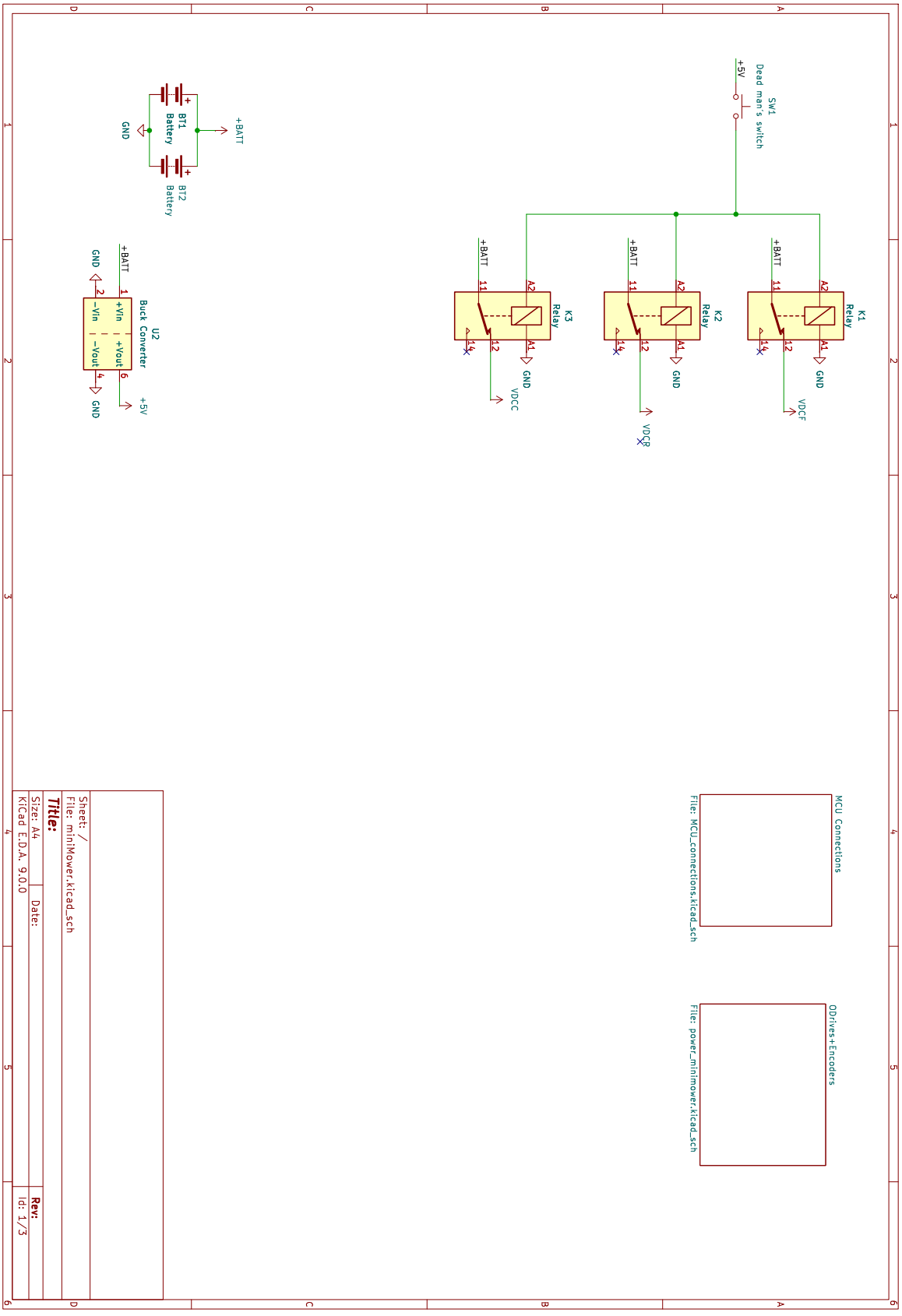

STM connectors

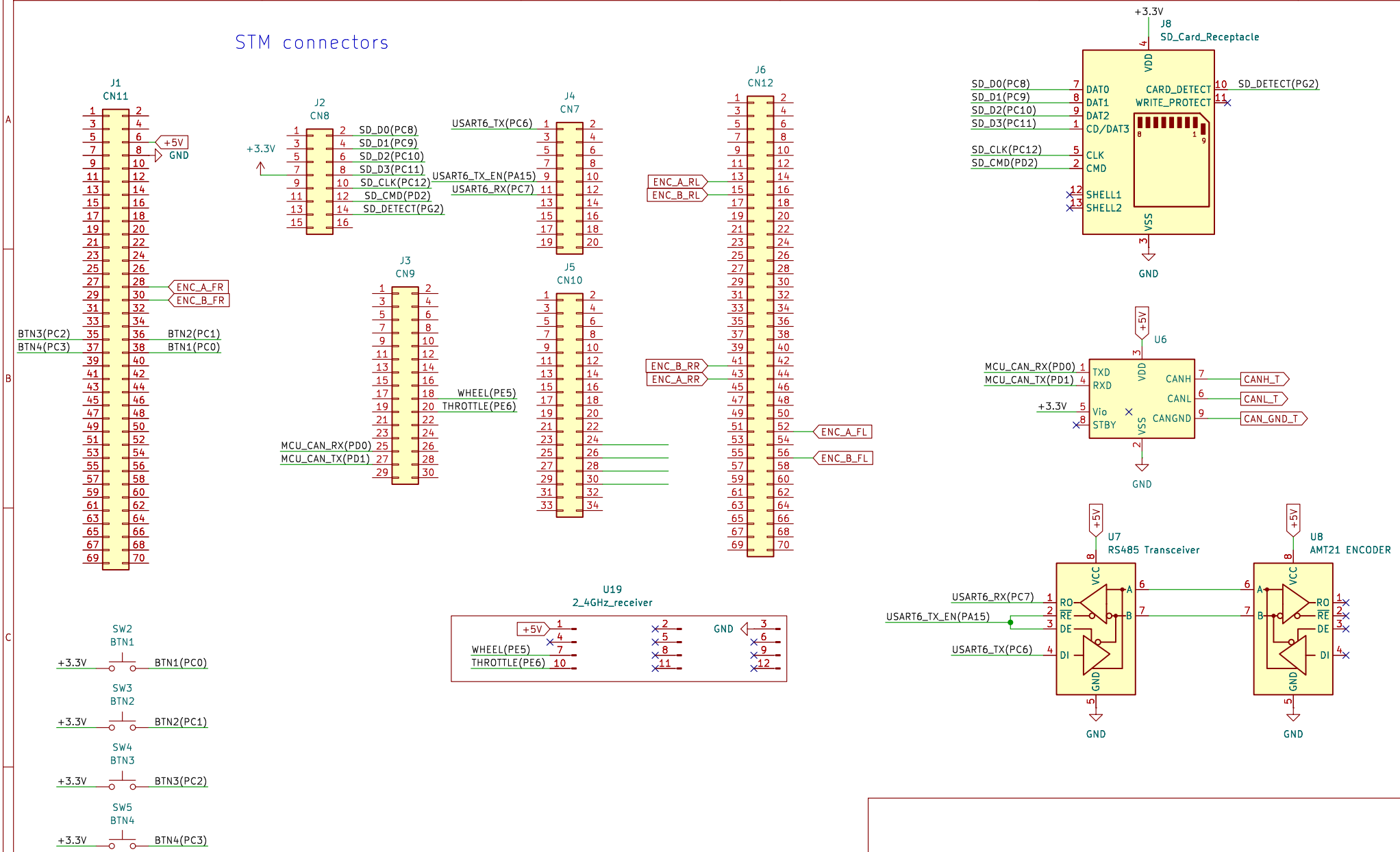

Sheet: /MCU Connections/
File: MCU_connections.kicad_sch

Title:

Size: A4	Date:	**Rev:**
KiCad E.D.A. 9.0.0		Id: 2/3

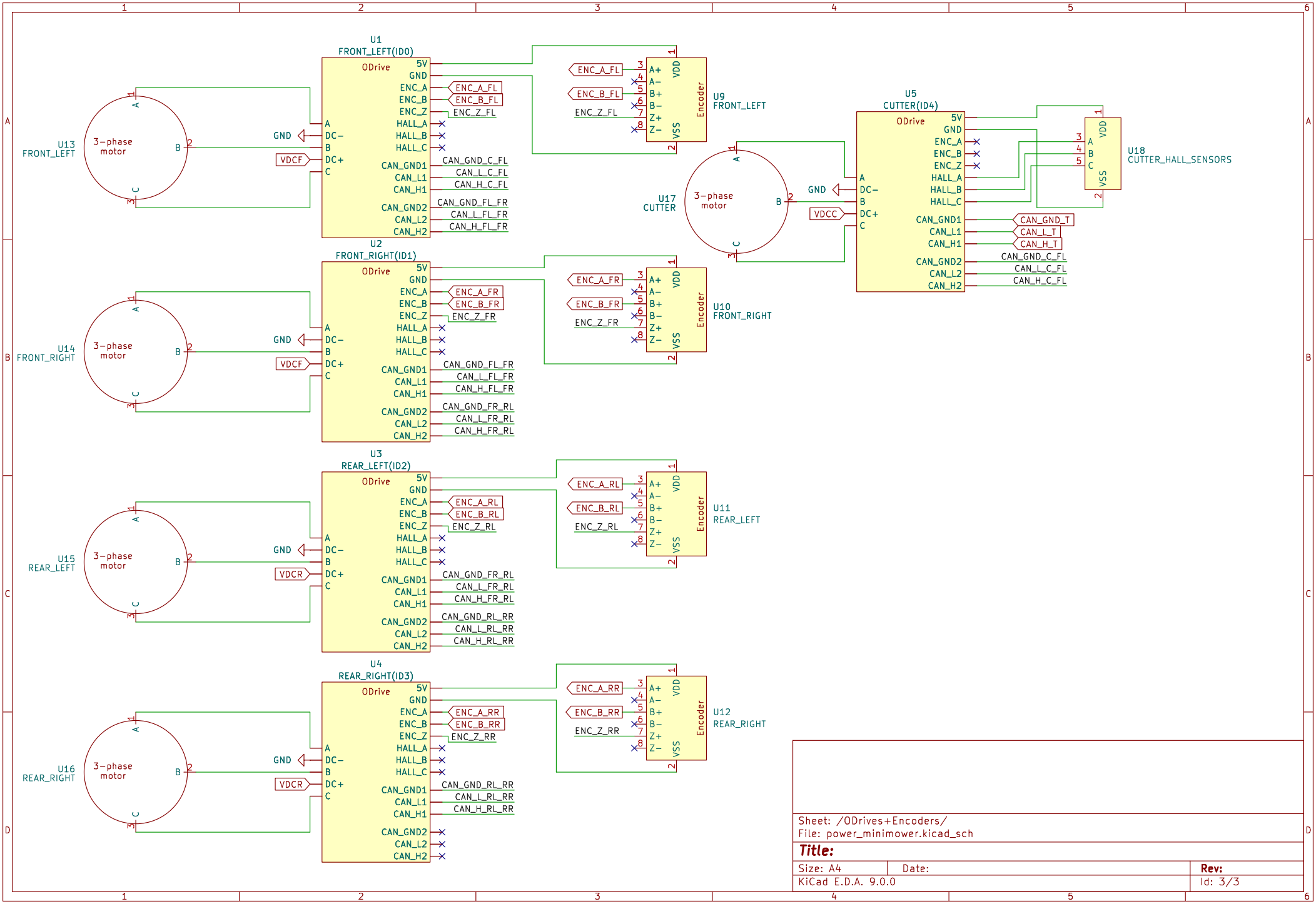

Sheet: /ODrives+Encoders/
File: power_minimower.kicad_sch

Title:

Size: A4	Date:	**Rev:**
KiCad E.D.A. 9.0.0		Id: 3/3

A.8 In-Plane Kinematics

The derivation of the kinematics is based on Figure A.4.

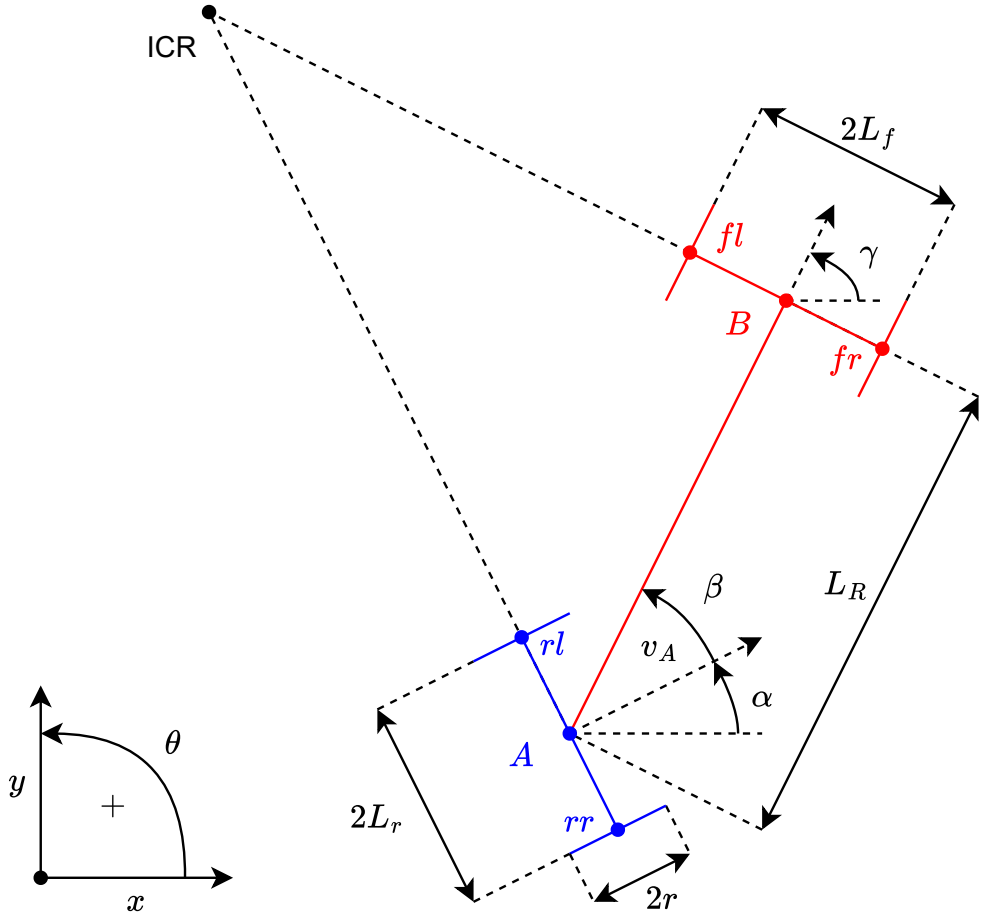

Figure A.4

Figure used for the derivation of the kinematics.

Deriving the kinematics entails converting the selected velocities v_A and $\dot{\beta}$ to all the generalised velocities $\dot{\mathbf{q}}$ as visualised below:

$$\dot{\mathbf{q}} = \mathbf{S}\boldsymbol{\eta} \tag{A.40}$$

$$\begin{bmatrix} \dot{x}_A \\ \dot{y}_A \\ \dot{\alpha} \\ \dot{\gamma} \\ \dot{\phi}_{rl} \\ \dot{\phi}_{rr} \\ \dot{\phi}_{fl} \\ \dot{\phi}_{fr} \end{bmatrix} = \begin{bmatrix} ? & ? \\ ? & ? \\ ? & ? \\ ? & ? \\ ? & ? \\ ? & ? \\ ? & ? \\ ? & ? \end{bmatrix} \begin{bmatrix} v_A \\ \dot{\beta} \end{bmatrix}$$

$\dot{x}_A$ and $\dot{y}_A$ are found by projecting the v_A onto the global axes using the α, they are thereby:

$$\dot{x}_A = \cos(\alpha) v_A \tag{A.41}$$

$$\dot{y}_A = \sin(\alpha) v_A \tag{A.42}$$

The angular velocities are given by the tangential velocity divided by the turning radius. The turning radius for point A is found by utilising the right angle triangle formed by point A, B and the ICR. r_A and the resulting angular velocities are then:

$$r_A = \frac{L_R}{\cos\left(\frac{\pi}{2} - \beta\right)} = \frac{L_R}{\sin(\beta)} \tag{A.43}$$

$$\dot{\alpha} = \frac{v_A}{r_A} - \dot{\beta} = v_A \frac{\sin(\beta)}{L_R} - \dot{\beta} \tag{A.44}$$

$$\dot{\gamma} = v_A \frac{\sin(\beta)}{L_R} \tag{A.45}$$

For the wheel velocities, the distance to the ICR from each wheel is first determined, again using the right-angle triangle

$$r_{rl} = r_A - L_r \tag{A.46}$$

$$r_{rr} = r_A + L_r \tag{A.47}$$

$$r_B = \tan\left(\frac{\pi}{2} - \beta\right) L_R \tag{A.48}$$

$$r_{fl} = r_B - L_f \tag{A.49}$$

$$r_{fr} = r_B + L_f \tag{A.50}$$

The front wheels are not affected by $\dot{\beta}$ and their rotational angular velocities are thereby given by:

$$\dot{\phi}_{fl} = v_A \frac{r_{fl}}{r_A r} = v_A \left(\frac{\cos(\beta)}{r} - \frac{L_f \sin(\beta)}{L_R r}\right) \tag{A.51}$$

$$\dot{\phi}_{fr} = v_A \frac{r_{fr}}{r_A r} = v_A \left(\frac{\cos(\beta)}{r} + \frac{L_f \sin(\beta)}{L_R r}\right) \tag{A.52}$$

The rear wheels are additionally affected by $\dot{\beta}$ according to their distance from point A L_r

$$\dot{\phi}_{rl} = v_A \frac{r_{rl}}{r_A r} + \dot{\beta}\frac{L_r}{r} = v_A \left(\frac{1}{r} - \frac{L_r \sin(\beta)}{L_R r}\right) + \dot{\beta}\frac{L_r}{r} \tag{A.53}$$

$$\dot{\phi}_{rr} = v_A \frac{r_{rr}}{r_A r} - \dot{\beta}\frac{L_r}{r} = v_A \left(\frac{1}{r} + \frac{L_r \sin(\beta)}{L_R r}\right) - \dot{\beta}\frac{L_r}{r} \tag{A.54}$$

Factoring out v_A and $\dot{\beta}$ results in the **S** given in Eqn. (6.28)

$$\mathbf{S} = \begin{bmatrix} \cos(\alpha) & 0 \\ \sin(\alpha) & 0 \\ \frac{\sin(\gamma-\alpha)}{L_R} & -1 \\ \frac{\sin(\gamma-\alpha)}{L_R} & 0 \\ \frac{1}{r} - \frac{L_r \sin(\gamma-\alpha)}{L_R r} & \frac{L_r}{r} \\ \frac{1}{r} + \frac{L_r \sin(\gamma-\alpha)}{L_R r} & -\frac{L_r}{r} \\ \frac{\cos(\gamma-\alpha)}{r} - \frac{L_f \sin(\gamma-\alpha)}{L_R r} & 0 \\ \frac{\cos(\gamma-\alpha)}{r} + \frac{L_f \sin(\gamma-\alpha)}{L_R r} & 0 \end{bmatrix}$$

A.9 Dynamic Model Derivation Script

```
%% Define all parameters and coordinates
syms L_r L_f L_R r d d_1 d_2
assume([L_r L_f L_R r], {'real', 'positive'});
assume([d d_1 d_2],'real');
syms x_A(t) y_A(t) alpha(t) gamma(t) phi_fl(t) phi_fr(t) phi_rl(t) phi_rr
   (t) v_A(t) beta(t) t_rl(t) t_rr(t) t_fl(t) t_fr(t)
assume([t x_A(t) y_A(t) alpha(t) gamma(t) phi_rl(t) phi_rr(t) phi_fl(t)
   phi_fr(t) v_A(t) beta(t) t_rl(t) t_rr(t) t_fl(t) t_fr(t)], 'real');

q = [x_A(t); y_A(t); alpha(t); gamma(t); phi_rl(t); phi_rr(t); phi_fl(t);
    phi_fr(t)];
dq = diff(q,t);
ddq = diff(dq,t);

%% Position and rotation matrices
r_rl_A = [0; L_r];
r_rr_A = [0; -L_r];
r_AB_B = [L_R; 0];
r_fl_B = [0; L_f];
r_fr_B = [0; -L_f];
r_Ac_B = [d; 0];
r_A = [x_A(t); y_A(t)];
dr_A = diff(r_A,t);
R_1 = [cos(alpha(t)), -sin(alpha(t))
       sin(alpha(t)), cos(alpha(t))];
R_2 = [cos(gamma(t)), -sin(gamma(t))
       sin(gamma(t)), cos(gamma(t))];

r_rl = r_A + R_1*r_rl_A;
r_rr = r_A + R_1*r_rr_A;
r_c = r_A + R_2*r_Ac_B;
r_B = r_A + R_2*r_AB_B;
r_fl = r_A + R_2*(r_AB_B + r_fl_B);
r_fr = r_A + R_2*(r_AB_B + r_fr_B);

%% Velocities
dr_rl = diff(r_rl,t);
dr_rr = diff(r_rr,t);
dr_c = diff(r_c,t);
dr_B = diff(r_B,t);
dr_fl = diff(r_fl,t);
```

```
dr_fr = diff(r_fr,t);

%% Kinematics
beta_sub = gamma(t) - alpha(t);
ra_B = simplify(L_R/cos(pi/2 - beta_sub));

ra_rl = (ra_B - L_r);
ra_rr = (ra_B + L_r);

ra_fl = simplify(expand((tan(pi/2 - beta_sub)*L_R) - L_f));
ra_fr = simplify(expand((tan(pi/2 - beta_sub)*L_R) + L_f));


S = simplify(expand([cos(alpha(t)), 0
                     sin(alpha(t)), 0
                     1/ra_B, -1
                     1/ra_B, 0
                     ra_rl/(r*ra_B), L_r/r
                     ra_rr/(r*ra_B), -L_r/r
                     ra_fl/(r*ra_B), 0
                     ra_fr/(r*ra_B), 0]));
dS = diff(S,t);

%% Constraints
vec_alpha = [cos(alpha(t)); sin(alpha(t))];
vec_alpha_perp = [-vec_alpha(2); vec_alpha(1)];
vec_gamma = [cos(gamma(t)); sin(gamma(t))];
vec_gamma_perp = [-vec_gamma(2); vec_gamma(1)];

c = simplify(expand([(dr_A.')*vec_alpha_perp
                     (dr_B.')*vec_gamma_perp
                     (dr_rl.')*vec_alpha - r*dq(5)
                     (dr_rr.')*vec_alpha - r*dq(6)
                     (dr_fl.')*vec_gamma - r*dq(7)
                     (dr_fr.')*vec_gamma - r*dq(8)]));

syms lambda [6 1]
assume(lambda, 'real')
Lambda = equationsToMatrix2(c,dq);

%% Energies

syms I_w I_m m_w I_r m_r I_f m_f h a
```

```
assume([I_w I_m m_w I_r m_r I_f m_f h],{'real', 'positive'});


% Rear body
E_r = 1/2*m_r*(sum(dr_A.^2)) + 1/2*I_r*dq(3)^2;

% Front body
E_f = 1/2*m_f*(sum(dr_c.^2)) + 1/2*I_f*dq(4)^2;

% Wheels
E_w_rl = 1/2*m_w*(sum(dr_rl.^2)) + 1/2*I_m*dq(3)^2 + 1/2*I_w*dq(5)^2;
E_w_rr = 1/2*m_w*(sum(dr_rr.^2)) + 1/2*I_m*dq(3)^2 + 1/2*I_w*dq(6)^2;
E_w_fl = 1/2*m_w*(sum(dr_fl.^2)) + 1/2*I_m*dq(4)^2 + 1/2*I_w*dq(7)^2;
E_w_fr = 1/2*m_w*(sum(dr_fr.^2)) + 1/2*I_m*dq(4)^2 + 1/2*I_w*dq(8)^2;

% Total
T = collect(simplify(expand(E_r + E_f + E_w_rl + E_w_rr + E_w_fl + E_w_fr
   )),dq);
R = 1/2*h*(sum(dq(5:end).^2)); % Rayleigh dissipation function
% R = 1/2*h*(sum(tanh(a*dq(5:end))));

u = [t_rl(t); t_rr(t); t_fl(t); t_fr(t)];

E = [zeros(4,4)
     eye(4,4)];

syms u_f [2 1]
% E = [zeros(4,2)
%      S(5:end,:)];

eta = [v_A(t); diff(beta(t),t)];
deta = diff(eta,t);
S_beta = subs(S,gamma(t)-alpha(t),beta(t));

dq_sub = simplify(S*eta);
ddq_sub = simplify(diff(S*eta,t));
dq_sub_beta = simplify(S_beta*eta);
ddq_sub_beta = simplify(diff(S_beta*eta,t));
LG_eqn = collect(simplify(diff(gradient(T,dq),t) - gradient(T,q)),[ddq;dq
   ]) == E*u + collect(Lambda.'*lambda,[cos(alpha(t)), sin(alpha(t)), cos
   (gamma(t)), sin(gamma(t)), L_r, L_f])
```

```
%% System matrices
H = simplify(equationsToMatrix2(lhs(LG_eqn),ddq))
C = simplify(equationsToMatrix2(lhs(LG_eqn),dq))
%W = simplify(equationsToMatrix2(gradient(R,dq),dq))

sub_param = [m_f+m_r+4*m_w; 2*L_R*m_w+d*m_f; 2*m_w*L_r^2+2*I_m+I_r; 2*m_w
   *L_R^2+2*m_w*L_f^2+m_f*d^2+I_f+2*I_m];
syms m J J_A J_B
param_sub = [m; J; J_A; J_B];

H_bar = collect(simplify(expand(S.'*H*S)),[cos(2*(q(4)-q(3)));sin(2*(q(4)
   -q(3)))]);
H_bar_beta = subs(H_bar,gamma(t)-alpha(t),beta(t));
C_bar = collect(simplify(expand(S.'*(H*dS + C*S))),dq(4)-dq(3));
C_bar_beta = collect(simplify(expand(subs(C_bar,[dq(4)-dq(3),q(4)-q(3)],[
   eta(2),beta(t)]))),eta);
E_bar = simplify(expand(S.'*E));
E_bar_beta = subs(E_bar,gamma(t)-alpha(t),beta(t));

f_deta_base = collect(simplify(expand(H_bar\((-C_bar)*eta))),eta);
f_deta_base = collect(simplifyFraction(expand(subs(f_deta_base,[dq(4)-dq
   (3), q(4) - q(3)],[eta(2), beta(t)]))),eta);

f_deta_u = collect(simplify(expand(subs(H_bar\(E_bar*u), q(4) - q(3),
   beta(t)))),u);

f_deta = f_deta_base + f_deta_u
```

A.10 Physically Motivated State-Feedback Controller Parameters

Name	Symbol	Value
Front half track width	L_f	0,1635 m
Rear half track width	L_r	0,1535 m
Wheelbase	L_R	0,591 m
Front CoM offset	d	0,357 m
Wheel assembly mass	m_w	1,9 kg
Wheel assembly MoI about diameter	I_m	$8{,}17 \cdot 10^{-3}$ kg m^2
Wheel rotational MoI	I_w	$8{,}22 \cdot 10^{-3}$ kg m^2
Rear body mass	m_r	0,4 kg
Rear body MoI	I_r	$1{,}51 \cdot 10^{-3}$ kg m^2
Front body mass	m_f	6,145 kg
Front body MoI about CoM	I_f	$1{,}88 \cdot 10^{-3}$ kg m^2
Wheel radius	r	0,105 m

Table A.1
Model/controller parameters.

A.11 Transmitter Trigger and Wheel mapping

The PWM duty cycle to normalised input can be seen in Figure A.5.

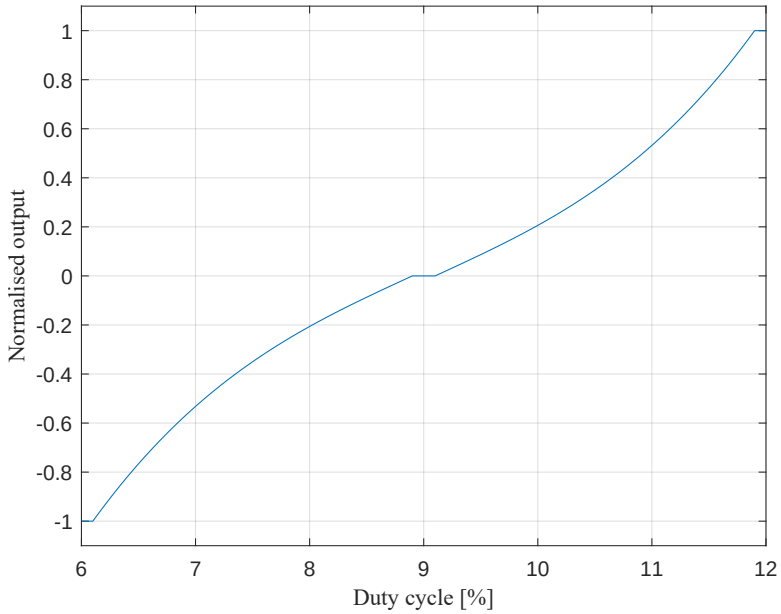

Figure A.5

Dead zones are utilised in the middle and at the extremes, due to tolerances on the PWM duty cycles. Between the middle dead zone and the outer dead zone, a cubic polynomial is used to map the references. This makes the robot easier to control at lower velocities and articulation angles.

A.12 Zip File

1. item. File name: Turf Tank Two Robot Making Audible Noise.MOV
2. item. File name: MowerClimbingHill.MOV